Latitudinal Variations of Denudation Rates along the Western Andes in South America derived from Cosmogenic Radionuclides

Dissertation

der Mathematisch-Naturwissenschaftlichen Fakultät

der Eberhard Karls Universität Tübingen

zur Erlangung des Grades eines

Doktors der Naturwissenschaften

(Dr. rer. nat.)

vorgelegt von

Jessica Steinbach geb. Starke

aus Berlin

Tübingen

2019

Gedruckt mit Genehmigung der Mathematisch-Naturwissenschaftlichen Fakultät der Eberhard Karls Universität Tübingen.

Tag der mündlichen Prüfung:	9. Juli 2019
Dekan:	Prof. Dr. Wolfgang Rosenstiel
1. Berichterstatter:	Prof. Dr. Todd Ehlers
2. Berichterstatter:	Prof. Dr. Tibor Dunai

Erklärung

Ich erkläre hiermit, dass ich die zur Promotion eingereichte Arbeit selbständig verfasst, nur die angegebenen Quellen und Hilfsmittel benutzt und wörtlich oder inhaltlich übernommene Stellen als solche gekennzeichnet habe. Ich erkläre, dass die Richtlinien zur Sicherung guter wissenschaftlicher Praxis der Universität Tübingen (Beschluss des Senats vom 25.5.2000) beachtet wurden. Ich versichere an Eides statt, dass diese Angaben wahr sind und dass ich nichts verschwiegen habe. Mir ist bekannt, dass die falsche Abgabe einer Versicherung an Eides statt mit Freiheitsstrafe bis zu drei Jahren oder mit Geldstrafe bestraft wird.

Tübingen, 30. Januar 2019

WHAT DID DARTH VADER TELL THE GEOLOGIST? MAY THE QUARTZ BE WITH YOU!

Anonymous Author

Abstract

Tectonic, climatic and biotic forces interact and imprint surface processes that shape topographic relief. The combination of chemical weathering and physical erosion on the Earth's surface is defined as denudation rate. Catchment- averaged denudation rates are one of the main parameters in geological research to quantify surface processes over millennial time scales. The advantage of this method is to identify the characteristics of surface processes previous to human impact.

Denudation rates are derived from cosmogenic nuclides which are rare isotopes that are created by cosmic radiation, such as ^{10}Be and ^{26}Al. Cosmogenic nuclides are produced in the atmosphere (meteoric-produced isotopes) or within the mineral structure of different rock material at the surface (in situ-produced isotopes). In situ-produced ^{10}Be is commonly obtained from quartz which is one of the most frequent minerals on the Earth's surface and, hence, allows a wide range of applications for this method.

The identification of dominant natural controls on surface processes in different environmental settings is challenging. With this study, for the first time, this challenge can be solved by including catchment-averaged denudation rates in multivariate statistical-analyses along with tectonic, climatic and biotic catchment parameters. The objective of this thesis is to investigate the dominant natural controls on catchment-averaged denudation rates within different environmental end-members of the Western Andes in South America. The study area covers the environmental end-members reaching from the hyper arid Atacama Desert to the glaciated regions of the Northern Patagonian Ice Fields.

The results of this thesis show that local tectonic processes have the highest influence on denudation rates in the arid to hyper arid environments of northern Chile. In between the environmental end-members the effect of vegetation and precipitation on denudation rate varies depending on the initial vegetation-cover amount. In environments with high initial vegetation cover, vegetation is decelerating sediment transportation and is limiting the maximum variation in denudation rates. In the glaciated environment of the Northern

Patagonian Ice Field, the latitudinal variation of denudation rates is dependent on the variations in vegetation cover in glaciated and deglaciated catchments.

Zusammenfassung

Topographisches Relief wird durch tektonische, klimatische und biotische Prozesse beeinflusst, die interagieren und die Erdoberfläche prägen. Die Kombination aus chemischer Verwitterung und physikalischer Erosion auf der Erdoberfläche wird als Denudationsrate definiert. Denudationsraten werden über Flusseinzugsgebiete gemittel und sind einer der wichtigsten Parameter zur Quantifizierung von Oberflächenprozessen über die Zeitspanne von Jahrtausenden in der geologischen Forschung. Der Vorteil dieser Methode besteht darin, Oberflächenprozesse zeitlich vor dem Einfluss des Menschen zu identifizieren.

Denudationsraten werden von kosmogenen Nukliden abgeleitet, bei denen es sich um seltene Isotope handelt, die durch kosmische Strahlung erzeugt werden, beispielsweise ^{10}Be und ^{26}Al. Kosmogene Nuklide werden in der Atmosphäre (meteorisch erzeugte Isotope) oder in der Mineralstruktur verschiedener Gesteinsmaterialien an der Oberfläche (in situ produzierte Isotope) erzeugt. In situ produziertes ^{10}Be wird im Allgemeinen aus Quarz gewonnen, das zu den häufigsten Mineralien auf der Erdoberfläche zählt, wodurch dieses Verfahren für eine Vielzahl von Anwendungen eingesetzt werden kann.

Die Identifikation von dominierenden natürliche Einflussfaktoren auf Oberflächen-prozesse aus verschiedenen Umweltzonen ist herausfordernd. Mit dieser Arbeit wird diese Herausforderung zum ersten Mal mittels einer multivariaten statistischen Analyse und durch die darin angewandte Kombination von Denudationsraten und tektonischen, klimatischen sowie biotischen Flusseinzugsgebietsparametern gelöst. Das Ziel dieser Arbeit ist es, die dominierenden natürlichen Einflussfaktoren auf Denudationsraten in verschiedenen Endgliedern von Umweltzonen der westlichen Anden in Südamerika zu untersuchen. Das Untersuchungsgebiet umfasst die Entglieder der Umweltzonen von der hyperariden Atacama-Wüste bis zu den vergletscherten Regionen der nordpatagonischen Eisfelder.

Die Ergebnisse dieser Arbeit zeigen, dass die in den ariden bis hyperariden Umweltzonen von Nordchile, lokalisierte tektonische Prozesse den höchsten Einfluss auf die

Denudationsraten haben. Zwischen den Endglieder der Umweltzonen variiert die Auswirkung von Vegetation und Niederschlag auf die Denudationsrate in Abhängigkeit von der anfänglichen Vegetationsbedeckungsmenge. In Umwelzonen mit einer hohen anfänglichen Vegetationsbedeckung verlangsamt die Vegetation den Sedimenttransport und begrenzt die maximale Variation der Denudationsraten. In der vergletscherten Umweltzone des nördlichen Patagonischen Eisfelds wird die maximale Variation in Denudationsraten durch die Variationen in der Vegetationsentwicklung limitiert, die linear mit dem Denudationsratenmuster zusammenhängt.

Table of contents

Introduction

1 Motivation and objectives

1.1 Background

Erosion is a physical process of transporting material by natural forces (e.g. wind, water). In contrast, weathering does not involve movement but breaks down and dissolves rocks by chemical alteration (Chesworth, 1992). Quantifying chemical weathering and physical erosion has importance for a wide range of research questions in geology, geomorphology, biogeochemistry and agricultural sciences. Weathering and erosion are the fundamental processes for soil development or loss and therefore define agricultural productivity (Stamey and Smith, 1964). In biogeochemistry, the release and transport of solutes and nutrients to rivers and oceans is essential for environmental engineering and monitoring (Schlesinger and Bernhardt, 2013). Erosion rate and sediment flux measurements are used for geomorphological risk assessment, which identifies the vulnerability of regions that form habitats for humans, fauna and flora (Morgan and Rickson, 2003). In geology, large-scale continental erosion triggers processes that drive landscape evolution and mountain building (Pinet and Souriau, 1988).

A major challenge in geosciences is to reconstruct processes and environments without agricultural influence and human impact. Determining weathering and long-term erosion over millennial timescales prior to human impact is possible using cosmogenic nuclides. Cosmogenic nuclide analyses provide opportunities for dating surfaces and measuring catchment-averaged denudation rates. The latter are defined as a combination of chemical weathering and physical erosion averaged over river catchment scale (von Blanckenburg, 2005).

Tectonic, climatic and biotic processes interact and imprint topographic relief. Cosmogenic nuclide analyses elucidate landscape dynamics and the controls on the temporal and spatial evolution of topography (von Blanckenburg, 2005). Consequently, to resolve landscape dynamics, the identification of relationships between tectonic, climatic and vegetational parameters and the correlation to catchment-wide denudation rates over spatial gradients is needed. Solving major questions of landscape dynamics and paleo-environments, provides new opportunities to enhance landscape-forecast models on Earth and to reconstruct paleo-landscapes of other Earth-like planets (Thomas et al., 2005).

1.2 Study Area: Andean Mountains

This thesis is organized in three scientific chapters (PAPER I to III). The scientific chapters I to II study the Western Andean Margin of southern Peru and northern to central Chile along the mountain ranges of the Coastal and Western Cordilleras. The study area of the science chapter III is situated in southern Chile in the northern Patagonian ice fields and fjord lands (Figure 1A).

The Western Andes represent an ideal research setting of an approximately similar tectonic setting within a significant climatic and vegetational gradient. Figure 1B exemplarily illustrates this high climatic gradient in South America by means of mean annual precipitation (MAP). The combination of unique conditions in the Western Andes has high potential to disentangle specific processes that influence denudation rates.

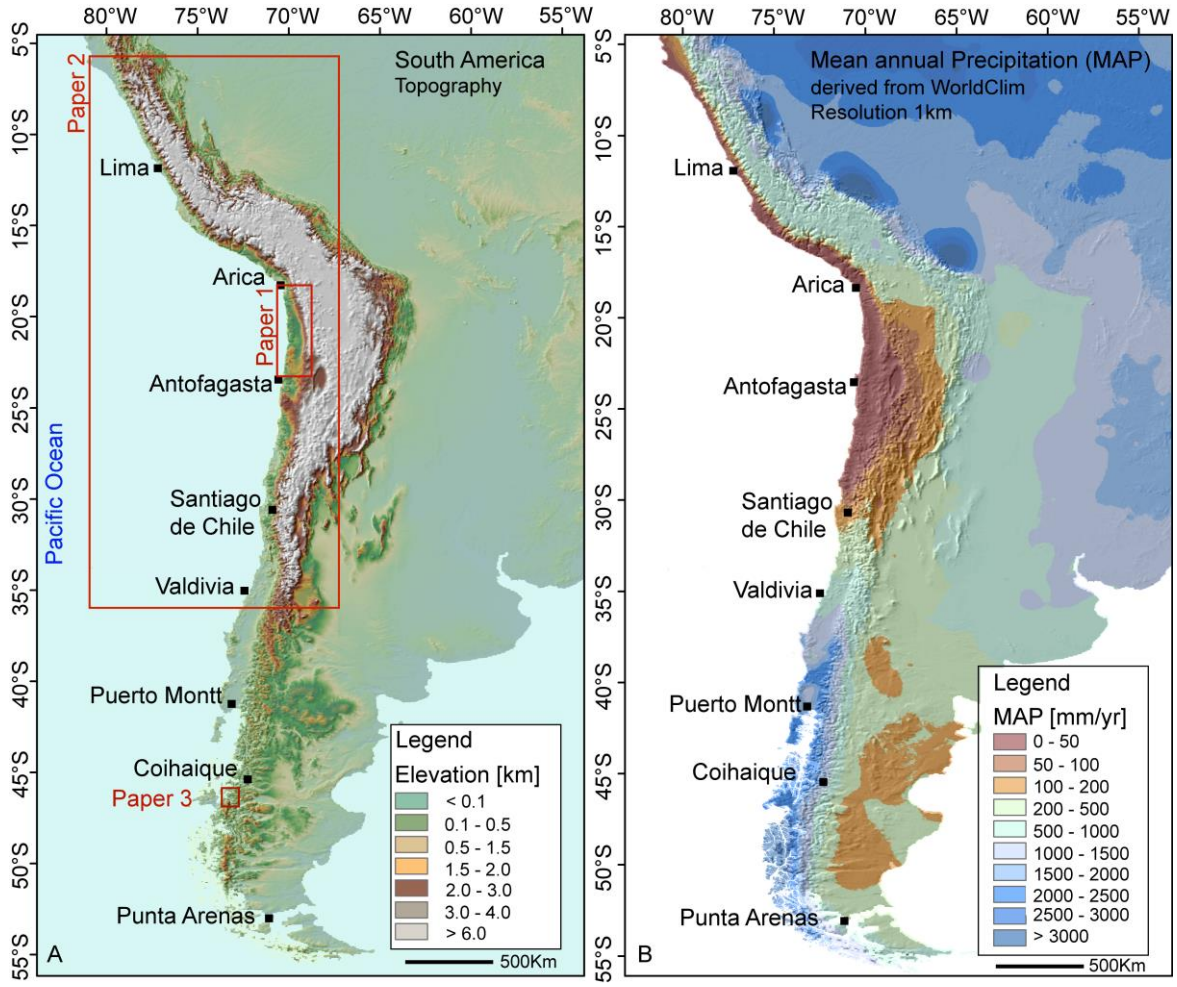

Figure 1. A) Topographic overview of South America derived from SRTM (USGS, 2000). Study areas of the science chapters (PAPER I to III) of this thesis are shown in red boxes. B) Mean annual precipitation (MAP) map of South America derived from WorldClim (Fick and Hijmans, 2017).

Today topographic relief in South America is dominated by the Andes Mountains, which extend along the Pacific Coast with elevations up to 6 km above sea level (Figure 1). The Andes are primarily created by the convergence of the Nazca and South American tectonic plates (Allmendinger et al., 1997). The exact timing and sequence of the Andean mountain building as well as the change in landscape dynamics in response to the mountain evolution are still a matter of debate (Oncken et al., 2006).

1.3 Objectives and hypotheses

This thesis quantifies catchment-averaged denudation rates at the Western Andes in South America and evaluates which parameters and processes have the strongest influence on denudation rates. The thesis approach aims to analyze denudation rates derived from different environments which will be described as environmental end-members in the thesis. One environmental end-member is the hyper arid Atacama Desert in northern Chile that is assumed to represent the driest environment on Earth (Amundson et al., 2012). The opposite environmental end-member is the glaciated environment of the Northern Patagonian Ice Fields (Warren and Sugden, 1993). With reference to the thesis approach three general objectives and hypotheses can be identified:

(1) **[Tectonic and climatic control on denudation rates in arid to hyper arid regions]** The first objective aims to understand the interaction of tectonic and climatic parameters that influence denudation rates in an end-member environment of arid to hyper arid climate conditions. Climate conditions range from arid to hyper arid characteristics that are expected to have a low potential to overprint denudation rates due to low precipitation that is limiting sediment-transportation efficiency. The study area is situated in a syntaxial orogen in Northern Chile. In a syntaxial orogeny, a subduction zone geometry is seismically described by a bulge (or slight shallowing in plate dip) in the subducting plate (Hayes et al., 2012). However, definitions of syntaxial orogens vary within the literature. This thesis follows the definition of Bendick and Ehlers (2014) which states that a syntaxis is the narrow, cuspate region linking two adjacent subduction segments, and includes both the down going and overriding plates.

    In this environmental setting, the thesis tests the following hypothesis: If the syntaxial geometry of the subducting Nazca plate causes spatial variations in rock uplift, then (1) this variation is represented in long-wavelength (latitudinal) variations in topography and, then (2) the denudation rates increase towards the center of the syntaxial bend.

(2) **[Influence of vegetation cover on denudation rates across climate gradients]** The second objective aims to compliment the results from the first objective by extending the analysis to regions that cross climate gradients. Consequently, denudation rates of catchments draining the Western Andes are analyzed from 6°S to 36°S latitude in Southern Peru and Northern to Central Chile (Figure 1). In addition, to the analysis of the traditional tectonic and climatic parameters the influence of

vegetation on denudation rates is explored in this study. The impact of vegetation on the shape and evolution of Earth's surface ranges from (1) the microscopic scale of Mycorrhiza weathering for plant nutrition to (2) macroscopic scales where plants retard hillslope erosion, stabilize environments for sediment deposition, and affect precipitation through evapotranspiration and leaf phenology (Schwartzman and Volk, 1989; Berner, 1997; Retallack, 1997; Derry, 2006; Stokes et al., 2008; Dosseto et al., 2010; Galy et al., 2015; Wang et al., 2016). This analysis represents a new approach by using vegetation cover as a non-traditional parameter in geological research of cosmogenic nuclides. Therefore, it can link climate and surface processes from a new perspective.

With respect to this objective, the thesis hypothesizes the following: If the latitudinal gradient in vegetation cover influences the sediment transport on catchment-scale, then the denudation rates adjust to this gradient. This implies that in regions of low vegetation density high variations in denudation rate occur that are proportional to the amount of precipitation. In regions of high vegetation density low variations of denudation rate are present and the influence of precipitation is saturated.

(3) **[Variation of denudation rates in glacial settings]** The third objective explores the variation of denudation rates in the end-member environment of glaciated regions from 43°S to 47°S in Southern Chile (Figure 1). This study focuses on the area north of the present-day Northern Patagonian Ice Field. Glaciated environments are characterized by the impact of glacial activity on orogen erosion, which is reflected in accelerated denudation rates. In comparison to the first two objectives, the third objective investigates denudation rates in a smaller latitudinal scale and compares partly glaciated and deglaciated catchments. Furthermore, within the third objective, the thesis investigates effects of grain sizes, denudation rates and drainage distance on denudation rates and analyses the potential influence of climate, tectonic and biotic parameters on erosion rate.

Within this objective, the study tests the hypothesis: If the difference in timing of deglaciation is influencing the environmental setting, then we identify high vegetation cover and low denudation rates in catchments that have been deglaciated earlier and low vegetation cover and high denudation rates in catchments that are still partly glaciated.

2 Methods

The objectives of the thesis are investigated by combining three main methods. The first two methods aim to analyze remote sensing and geochemical datasets on a watershed catchments scale. The results of these two methods identify catchment parameters and calculate denudation rates. The third method, multivariate statistical analysis, is applied to identify the most important factor influencing denudation rates from all available data. In the following sections, these three methods are introduced.

2.1 Remote sensing and modelled datasets

The analysis of surface processes on catchment-scale requires the acquisition of information from remote sensing and modelled datasets. This study identifies catchment parameters of topographic and biotic variables from remote sensing data. Catchment parameters of for example local relief or slope are calculated from the Shuttle Radar Topography Mission (SRTM) digital elevation model (DEM) with a resolution of 90m or 30m (USGS, 2000). Catchment-wide vegetation cover is analysed using the 1km MODIS-based Green Vegetation Fraction with a time resolution from 2001-2012 (Broxton et al., 2014). The vegetation type is extracted by using MODIS landcover (2001-2012) with a data resolution of 0.5°-0.5° (Broxton et al., 2014).

In contrast to remote sensing data, climate and paleoclimate parameters are derived from modelled datasets. Mean annual precipitation (MAP) for example is calculated from (1) the data product TRMM 2B31 with a spatial resolution of 5x5 km (Bookhagen, 2013), (2) from WorldClim with a 1 km spatial resolution (Fick and Hijmans, 2017) or (3) from CHELSA with a 1 km spatial resolution (Karger et al., 2017). Paleoclimate data of different time slices such as the Last Glacial Maximum (LGM), Present Day (PD), and Pre-Industrial (PI) time, is derived from the ECHAM5 global atmospheric general circulation model at a spectral resolution of T159 (~80x80 km) (Mutz et al., 2018).

The analysis of modelled climate parameters is chosen instead of measured climate parameters in order to reduce uncertainties and bridge the difference in spatial and time resolution as well as sensitivity between geochemical and geomorphological datasets. Measured climate parameters are very sensitive to capture extreme rain events of a few hours and single days in response to ENSO-related variations (Curtis et al., 2007). In particular in the arid setting of the study area, it remains unclear how extreme precipitation events are converted into surface runoff (Grosjean et al., 2003).

2.2 Cosmogenic nuclide-derived denudation rates

2.1.1 Theory

Cosmogenic nuclides are rare isotopes (nuclides) that are created by cosmic radiation. They occur as stable noble gas isotopes ^{3}He and ^{21}Ne or as radioactive isotopes such as ^{10}Be, ^{26}Al, ^{36}Cl or ^{14}C. This thesis concentrates on the analysis of the radionuclides ^{10}Be and ^{26}Al. The Earth is constantly bombarded by cosmic radiation. Primary cosmic rays collide with upper atmosphere atoms and produce secondary particles that produce cosmogenic nuclides in the atmosphere (e.g. meteoric ^{10}Be, ^{26}Al) or in mineral grains (e.g. in-situ ^{10}Be, ^{26}Al) (von Blanckenburg and Willenbring, 2014) (Figure 2).

The dominant production mechanisms of ^{10}Be and ^{26}Al are nucleon spallation and negative muon capture. During negative muon capture, a muon is captured into an orbit, reacts with a proton, simultaneously forms a neutron and leads to a break-up of the target nucleus (e.g. O and C for ^{10}Be and

Si for ^{26}Al) through the excess energy that is released. This reaction only accounts for about 2% of the total production. In contrast, the frequent reaction of nucleon spallation means that the secondary particle impact produces kinetic energy that breaks up the target nucleus. Due to the loss of energy in the secondary cascade of particles, the production of in situ-produced nuclides is lower than of meteoric nuclides (e.g. in-situ nuclides have only 2-20 atoms $g_{mineral}^{-1}$ yr^{-1}) (Gosse and Phillips, 2001).

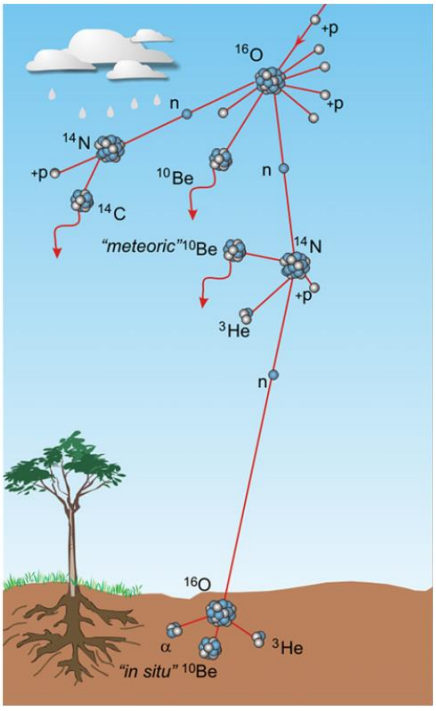

Figure 2. Production mechanism of meteoric and in-situ ^{10}Be by cosmic rays and secondary particles (von Blanckenburg and Willenbring, 2014).

The production of in situ-produced nuclides decreases exponentially with the adsorption depth. The absorption depth describes the decrease of the cosmic ray mean free path (Λ) due to the density of the mineral material with which the cosmic rays interact (Lal, 1991). For example, at 2 m depth in a rock or sediment material the production of nuclides with reference to nucleonic absorption is lowered by 3% compared to the surface production. In contrast, muonic absorption can contribute to production of cosmogenic nuclides in deeper rock or sediment layers (7 to 10m) because the decrease of production with depth is slower (Dunai, 2010) (Figure 3).

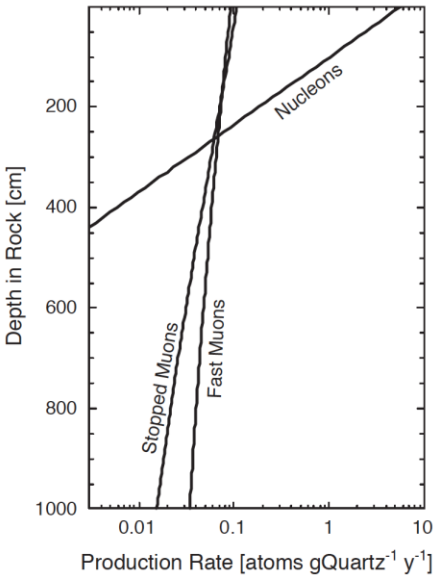

Figure 3. Exponential decrease of cosmogenic nuclide production with adsorption depth (von Blanckenburg, 2005).

Production rates of ^{10}Be and ^{26}Al vary with latitude, altitude and over time. Due to production processes, the in situ-produced ^{10}Be and ^{26}Al can only be found in material that has been exposed to cosmic radiation where it decays. Following, the radionuclide ^{10}Be decays with a half-life of 1.39 Myr and ^{26}Al with a half-life of 0.72 Myr (Nishiizumi et al., 2007; Chmeleff et al., 2009; Korschinek et al., 2009). Shielding of cosmic radiation is commonly considered by correcting surfaces for topographic shielding (e.g. mountains or steep slopes), glacier or snow shielding or self-shielding, which is caused by the thickness of a sample. The production rates for in situ- produced ^{10}Be and ^{26}Al can been calibrated with analysis of ^{10}Be concentrations of surfaces of known age such as glacially-polished areas or landslides and are scaled to sea level high latitude. Different scaling frameworks exist and are constantly modified and improved. Scaling frameworks can be classified into constant production rate models (e.g. Lal, 1991) and time-varying production models (e.g. Dunai, 2001; Lifton et al., 2005). The time-varying production models take into account changes in the strength of the Earth's magnetic, whereas the constant production rate models assume a constant magnetic field over time. Depending on the scaling framework, production rates at sea level high latitude for ^{10}Be produced by spallation vary between 5 to 3.7 atoms g_{qtz}^{-1} yr^{-1} (Dunai, 2010; Philipps et al., 2016).

Cosmogenic nuclides offer a wide range of applications in geology and geomorphology (von Blanckenburg and Willenbring, 2014). (1) The use of single or multiple nuclides enables burial age determination for sediment and rock surfaces that once were exposed to cosmic radiation but have been buried since then. This technique takes advantage of the radioactive decay of cosmogenic nuclides and is commonly applied to cosmogenic-nuclide pairs with different half-lives. (2) Exposure age determination is used to investigate the time elapsed since a rock or sediment surface has been exposed

to cosmic radiation if no surface erosion or sediment accumulation has occurred since formation. The age of landforms in glacial settings, fluvial terraces or lava flows can be successfully determined with this technique. (3) The concentration of cosmogenic nuclides can be used to determine denudation rates of river catchments on a surface of long-term steady erosion. A detailed method description of catchment- averaged denudation rates is shown in section 2.1.3. Finally, the number of cosmogenic nuclide applications is steadily increasing, and recent investigations show the possibility of calculating soil production rates of weathering rates (von Blanckenburg and Willenbring, 2014; Schaller et al., 2018).

2.1.2 Sample preparation

This thesis focuses on the determination of catchment-averaged denudation rates by using in situ-produced ^{10}Be and ^{26}Al in quartz. In order to measure ^{10}Be and ^{26}Al, the target mineral quartz needs to be extracted from the initial sample material that is collected in a river catchment.

Detrital sample material is sieved to 250–1000µm and separated into a non-magnetic and magnetic fraction using a strong magnetic field. The non-magnetic fraction is sequentially cleaned to pure quartz with 10% hydrochloric acid for 48h, boiling pyrophosphoric acid and then boiling sodium hydroxide, concentrated aqua regia for 24 h and 5% hydrofluoric acid for three to five weeks. The remaining pure quartz is leached with concentrated hydrofluoric acid and aqua regia to remove meteoric-produced ^{10}Be and ^{26}Al that is situated at the outer rim of the sand grain before spiking with ^{9}Be carrier. Samples are not spiked with aluminum. Depending on each sample, approximately 200 to 300µg of ^{9}Be carrier was added to approximately 20 to 100g pure quartz.

The in situ-produced nuclides of ^{10}Be and ^{26}Al were separated by using the standard separation method of von Blanckenburg et al. (2005) and Wittmann et al. (2007). This standard separation method includes the following steps: First the leached quartz is dissolved with concentrated hydrofluoric acid. Second, the dissolved material is converted into a 6 molar hydrochloric acid. Third, an ion exchange procedure using an ion exchange resin (anion resin) within a column separation removes all other elements from the material accept for beryllium and aluminum. Fourth, the column separation is performed a second time with a different ion exchange resin (cation resin) in order to separate beryllium. The remaining aluminum-bearing material is a third time loaded into a column separation (anion resin) to clean the material to a state that only aluminum is left. Fifth, beryllium is precipitated by using ammonia. The remaining material of separated beryllium and aluminum is oxidized and pressed into copper targets with niobium for the beryllium measurement and silver for the aluminum measurement. Consequently, the ratios of ^{10}Be/^{9}Be and ^{26}Al/^{27}Al were measured as BeO and Al_2O_3 targets by accelerator mass spectrometry (AMS) at the University of Köln. Native Al concentration measurements were performed by inductively coupled plasma-optical emission spectrometry (ICP-OES) at the University of Tübingen.

2.1.3 Catchment-averaged denudation rates

Catchment-averaged denudation rates from river sediments are sensitive to the combined effects of physical erosion and chemical weathering over the catchment area. In the publications (PAPER I to III) the term denudation rates and erosion rates are equally used and mean the same.

The calculation of catchment-averaged denudation rates relies on the following main assumptions: (1) At an isotopic steady-state condition the radioactive decay and the cosmogenic nuclide export in the river equals the averaged in-situ production of cosmogenic nuclides in the catchment (von Blanckenburg, 2005) (2) Every catchment subarea contributes quartz material, weathering or erosional processes do not enrich the quartz material and different grain sizes have a homogeneous nuclide concentration (Dosseto and Schaller, 2016); (3) Sediment storage is insignificant in the catchment, transport time of sediment is short, and the catchment is large enough to have a low frequency of landslides and debris flows; (4) Shielding of the surface by glaciers, snow, and vegetation is minor (von Blanckenburg, 2005; Dosseto and Schaller, 2016).

One of the first general equations to calculate cosmogenic nuclide concentrations at depth was introduced by Lal (1991) and is shown in the following equation:

$$N(z,t) = N(z,0)e^{-\lambda t} + \frac{P(0)}{\lambda+\frac{\rho\varepsilon}{\Lambda}} e^{\frac{-z\times\rho}{\Lambda}} \times \left(1 - e^{1\left(\lambda+\frac{\rho\varepsilon}{\Lambda}\right)t}\right) \quad (1)$$

where N is the nuclide concentration, $N(z,0)e^{-\lambda t}$ is the nuclide inheritance, λ is the half-life of the nuclide, t is time, P(0) is the nuclide production rate, ρ is the material density (e.g. quartz), ε is the denudation rate, Λ is the cosmic ray mean free path and z is the adsorption law ($z = \Lambda/\rho$). Assuming that no cosmogenic nuclide inheritance is influencing the nuclide concentration the term $N(z,0)e^{-\lambda t}$ equals zero and can be removed from the equation:

$$N(t) = \frac{P(0)}{\lambda+\frac{\rho\varepsilon}{\Lambda}} \times \left(1 - e^{-\left(\lambda+\frac{\rho\varepsilon}{\Lambda}\right)t}\right) \quad (2)$$

In a landscape that is in isotopic steady state, the surface nuclide concentration remains constant because nuclide production and surface denudation are present over a long period of time (e.g. $t > \rho\varepsilon/\Lambda$). In this case, the equation can be further simplified to:

$$N(t) = \frac{P(0)}{\lambda+\frac{\rho\varepsilon}{\Lambda}} \quad (3)$$

which represents the basic steady-state equation to calculate catchment-averaged denudation rates and shows that the nuclide concentration N(t) of for example ^{10}Be and ^{26}Al at the Earth's surface is inversely proportional to the denudation rate.

The advantage of calculating denudation rates from cosmogenic nuclides is that denudation rates are insensitive to short-term changes and are averaging over timescales of natural geomorphic processes (10^4 to 10^6 yr). The averaging time scale is a result of dividing the denudation rate by the adsorption depth scale (z) and is also called apparent age. This averaging time scale corresponds to the accumulation of cosmogenic nuclides in a setting where material moves towards the surface and results in a damping of the cosmogenic nuclide signal (von Blanckenburg, 2005).

2.2 Statistical analysis

Statistical analyses where more than two variables are simultaneously analyzed are classified as multivariate statistics. Examples of multivariate statistical methods are the discriminant analysis, the principal component analysis or the factor analysis (Tabachnick and Fidell, 2007). The factor analysis is applied in studies with a large number of variables that characterize objects or processes (Figure 4). In medical research or social sciences, the factor analysis is frequently used to identify variables that measure different aspects of the same underlying, driving factor of human behavior (Thompson, 2004). In geosciences, the factor analysis is applied to identify geomorphological processes that drive chemical compositions in lake sediments (Hartmann and Wünnemann, 2009) or to identify the driving factor that has the highest impact on denudation rates (PAPER I). Limits and assumptions of the factor analysis are: (1) a sufficient sample size with a proposed sample-variable ratio of 5:1 (Hair et al., 1998), (2) a normal variable distribution with a minor occurrence of outliers or missing values (Thompson, 2004) and (3) a multicollinearity in the correlation matrix with observed correlation coefficients vales ranging between 0.5 to 1 (Hutcheson, 1999).

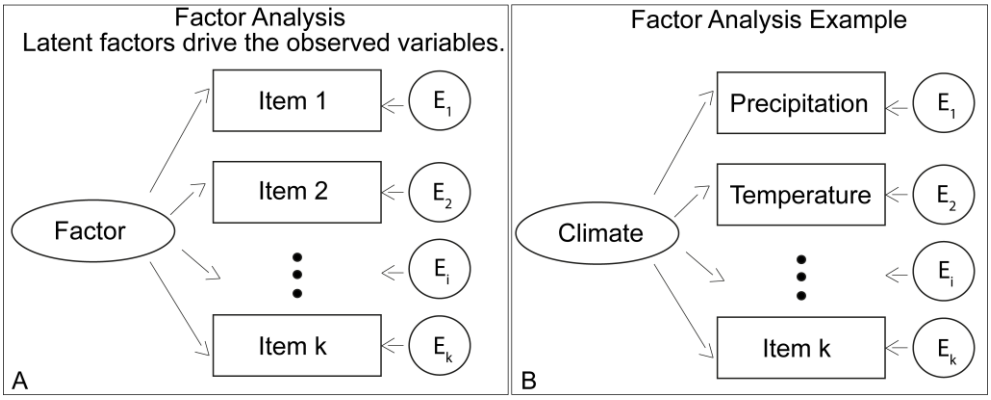

Figure 4. A) Conceptual overview of the factor analysis. The oval represents latent, unobserved factors, rectangles represent observed variables at the sample level including measured errors (E) (modified after Matsunaga, 2010). B) Example of a factor in geological applications (modified after Matsunaga, 2010).

The factor analysis describes variability among observed and correlated variables and extracts a few common latent characteristics from a large set of manifest variables (e.g. factors). This analysis performs a multivariate data reduction by detecting linear correlations with a maximum likelihood estimate (Kaiser, 1956; Tucker and Lewis, 1960; Knott and Bartholomew, 1999; Reymant and Jvreskog, 1996) and can be described by:

$$X_{(N\times p)} = F_{(N\times k)}A'_{(k\times p)} + E_{(N\times p)} \tag{4}$$

where X is the data matrix with N elements and p variables, F the factor score matrix with k the number of factors to be used, A' the factor loading matrix, plus the error term E (Reymant and Jvreskog, 1996). A z-transformation was applied on the X data matrix to provide an interpretation independent of unit dimension. A z-transformation can be calculated from the following formula:

$$z = (V - \mu)/\sigma \tag{5}$$

where z is the z-score, V is the value of the element, μ is the population mean, and σ is the standard deviation. The factor analysis was performed in R-mode, which means that the *X* data matrix is transformed into a correlation matrix R before it starts to compute the factor loadings. The fundamental equation for all forms of an R-mode factor analysis is (Reymant and Jvreskog, 1996):

$$x = Af + e \tag{6}$$

x is a column vector representing one object of the data matrix X, A is the factor loading matrix, f and *e* are corresponding row vectors of F and E described above. We derive equation 4 by transforming equation 2 in scalar notation. Consequently, for any given value of the data matrix of the n-th row and i-th column the equation 5 is valid (Reymant and Jvreskog, 1996):

$$x_{ni} = \sum_{j=1}^{k} f_{nj}a_{ij} + e_{ni} \tag{7}$$

Following equation 5, we obtain for any row (x´) of the data matrix X (Reymant and Jvreskog, 1996):

$$x' = f'A' + e' \tag{8}$$

The transpose of equation 8 is the fundamental equation 4, the data matrix X, the factor score matrix F, the factor loading matrix A, plus the error term E. In this thesis the factor analysis is calculated in R-mode. R-mode factor analysis investigates the relation between individual variables whereas the Q-mode analysis explores the relation between different sample sets. The z-transformation is applied on the data set to provide an interpretation independent of scale. The z- transformation is an equation to scale the mean of the variables to 0 and the standard deviation to 1 (Thompson, 2004). The calculated factor loading results are varimax rotated (orthogonal rotated by 90°) to simplify the interpretation. This

is possible because the varimax rotation produces a small number of large loadings and a large number of zero loadings (Figure 5) (Reymant and Jvreskog, 1996).

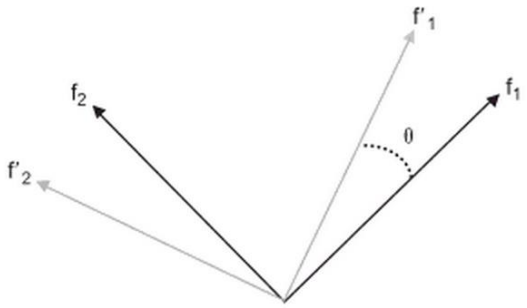

Figure 5. Example of an orthogonal rotation (Menke, 2012). The factor f1 and f2 are rotated by the angle θ and the orthogonal vectors f'1 and f'2 are created.

3 Synthesis and main outcome

This thesis quantifies catchment-averaged denudation rates within the range of environmental end-members, from hyper arid to glaciated settings. The most important factors and processes influencing denudation patterns are identified for the Western Andes in southern Peru, northern and central Chile as well as for the Patagonian Andes in Chile. The most important conclusions based on objectives (1-3) are listed below and are followed by a more detailed description:

(1) In the arid to hyper arid regions of northern Chile (Atacama Desert), precipitation rates are too low to trigger denudation rates that adjust to the variation in long wavelength variations in topography. Consequently, local tectonic processes of (e.g.) smaller scale faulting show the highest influence on catchment-averaged denudation rates (PAPER I).

(2) For different climate settings, the effect of vegetation and precipitation on denudation rate varies depending on the vegetation-cover amount. In environments with low initial vegetation, denudation is mainly controlled by climate of tectonic parameters. In environments with high initial vegetation cover, vegetation is decelerating sediment transportation and is limiting the maximum variation in denudation rates (PAPER II).

(3) In the glaciated environment of the Northern Patagonian Ice Field, the latitudinal variation of denudation rates is dependent on variations in vegetation cover, which are linearly related to the denudation rate patterns in first order. In second order, differences in denudation rates between partly glaciated and deglaciated catchments are identified (PAPER III).

(1) Tectonic and climatic control on denudation rates in arid to hyper arid regions

In arid to hyper arid regions, main processes controlling denudation rates are local tectonics such as smaller scale faulting. These controls are identified by the strong correlation and covariation of denudation rate to channel steepness. The results imply an insignificant effect of climate parameters on the denudation rates, however the utilized precipitation data is modelled and limited to a short, recent record of eight years. A systematic decrease in denudation rates with increasing distance from the syntaxial bend in the Andes is not clearly observed. This result is in contrast to spatial patterns in exhumation rates observed from thermochronology in the significantly more erosive Himalayan and southeast Alaskan syntaxes. Although a clear signal of denudation rate variations with distance from the South American syntaxis is lacking, regional trends in topography in this arid region display a decrease in maximum elevations away from the syntaxes. This trend in topography is in compliance to the rock uplift pattern predicted by Bendick and Ehlers (2014) for upper plate deformation above a subducting indenter (Hayes et al., 2012). In the studied arid to hyper arid region, insufficient precipitation is available to erode the long wavelength variations in topography. The thesis concludes that in this arid setting with low potential for erosion, the tectonic controls on rock uplift outpace the ability of surface processes to denude and reflect regional scale tectonic processes.

(2) Influence of vegetation cover on denudation rates across climate gradients

Several broader implications for the vegetation cover and precipitation effects on denudation are identified. First, the analyses identify that the effect of vegetation and precipitation on catchment-averaged denudation rate varies depending on the vegetation-cover amount in specific climate regimes. In regimes with sparse vegetation the amount of vegetation cover allows an increase of erosion with increasing precipitation. In regimes where dense vegetation occurs the vegetation cover inhibit the maximum variation of erosion. Second, the identification of regimes implies that studies focusing on individual catchments with a spatial extent smaller than the larger scale interactions identified here, may insufficiently resolve vegetation-erosion rate interactions. Thus, the results indicate that smaller scale studies are less likely to identify the range of vegetation-cover effects on denudation rates documented here. Besides, such studies may be located at or across regimes where different behaviors exist. Third, results from previous studies (Carretier et al., 2013; Acosta et al., 2015; Olen et al., 2016) show both correlations and anti-correlations between vegetation cover, precipitation and denudation rates. These conflicting results may have occurred in areas that are located at, or straddle, the regimes identified here. Finally, our results demonstrate that previous concepts of a vegetation control on soil erosion (Gyssels et al., 2005) can also be applied to large-scale and long-term denudation rate studies.

(3) Variation of denudation rates in glacial settings

Variations of denudation rate in glacial settings are dependent on vegetation cover and differences in timing of deglaciation and ice cover. Denudation rates derived from partly glaciated and deglaciated catchments show significant differences in latitudinal trend in northern Patagonia. Denudation rates from partly glaciated catchments with low vegetation cover show higher values than in catchments without glacier cover and higher vegetation density. Based on the geomorphological setting, it is not possible to disentangle the vegetational and glacial influence on erosion rates. This study identifies grain size effects on denudation rates caused by differences in drainage distance. Any potential effect on denudation rates by long wavelength tectonic processes or tectonic uplift rates cannot be identified.

4 Future perspectives

The broader implications of this thesis show that applying non-traditional tools and parameters is very useful to identify new interactions from new perspectives. The use of multivariate statistical analysis enables the identification of relationships between a large set of parameters that are not necessarily linearly correlated. Multivariate statistical analysis are known, but not widely used in geomorphological or geochemical analysis but are recommended to become a standard research tool. In addition, the influence of biota on surface processes over geological timescales is an important interaction that deserves more attention in classical geological research. The analysis of biological processes and parameters with reference to catchment-averaged denudation rates is a successful strategy to draw a more complete picture about the complex interactions of surface processes in different environmental settings.

The publications developed in the course of this thesis reveal shortcomings and therefore yield information on potential future research topics. To resolve these shortcomings, four options are presented in the following:

i. The interpretations in PAPER I are based on the assumption that the influence of climate on denudation rates can only be identified by mean annual precipitation data derived from modelled climate datasets. However, it remains unclear if this approach correctly represents the driving climate forces modulating the denudation rates in this region. Denudation rates from fluvial systems in central and northern Chile are thought to be controversial archives of climate variability. Previous work suggests that the rivers are mainly recording erosion after extreme precipitation events rather than long-term surface runoff (Carretier et al., 2012; Grosjean et al.,

2003). Further research could focus on investigating (a) which amount of measured precipitation is effectively converted into surface runoff that is able to excavate sediment from the catchment slopes and (b) if denudation rates reproduce the same results in El Niño years where huge and dangerous flooding's occur in comparison to years without any precipitation in the Atacama desert.

ii. The results of PAPER II and III underline the importance of biota in geological research. Mean annual vegetation cover and vegetation type are assumed to correctly represent the vegetational gradient and biotic characteristics. However, from a biological perspective, vegetation cover derived from remote sensing and measurement of green fraction reflection is connected to high uncertainties. Vegetation density does not equal vegetation cover, however it is assumed to be equal in PAPER II. Future geological research is recommend to analyze further biological parameters such as leaf index, photosynthesis capacity, and root depth or density to more effectively represent vegetation density. The combined effect of flora and fauna on surface processes over geological time scales remains a gap in research. In addition, denudation rate represents physical erosion as well as chemical weathering. The effect of biota on weathering is presumably the missing key to correctly interpret catchment-averaged denudation rates.

iii. It is not within the scope of this thesis to assess if the observations for present-day denudation rates can be transferred to paleo-denudation rates. Further research could focus on the development of paleo-denudation models that take into account geological and biological parameters of different time-slices. Using these models, calculated paleo-denudation rates could be compared to measured cosmogenic nuclide-derived paleo-denudation rates to resolve interpretation mismatches.

iv. The data compilation of this thesis covers are large spatial extent across the Western and Patagonian Andes. Currently, a comparable denudation-rate dataset for marine cores does not exist. Therefore, future research could focus on the measurement of in situ-produced ^{10}Be concentrations of marine cores from South America. With this new compilation it would be possible to compare terrestrial denudation rates to offshore denudation rates. For the first time test samples of the marine core (GeoB 7136-2) have been successfully measured and the resulting ^{10}Be concentrations are presented in the appendix of this thesis.

Bibliography

Acosta, V. T., Schildgen, T. F., Clarke, B. A., Scherler, D., Bookhagen, B., Wittmann, H., et al. (2015). Effect of vegetation cover on millennial-scale landscape denudation rates in East Africa. *Lithosphere* 7, 408–420. doi:10.1130/L402.1.

Allmendinger, R. W., Jordan, T. E., Kay, S. M., and Isacks, B. L. (1997). The Evolution of the Altiplano-Puna Plateau of the Central Andes. *Annual Review of Earth and Planetary Sciences* 25, 139–174. doi:10.1146/annurev.earth.25.1.139.

Amundson, R., Dietrich, W., Bellugi, D., Ewing, S., Nishiizumi, K., Chong, G., et al. (2012). Geomorphologic evidence for the late Pliocene onset of hyperaridity in the Atacama Desert. *GSA Bulletin* 124, 1048–1070. doi:10.1130/B30445.1.

Bendick, R., and Ehlers, T. A. (2014). Extreme localized exhumation at syntaxes initiated by subduction geometry. *Geophysical Research Letters* 41, 5861–5867. doi:10.1002/2014GL061026.

Berner, R. A. (1997). The Rise of Plants and Their Effect on Weathering and Atmospheric CO_2. *Science* 276, 544–546. doi:10.1126/science.276.5312.544.

Broxton, P. D., Zeng, X., Scheftic, W., and Troch, P. A. (2014). A MODIS-Based Global 1-km Maximum Green Vegetation Fraction Dataset. *J. Appl. Meteor. Climatol.* 53, 1996–2004. doi:10.1175/JAMC-D-13-0356.1.

Carretier, S., Regard, V., Vassallo, R., Aguilar, G., Martinod, J., Riquelme, R., et al. (2013). Slope and climate variability control of erosion in the Andes of central Chile. *Geology* 41, 195–198. doi:10.1130/G33735.1.

Chesworth, W. (1992). "Chapter 2 - Weathering systems," in *Developments in Earth Surface Processes* Weathering, Soils & Paleosols., eds. I. P. Martini and W. Chesworth (Elsevier), 19–40. doi:10.1016/B978-0-444-89198-3.50007-6.

Derry, L. A. (2006). Fungi, Weathering, and the Emergence of Animals. *Science* 311, 1386–1387. doi:10.1126/science.1124183.

Dosseto, A., Hesse, P. P., Maher, K., Fryirs, K., and Turner, S. (2010). Climatic and vegetation control on sediment dynamics during the last glacial cycle. *Geology* 38, 395–398. doi:10.1130/G30708.1.

Dosseto, A., and Schaller, M. (2016). The erosion response to Quaternary climate change quantified using uranium isotopes and in situ-produced cosmogenic nuclides. *Earth-Science Reviews* 155, 60–81. doi:10.1016/j.earscirev.2016.01.015.

Dunai, T. J. (2000). Scaling factors for production rates of in situ produced cosmogenic nuclides: a critical reevaluation. *Earth and Planetary Science Letters* 176, 157–169. doi:10.1016/S0012-821X(99)00310-6.

Fick, S. E., and Hijmans, R. J. (2017). WorldClim 2: new 1-km spatial resolution climate surfaces for global land areas: NEW CLIMATE SURFACES FOR GLOBAL LAND AREAS. *International Journal of Climatology*. doi:10.1002/joc.5086.

Galy, V., Peucker-Ehrenbrink, B., and Eglinton, T. (2015). Global carbon export from the terrestrial biosphere controlled by erosion. *Nature*. doi:10.1038/nature14400.

Gosse, J. C., and Phillips, F. M. (2001). Terrestrial in situ cosmogenic nuclides: theory and application. *Quaternary Science Reviews* 20, 1475–1560.

Grosjean, M., Cartajena, I., Geyh, M. A., and Nunez, L. (2003). From proxy data to paleoclimate interpretation: the mid-Holocene paradox of the Atacama Desert, northern Chile. *Palaeogeography, Palaeoclimatology, Palaeoecology* 194, 247–258.

Gyssels, G., Poesen, J., Bochet, E., and Li, Y. (2005). Impact of plant roots on the resistance of soils to erosion by water: a review. *Progress in Physical Geography* 29, 189–217. doi:10.1191/0309133305pp443ra.

Hair, J. F., Tatham, R. L., Anderson, R. E., and Black, W. (1998). *Multivariate Data Analysis*. 5th edition. Upper Saddle River, N.J: Prentice Hall.

Hartmann, K., and Wünnemann, B. (2009). Hydrological changes and Holocene climate variations in NW China, inferred from lake sediments of Juyanze palaeolake by factor analyses. *Quaternary International* 194, 28–44. doi:10.1016/j.quaint.2007.06.037.

Hayes, G. P., Wald, D. J., and Johnson, R. L. (2012). Slab1.0: A three-dimensional model of global subduction zone geometries. *J. Geophys. Res.* 117, B01302. doi:10.1029/2011JB008524.

Hutcheson, G. (1999). *The Multivariate Social Scientist*. 6 Bonhill Street, London EC2A 4PU: SAGE Publications, Ltd. doi:10.4135/9780857028075.

Kaiser, H. F. The varimax criterion for analytic rotation in factor analysis. *Psychometrika* 23, 187–200. doi:10.1007/BF02289233.

Karger, D. N., Conrad, O., Böhner, J., Kawohl, T., Kreft, H., Soria-Auza, R. W., et al. (2017). Climatologies at high resolution for the earth's land surface areas. *Scientific Data* 4, sdata2017122. doi:10.1038/sdata.2017.122.

Knott, M., and Bartholomew, D. J. (1999). *Latent variable models and factor analysis*. London, UK: Edward Arnold Available at: http://www.hoddereducation.co.uk [Accessed June 29, 2016].

Korschinek, G., Bergmaier, A., Faestermann, T., Gerstmann, U. C., Knie, K., Rugel, G., et al. (2010). A new value for the half-life of 10Be by Heavy-Ion Elastic Recoil Detection and liquid scintillation counting. *Nuclear Instruments and Methods in Physics Research Section B: Beam Interactions with Materials and Atoms* 268, 187–191. doi:10.1016/j.nimb.2009.09.020.

Lal, D. (1991). Cosmic ray labeling of erosion surfaces: in situ nuclide production rates and erosion models. *Earth and Planetary Science Letters* 104, 424–439. doi:10.1016/0012-821X(91)90220-C.

Lifton, N., Sato, T., and Dunai, T. J. (2014). Scaling in situ cosmogenic nuclide production rates using analytical approximations to atmospheric cosmic-ray fluxes. *Earth and Planetary Science Letters* 386, 149–160. doi:10.1016/j.epsl.2013.10.052.

Madella, A., Delunel, R., Akçar, N., Schlunegger, F., and Christl, M. (2018). 10 Be-inferred paleo-denudation rates imply that the mid-Miocene western central Andes eroded as slowly as today. *Scientific Reports* 8, 2299. doi:10.1038/s41598-018-20681-x.

Matsunaga, M. (2010). How to Factor-Analyze Your Data Right: Do's Don'ts, and How-To's. *International Journal of Psychological Research, ISSN 2011-7922, Vol. 3, Nº. 1, 2010, pags. 97-110* 3.

Menke, W. (2012). *Geophysical Data Analysis: Discrete Inverse Theory: MATLAB Edition*. 3rd ed. Waltham, MA: Academic Press.

Morgan, R. P. C., and Rickson, R. J. (2003). *Slope Stabilization and Erosion Control: A Bioengineering Approach*. Taylor & Francis.

Nishiizumi, K., Imamura, M., Caffee, M. W., Southon, J. R., Finkel, R. C., and McAninch, J. (2007). Absolute calibration of 10Be AMS standards. *Nuclear Instruments and Methods in Physics Research Section B: Beam Interactions with Materials and Atoms* 258, 403–413. doi:10.1016/j.nimb.2007.01.297.

Olen, S. M., Bookhagen, B., and Strecker, M. R. (2016). Role of climate and vegetation density in modulating denudation rates in the Himalaya. *Earth and Planetary Science Letters* 445, 57–67. doi:10.1016/j.epsl.2016.03.047.

Oncken, O., Hindle, D., Kley, J., Elger, K., Victor, P., and Schemmann, K. (2006). "Deformation of the Central Andean Upper Plate System — Facts, Fiction, and Constraints for Plateau Models," in *The Andes: Active Subduction Orogeny* Frontiers in Earth Sciences., eds. O. Oncken, G. Chong, G. Franz, P. Giese, H.-J. Götze, V. A. Ramos, et al. (Berlin, Heidelberg: Springer Berlin Heidelberg), 3–27. doi:10.1007/978-3-540-48684-8_1.

Phillips, F. M., Argento, D. C., Balco, G., Caffee, M. W., Clem, J., Dunai, T. J., et al. (2016). The CRONUS-Earth Project: A synthesis. *Quaternary Geochronology* 31, 119–154. doi:10.1016/j.quageo.2015.09.006.

Pinet, P., and Souriau, M. (1988). Continental erosion and large-scale relief. *Tectonics* 7, 563–582. doi:10.1029/TC007i003p00563.

Retallack, G. J. (1997). Early Forest Soils and Their Role in Devonian Global Change. *Science* 276, 583–585. doi:10.1126/science.276.5312.583.

Reyment, R. A., and Jvreskog, K. G. (1996). *Applied Factor Analysis in the Natural Sciences*. Cambridge University Press.

Schaller, M., Ehlers, T. A., Lang, K., Schmid, M., and Fuentes-Espoz, J. P. (2018). Addressing the contribution of climate and vegetation cover on hillslope denudation, Chilean Coastal Cordillera (26°–38°S) – ScienceDirect, doi.org/10.1016/j.epsl.2018.02.026

Schlesinger, W. H., and Bernhardt, E. S. (2013). *Biogeochemistry: An Analysis of Global Change*. Academic Press.

Schwartzman, D. W., and Volk, T. (1989). Biotic enhancement of weathering and the habitability of Earth. *Nature* 340, 457–460. doi:10.1038/340457a0.

Stamey, W. L., and Smith, R. M. (1964). A CONSERVATION DEFINITION OF EROSION TOLERANCE: *Soil Science* 97, 183–186. doi:10.1097/00010694-196403000-00006.

Starke, J., Ehlers, T. A., and Schaller, M. (2017). Tectonic and Climatic Controls on the Spatial Distribution of Denudation Rates in Northern Chile (18°S to 23°S) Determined From Cosmogenic Nuclides: ^{10} Be Denudation Rates in Northern Chile. *Journal of Geophysical Research: Earth Surface*. doi:10.1002/2016JF004153.

Stokes, A., Norris, J. E., Beek, L. P. H. van, Bogaard, T., Cammeraat, E., Mickovski, S. B., et al. (2008). "How Vegetation Reinforces Soil on Slopes," in *Slope Stability and Erosion Control: Ecotechnological Solutions*, eds. J. E. Norris, A. Stokes, S. B. Mickovski, E. Cammeraat, R. van Beek, B. C. Nicoll, et al. (Springer Netherlands), 65–118. doi:10.1007/978-1-4020-6676-4_4.

Tabachnick, B. G., and Fidell, L. S. (2007). *Using multivariate statistics, 5th ed*. Boston, MA: Allyn & Bacon/Pearson Education.

Thomas, M., Clarke, J. D. A., and Pain, C. F. (2005). Weathering, erosion and landscape processes on Mars identified from recent rover imagery, and possible Earth analogues. *Australian Journal of Earth Sciences* 52, 365–378. doi:10.1080/08120090500134597.

Thompson, B. (2004). *Exploratory and confirmatory factor analysis: Understanding concepts and applications*. Washington, DC, US: American Psychological Association doi:10.1037/10694-000.

Tucker, L. R., and Lewis, C. A reliability coefficient for maximum likelihood factor analysis. *Psychometrika* 38, 1–10. doi:10.1007/BF02291170.

USGS (2000). Shuttle Radar Topography Mission. 3 Arc Second scene SRTM_u03_n008e004, Unfilled Unfinished 2.0, Global Land Cover Facility, University of Maryland, Collage Park, Maryland. Available at: http://glcf.umd.edu/data/srtm/ [Accessed October 2, 2017].

von Blanckenburg, F. (2005). The control mechanisms of erosion and weathering at basin scale from cosmogenic nuclides in river sediment. *Earth Planet. Sci. Lett.* 237, 462–479. doi:10.1016/j.epsl.2005.06.030.

von Blanckenburg, F., and Willenbring, J. K. (2014). Cosmogenic Nuclides: Dates and Rates of Earth-Surface Change. *Elements* 10, 341–346. doi:10.2113/gselements.10.5.341.

Wang, S., Fu, B., Piao, S., Lu, Y., Ciais, P., Feng, X., et al. (2016). Reduced sediment transport in the Yellow River due to anthropogenic changes. *Nat. Geosci.* 9, 38-+. doi:10.1038/NGEO2602.

Warren, C. R., and Sugden, D. E. (1993). The Patagonian Icefields: A Glaciological Review. *Arctic and Alpine Research* 25, 316. doi:10.2307/1551915.

Wittmann, H., von Blanckenburg, F., Kruesmann, T., Norton, K. P., and Kubik, P. W. (2007). Relation between rock uplift and denudation from cosmogenic nuclides in river sediment in the Central Alps of Switzerland. *J. Geophys. Res.* 112, F04010. doi:10.1029/2006JF000729.

Contributions to scientific publications

PAPER I

Starke, Jessica, Ehlers, A. T. and Schaller, M.: *Tectonic and climatic controls on the spatial distribution of denudation rates in northern Chile (18°S to 23°S) determined from cosmogenic nuclides*. Published in Journal of Geophysical Research: Earth Surface. doi:10.1002/2016JF004153 (2017)

Scientific ideas	Data generation	Analysis and interpretation	Paper writing
Supported development of scientific ideas by all co-authors	Generation of all data presented in the paper.	Analysis and interpretation supported by all co-authors	All paper writing, proof-reading and comments by all co-authors

PAPER II

Starke, Jessica, Ehlers, A. T. and Schaller, M: *Latitudinal variations of vegetation and erosion rates identified along western South America*. Submitted to Science (2018). In review.

Scientific ideas	Data generation	Analysis and interpretation	Paper writing
Supported development of scientific ideas by all co-authors	Generation of all data presented in the paper.	Analysis and interpretation supported by all co-authors	All paper writing, proof-reading and comments by all co-authors

PAPER III

Starke, Jessica, Ehlers, A. T. and Schaller, M.: *Vegetation influence on Holocene catchment-wide erosion rates in northern Patagonia (Chile) determined from cosmogenic radionuclides*. In preparation and close to submission.

Scientific ideas	Data generation	Analysis and interpretation	Paper writing
Supported development of scientific ideas by all co-authors	Generation of all data presented in the paper.	Analysis and interpretation supported by all co-authors	All paper writing, proof-reading and comments by all co-authors

Paper I

Tectonic and climatic controls on the spatial distribution of denudation rates in northern Chile (18°S to 23°S) determined from cosmogenic nuclides

Jessica Starke[1], Todd A. Ehlers[1] and Mirjam Schaller[1]

[1]Department of Geosciences, Eberhard Karls University Tübingen, 72074 Tübingen, Germany

Published in *Journal of Geophysical Research: Earth Surface*, 25 October 2017.

Key Points

- Analyzing tectonic and climatic influences on ^{10}Be and ^{26}Al derived denudation rates at in a syntaxial orogen
- Significant correlation and covariation of denudation rates and channel steepness indices
- Catchment-scale tectonic processes rather than orogen-scale topographic trends control denudation rates in this arid setting

Abstract

In the arid region of northern Chile the environmental conditions are favorable for measuring tectonic and climatic influences on catchment denudation rates in the absence of vegetation. Previous studies of denudation rates from cosmogenic ^{10}Be and ^{26}Al concentrations are limited to single drainages. In this study, we examine catchment- to orogen-scale spatial variation in denudation rates between 18 and 23°S in the Coastal and Western Cordilleras of northern Chile. ^{10}Be and ^{26}Al data were obtained from 33 catchments to examine the relative roles of tectonics and climate on catchment-averaged denudation rates. At broader scales, we examine whether denudation rates and orogen topography reflect the 3-D plate geometry of the region. Cosmogenic nuclide-derived denudation rates range from 0.4±0.5 to 20.6±1.5 m/Myr in the Coastal Cordillera and from 1.4±0.7 to 168.0±19.8 m/Myr in the Western Cordillera. The controls on the denudation rates are evaluated using a statistical factor analysis of 10

selected catchment parameters. Denudation rates indicate a strong linear relationship with channel steepness indices but insignificant correlations and covariation with mean annual precipitation rates, drainage area, stream order, mean elevation, mean local relief, mean basin slope and analyzed grain size of the sampled sediments. Moreover, denudation rates are better correlated with tectonic controls at catchment scale than orogen-scale plate tectonics in the Western and Coastal Cordillera.

1 Introduction

The tectonic and climatic controls on the temporal evolution of topography in active mountain belts can be investigated by landscape-scale denudation rates that correlate with precipitation rates, channel steepness indices, mean basin slopes, local relief or rock uplift rates [*Summerfield and Hulton*, 1994; *Montgomery and Brandon*, 2002; *Wittmann et al.*, 2007; *DiBiase et al.*, 2010]. Cosmogenic nuclide-derived denudation rates are a valuable tool for understanding landscape dynamics over millennial timescales [*von Blanckenburg*, 2006; *Dunai*, 2010]. However, the degree to which climate and tectonic processes control denudation rates is not completely understood in mountain belts with an arid climate. Furthermore, rarely are cosmogenic nuclide studies conducted to determine orogen-scale plate tectonic controls on denudation rates. In this study, we focus on understanding catchment to orogen-scale spatial variations in denudation rates and topography in the arid to hyperarid region of northern Chile. The ~550 km latitudinal extent of our study area is situated in a convergent, tectonic setting near the syntaxis of the Central Andes. The arid and mainly abiotic environment in northern Chile [*Vidiella et al.*, 1999] preserves one of the oldest landscapes globally [*Dunai et al.*, 2005]. Annual precipitation rates show hyperarid conditions with rainfall ranging from 1 to 80 mm/a recorded by meteorological stations at the cities of Arica, Iquique and Antofagasta. Decreasing gradients in precipitation are observed from north to south between 18° to 24°S and observed from east to west (from Western Cordillera to Coastal Cordillera) [*Schulz et al.*, 2012]. The region is well situated to investigate the tectonic and climate control of denudation in the absence of vegetation (due to low precipitation rates), where complex feedback loops between vegetation density, surface and hillslope processes are avoided [*Acosta et al.*, 2015; *Olen et al.*, 2016]. In this study, we evaluate the hypothesis that the geometry of the subducting Nazca plate produces a tectonically controlled localization of denudation rates into a “bulls-eye” pattern near the Arica Bend in the Andes. The influence of climate on denudation rates in a syntaxial orogen with low precipitation rates is a topic that has received little attention.

The tectonic setting of the Central Andes is characterized by an ocean-continent convergent plate boundary. The subduction zone geometry is described seismically by a bulge (or slight shallowing in plate dip) in the subducting plate located near the Arica Bend (Figure 1b) [*Hayes et al.*, 2012]. Definitions of syntaxial orogens vary within the literature. Here we follow the definition of *Bendick and Ehlers* [2014] which states that a syntaxis is the narrow, cuspate region linking two adjacent subduction

segments, and includes both the down going and overriding plates. The subducting Nazca Plate in this region bends roughly parallel to the west coast of South America around ~18.5°S [*Isacks*, 1988] at the Arica Bend making this region a syntaxial orogen. Variations in the geometry of the subducting plate at a syntaxis occur due to 3D plate bending required to accommodate subduction on a sphere. These variations in plate geometry are important because bending of adjacent subducting plate segments leads to a concentration of strain and stress at the transition zone (or cuspate region) between the segments. The bulge in the subducting plate beneath a syntaxis results from the flexural stiffening of the plate during bending [*Mahadevan et al.*, 2010]. The flexurally stiffened bulge functions as a rigid indenter and can influence the overriding plate by localizing deformation into a "bulls-eye" pattern and increasing denudation rates [*Bendick and Ehlers*, 2014].

Previous, well studied, examples of syntaxial orogens include the western and eastern Himalayan Syntaxes or the St. Elias Mountains in Alaska, which are zones of high and rapid surface uplift as well as localized denudation in the syntaxes [*Zeitler et al*., 2001; *Koons et al*., 2013; *Bendick and Ehlers* 2014; *Falkowski et al.*, 2014; *Scherler et al.*, 2014]. While the Andean syntaxis is not commonly labeled as such, the 3D geometry of the plate is similar, as are many other subduction zones around the world (e.g. the Cascadia subduction zone, North America). One key difference between the Andean syntaxis and the Himalayan and St. Elias syntaxes is that the Andean location represents an arid end-member. To the best of our knowledge, no previous studies have evaluated long-wavelength, plate geometry driven variations in denudation in an arid environment. Thus, the Andean syntaxis is well-suited to evaluate if certain climatic and tectonic conditions (as suggested for the Himalaya and southeast Alaska) are required to produce a "focused bulls-eye" pattern in deformation and denudation above the syntaxis according to the indenter geometry of the subducting plate [c.f., *Koons et al.* 2013; *Bendick and Ehlers*, 2014]. Regional climate or tectonic influences on denudation rates might only be visible in the topography if denudation cannot keep up with deformation associated with the subducting plate geometry. How, or if, denudation rates and orogen topography reflect the 3D plate geometry in an arid setting is unstudied and is a component of this study.

In this study, we investigate the latitudinal gradient of denudation rates around the arid end-member syntaxial orogen of western South America (northern Chile). We do this over millennial timescales using cosmogenic nuclides. The study compliments previous work [*Kober et al.*, 2009; *Abbühl et al.*, 2010, 2011 a and b; *Placzek et al.*, 2010; *Jungers et al.*, 2013; *Carretier et al.*, 2015a and b] by investigating gradients of denudation rates and the control on denudation rates from 18°S to 23°S covering multiple catchments. A data set of 34 new ^{10}Be and eight ^{26}Al derived catchment-averaged denudation rates are presented for northern Chile.

We test the hypothesis that the bent geometry of the subducting Nazca plate causes spatial variations in rock uplift that are represented in long-wavelength (latitudinal) variations in topography and denudation

rates. We expect that the denudation rates increase towards the center of the syntaxial bend of the Central Andes and are not influenced by precipitation gradients due to the high aridity of the investigated region. We test this hypothesis by answering the questions: How do ^{10}Be derived denudation rates vary in the north-south and east-west directions on the southern limb of the Arica Bend? Are denudation rates more strongly related to latitudinal variations in tectonic or climate-related parameters?

2 Study Area

2.1 Geological Background

Plate convergence related mountain building in the Central Andes started around 40 Myr ago [*Barnes and Ehlers*, 2009], despite a much longer history of plate subduction and arc volcanism along the western margin. The evolution of the vertical relief was most likely initiated by two flat-ramp thrust systems at the western Andean margin [*Armijo et al.*, 2015]. It resulted in the evolution of five main geologic domains that characterize the western continental margin of the Central Andes in northern Chile (Figure 1a): the Coastal Cordillera (CC), the Central Depression (CD), the Western Cordillera (WC), the Altiplano (AP) and the Calama Basin (CB). The timing of Andean arc activity in northern Chile can be summarized by Jurassic arc activity (195 to 130 Myr) along the Coastal Cordillera, mid Cretaceous arc activity (129 to 90 Myr) in the Central Depression, late Cretaceous-Eocene arc activity (78 to 37 Myr) in the Western Cordillera and Neogene to modern volcanic arc activity (26 Myr to recent) from the Western Cordillera to the Altiplano [*Scheuber and Reutter*, 1992; *Haschke et al.*, 2006]. The study area covers three of these geologic domains including the Coastal Cordillera, the Central Depression, and the Western Cordillera (Figure 1a). The Coastal Cordillera is a remnant of Jurassic to Early Cretaceous arc magmatism consisting of plutons (Figure 1b) and include mainly lithologies of granodiorites, andesites and gabbros [*Scheuber and Gonzalez*, 1999; *Hartley et al.*, 2000; *González et al.*, 2003]. This domain is located parallel to the Western Cordillera and is characterized by a series of east-west reverse faults (Figure 1a). Formed during the late Miocene some of these faults were reactivated in the Quaternary and induce compression parallel to the plate boundary [*Allmendinger et al.*, 2005]. The Arica Bend between 17-20°S is a feature of the Coastal Cordillera showing low coastal uplift rates [*Madella et al.*, 2016]. The Central Depression is separated from the Coastal Cordillera by a gradual topographic boundary and the north trending Atacama fault zone [*Scheuber and Andriessen*, 1990]. The east-west fault systems of the Coastal Cordillera become blind [*Allmendinger et al.*, 2005] in the Central Depression consisting of sedimentary infill of Oligocene to Holocene age (Figure 1b) [*Hartley et al.*, 2000]. The north trending active strike-slip Argomedo-West Fissure fault system (Figure 1a) is the major boundary to the west where the Central Depression meets the Western Cordillera [*Armijo et al.*, 2010]. The Western Cordillera is composed of late Cretaceous to Miocene volcanic strata

(Figure 1b) and structurally characterized by dextral, orogen-parallel strike-slip-faults [*Reutter et al.*, 1996].

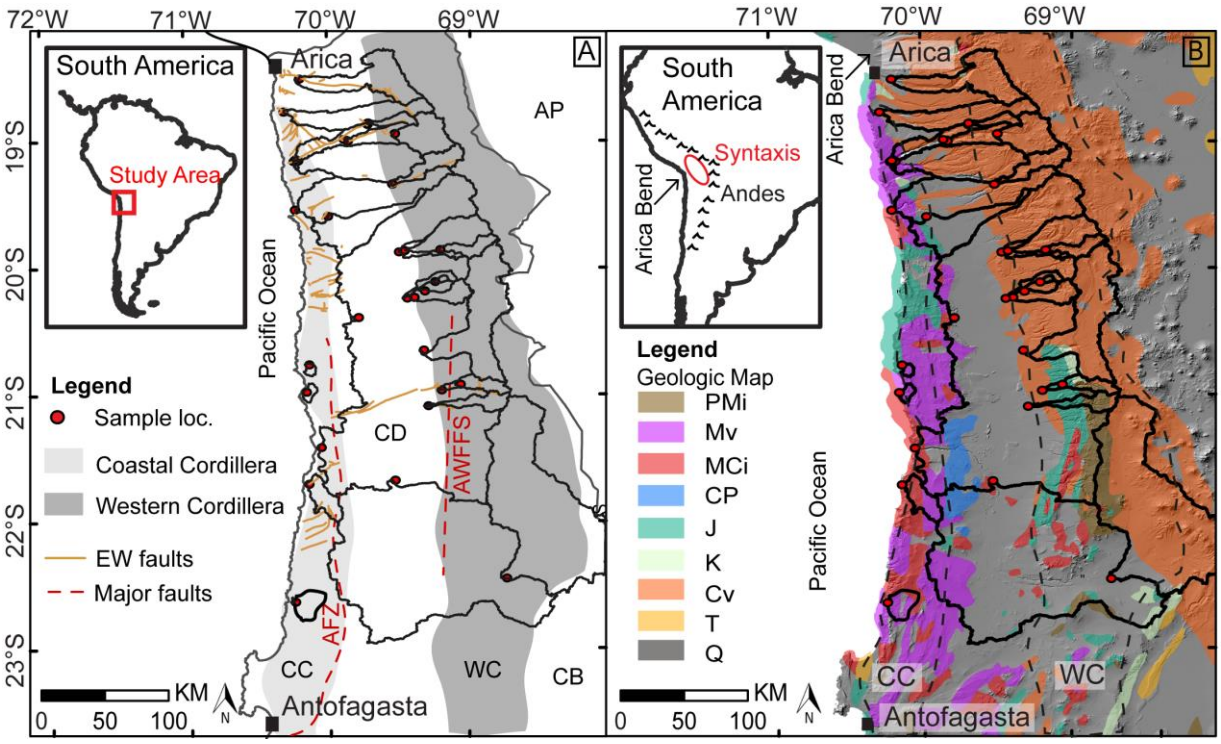

Figure 1. Overview of the study area in northern Chile, South America. 1a: Geologic domains of Coastal Cordillera (CC), Central Depression (CD), Western Cordillera (WC), Alitplano (AP) and Calama Basin (CB) are displayed. Major faults and EW faults are extracted from the database of faults *USGS* [2013] and *Allmendinger et al.* [2005]. Major faults include the Atacama fault zone (AFZ) and the Argomedo-West Fissure fault system (AWFFS). Sample locations are marked in red dots and sampled catchments in black polygons. 1b: Geological map after geo6ag [*USGS*, 2016]. The black dashed lines highlight the extent of the Coastal Cordillera (CC) and Western Cordillera (WC). Units in the geologic map refer to Paleozoic-Mesozoic intrusive of igneous and metamorphic rocks (PMi), Mesozoic volcanics of igneous and metamorphic rocks (Mv), Mesozoic-Cenozoic intrusive igneous and metamorphic rocks (MCi), Permian–Carboniferous sedimentary rocks (CP), Jurassic sedimentary rocks (J), Cretaceous sedimentary rocks (K), Creteceous-Tertiary volcanics and metamorphic rocks (Cv), Tertiary sedimentary rocks (T), Quaternary sedimentary rocks (Q). The syntaxis area labeled in panel b (inset) represents the region above which the subducting plate is bent between the Peru and Chilean segments of the subduction zone (see *Bendick and Ehlers*, 2014 for a description of syntaxial orogen geometry).

2.2 Geomorphic Setting

The Coastal and Western Cordilleras are north-south oriented mountain ranges (Figure 1a). The Coastal Cordillera is characterized by a ~1 km high Coastal escarpment and has a maximum elevation of about 1.5 km above sea level (Figure 2a). Rapidly increasing elevations of the Western escarpment are typical for the Western Cordillera that has a maximum altitude of about 4.5 km (Figure 2a). East-west trending rivers incise both the Coastal and Western Cordilleras and reflect a hydrological change around 21°S in the Western Cordillera. Perennial streams are situated north of 21°S whereas in the south mainly ephemeral streams occur [*Nester et al.*, 2007]. In the Atacama region south of 21°S exposure ages of 9 to 37 Myr revealed slow denudation rates since 25 Myr [*Dunai et al.*, 2005].

Present-day processes show the importance of fluvial and mass wasting processes in the study area. Previous studies have documented the control on knickzones in many of the rivers draining the Western Cordillera [*Abbühl et al*., 2011b; *Trauerstein et al*., 2013; *D'Arcy and Whittaker*, 2014] related to a relative surface uplift of at least 1 km since 10 Myr [*Hoke et al*., 2007; *Jordan et al*., 2010]. Large-scale landslides (up to 9 km3) have been identified in the Coastal and Western Cordilleras between 18°S to 24°S [Mather et al., 2014]. These events are associated with large-magnitude earthquakes [*Strasser and Schlunegger*, 2005; *Pinto et al*., 2008, *Crosta et al*., 2014; *Mather et al.*, 2014].

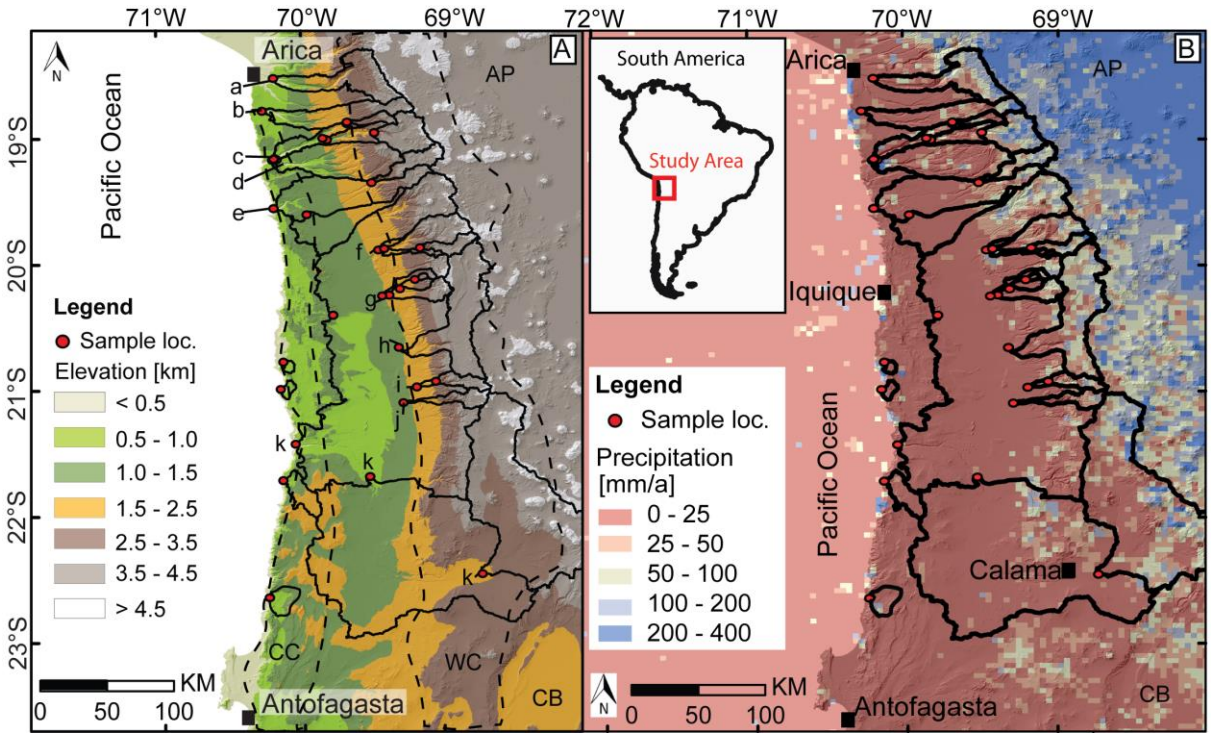

Figure 2. Overview of topography and precipitation rates in the study area. 2a: Topographic map shows elevation differences in colors. The black dashed lines highlight the extent of the Coastal Cordillera (CC) and Western Cordillera (WC). The letters near the sample location denote the rivers, which were sampled. Following rivers are highlighted: Rio Azapa (a), Rio Chaca (b), Rio Camarones (c), Rio Chiza (d), Rio Tana and Tilviche (e), Rio Tarapaca (f), Rio Mamina (g), Rio Chacarilla (h), Rio Guatacondo (i), Rio Mani (j) and the Rio Loa (k). In locations without letters the river name is not known. 2b: Precipitation map showing the annual mean precipitation rates derived from the data product of TRMM2b31 [*Bookhagen and Strecker*, 2008] and sample locations.

2.3 Climate

The principal controls on the arid climate of northern Chile between 18° and 23° S are the Southeast Pacific Ocean atmospheric high-pressure system, upwelling of cold water from the Humboldt Current, and the Andean rain shadow blocking moisture from the Atlantic Ocean [*Hartley and Chong*, 2002; *Garreaud et al.*, 2003; *Houston and Hartley*, 2003; *Rutllant*, 2003; *Ehlers and Poulsen*, 2009; *Jeffery et al.*, 2012; *Schulz et al.*, 2012]. Modern precipitation rates are mainly influenced by the El-Niño-Southern Oscillation (ENSO) and show hyperarid conditions with rainfall ranging from 1 to 80 mm/a recorded

by meteorological stations at the cities of Arica, Iquique and Antofagasta [*Schulz et al.*, 2012]. An overview of annual precipitation rates is given in Figure 2b. Past climate records indicate a repeated onset of hyperaridity since 14 Myr in the Atacama region [*Jordan et al.*, 2014] and result in conflicting interpretations from sedimentary and geomorphic records. A transition of precipitation rates from semiarid to present-day hyperarid conditions was interpreted from paleosol evidence and is thought to have occurred as early as 13 Myr [*Rech et al.*, 2006] due to surface elevation changes of the Andean Plateau [*Ehlers and Poulsen*, 2009; *Insel et al.*, 2009]. Basin sediments indicated that semiarid climate conditions dominated during the Miocene to early Pliocene in the northern Atacama region [*Hartley and Chong*, 2002; *Kirk-Lawlor et al.*, 2013; *Schlunegger et al.*, 2017]. Geomorphic evidence revealed aridification in the late Pliocene or early Pleistocene [*Amundson et al.*, 2012] whereas wetter conditions dominated in the early to mid-Miocene [*Oerter et al.*, 2016].

3 Methods

3.1 Cosmogenic Nuclide-Derived Denudation Rates

Cosmogenic nuclide-derived denudation rates from river sediments are sensitive to the combined effects of physical erosion and chemical weathering over the catchment area. Calculation of denudation rates from these data rely on the following assumptions: (1) At an isotopic steady state condition the radioactive decay and the cosmogenic nuclide export in the river equals the averaged in-situ production of cosmogenic nuclides in the catchment [*von Blanckenburg*, 2006]; (2) Every catchment subarea contributes quartz material, weathering or erosional processes do not enrich the quartz material and different grain sizes have a homogeneous nuclide concentration [*Dosseto and Schaller*, 2016]; (3) Sediment storage is insignificant in the catchment, transport time of sediment is short, and the catchment is large enough to have a low frequency of landslides and debris flows; (4) Shielding of the surface by glaciers, snow, and vegetation is minor [*von Blanckenburg*, 2006; *Dosseto and Schaller*, 2016]. Any violation of these assumptions and systematic biases will be addressed in the discussion section 5.2.

Steady-state catchment-averaged denudation rates over timescales of $<\sim 10^6$yr were calculated from the blank corrected ^{10}Be and ^{26}Al concentrations, in the following labelled as ^{10}Be and ^{26}Al corrected concentrations. Different response times of ^{10}Be and ^{26}Al are a result of their specific decay constant and are an indicator of perturbation of steady state denudation, which can be only identified by comparing ^{10}Be and ^{26}Al concentration of the same sample [*Owen et al.*, 2011]. The cosmogenic isotope concentration (C) of ^{10}Be and ^{26}Al at the Earth's surface is inversely proportional to the denudation rate (E) assuming that the surface is steadily eroding and described in the following equation [Schaller et al., 2002]:

$$C = P_{\mathrm{Nuc}}(0)\times\sum_{i=1}^{2}\frac{a_i}{\left(\lambda+\frac{\rho\times E}{b_i}\right)} + P_{\,\mu\mathrm{stopped}}(0)\times\sum_{j=1}^{3}\frac{a_j}{\left(\lambda+\frac{\rho\times E}{b_j}\right)} + P_{\,\mu\mathrm{fast}}(0)\times\sum_{k=1}^{3}\frac{a_k}{\left(\lambda+\frac{\rho\times E}{b_k}\right)} \quad (1)$$

where C is the isotope concentration (atoms/g(qtz)), E is the denudation rate (cm/yr), λ is the decay constant (^{10}Be 4.99E-07 ± 0.43E-08 yr^{-1} and ^{26}Al 9.83E-07 ± 2.50E-08 yr^{-1} [*Chmeleff et al.*, 2010; *Korschinek et al.*, 2010; *Balco et al.*, 2013]), ρ is the rock density (2.4 ± 0.2 g/cm^{-3}), and t is the time (yr). $P_{nuc}(0)$, $P_{\mu stopped}(0)$ and $P_{\mu fast}(0)$ are the surface production rates of cosmogenic nuclides (atoms/g*yr) by spallation, stopped and fast muons. The coefficients $a_{i,j,k}$ (dimensionless) and $b_{i,j,k}$ (g/cm^2) are used for depth scaling of the production rates and reported by *Schaller et al.* [2002]. The nucleonic and muonic production rates were scaled using the time-dependent scaling laws of *Dunai* [2000] and those of *Schaller et al.* [2002]. Sea level high latitude (SLHL) nucleonic production rates (P_{nuc}) for ^{10}Be and ^{26}Al are based on the values 4.431 ± 0.506 atoms/g*yr (^{10}Be) and 29.8 ± 1.3 atoms/g*yr (^{26}Al) reported in *Balco et al.* [2008]. The fast and stopped muonic production rates use the values 0.037 ± 0.005 atoms/g*yr (^{10}Be $P_{\mu fast}$), 0.025 ± 0.002 atoms/g*yr (^{10}Be $P_{\mu stopped}$), 0.352 ± 0.042 atoms/g*yr (^{26}Al $P_{\mu fast}$) and 0.307 ± 0.028 atoms/g*yr (^{26}Al $P_{\mu stopped}$) provided by *Balco et al.* [2013]. The catchment-averaged production rate is the average production rate for each DEM pixel (90 m resolution) in the catchment area. Each single production rate was corrected for topographic shielding following the procedure described in *Dunne et al.* [1999] and *Norton and Vanacker* [2009]. Corrections for lithology and snow shielding were not applied because (1) catchments with similar rock type (Jurassic and Cretaceous monzodiorites, granodiorites and granites) were targeted to provide more uniform quartz content between catchments. (2) Mean annual snowfall is low in this region and close to 0 mm/a in the Coastal Cordillera and restricted to elevations above 4500m for the Western Cordillera [*Kober et al.*, 2007]. Furthermore, sufficient meteorological information is not available from the Western Cordillera to provide a reliable estimate of any effect present in the higher reaches of the catchments sampled. We calculate the uncertainties in denudation rates using a Monte Carlo simulation of error propagation. The error propagation includes the production rate error of nucleonic, fast and stopped muonic production, a 5% DEM altitude error for the production rate, the decay constant error, the rock density error and the ^{10}Be concentration error.

Detrital samples were collected from 33 rivers with catchment sizes between 61 km^2 and about 42,600 km^2 (Table 1) for measurements of in situ-produced ^{10}Be and ^{26}Al. Catchments of similar stream order, similar catchment size, and similar quartz-rich lithology were selected. The lithologies were mostly Jurassic and Cretaceous monzodiorites, granodiorites and granites. The catchments are separated by ~50km. From each sample either the preferred 500 to 1000 µm, or in cases of insufficient quartz mass (sample ID 14, 17, 23, 29, 30 and 34), the 250 to 500 µm grain size fraction was sieved and cleaned to pure quartz (Table 1). Approximately 200 µg of ^{9}Be was added to approximately ~20 g pure quartz. ^{10}Be

and ^{26}Al were separated by using the standard separation method of *von Blanckenburg et al.* [2004] and *Wittmann et al.* [2007]. The ratios of $^{10}Be/^{9}Be$ and $^{26}Al/^{27}Al$ were measured as BeO and Al_2O_3 targets by accelerator mass spectrometry (AMS) at the University of Köln. Stable Al concentration measurements were performed by inductively coupled plasma-optical emission spectrometry (ICP-OES) at the University of Tübingen. Sample ID 22b (Table 1) was measured twice to test reproducibility of the method.

3.2 Analysis of Catchment Parameters

Catchment parameters of mean elevation, mean basin slope, mean 5km radius local relief, stream order, mean normalized channel steepness index (mean k_{sn}) and mean annual precipitation rate were calculated for comparison to denudation rates. A minimum drainage area for initiating the stream order was set with an area of 1 km^2. These parameters were computed using the Shuttle Radar Topography Mission (SRTM) digital elevation model (DEM) with a resolution of 90m. Topographic parameters were analyzed using ArcGIS, TopoToolboxv2 [*Schwanghart and Scherler*, 2014] and the Stream Profiler Matlab scripts of *Whipple et al*. [2007].

The normalized channel steepness index (k_{sn}) [*Wobus et al*., 2006] was calculated to characterize the geometry of river longitudinal profiles. The stream power-law function shows the relation between slope and drainage area by the functional relationship:

$$S = k_s \times A^{-\theta} \tag{2}$$

where S is the local channel gradient (m/m), k_s the steepness index (m^{-1}), A is the upstream drainage area (m^2) and θ is the concavity index (dimensionless) [*Hack*, 1973; *Kirby and Whipple*, 2001; *Wobus et al*., 2006]. The advantage of using k_{sn} is the quantification of the local specific channel steepness to the steepness of an equilibrium river [*Ouimet et al*., 2009; *Whittaker*, 2012], which then enables comparison between rivers in different regions. We calculated the normalized k_s (k_{sn}) by using a reference concavity of 0.45, a smoothing window of 500m and a contour sampling interval of 20 m. The resulting k_{sn} values were clipped to the size of the catchments and used to calculate the mean k_{sn}.

The global Tropical Rainfall Measurement Mission (TRMM 2B31) provides a high-resolution spatiotemporal distribution of precipitation from 1998 to 2006 with a 5x5 km grid resolution (Figure 2b). The data are reported in terms of mean annual precipitation [*Bookhagen and Strecker*, 2008] and provide a complete record of precipitation data in this study area. Satellite derived precipitation is needed because of the low density of weather stations in the region [*Schulz et al.*, 2012]. Limits of the TRMM product can occur by trying to capture extreme rain events of a few hours and single days in response to ENSO related variations [*Curtis et al.*, 2007]. The TRMM product is mostly insensitive to the detection of hydrometeors such as small liquid water particles found in fog or low clouds [*Duan et al.*, 2015]. The

effects of the spatial and temporal variability of fog in the Coastal Cordillera and the Central Depression [*Cereceda et al.*, 2008] could be therefore underestimated.

3.3 Factor Analysis Model

Factor analysis is a multivariate statistical method that extracts from a large set of variables a few common latent characteristics by detecting linear correlations with a maximum likelihood estimate [*Kaiser*, 1957; *Tucker and Lewis*, 1973; *Knott and Bartholomew*, 1999]. Similar to a principal component analysis, the approach groups correlated variables into a smaller number of "factors" that reduces system complexity and identifies the primary controls on a system by identifying correlations and covariations. The factors are linear combinations of the original variables. Factor loadings are the correlations between the original variables and the factors and represent the calculation of catchment parameter covariation. The factor analysis model can be described by:

$$X_{(N\times p)} = F_{(N\times k)}A'_{(k\times p)} + E_{(N\times p)} \quad (3)$$

where X is the data matrix with N elements and p variables, F the factor score matrix with k the number of factors to be used, A' the factor loading matrix, plus the error term E [*Reyment and Jvreskog*, 1996]. Additional details of the method used here are described in *Hartmann and Wünnemann* [2009]. The data matrix X contains ten variables of the sampled basins from 18.52°S to 22.64°S. Replicate measurements and one sample disturbed by a neighbouring large landslide (Table 1, sample ID 22b + 10) were excluded. The independent variable in the data matrix is the latitude. The dependent variables contain the catchment characteristics of drainage area, mean elevation, ^{10}Be blank corrected concentration, denudation rate, mean annual precipitation, stream order [*Strahler*, 1957], mean k_{sn}, grain size used to measure the ^{10}Be concentration, mean basin slope and mean local relief (5 km radius). With increasing number of variables, the robustness of the factor analysis increases. We used both the ^{10}Be concentrations as well as the denudation rates because we know that from these two variables an inverse relation is expected. The same holds for drainage area and stream order, which are expected to show a positive relationship. By using these variables, we can check the results of the factor analysis. A z-transformation was applied on the X data matrix to provide an interpretation independent of unit dimension. The factor analysis model was performed in R-mode, which means that the X data matrix is transformed into a correlation matrix R before factor loadings are computed.

4 Results

4.1 The Coastal Cordillera

4.1.1 ^{10}Be Concentrations and Derived Denudation Rates

Analyses of five blank corrected ^{10}Be measurements and one duplicate analysis provide insight into the erosional characteristics of the coastal escarpment of the Coastal Cordillera between 20°S to 23°S (Figure 3a). Table 1 illustrates the nuclide concentrations along the Coastal Cordillera that range between 25.1 ± 1.1 to 521.3 ± 16.2 10^4 atoms/g(qtz). Denudation rates were calculated from ^{10}Be concentrations (Figure 3a, 4a). In the Coastal Cordillera denudation rates vary between 0.4 ± 0.5 to 20.6 ± 1.5 m/Myr (Figure 4a). The general latitudinal trend in the data is an increase in the denudation rate from north to south (Figure 4a). The analysis of sample ID 22b represents a reanalysis of sample ID 22a and was conducted for evaluating the reproducibility of samples. The reanalysis results show that the derived denudation rates of sample ID 22a and ID 22b are in the same range. Denudation rates of 0.4 ± 0.5 m/Myr were measured for ID 22a and 0.3 ± 1.2 m/Myr for ID 22b, respectively.

4.1.2 Mean Basin Slope, Relief and Precipitation

The catchment parameters of mean basin slope and mean local relief reflect the degree to which the surface is incised by climate or tectonic driven denudation. In this study mean basin slope and mean local relief scale non-linearly with mean precipitation rates and seem to be decoupled from denudation rates. The mean local relief ranges between 365 ± 135m and 881 ± 38m and is characterized by large 2-sigma standard deviations (Figure 4b). Figure 4c shows the catchment-averaged mean slopes. The large 2-sigma standard deviations from the mean slopes are given in Table 2 and are not illustrated to enhance the figure clearness. Catchment-averaged mean slopes are clustered into two groups between 10° to 16° and 2° to 8°, respectively. To investigate climate control on denudation, the TRMM derived catchment-wide mean annual precipitation rates were included (Figure 4e). The mean precipitation rates vary between 0 mm/a and 116 mm/a. Four out of five catchments draining the Coastal Cordillera have mean precipitation rates of less than 40mm/a.

4.1.3 Normalized Channel Steepness Index (k_{sn})

Figure 4d shows the mean channel steepness index and the 2-sigma standard deviation for the main channels of each of the five drainage basins. The results show pronounced variations in the channel steepness depending on the location of the channels. Drainage basins with channels located at the coastal scarp display the highest k_{sn} values relative to the plateau of the Coastal Cordillera and the Central Depression. Mean k_{sn} values for each catchment vary between 37±15$m^{0.9}$ and 136±112$m^{0.9}$ (Table 2).

Large 2-sigma standard deviations from mean k_{sn} values are observed in the catchments due to the rapid increase of elevation at the coastal scarp.

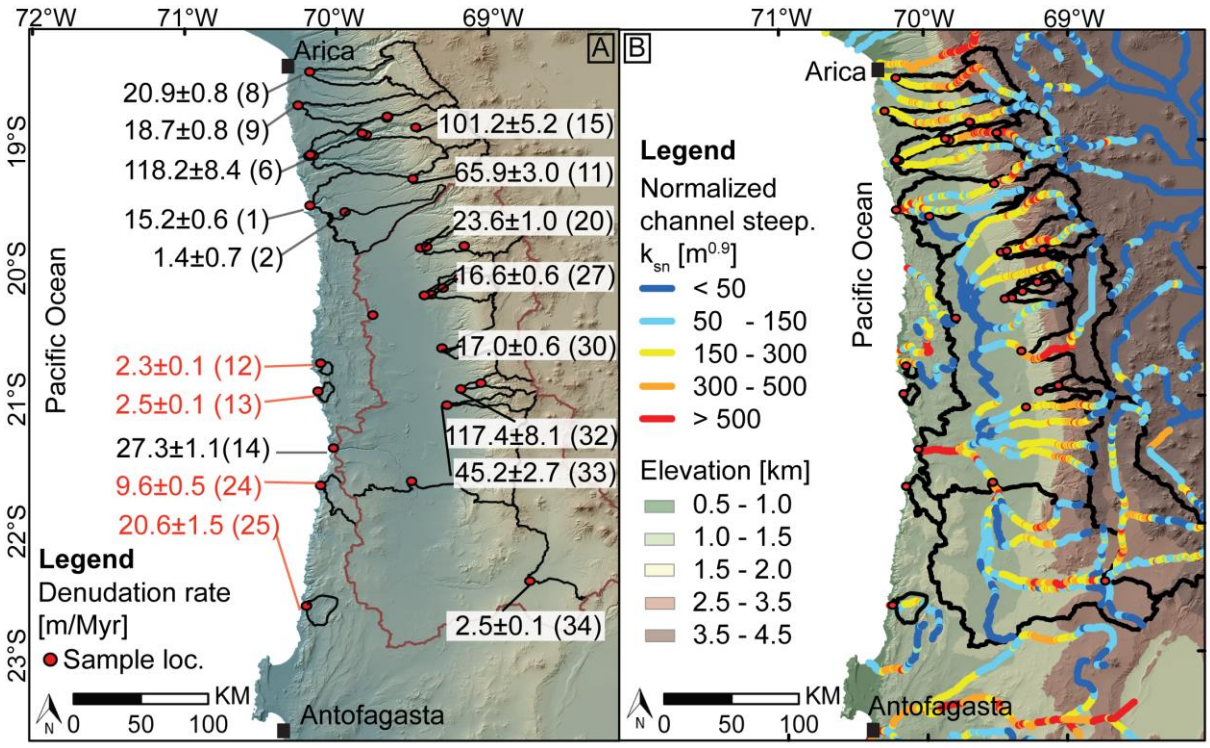

Figure 3. Denudation rates and normalized channel steepness indices of the study area. 3a: The spatial distribution of selected denudation rates is illustrated in red for the Coastal Cordillera and in black for the Western Cordillera. The catchment borders are shown in black, except for the Rio Lluta catchment that is illustrated with brown lines. Please note that not all data are shown. Numbers in brackets refer to sample ID in Table 1. 3b: Digital Elevation Model of SRTM 90m colour coded by elevation and colour coded normalized channel steepness indices (k_{sn}). Cold colours refer to low normalized channel steepness indices whereas warm colours document high indices.

4.2 The Western Cordillera

4.2.1 ^{10}Be and ^{26}Al Concentrations and Derived Denudation Rates

The measured nuclide concentrations for ^{10}Be are given in Table 1, and for ^{26}Al in Table 3. The spatial distribution of the denudation rates is shown in Figures 3a and 4f. The measured ^{10}Be concentrations extend from 18°S to 23°S and provide information about the spatial variation of drainage basin denudation rates along the Western Cordillera. The values range from 7.3 ± 0.4 to 441.9 ± 13.5 10^4 atoms/g(qtz). The nuclide concentrations are generally lower than those measured at the Coastal Cordillera. Catchments draining the Western Cordillera have a denudation rates up to 2 orders of magnitude higher, 1.4 ± 0.7 to 168.0 ± 19.8 m/Myr, than catchments in the Coastal Cordillera (Figure 3a, compare also Figure 4f and 4a). Two catchments of the Western Cordillera including the exorheic Camarones basin around 19°S and the endorheic Guatacondo basin at 21°S, yield the highest catchment-

averaged denudation rates of the study area, 165.2 ± 25.3 and 168.0 ± 19.7 m/Myr (Figure 4f). One sample from the Rio Camarones, ID 10 (Table 1), is considered unreliable because of a large landslide documented by *Mather et al.* [2014] above the sample site.

Analyses of ^{26}Al concentrations from eight samples range from 54.2 ± 4.1 to 2138.5 ± 71.1 10^4 atoms/g(qtz) (Table 3). The calculated denudation rates of ^{26}Al range from 5.3 ± 0.3 to 274.8 ± 53.9 m/Myr including the sample, ID 5 (Table 3) that is considered unreliable due to a large landslide [*Mather et al.*, 2014]. The denudation rates derived from ^{26}Al and ^{10}Be are within the same range of uncertainty (Table 3). The ratio of ^{26}Al and ^{10}Be is sensitive to the exposure history of a sample due to differences in the radioactive decay rate. The evolution of ^{26}Al/^{10}Be with time is shown in the erosion island plot ('Banana plot' Figure 5). The ratio varies between 6.3 ± 0.2 to 7.4 ± 0.6 (Table 3) and suggests minimal effects from sediment storage and recycling in the samples analyzed. These results differ from the results of *Jungers et al.* [2013] who sampled alluvial deposits and found sediment recycling to be significant.

4.2.2 Mean Basin Slope, Relief and Precipitation

The Western Cordillera as well as the Coastal Cordillera indicate a decoupling between denudation rates, mean basin slope morphology, local relief and precipitation rates. Mean local relief for each basin covers a wide range of values and show large 2-sigma standard deviations for the Western Cordillera (Figure 4g). Catchment-averaged mean slopes are distributed in the same groups as the Coastal Cordillera, between 10° to 16° or from 2° to 8°, respectively (Figure 4h). Mean precipitation rates range from 6 mm/a to 115 mm/a. The highest rates can be found around 19°S. The spatial distribution displays a decreasing trend from north to south for catchments draining the Western Cordillera (Figure 4j).

4.2.3 Normalized Channel Steepness (k_{sn})

The highest k_{sn} values in the Western Cordillera are clustered along the steep scarp of the Western Cordillera between elevations of 2.5 and 3.5 km surface elevation (Figure 3b, 4i) along similar lithology of Cretaceous and Tertiary volcanic strata (Figure 1b). Lower k_{sn} values are concentrated in the diffuse and rounded landscapes of the Central Depression as well as in the Altiplano. Mean k_{sn} values for each catchment, ranging from 42 ± 34 $m^{0.9}$ to 230 ± 140 $m^{0.9}$, exhibit a large 2-sigma standard deviation especially for basins reaching higher elevations (Table 2).

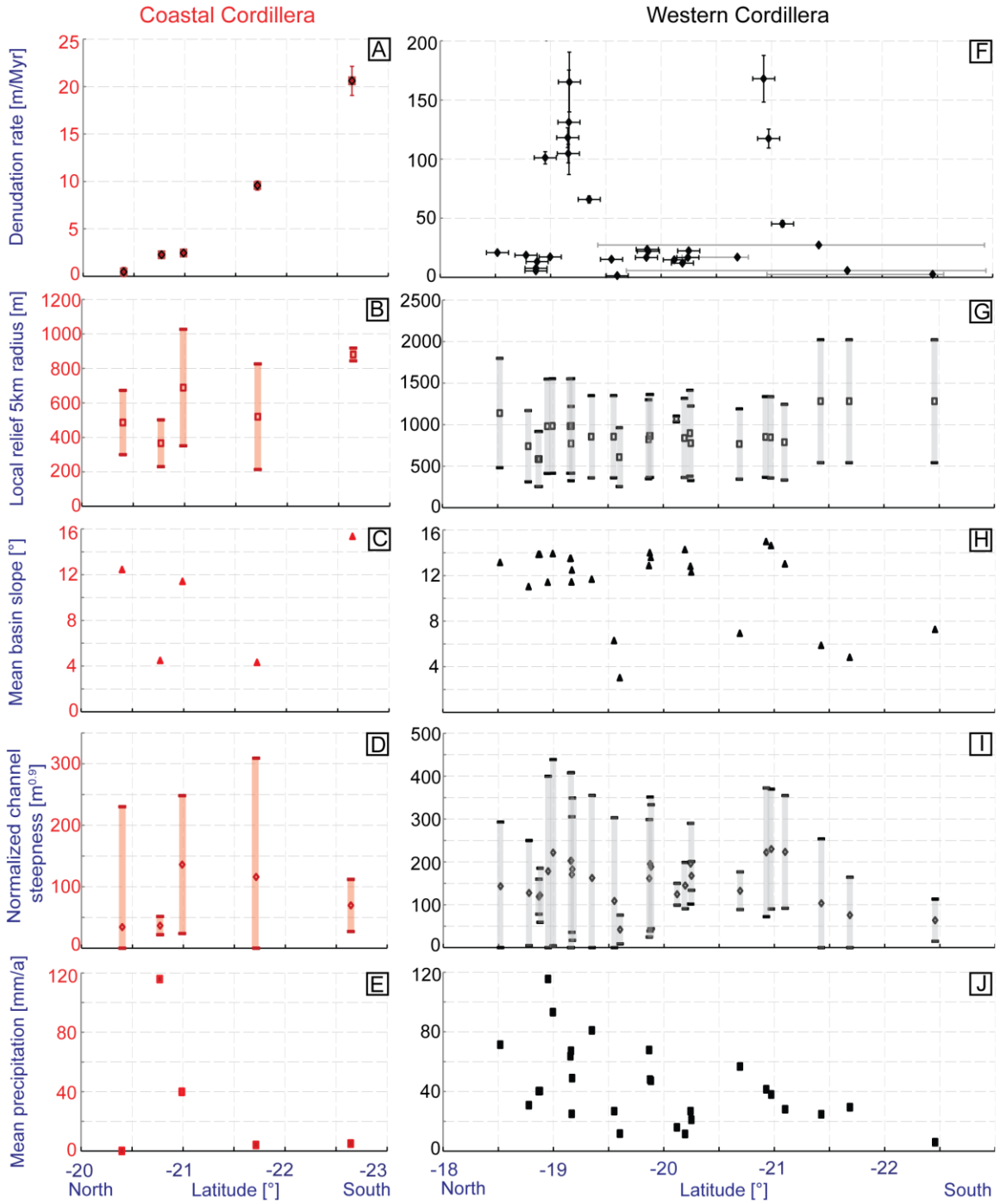

Figure 4. Summary of catchment characteristics in Western and Coastal Cordilleras versus latitude. 4a and 4f: Denudation rates with 1-sigma uncertainty. Horizontal error bars describe the latitudinal extent of the catchments. Please note differences in the y- and x-axis from left and right- hand panels. 4b and 4g: Local relief of 5km radius. Error bars show 2-sigma standard deviation from mean value. 4c and 4h: Mean basin slope. 2-sigma standard deviation is given in Table 2 and not shown to enhance the figure clarity. 4d and 4i: Normalized channel steepness indices showing mean value and standard deviation. 4e and 4j: Catchment-wide annual mean precipitation derived from TRMM2b31.

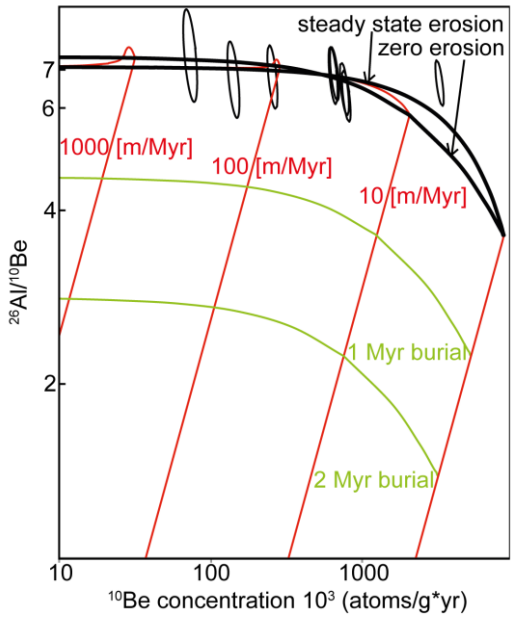

Figure 5. Erosion island plot ('Banana plot'). $^{26}Al/^{10}Be$ ratio versus ^{10}Be concentration (normalized to sea level high latitude (SLHL)). The diagram shows conditions of constant exposure by zero erosion and steady state erosion (black lines) and predicted changes due to different periods of burial deposition (green lines). Red lines reproduce the denudation rates. The black ellipses illustrate the sample results according to their $^{26}Al/^{10}Be$ ratio and denudation rate including the 1σ error. The figure was produced with the add-in CosmoCalc [*Vermeesch*, 2007].

4.3 Latitudinal Gradient of Topography

Latitudinal variations in topography were investigated with 50 and 100km wide swath- profiles for the Western Cordillera, Central Depression and Coastal Cordillera (Figure 6a). Swath- profiles of 50km width were used to capture the Central Depression and Coastal Cordillera that have a smaller width than the Western Cordillera. The analysis provides information about regional differences in topography. This analysis is needed because measured denudation rates (Figure 3a, 4a and 4f) are extremely low in this region and may not reflect large-scale topographic trends. The results compiled for the Western Cordillera, Central Depression, and Coastal Cordillera show a slightly decreasing topographic geometry from north to south until 21°S (Figure 6b, 6c and 6d). South of 21°S topography becomes more complex and shows different patterns for the Western Cordillera, Central Depression and Coastal Cordillera. In Figure 6b it is visible that the Western Cordillera decreases rapidly in elevation at 22.5°S, which marks the start of the Calama Basin with lower surface elevations. The swath- profile for the Central Depression illustrates an overall topography with a concave shape and the lowest elevation at 21.5°S (Figure 6c). The lowest point of surface elevation can be attributed to the incision of the Rio Loa. Comparing the Western and Coastal Cordillera, an inverse topography is noticeable for the Coastal Cordillera (Figure 6d).

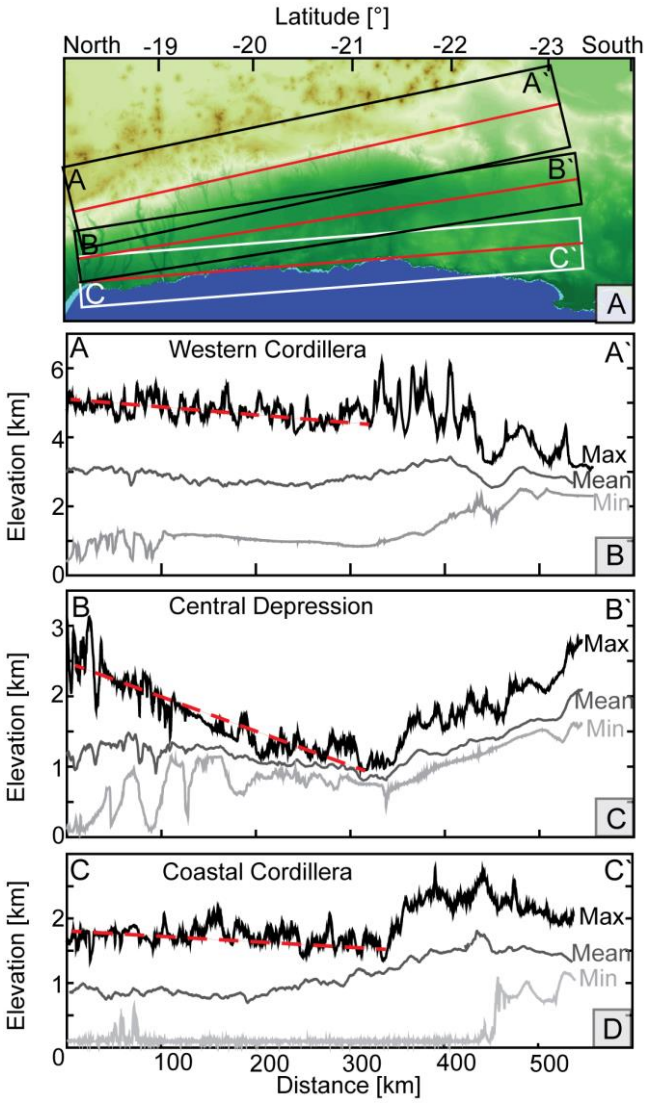

Figure 6. Latitudinal topographic characteristics. 6a: Top panel shows swath positions in DEM. 6b: Swath- profile of Western Cordillera (600kmx100km). 6c: Swath- profile of Central Depression (600kmx50km). 6d: Swath- profile of Coastal Cordillera (600kmx50km). Red dashed lines in A, B and C indicate the topographic trends measured from north to south.

4.4 Correlation and Covariation of Catchment Parameters

The factor analysis calculated correlation coefficients (R) at the 95% confidence level and modeled the multivariate covariation of catchment parameters that are reported as factor loadings. Table 4 contains a complete list of the correlation coefficients and the factor loadings are reported in Table 5. Correlation and covariation are statistical methods to explore the strength of linear association between parameters. Parameters with no relationship or with a non-linear relationship are not accounted in the analysis. Results of the correlation coefficient R (Table 4) display strong and significant positive correlations for the parameters of mean elevation and mean slope (0.56) as well as mean k_{sn} and mean elevation (0.65). Furthermore, a strong positive linear correlation occurs for denudation rate and mean k_{sn} (0.61). The

mean annual precipitation rate is not significantly correlated with other catchment parameters except for a very weak negative linear correlation with the ^{10}Be corrected concentration (-0.36).

The factor loadings represent the calculation of catchment parameter covariation and are clustered into three groups (factors). The number of factors is selected by the Kaiser-criteria with an eigenvalue greater than one. The three factors are sorted by decreasing order of explained variance and explain in total about 62% of the variance in catchment parameters (Table 5). The first factor explains about 23% of the total variance and is associated with drainage area, stream order and mean local relief. The second factor accounts for about 21% of the variance. It leads to the selection of denudation rate and indicates the mean k_{sn} as a covarying parameter. The third factor selects the mean basin slope as well as the mean elevation and explains about 18% of the total variance. The latitudinal distribution of covarying parameters grouped in factors is shown in Figure 7. Strong covariation of the first factor, area, stream order and mean local relief, can be found at 21.5°S. The denudation rate and mean k_{sn} strongly covary at 19°S and 21°S. The last factor, mean elevation and mean basin slope, show the strongest covariation at 20°S.

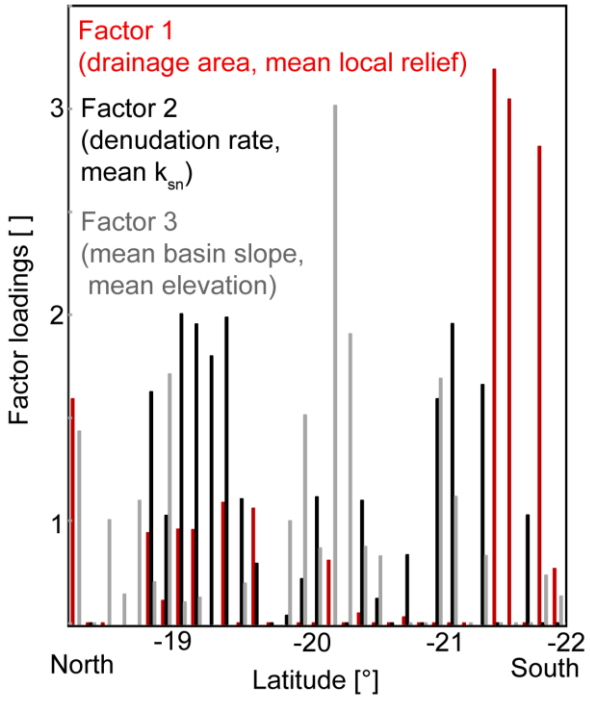

Figure 7. Factor loadings plotted versus latitude showing the distribution and highest covariance of catchment parameters for a given latitude. Red bars show factor 1, black bars factor 2 and grey bars factor 3. The calculated factor loadings are dimensionless and sorted by decreasing explained variance.

Table 1
^{10}Be Analytical and Denudation Rate Data

ID	Drainage area (km^2)	Sample lat (deg)	Sample long (deg)	m(qtz) (g)	Grain size (mm)	Ptot (atoms/g (qtz)*yr)	^{10}Be corr. conc. (10^4atoms/g (qtz))[a]	Uncertainty ($\pm10^4$ atoms/g (qtz))	Denudation rate (m/Myr)	Uncertainty (±m/Myr)	Apparent age (kyr)	Uncertainty (±kyr)
Western Cordillera												
1	4670	−19.55089	−70.19434	21.4	0.5–1	14.2	64.0	2.2	15.2	0.6	45.0	4.9
2	1288	−19.60263	−69.96312	24.4	0.5–1	8.1	317.0	9.7	1.4	0.7	389.5	38.3
3	633	−19.34849	−69.51186	20.1	0.5–1	37.0	38.4	1.4	65.9	3.0	10.4	1.1
4	4744	−19.16942	−70.20037	20.0	0.5–1	18.9	8.1	0.5	165.2	25.3	4.3	0.4
5	2284	−19.16528	−70.16817	19.0	0.5–1	13.7	7.5	0.7	131.2	44.2	5.5	0.5
6	2398	−19.15475	−70.18531	23.0	0.5–1	23.9	14.1	0.6	118.2	8.4	5.9	0.6
7	2367	−19.15947	−70.19036	19.9	0.5–1	24.4	16.2	0.8	104.7	7.8	6.6	0.7
8	1801	−18.51871	−70.18941	24.4	0.5–1	23.4	76.0	2.6	20.9	0.8	32.5	3.5
9	1501	−18.77716	−70.26838	23.0	0.5–1	17.9	65.4	2.2	18.7	0.8	36.5	3.8
10	1526	−19.0072	−69.8206	23.4	0.5–1	30.6	7.3	0.4	289.8	26.9	2.4	0.3
11	435	−18.99569	−69.84812	23.5	0.5–1	19.9	78.2	2.5	17.2	0.6	39.4	4.3
14	42617	−21.42659	−70.05085	18.1	0.25–0.5	14.7	37.6	1.3	27.3	1.1	25.6	2.7
15	1028	−18.95096	−69.49113	24.4	0.5–1	37.6	25.5	1.0	101.2	5.2	6.8	0.7
16	228	−18.8779	−69.68276	19.7	0.5–1	27.5	138.1	4.4	13.3	0.6	50.3	4.9
17	162	−18.86769	−69.67751	21.6	0.25–0.5	28.7	243.6	7.5	7.7	0.3	84.7	9.0
18	228	−18.86675	−69.68132	23.2	0.5–1	27.5	322.1	10.0	5.4	0.2	117.1	12.0
19	1565	−19.88353	−69.46416	19.9	0.5–1	33.9	103.7	3.4	22.0	0.7	30.6	3.4
20	1452	−19.8744	−69.42287	19.2	0.5–1	35.6	101.3	3.4	23.6	1.0	28.5	2.9
21	352	−19.86701	−69.17344	19.7	0.5–1	40.1	159.2	5.2	16.8	0.6	39.7	4.2
23	23201	−21.6853	−69.52814	19.1	0.25–0.5	16.1	182.4	5.7	5.7	0.3	113.4	11.7
26	61	−20.1191	−69.20985	19.1	0.5–1	31.6	142.5	4.7	14.8	0.5	45.1	4.9
27	499	−20.24223	−69.39035	19.0	0.5–1	28.1	112.2	3.8	16.8	0.6	39.9	4.4
28	194	−20.24965	−69.43873	20.3	0.5–1	20.2	61.7	2.3	22.4	1.0	30.6	3.3
29	223	−20.19265	−69.31455	21.0	0.25–0.5	19.8	110.4	3.5	12.0	0.5	55.7	5.8
30	223	−20.69	−69.27	18.3	0.25–0.5	19.5	77.8	2.5	17.0	0.6	39.9	4.2
31	400	−20.92806	−69.06219	7.5	0.5–1	37.0	15.1	0.9	168.0	19.7	4.1	0.5
32	463	−20.97284	−69.19701	18.1	0.5–1	33.7	19.7	0.9	117.4	8.1	5.9	0.6
33	499	−21.09846	−69.29047	17.1	0.5–1	33.3	50.3	1.8	45.2	2.7	15.1	1.5
34	8518	−22.45746	−68.73074	18.6	0.25–0.5	18.8	441.9	13.5	2.5	0.1	235.5	24.0
Coastal Cordillera												
12	75	−20.77136	−70.1334	16.7	0.5–1	4.4	116.8	3.7	2.3	0.1	267.7	28.2
13	112	−20.98845	−70.1528	19.4	0.5–1	4.5	112.1	3.8	2.5	0.1	250.7	26.6
22a	591	−20.40027	−69.78211	18.5	0.5–1	6.1	521.3	16.2	0.4	0.5	854.7	86.4
22b	591	−20.40027	−69.78211	22.3	0.5–1	6.1	649.0	19.7	0.3	1.2	1064.0	110.0
24	559	−21.71416	−70.13986	13.3	0.5–1	7.8	56.1	1.9	9.6	0.5	72.3	7.5
25	1556	−22.64401	−70.24519	14.7	0.5–1	7.1	25.1	1.1	20.6	1.5	35.2	3.5

[a]The ^{10}Be-corrected concentration was blank-corrected with the averaged ^{10}Be blank concentration of 8.19E04 atoms/g(qtz).

Table 2
Catchment Parameters

ID	Sample name	River name	Mean elev. (m)	Mean precip. (mm/a)	Stream order (Strahler count)	Mean k_{sn} (m^{09})	STD k_{sn} (m^{09})	Mean basin slope (deg)	STD slope (deg)	Mean local relief (5 km radius in m)	STD local relief (5 km radius in m)
Western Cordillera											
1	15CL002	Tana	2017	27	6	109	194	6	8	855	494
2	15CL008	Tana	1479	12	5	42	34	3	5	609	353
3	15CL011	Tana	3925	81	4	162	193	12	8	855	494
4	15CL012	Camarones	2475	49	6	183	166	12	9	984	569
5	15CL014	Camarones	2062	25	5	170	135	11	9	772	446
6	15CL015	Camarones	2889	64	6	202	205	14	9	983	568
7	15CL016	Camarones	2924	67	6	203	205	14	9	983	568
8	15CL018	Azapa	2926	71	5	143	150	13	10	1139	658
9	15CL019	Chaca	2357	31	4	127	123	11	9	741	428
10	15CL020	Camarones	3491	91	5	221	217	14	9	983	569
11	15CL021	Camarones	2747	93	3	222	217	14	9	883	521
14	15CL028	Loa	2100	25	8	103	150	6	7	1282	740
15	15CL031	Camarones	3998	115	5	178	222	11	8	980	567
16	15CL034	Camarones	3420	40	1	122	63	14	7	586	331
17	15CL035	Camarones	3507	40	3	119	41	14	7	586	332
18	15CL036	Camarones	3424	40	2	119	41	14	7	586	331
19	15CL041	Tarapaca	3706	47	5	189	145	14	8	863	499
20	15CL042	Tarapaca	3827	48	3	195	156	14	8	863	497
21	15CL045	Tarapaca	4104	68	4	162	137	13	8	824	476
23	15CL049	Loa	2310	29	7	76	89	5	6	1282	740
26	15CL057	Mamina	3667	16	2	124	25	18	7	1068	338
27	15CL058	Mamina	3304	27	5	196	94	13	8	897	517
28	15CL059	Mamina	2782	21	3	167	34	12	8	776	448
29	15CL061	Mamina	2856	12	1	145	54	14	8	839	476
30	15CL063	Chacarilla	2770	57	5	132	44	7	7	767	423
31	15CL065	Guatacondo	3933	41	2	222	150	15	10	852	486
32	15CL069	Guatacondo	3702	38	4	230	140	15	9	847	488
33	15CL070	Mani	3647	28	4	223	131	13	8	788	455
34	15CL075	Loa	2818	6	7	64	49	7	7	1282	740
Coastal Cordillera											
12	15CL026	/	697	116	3	37	15	4	4	365	135
13	15CL027	/	721	40	3	136	112	11	7	689	338
22	15CL047	/	1149	0	2	34	195	12	7	486	186
24	15CL054	/	1460	4	4	116	193	4	4	519	306
25	15CL055	/	1345	5	5	70	42	15	11	881	38

Table 3
^{26}Al Analytical and Denudation Rate Data

ID	Sample name	Sample lat. (deg)	Sample long.(deg)	Ptot (atoms/g*yr)	m(qtz) (g)	^{26}Al corr. Concentration[a] (10^4 atoms/g (qtz))	Uncertainty ($\pm10^4$ atoms/g (qtz))	Denudation rate (m/Myr)	Uncertainty (±m/Myr)	^{26}Al/^{10}Be ratio	Uncertainty ±ratio
Western Cordillera											
1	15CL002	−19.55089	−70.19434	93.31	21.41	437.9	20.1	14.5	1.1	6.8	0.3
2	15CL015	−19.15475	−70.18531	164.46	23.00	94.9	5.8	124.3	15.1	6.7	0.4
8	15CL018	−18.51871	−70.18941	159.23	24.35	493.0	19.8	22.0	1.5	6.5	0.3
9	15CL019	−18.77716	−70.26838	121.24	22.99	449.8	18.3	18.4	1.3	6.9	0.3
10	15CL020	−19.0072	−69.8206	208.28	23.38	54.2	4.1	274.8	53.9	7.4	0.6
11	15CL021	−18.99569	−69.84812	134.81	23.46	492.5	19.1	18.6	1.3	6.3	0.2
15	15CL031	−18.95096	−69.49113	254.60	24.40	173.2	8.8	103.0	9.7	6.8	0.3
18	15CL036	−18.86675	−69.68132	186.58	23.22	2138.5	71.1	5.3	0.3	6.6	0.2

[a]The ^{26}Al-corrected concentration was corrected with the averaged ^{26}Al blank concentration of 3.70E04 atoms/g(qtz).

Table 4
Factor Analysis Results for Correlation Coefficient[a]

Parameters	Drainage area	Mean elevation	^{10}Be corr. concentration	Denudation rate	Mean precipitation	Stream order	Mean k_{sn}	Grain size	Mean basin slope	Mean local relief
Drainage area	**1.00**	−0.16	−0.02	−0.06	−0.16	0.61	−0.24	−0.54	−0.43	0.57
Mean elevation	−0.16	**1.00**	−0.18	0.30	0.26	−0.15	0.65	0.02	0.56	0.30
^{10}Be corr. concentration	−0.02	−0.18	**1.00**	−0.54	−0.36	−0.17	−0.63	−0.25	−0.17	−0.20
Denudation rate	−0.06	0.30	−0.54	**1.00**	0.25	0.18	0.61	0.27	0.30	0.21
Mean precipitation	−0.16	0.26	−0.36	0.25	**1.00**	0.01	0.32	0.22	0.05	0.00
Stream order	0.61	−0.15	−0.17	0.18	0.01	**1.00**	−0.06	−0.27	−0.49	0.63
Mean k_{sn}	−0.24	0.65	−0.63	0.61	0.32	−0.06	**1.00**	0.31	0.56	0.23
Grain size	−0.54	0.02	−0.25	0.27	0.22	−0.27	0.31	**1.00**	0.33	−0.35
Mean basin slope	−0.43	0.56	−0.17	0.30	0.05	−0.49	0.56	0.33	**1.00**	0.07
Mean local relief	0.57	0.30	−0.20	0.21	0.00	0.63	0.23	−0.35	0.07	**1.00**

[a]A correlation coefficient of 1.00 describes the maximum positive linear correlation and is highlighted in bold numbers.

Table 5
Factor Analysis Results for Factor Loading Values[a]

Parameters	Factor 1	Factor 2	Factor 3
Drainage area	**0.73**	−0.09	−0.23
Mean elevation	0.02	0.31	**0.67**
^{10}Be corr. concentration	−0.08	−0.74	−0.10
Denudation rate	0.06	**0.68**	0.20
Mean precipitation	−0.07	0.41	0.04
Stream order	**0.79**	0.24	−0.35
Mean k_{sn}	−0.07	**0.76**	0.54
Grain size	−0.47	0.34	0.10
Mean basin slope	−0.28	0.14	**0.83**
Mean local relief	**0.92**	0.12	0.37

[a]Values in bold show the components of the specific factors.

5 Discussion

5.1 Synthesis of Observations

Cosmogenic nuclide derived denudation rates obtained from ^{10}Be and ^{26}Al in this study are two orders of magnitude lower than denudation rates measured from the eastern side of the Andes in Bolivia [*Safran et al.*, 2005; *Insel et al.*, 2010]. Comparisons of all measured ^{10}Be concentrations of this study indicate higher values in the Coastal Cordillera than of the Western Cordillera. This suggests that the basins of the Western Cordillera are eroding more rapidly than the basins in the Coastal Cordillera (compare Figure 4a and 4f). Latitudinal variations in denudation rates do not display a continuous signal following the trend in the topography (compare Figure 4a and 4f and 6a, b and c). Rather, the latitudinal variation in denudation rates indicates two peaks of increased denudation rates at 19°S and 21°S that are most likely controlled by local catchment characteristics. The factor analysis model indicates that denudation rates show a strong linear correlation and covariation with the channel steepness whereas the TRMM derived mean annual precipitation does not show a significant relation to other basin parameters. The reliability and control of denudation rates will be discussed in the following section.

5.2 Reliability of Denudation Rates

As an independent check on the results presented here, three catchments draining the Western Cordillera and one catchment draining the Coastal Cordillera were calculated in the CRONUS-Earth ^{10}Be erosion rate calculator – with the latest version 2.3 [*Balco et al.*, 2008; *Borchers et al.*, 2016]. The results from CRONUS-Earth 2.3 are reported in Table 6. Comparing the denudation rates of our method to the results of CRONUS-Earth with different scaling schemes and the new calibrated production rates (spallation) of *Borchers et al.* [2016] the denudation rates resulting from CRONUS are within the same range of uncertainty (Table 6). The values of the investigated denudation rates are also consistent with previous studies. For example, the range of denudation rates in this study are consistent with denudation rates north of our study area at 18°S reported by *Kober et al.* [2009] from the Rio Lluta. The low denudation rates from the Altiplano in this study of 2.5 ± 0.1 m/Myr (ID 34, Table 1), are in the same range as the

results < 10 to 20 m/Myr published by *Karátson et al.* [2012]. The Rio Chiza analyzed by *Carretier et al.* [2015a] was resampled in our study. The denudation rate is 131.2 ± 44.2 m/Myr and is within the uncertainty of the published value, 87 ± 20 m/Myr [*Carretier et al.,* 2015a].

However, potentially systematic biases in denudation rates can occur due to some of the (commonly made) assumptions associated with this method. These assumptions include:

(1) Similar quartz content in lithologies. The contribution of material from subcatchments without quartz [*Dosseto and Schaller*, 2016] appears to be minor in this study. The similarity in denudation rates across lithologically different catchments and the observation of different denudation rates in similar lithologies (Figure 1b) suggests that any effects of varying quartz amounts in each catchment is muted in terms of the overall production of ^{10}Be and ^{26}Al. For example, in each of the catchments of the Coastal Cordillera, the substrate is dominated by the same granodiorite and andesite of Jurassic age but the denudation rates vary by one order of magnitude (Figure 1b).

(2) Effect of bedrock landsliding (or other stochastic erosional events) is negligible. An increasing amount of deep bedrock landsliding can bias denudation rates. This effect can be avoided by sampling larger catchments [*Niemi et al.*, 2005]. One sample from the Rio Camarones, ID 10 (Table 1), is considered to not represent the long-term denudation rate because of a large landslide documented by *Mather et al.* [2014] directly above (~200 m) the sample site. Any strong correlations between the catchment size (area) and the denudation rate cannot be confirmed (Table 4). Any strong significant trend of increased denudation rates and the mean catchment elevation is also not evident (Table 4). However, it is difficult to completely exclude such biases because the total contribution of seismic activity triggered landslides to the main erosional mechanism in the study area is unclear.

(3) Effect of sediment storage and variable transport time is neglible. Sediment transport times in northern Chile for the Western Cordillera and Coastal Cordillera are not well known because, although previous studies have addressed this topic with two different results. First, previous studies [*Grosjean et al.*, 2003; *Carretier et al.*, 2012] reported short and infrequent sediment transportation times after extreme precipitation events. In March 2015 extreme precipitation events increased quickly sediment budget and transportation time in northern and central Chile [*Barrett et al.*, 2016]. A short transport time is evident for the Rio Lluta in northern Chile draining the Western Cordillera [*Kober et al.*, 2007]. Decadal records of sediment budgets from gauging stations show the same denudation rates as those determined from cosmogenic nuclides in the Rio Lluta. The effect of complex exposure histories in this region is mostly observed for non-bedrock samples of boulders and clasts and is rather an exception as document by *Kober et al.*, [2007]. The Rio Lluta drainage is of a similar size to the basins sampled in our study and the catchment averaged cosmogenic nuclide measurements we (and *Kober et al*., [2007]) present were obtained from modern river channel sediments. Thus, following from *Kober et al*. [2007] we conclude the sampling procedure used in this study reflects catchment average denudation rates.

Second, other studies [*Biermann and Nichols*, 2004; *Nichols et al.*, 2005; *Nishiizumi et al.*, 2005; *Placzek et al.*, 2010; *Jungers et al.*, 2013] reported ^{10}Be accumulation during sediment transport within catchments in arid regions. These studies concluded that cosmogenic derived denudation rates might instead represent transport rates (rather than catchment denudation rates). This would result in increasing ^{10}Be concentration with increasing travelling distance and catchment area. However, such relationships are not found in our dataset. More specifically, alluvial fan sediments, boulders, channel gravels and depth profiles of the Atacama Desert between 23°S and 24°S revealed complex exposure history during the Quaternary [*Jungers et al.*, 2013] and have shown high cosmogenic nuclide concentrations [*Placzek et al.*, 2010] near the Calama Basin south of this study area. The mean blank corrected ^{10}Be concentrations vary between 545.1 ± 15.5 10^4 atoms/g(qtz) [*Jungers et al.*, 2013] and 1031.6 ± 38.4 10^4 atoms/g(qtz) [*Placzek et al.*, 2010]. However, the mean blank corrected ^{10}Be concentrations of this study are significantly lower than the cosmogenic nuclide concentrations found by *Jungers et al.* [2013] and *Placzek et al.* [2010] where our results are 104.7 ± 3.4 10^4 atoms/g(qtz) for the Western Cordillera and 246 ± 7.7 10^4 atoms/g(qtz) for the Coastal Cordillera. The most likely explanation for the difference between our results and those of *Jungers et al.* [2013] and *Placzek et al.* [2010] stems from the geomorphological setting and the material sampled in the field. In contrast to the previous studies, our sampling targeted modern (active, or recently active) channels where either flowing water was present at the time of sampling, or (in the case of ephemeral flow) fluvial deposits within the channel (e.g. cross bed sets, sediments with ripple marks, and imbricated clasts) were clearly visible and could be sampled.

Furthermore, we highlight from our results that the condition of steady-state long-term denudation is fulfilled, and that our samples do not appear to be shielded by burial deposition. The effect of shielding was tested by means of ^{26}Al/^{10}Be ratio calculation of the Western Cordillera and is illustrated in Figure 5. The evolution of the ^{26}Al/^{10}Be ratio with time indicates the exposure history of a sample. Continuously exposed surfaces eroding in a steady-state condition follow the steady state denudation line (thick black line Figure 5). Samples that plot below this line experienced a complex exposure of burial deposition. The so-called "forbidden zone" [*Lal*, 1991] is located above the steady-state denudation line and indicates errors in the sample preparation or production rate values. Seven out of eight ratios follow the steady-state denudation line and suggest that they have been continually exposed at the surface. One ratio is slightly in the forbidden zone although there is no evidence of ^{26}Al contamination from the laboratory procedure because the measured ^{26}Al blanks are not increased. Assuming that the measured ^{26}Al/^{10}Be ratios are only representative for the Western Cordillera it is difficult to extrapolate this conclusion to the Central Depression or Coastal Cordillera. Catchments exclusively draining the Central Depression were not sampled to avoid sampling alluvial fans. The Coastal Cordillera was sampled according to the same strategy of the Western Cordillera and we collected sediments from active streams and recently active streams with wet sediments of no evidence of burial deposition. To summarize, we

assume that our dataset represents long-term denudation rates because we find no evidence of burial deposition or complex exposure history.

Table 6
Comparison of Denudation Rates to CRONUS-Earth Denudation Rates[a]

Sample ID	Sample name	Scaling scheme for spallation	Desilets and Zreda (2003) and Desilets et al. (2006)[b]		Dunai (2001)[c]		Lifton et al. (2005)[d]		Time-dependent Lal (1991)/Stone (2000)[e]		This study and Balco et al. (2008)[f]	
			Denudation rate (m/Myr)	External uncertainty (m/Myr)	Denudation rate (m/Myr)	External uncertainty (m/Myr)	Denudation rate (m/Myr)	External uncertainty (m/Myr)	Denudation rate (m/Myr)	External uncertainty (m/Myr)	Denudation rate (m/Myr)	External uncertainty (m/Myr)
8	15CL018		22.86	10.31	22.62	10.24	22.95	10.42	22.69	2.17	20.91	0.78
9	15CL019		18.8	8.52	18.76	9.81	18.91	8.63	19.26	1.84	18.72	0.79
6	15CL015		111.57	50.04	112.32	50.54	110.03	49.7	109.69	10.7	104.67	7.85
25	15CL055		26.25	11.94	27.02	13.97	26.65	12.2	28.44	2.71	20.61	1.53

[a]The following CRONUS-Earth input was used: 15CL018-18.51871-70.18941 2926 std 2 2.4 1 759969 25654 KNSTD, 15CL019-18.77716-70.26838 2357 std 2 2.41 654193 22313 KNSTD, 15CL015-19.15475-70.18531 2889 std 2 2.4 1 140970 6445 KNSTD, 15CL055-22.64401-70.24519 1345 std 2 2.4 1 250863 10804 KNSTD. [b]Reference production rates (spallation) for ^{10}Be are 3.69 atoms/g(qtz)*yr (Borchers et al., 2016). [c]Reference production rates (spallation) for ^{10}Be are 3.7 atoms/g(qtz)*yr (Borchers et al., 2016). [d]Reference production rates (spallation) for ^{10}Be are 4.06 atoms/g(qtz)*yr (Borchers et al., 2016). [e]Reference production rates (spallation) for ^{10}Be are 4.01 atoms/g(qtz)*yr (Borchers et al., 2016). [f]Reference production rates (spallation) for ^{10}Be are 4.43 atoms/g(qtz)*yr (Borchers et al., 2016).

5.3 Controls on East-West Variation of Denudation Rates

East-west variations in denudation rates between the Coastal and Western Cordillera can be observed in two settings. The first is expressed in the difference in denudation rates between the catchments of the Coastal Cordillera and the Western Cordillera. The difference is evident in Figure 4a and 4f where rates range between 0.4 ± 0.5 to 20.6 ± 1.5 m/Myr in the Coastal Cordillera and 1.4 ± 0.7 to 168.0 ± 19.7 m/Myr in the Western Cordillera. Higher ^{10}Be concentration and, therefore lower denudation rates can be found in the Coastal Cordillera. This increase in isotope concentration can be related to an increase in sediment residence time within the catchment by the lack of precipitation available to transport material downslope. The Coastal Cordillera catchments are mainly characterized by ephemeral channels that flow only for days after rainfall events, which might explain the increase of residence time.

The second east-west variation is documented by changes in denudation rates along the river profiles in the Western Cordillera itself. Figure 8 illustrates these changes and shows four examples of drainage basins at 19°S, 19.5°S, 20.2°S and 21.9°S. The general pattern of east-west variations in denudation rate is heterogeneous and highly influenced by basin-specific conditions as described below.

(1) The Rio Camarones, at 19°S (Figure 8a), shows both observations of decreasing denudation rates with decreasing stream order and increasing elevation within its mostly concave river profile. Fifth-order channels have a denudation rate of 131.2 ± 44.2 m/Myr and third-order streams exhibit a denudation rate of 7.7 ± 0.3 m/Myr (Table 1 and Table 2). Low denudation rates were calculated (sample ID 17) (Figure 8a) near the Oxaya ignimbrites above a convex knickpoint of a tributary with moderate to shallow channel steepness in the Western Cordillera. The Oxaya ignimbrites form the top of the Oxaya formation at the Camarones valley and are dated to about 20.6 ± 0.8 Myr (K–Ar, biotite) [*von Rotz et al.*, 2005]. The Rio Camarones is characterized by strong incision into the Coastal Cordillera [*Farías et al.*, 2005] and displays rapid denudation rates of 165.2±25.3 m/Myr at the outlet near to the coast. The Rio Camarones shows a number of undated landslides within the main channel that are triggered mainly by local tectonic activity of the Moquella Flexure, which could cause the increased denudation rates of fifth-order streams [*Pinto et al.*, 2004; *Pinto et al.*, 2008].

(2) The Rio Tana, at 19.5°S (Figure 8b), shows a denudation rate of 15.2±0.6 m/Myr at the west coast (downstream) of the convex knickzone in the Coastal Cordillera, a denudation rate of 1.4±0.7 m/Myr for a tributary of the Rio Tana east (upstream) of the convex knickzone and a denudation rate of 65.9±3.0 m/Myr west of the concave knickzone in the Western Cordillera (Figure 8b). The Rio Tana, including the Tana canyon, is characterized by an upstream convex knickzone that is currently 43 km away from the coast and highlights the boundary between increased incision in the western portion of the Coastal Cordillera and decreased incision east of the knickzone in the Central Depression [*Kirk-Lawlor et al.*, 2013; *Coudurier-Curveur et al.*, 2015]. The incision of the Tana canyon started around 6.4 Myr [*Hoke*

et al., 2007] and cut through the Coastal Cordillera around 3.5 Myr [*Kirk-Lawlor et al.,* 2013]. The denudation rates are slower than the denudation rates of the Rio Camarones indicating that the Rio Tana has lower stream power to incise the bedrock than the rivers in the north as previously suggested by *Hoke et al.* [2007].

(3) In contrast to the Rio Tana, the Rio Aroma, at 20.2°S (Figure 8c), is an endorheic stream associated with alluvial fan deposition that goes subsurface before it reaches the Central Depression. The river profile shows a concave shape with no major knickzones. The Rio Aroma drainage reveals three main flexures showing recent activity in the Aroma earthquake in 2001 and a relative surface uplift since 27 Myr of about 700 to 420 m [*Farías et al.,* 2005]. The denudation rates decrease slightly with stream order from 16.8±0.6 to 12.0±0.5 m/Myr but do not appear to be strongly impacted by the tectonic activity or by earthquake triggered landslides.

(4) The Rio Loa, at 21.9°S (Figure 8d), displays decreasing denudation rates with increasing elevation of the main stream. West of the Coastal Cordillera at the outlet of the Rio Loa the denudation rate is 27.3±1.1 m/Myr. East of the Coastal Cordillera the denudation rates decrease to a value of 5.7±0.3 m/Myr and the slowest denudation rates with 2.5±0.1 m/Myr can be found on the Altiplano. The Rio Loa is the only exorheic river system between 19°35′S and 23°S and has its source on the Altiplano [*Coudurier-Curveur et al.,* 2015]. The Rio Loa, characterized by several convex and concave knickpoints, and the Rio Tana exhibit the smallest extent of knickpoints migration for the four rivers presented in Figure 8. The incision of the Rio Loa into the Coastal Cordillera started after 6 Myr ago and resulted in a base level drop of approximately 1000 m [*Sáez et al.,* 2012]. This base level drop initiated the capture of single drainages from the location of the Rio Loa until the location of the Rio Tana in the north [*Hoke et al.,* 2007].

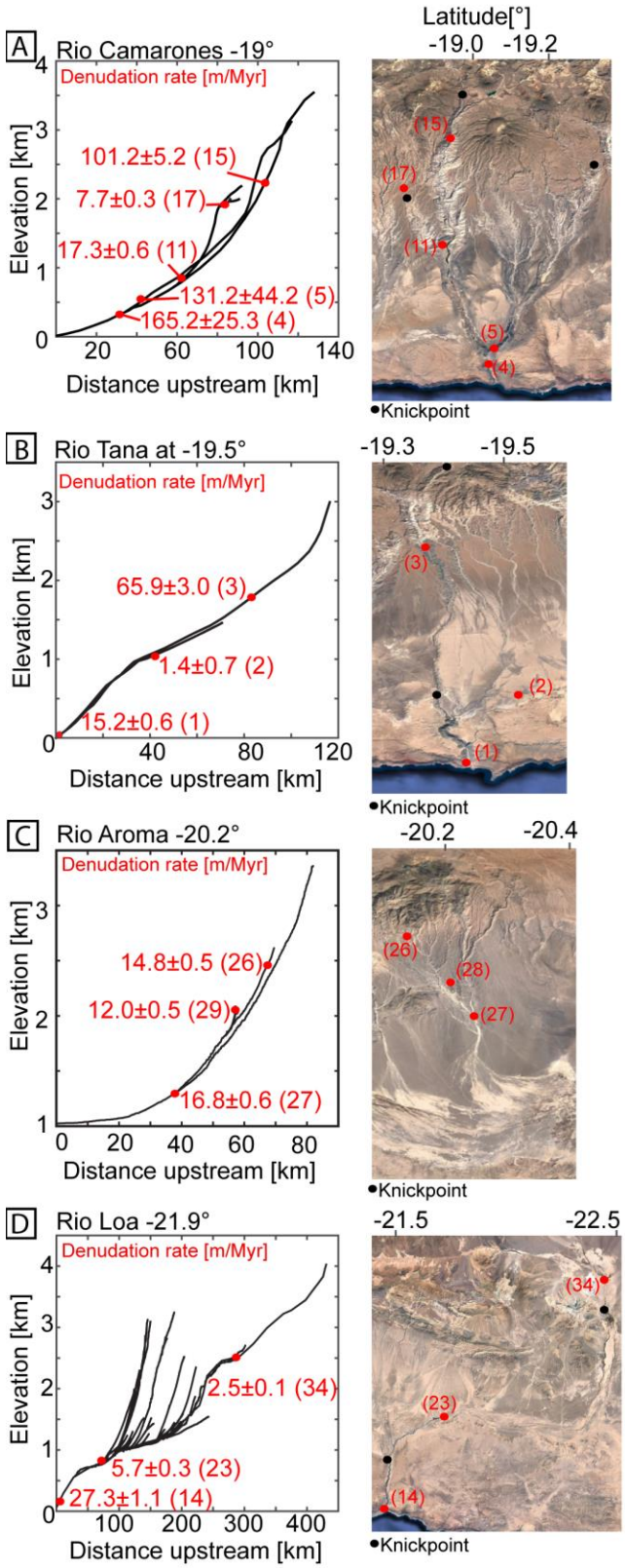

Figure 8. Longitudinal river profiles. Left panels show sample location and denudation rate. Right panels display the catchment images (Google Earth), knickpoints (black dots) and sample locations (red dots). 8a: Rio Camarones profiles. 8b: Rio Tana profiles. 8c: Rio Aroma profiles. 8d: Rio Loa profiles.

5.4 Controls on North-South Variation of Denudation Rates

Latitudinal variations can be explored by the factor analysis model, which quantifies correlations and covariation with reference to the latitude of the river basin. Figure 7 summarizes the calculated three factors and the degree of latitudinal occurrence. The factors are sorted by decreasing explained variance (1) The first factor of the analysis indicates that the variables catchment area, stream order and mean local relief have a strong covariance and a major impact on the data set around 21.5°S. At this location, we sampled the Rio Loa and the Coastal Cordillera, which represent the end members of a very large catchment (around 43,000 km^2), and a very small catchment (around 111 km^2 area). (2) The second factor is characterised by a high factor loading of the denudation rate and the mean k_{sn} at 19°S and 21°S. This strong linear relationship indicated by correlation as well as covariation is attributed to local tectonic effects, for instance landslides triggered by seismic activity, which strongly imprint the denudation rate locally compared to other regions. (3) The third factor is associated with the covariation of mean elevation and mean basin slope around 20°S. This factor is sensitive to the sampling strategy and reflects the fact that we sampled smaller catchments in higher elevations thereby leading to higher mean basin slope values. As such, the benefit of the third factor is to identify a spatial methological bias (Figure 7). In total about 62% of the variance is explained, but the analysis also indicates that the existing dataset is heterogeneous and does not explain 38% of the data variance. Adding parameters, particularly for climate such as discharge, temperature or extreme climatic events, could enhance to some degree the explained variance, but the heterogeneity of the existing data would still influence the factor analysis. Thus, the results presented here give us a good indication of covarying parameters and their degree of latitudinal control. We quantified the intensity of covariation spatially and can exclude parameters with minor impact on the dataset such as the catchment-wide mean annual precipitation (Table 5).

In this study the catchment-wide mean annual precipitation based on the TRMM data was chosen to represent the climate parameter but the results are insignificantly correlated and show no covariation to other parameters (Tables 4 and 5). Whereas denudation rates integrate over the mean apparent age of 117kyr, the timescale of the TRMM data set spans only 8 yr not capturing climate changes that may have occurred. The TRMM data set averages out stochastic variations in rainfall for the eight years of data where annual-averaged rainfall is available (Figure 2b). Thus, the accuracy of the precipitation rate is biased by the sensitivity to precipitation type that can lead to an underestimation of orographic rainfall [*Huffman et al.*, 2007; *Chen et al.*, 2013]. A general inaccuracy can also occur in mountain ranges with short rainfall events or extreme climatic events that are not captured in this data set [*Bookhagen and Burbank*, 2006; *Islam et al.*, 2010]. All these limitations could combine together in northern Chile to account for part of the unexplained 38% in the variance in the factor analysis. This interpretation suggests that TRMM based precipitation rates do not necessarily represent the driving climate forces modulating the denudation rates in this region. It should be noted that denudation rates from fluvial

systems in central and northern Chile are thought to be controversial archives of climate variability. Previous work has suggested the rivers are mainly recording erosion after extreme precipitation events rather than long-term surface runoff [*Grosjean et al.,* 2003; *Carretier et al.,* 2012].

5.5 Hypothesis Evaluation and Tectonic Controls on Denudation Rates

In this study, we evaluate the hypothesis that the geometry of the subducting Nazca plate produces a tectonically controlled localization of denudation rates into a "bulls-eye" pattern near the Arica Bend in the Andes. We do this by collecting samples along two profile at different distances from the coast that extend south from the syntaxis, and therefore cover half of the a symmetric "bulls-eye" pattern [*Bendick and Ehlers,* 2014]. We find the following influence of the subducting plate geometry on denudation rates. First, the denudation rates from both the Coastal and Western Cordillera (Figure 4a, f) do not produce a discernable decrease in denudation rates from the syntaxis (Figure 1a) to the south as predicted. In fact, denudation rates in the Coastal Cordillera do the opposite and increase slightly to the south. Thus, the pattern of denudation rates in these settings is different than what is observed from thermochronometer data in the more erosive syntaxes of the Himalaya or southeast Alaska, or predicted in *Bendick and Ehlers* [2014]. However (second), this study area was investigated specifically because it represents an arid end-member compared to the other, better studied, syntaxial orogens. In an arid setting where there is insufficient precipitation to erode tectonically driven increases in elevation, denudation can be outpaced by tectonic rock uplift. As a result, the region could be climate limited in terms of producing a denudation signal of large-scale tectonic processes such that surface uplift, rather than denudation rates, may reflect this tectonic process. Indeed, our analysis of the trends in maximum topography (the least eroded portion of the remaining landscape) show a regional decrease in maximum elevations of the Coastal and Western Cordillera to the south from the syntaxis (Figure 6). This pattern in maximum elevations has a length scale of ~300 km and is similar to the predicted 300-400 km length scale of rock uplift patterns (measured from the center of the "bulls-eye" outward) suggested for a range of different subducting indenter geometries [see rock uplift velocities in Fig. 2d of *Bendick and Ehlers,* 2014]. From this, we conclude that in an arid syntaxial orogen the denudation rates are not influenced by the subducting plate geometry, but the regional topography may be.

In the remainder of this section, we discuss additional local and regional tectonic contributions to denudation rates attributed to this region. First, local (catchment-scale) tectonic effects are evident from our factor analysis that indicates a strong linear correlation and covariation of denudation rate and mean channel steepness index. In northern Chile, previous studies have suggested that river knickpoints and channel steepness indices are indicative of relative surface uplift [*Hoke et al.*, 2007; *Cooper et al.*, 2016]. Although denudation rates in this study cannot be related to absolute uplift rates of the Central Andes [*Regard et al.,* 2010], the spatial distribution of denudation rates and channel steepness indices are most

likely related to local, faulting controlled, tectonic or earthquake induced landslide activity where the highest denudation rates at 19°S and 21°S are observed. For example, east-west oriented faults extend from 19°S and 21.6°S and are mainly restricted to the Coastal zone of northern Chile [*Allmendinger et al.*, 2005] (Figure 1a). The EW-faults are the longest at 19°S in the Rio Camarones drainage basin. Evidence for a temporal clustering of seismic activity [*Mouslopoulou et al.*, 2016] and the occurrence of giant landslides at 19°S is suggested by previous work by *Pinto et al*. [2008] and *Crosta et al*. [2014]. The occurrence and concentration of mostly undated landslides could lead to the effect of ^{10}Be dissolution resulting in higher denudation rates in this setting. The occurrence of landslides due to seismic effects at 21°S may be a possible explanation for the high denudation rates of the Rio Guatacondo. Consequently, a coupling of denudation rates to tectonically induced landsliding rather than a coupling to local topographic trends or precipitation rates cannot be excluded.

Second, as previously mentioned on a regional-scale, changes in the maximum topography, rather than denudation rates, are suggestive of plate subduction geometry. However, there is one final note we should make concerning regional variations in topography and denudation rates around the syntaxis. Recent work by *Madella et al.* [2016] in southern Peru showed that the bend in the coastline at the Arica Bend (Figure 1) is characterized by low long-term plate coupling, low seismicity, low coastal uplift, and high sediment supply. They estimated the supply of post-10 Ma sediment by differencing the modern topography and the late Miocene pediplain they interpolated from available exposures. They conclude, contrary to our findings, that the sediment discharge near the Arica Bend yields higher sediment volumes than adjacent regions. Although our sampling approach extends over a large distance (400 km) from the center of the bend southward, there are several aspects of their results and ours that warrant future investigation. The difference between the results of *Madella et al.* [2016] and this study could be due to either: (a) differences in the integration timescale of the observations used (10^3 vs. 10^6 years), (b) differences in denudation rates in southern Peru vs. northern Chile are not distinguishable with our northern limit of sampling, or (c) discrepancies in the true vs. interpolated late Miocene surface used in their analysis. At this time, additional observations (e.g. cosmogenic-derived denudation rates) are needed from southern Peru to evaluate these different possible explenations.

6 Conclusions

We present 34 new ^{10}Be derived denudation rates from the arid end-member syntaxial orogen of South America in northern Chile. Samples were collected along north-south and east-west oriented profiles between 18°S to 23°S. Controls on the denudation rates were evaluated using a statistical factor analysis to reveal correlation and covariation of catchment parameters. The three main conclusions of this study are:

First, in the east-west direction the denudation rates of the Coastal Cordillera are one order of magnitude lower than in the Western Cordillera. In the north-south direction the Coastal Cordillera denudation rates increase towards the south, where no clear latitudinal trend in denudation rates is evident in the Western Cordillera.

Second, the main control on denudation rates indicated from the factor analysis is local tectonic (smaller scale faulting) processes that is identified by the strong correlation and covariation of the denudation rate to channel steepness. The effect of climate parameters on the denudation rates seems to be insignificant, although the precipitation data are limited to a short, recent record (eight years).

Third, a systematic decrease in denudation rates away from the syntaxial bend in the Andes (Figure 1b) is not clearly present. This is in contrast to spatial patterns in exhumation rates observed from thermochronology in the much more erosive Himalayan and southeast Alaskan syntaxes. Although a clear signal of denudation rate variations with distance from the South American syntaxis is lacking, regional trends in topography in this arid region (Figure 6) display a decrease in maximum elevations away from the syntaxes. This trend in topography is similar to the rock uplift pattern predicted by *Bendick and Ehlers* [2014] for upper plate deformation above a subducting indenter [*Hayes et al.*, 2012] and could reflect that there is simply not enough precipitation available in this region to erode the long wavelength variations in topography. We conclude that in this arid setting with low potential for erosion the tectonic controls on rock uplift may be outpacing the ability of surface processes to denude and reflect regional scale tectonic processes.

Acknowledgements

We would like to thank D. Kost for assistance with laboratory work and N. Avdievitch for help in the field. This work was supported by the European Research Council (ERC) Consolidator Grant to T. Ehlers (ERC-CoG 615703). We also would like to thank J. M. Buffington (Rocky Mountain Research Station), R. Delunel (University of Bern), A. Heimsath (Arizona State University) and one anonymous reviewer for their constructive reviews of this manuscript. Further information is included in the supporting material and data are available via the GFZ Data Services http://doi.org/10.5880/fidgeo.2017.004.

Supplementary to Paper I

This supplementary material aims to illustrate the results that were obtained to show the relationship between denudation rates with nine parameters analyzed in the main manuscript. Further information about when and how the data were collected or created as well as the general description of processing steps used are described in the main article.

Figure S1illustrates nine scatter plots that show the summarized results for the correlation coefficient on denudation rates to nine analyzed parameters. The data are plotted according to the data in Table 1 and Table 2. The correlation coefficients R of the scatter plots are the same as reported in Table 4 of the main article. In addition, the 95% level of significance is expressed with the p-value in each subplot. The p-value means that a value of 0 corresponds to a significant correlation in R and a low probability of observing the null hypothesis. If the value exceeds 0.05 the correlation is insignificant within 95% level of significance.

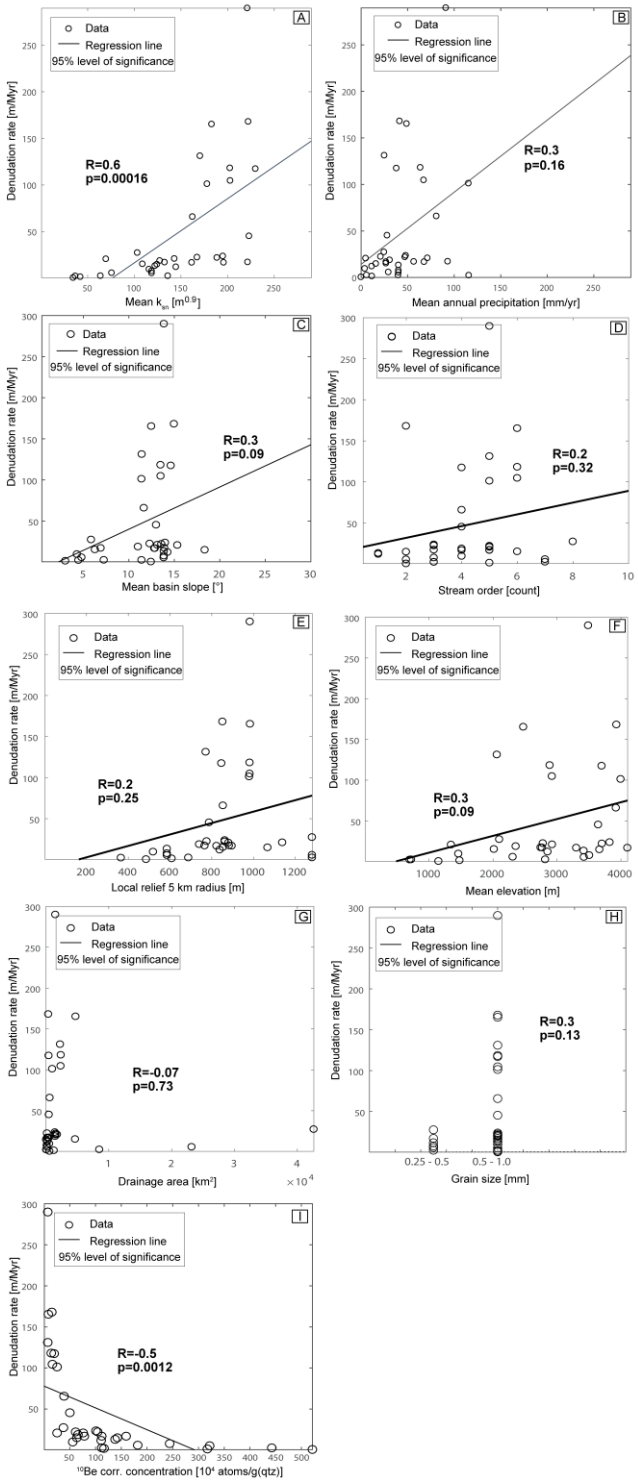

Figure S1. Correlation coefficient scatter plot. In all subplots the black line is the regression line for the plotted data. The p-value describes the significance of the correlation. S1a) The plot shows the correlation coefficient R for denudation rates with normalized channel steepness. S1b) The plot shows the correlation coefficient R for denudation rates with mean annual precipitation. S1c) Correlation coefficient R between denudation rate and mean basin slope. S1d) Correlation coefficient R between denudation rate and stream order. S1e) Correlation coefficient R between denudation rate and local relief. S1f) Correlation coefficient R between denudation rate and mean elevation. S1g) Correlation coefficient R between denudation rate and drainage area. S1h) Correlation coefficient R between denudation rate and grain size. S1i) Correlation coefficient R between denudation rate and ^{10}Be corrected

Bibliography

Abbühl, L. M., Norton, K. P., Schlunegger, F., Kracht, O., Aldahan, A., and Possnert, G. (2010). El Niño forcing on 10Be-based surface denudation rates in the northwestern Peruvian Andes? *Geomorphology* 123, 257–268. doi:10.1016/j.geomorph.2010.07.017.

Abbühl, L. M., Norton, K. P., Schlunegger, F., Kracht, O., Aldahan, A., and Possnert, G. (2011). Corrigendum to "El Niño forcing on 10Be-based surface denudation rates in the northwestern Peruvian Andes?" [Geomorphology 123 (2010) 257–268]. *Geomorphology* 129, 417. doi:10.1016/j.geomorph.2011.02.023.

Acosta, V. T., Schildgen, T. F., Clarke, B. A., Scherler, D., Bookhagen, B., Wittmann, H., et al. (2015). Effect of vegetation cover on millennial-scale landscape denudation rates in East Africa. *Lithosphere* 7, 408–420. doi:10.1130/L402.1.

Allmendinger, R. W., González, G., Yu, J., Hoke, G., and Isacks, B. (2005). Trench-parallel shortening in the Northern Chilean Forearc: Tectonic and climatic implications. *Geological Society of America Bulletin* 117, 89–104. doi:10.1130/B25505.1.

Amundson, R., Dietrich, W., Bellugi, D., Ewing, S., Nishiizumi, K., Chong, G., et al. (2012). Geomorphologic evidence for the late Pliocene onset of hyperaridity in the Atacama Desert. *Geological Society of America Bulletin* 124, 1048–1070. doi:10.1130/B30445.1.

Armijo, R., Rauld, R., Thiele, R., Vargas, G., Campos, J., Lacassin, R., et al. (2010). The West Andean Thrust, the San Ramón Fault, and the seismic hazard for Santiago, Chile. *Tectonics* 29, TC2007. doi:10.1029/2008TC002427.

Balco, G., and Shuster, D. L. (2009). Production rate of cosmogenic 21Ne in quartz estimated from 10Be, 26Al, and 21Ne concentrations in slowly eroding Antarctic bedrock surfaces. *Earth and Planetary Science Letters* 281, 48–58. doi:10.1016/j.epsl.2009.02.006.

Balco, G., Soreghan, G. S., Sweet, D. E., Marra, K. R., and Bierman, P. R. (2013). Cosmogenic-nuclide burial ages for Pleistocene sedimentary fill in Unaweep Canyon, Colorado, USA. *Quaternary Geochronology* 18, 149–157. doi:10.1016/j.quageo.2013.02.002.

Balco, G., Stone, J. O., Lifton, N. A., and Dunai, T. J. (2008). A complete and easily accessible means of calculating surface exposure ages or erosion rates from 10Be and 26Al measurements. *Quaternary Geochronology* 3, 174–195. doi:10.1016/j.quageo.2007.12.001.

Barnes, J. B., and Ehlers, T. A. (2009). End member models for Andean Plateau uplift. *Earth-Science Reviews* 97, 105–132. doi:10.1016/j.earscirev.2009.08.003.

Bendick, R., and Ehlers, T. A. (2014). Extreme localized exhumation at syntaxes initiated by subduction geometry. *Geophysical Research Letters* 41, 5861–5867. doi:10.1002/2014GL061026.

Bookhagen, B., and Burbank, D. W. (2006). Topography, relief, and TRMM-derived rainfall variations along the Himalaya. *Geophys. Res. Lett.* 33, L08405. doi:10.1029/2006GL026037.

Bookhagen, B., and Strecker, M. R. (2008). Orographic barriers, high-resolution TRMM rainfall, and relief variations along the eastern Andes. *Geophysical Research Letters* 35. doi:10.1029/2007GL032011.

Carretier, S., Regard, V., Vassallo, R., Martinod, J., Christophoul, F., Gayer, E., et al. (2015). A note on 10Be-derived mean erosion rates in catchments with heterogeneous lithology: examples from the western Central Andes. *Earth Surf. Process. Landforms* 40, 1719–1729. doi:10.1002/esp.3748.

Cereceda, P., Larrain, H., Osses, P., Farías, M., and Egaña, I. (2008). The spatial and temporal variability of fog and its relation to fog oases in the Atacama Desert, Chile. *Atmospheric Research* 87, 312–323. doi:10.1016/j.atmosres.2007.11.012.

Chen, Y., Ebert, E. E., Walsh, K. J. E., and Davidson, N. E. (2013). Evaluation of TRMM 3B42 precipitation estimates of tropical cyclone rainfall using PACRAIN data. *J. Geophys. Res. Atmos.* 118, 2184–2196. doi:10.1002/jgrd.50250.

Cooper, F. J., Adams, B. A., Blundy, J. D., Farley, K. A., McKeon, R. E., and Ruggiero, A. (2016). Aridity-induced Miocene canyon incision in the Central Andes. *Geology*, G38254.1. doi:10.1130/G38254.1.

Coudurier-Curveur, A., Lacassin, R., and Armijo, R. (2015). Andean growth and monsoon winds drive landscape evolution at SW margin of South America. *Earth and Planetary Science Letters* 414, 87–99. doi:10.1016/j.epsl.2014.12.047.

Curtis, S., Salahuddin, A., Adler, R. F., Huffman, G. J., Gu, G., and Hong, Y. (2007). Precipitation Extremes Estimated by GPCP and TRMM: ENSO Relationships. *J. Hydrometeor* 8, 678–689. doi:10.1175/JHM601.1.

D'Arcy, M., and Whittaker, A. C. (2014). Geomorphic constraints on landscape sensitivity to climate in tectonically active areas. *Geomorphology* 204, 366–381. doi:10.1016/j.geomorph.2013.08.019.

Davies, R. (2015). Northern Chile Floods March 2015 - Facts, Figures and Photos. *FloodList*. Available at: http://floodlist.com/america/northern-chile-floods-march-2015-facts-figures-and-photos [Accessed June 28, 2016].

DiBiase, R. A., Whipple, K. X., Heimsath, A. M., and Ouimet, W. B. (2010). Landscape form and millennial erosion rates in the San Gabriel Mountains, CA. *Earth Planet. Sci. Lett.* 289, 134–144. doi:10.1016/j.epsl.2009.10.036.

Duan, Y., Wilson, A. M., and Barros, A. P. (2015). Scoping a field experiment: error diagnostics of TRMM precipitation radar estimates in complex terrain as a basis for IPHEx2014. *Hydrol. Earth Syst. Sci.* 19, 1501–1520. doi:10.5194/hess-19-1501-2015.

Dunai, T. J. (2000). Scaling factors for production rates of in situ produced cosmogenic nuclides: a critical reevaluation. *Earth and Planetary Science Letters* 176, 157–169. doi:10.1016/S0012-821X(99)00310-6.

Dunai, T. J., López, G. A. G., and Juez-Larré, J. (2005). Oligocene–Miocene age of aridity in the Atacama Desert revealed by exposure dating of erosion-sensitive landforms. *Geology* 33, 321–324. doi:10.1130/G21184.1.

Dunne, J., Elmore, D., and Muzikar, P. (1999). Scaling factors for the rates of production of cosmogenic nuclides for geometric shielding and attenuation at depth on sloped surfaces. *Geomorphology* 27, 3–11. doi:10.1016/S0169-555X(98)00086-5.

Ehlers, T. A., and Poulsen, C. J. (2009). Influence of Andean uplift on climate and paleoaltimetry estimates. *Earth and Planetary Science Letters* 281, 238–248. doi:10.1016/j.epsl.2009.02.026.

Falkowski, S., Enkelmann, E., and Ehlers, T. A. (2014). Constraining the area of rapid and deep-seated exhumation at the St. Elias syntaxis, Southeast Alaska, with detrital zircon fission-track analysis. *Tectonics* 33, 597–616. doi:10.1002/2013TC003408.

Garreaud, R., Vuille, M., and Clement, A. C. (2003). The climate of the Altiplano: observed current conditions and mechanisms of past changes. *Palaeogeography, Palaeoclimatology, Palaeoecology* 194, 5–22. doi:10.1016/S0031-0182(03)00269-4.

Garzione, C. N., Hoke, G. D., Libarkin, J. C., Withers, S., MacFadden, B., Eiler, J., et al. (2008). Rise of the Andes. *Science* 320, 1304–1307. doi:10.1126/science.1148615.

Ghosh, P., Adkins, J., Affek, H., Balta, B., Guo, W., Schauble, E. A., et al. (2006). 13 C–18 O bonds in carbonate minerals: A new kind of paleothermometer. *Geochimica et Cosmochimica Acta* 70, 1439–1456.

González, G., Cembrano, J., Carrizo, D., Macci, A., and Schneider, H. (2003). The link between forearc tectonics and Pliocene–Quaternary deformation of the Coastal Cordillera, northern Chile. *Journal of South American Earth Sciences* 16, 321–342. doi:10.1016/S0895-9811(03)00100-7.

Hartley, A. J., and Chong, G. (2002). Late Pliocene age for the Atacama Desert: Implications for the desertification of western South America. *Geology* 30, 43. doi:10.1130/0091-7613(2002)030<0043:LPAFTA>2.0.CO;2.

Hartley, A. J., May, G., Chong, G., Turner, P., Kape, S. J., and Jolley, E. J. (2000). Development of a continental forearc: A Cenozoic example from the Central Andes, northern Chile. *Geology* 28, 331–334. doi:10.1130/0091-7613(2000)28<331:DOACFA>2.0.CO;2.

Hartmann, K., and Wünnemann, B. (2009). Hydrological changes and Holocene climate variations in NW China, inferred from lake sediments of Juyanze palaeolake by factor analyses. *Quaternary International* 194, 28–44. doi:10.1016/j.quaint.2007.06.037.

Haschke, M., Günther, A., Melnick, D., Echtler, H., Reutter, K.-J., Scheuber, E., et al. (2006). "Central and Southern Andean Tectonic Evolution Inferred from Arc Magmatism," in *The Andes* Frontiers in Earth Sciences., eds. O. Oncken, G. Chong, G. Franz, P. Giese, H.-J. Götze, V. A. Ramos, et al. (Springer Berlin Heidelberg), 337–353. doi:10.1007/978-3-540-48684-8_16.

Hayes, G. P., Wald, D. J., and Johnson, R. L. (2012). Slab1.0: A three-dimensional model of global subduction zone geometries. *J. Geophys. Res.* 117, B01302. doi:10.1029/2011JB008524.

Hoke, G. D., Isacks, B. L., Jordan, T. E., Blanco, N., Tomlinson, A. J., and Ramezani, J. (2007). Geomorphic evidence for post-10 Ma uplift of the western flank of the central Andes 18°30′-22°S: LATE MIOCENE UPLIFT IN NORTHERN CHILE. *Tectonics* 26, n/a-n/a. doi:10.1029/2006TC002082.

Houston, J., and Hartley, A. J. (2003). The central Andean west-slope rainshadow and its potential contribution to the origin of hyper-aridity in the Atacama Desert. *International Journal of Climatology* 23, 1453–1464. doi:10.1002/joc.938.

Huffman, G. J., Bolvin, D. T., Nelkin, E. J., Wolff, D. B., Adler, R. F., Gu, G., et al. (2007). The TRMM Multisatellite Precipitation Analysis (TMPA): Quasi-Global, Multiyear, Combined-Sensor Precipitation Estimates at Fine Scales. *J. Hydrometeor.* 8, 38–55. doi:10.1175/JHM560.1.

Insel, N., Ehlers, T. A., Schaller, M., Barnes, J. B., Tawackoli, S., and Poulsen, C. J. (2010). Spatial and temporal variability in denudation across the Bolivian Andes from multiple geochronometers. *Geomorphology* 122, 65–77. doi:10.1016/j.geomorph.2010.05.014.

Insel, N., Poulsen, C. J., and Ehlers, T. A. (2009). Influence of the Andes Mountains on South American moisture transport, convection, and precipitation. *Clim Dyn* 35, 1477–1492. doi:10.1007/s00382-009-0637-1.

Isacks, B. L. (1988). Uplift of the Central Andean Plateau and bending of the Bolivian Orocline. *J. Geophys. Res.* 93, 3211–3231. doi:10.1029/JB093iB04p03211.

Islam, M. N., Das, S., and Uyeda, H. (2010). Calibration of TRMM Derived Rainfall Over Nepal During 1998-2007. *The Open Atmospheric Science Journal* 4, 12–23. doi:10.2174/1874282301004010012.

Ivy-Ochs, S., Kober, F., Alfimov, V., Kubik, P. W., and Synal, H.-A. (2007). Cosmogenic 10Be, 21Ne and 36Cl in sanidine and quartz from Chilean ignimbrites. *Nuclear Instruments and Methods in Physics Research Section B: Beam Interactions with Materials and Atoms* 259, 588–594. doi:10.1016/j.nimb.2007.03.001.

Jeffery, M. L., Poulsen, C. J., and Ehlers, T. A. (2012). Impacts of Cenozoic global cooling, surface uplift, and an inland seaway on South American paleoclimate and precipitation δ18O. *Geological Society of America Bulletin* 124, 335–351. doi:10.1130/B30480.1.

Jordan, T. E., Kirk-Lawlor, N. E., Blanco, N. P., Rech, J. A., and Cosentino, N. J. (2014). Landscape modification in response to repeated onset of hyperarid paleoclimate states since 14 Ma, Atacama Desert, Chile. *Geological Society of America Bulletin* 126, 1016–1046. doi:10.1130/B30978.1.

Jordan, T. E., Nester, P. L., Blanco, N., Hoke, G. D., Dávila, F., and Tomlinson, A. J. (2010). Uplift of the Altiplano-Puna plateau: A view from the west. *Tectonics* 29, TC5007. doi:10.1029/2010TC002661.

Jungers, M. C., Heimsath, A. M., Amundson, R., Balco, G., Shuster, D., and Chong, G. (2013). Active erosion–deposition cycles in the hyperarid Atacama Desert of Northern Chile. *Earth and Planetary Science Letters* 371–372, 125–133. doi:10.1016/j.epsl.2013.04.005.

Kaiser, H. F. The varimax criterion for analytic rotation in factor analysis. *Psychometrika* 23, 187–200. doi:10.1007/BF02289233.

Karátson, D., Telbisz, T., and Wörner, G. (2012). Erosion rates and erosion patterns of Neogene to Quaternary stratovolcanoes in the Western Cordillera of the Central Andes: An SRTM DEM based analysis. *Geomorphology* 139–140, 122–135. doi:10.1016/j.geomorph.2011.10.010.

Kirby, E., and Whipple, K. (2001). Quantifying differential rock-uplift rates via stream profile analysis. *Geology* 29, 415–418. doi:10.1130/0091-7613(2001)029<0415:QDRURV>2.0.CO;2.

Kirk-Lawlor, N. E., Jordan, T. E., Rech, J. A., and Lehmann, S. B. (2013). Late Miocene to Early Pliocene paleohydrology and landscape evolution of Northern Chile, 19° to 20° S. *Palaeogeography, Palaeoclimatology, Palaeoecology* 387, 76–90. doi:10.1016/j.palaeo.2013.07.011.

Knott, M., and Bartholomew, D. J. (1999). *Latent variable models and factor analysis*. London, UK: Edward Arnold Available at: http://www.hoddereducation.co.uk [Accessed June 29, 2016].

Kober, F., Ivy-Ochs, S., Schlunegger, F., Baur, H., Kubik, P. W., and Wieler, R. (2007). Denudation rates and a topography-driven rainfall threshold in northern Chile: Multiple cosmogenic nuclide data and sediment yield budgets. *Geomorphology* 83, 97–120. doi:10.1016/j.geomorph.2006.06.029.

Kober, F., Ivy-Ochs, S., Zeilinger, G., Schlunegger, F., Kubik, P. W., Baur, H., et al. (2009). Complex multiple cosmogenic nuclide concentration and histories in the arid Rio Lluta catchment, northern Chile. *Earth Surf. Process. Landforms* 34, 398–412. doi:10.1002/esp.1748.

Lal, D. (1991). Cosmic ray labeling of erosion surfaces: in situ nuclide production rates and erosion models. *Earth and Planetary Science Letters* 104, 424–439. doi:10.1016/0012-821X(91)90220-C.

Mahadevan, L., Bendick, R., and Liang, H. (2010). Why subduction zones are curved: CURVED SUBDUCTION. *Tectonics* 29, n/a-n/a. doi:10.1029/2010TC002720.

Mather, A. E., Hartley, A. J., and Griffiths, J. S. (2014). The giant coastal landslides of Northern Chile: Tectonic and climate interactions on a classic convergent plate margin. *Earth and Planetary Science Letters* 388, 249–256. doi:10.1016/j.epsl.2013.10.019.

McPhillips, D., Bierman, P. R., Crocker, T., and Rood, D. H. (2013). Landscape response to Pleistocene-Holocene precipitation change in the Western Cordillera, Peru: 10Be concentrations in modern sediments and terrace fills. *J. Geophys. Res. Earth Surf.* 118, 2013JF002837. doi:10.1002/2013JF002837.

Mouslopoulou, V., Oncken, O., Hainzl, S., and Nicol, A. (2016). Uplift rate transients at subduction margins due to earthquake clustering. *Tectonics* 35, 2016TC004248. doi:10.1002/2016TC004248.

Nester, P. L., Gayo, E., Latorre, C., Jordan, T. E., and Blanco, N. (2007). Perennial stream discharge in the hyperarid Atacama Desert of northern Chile during the latest Pleistocene. *Proceedings of the National Academy of Sciences* 104, 19724–19729. doi:10.1073/pnas.0705373104.

Nishiizumi, K., Imamura, M., Caffee, M. W., Southon, J. R., Finkel, R. C., and McAninch, J. (2007). Absolute calibration of 10Be AMS standards. *Nuclear Instruments and Methods in Physics Research Section B: Beam Interactions with Materials and Atoms* 258, 403–413. doi:10.1016/j.nimb.2007.01.297.

Norton, K. P., and Vanacker, V. (2009). Effects of terrain smoothing on topographic shielding correction factors for cosmogenic nuclide-derived estimates of basin-averaged denudation rates. *Earth Surf. Process. Landforms* 34, 145–154. doi:10.1002/esp.1700.

Oerter, E., Amundson, R., Heimsath, A., Jungers, M., Chong, G., and Renne, P. (2016). Early to Middle Miocene climate in the Atacama Desert of Northern Chile. *Palaeogeography, Palaeoclimatology, Palaeoecology* 441, Part 4, 890–900. doi:10.1016/j.palaeo.2015.10.038.

Olen, S. M., Bookhagen, B., and Strecker, M. R. (2016). Role of climate and vegetation density in modulating denudation rates in the Himalaya. *Earth and Planetary Science Letters* 445, 57–67. doi:10.1016/j.epsl.2016.03.047.

Ouimet, W. B., Whipple, K. X., and Granger, D. E. (2009). Beyond threshold hillslopes: Channel adjustment to base-level fall in tectonically active mountain ranges. *Geology* 37, 579–582. doi:10.1130/G30013A.1.

Pinto, L., Hérail, G., Sepúlveda, S. A., and Krop, P. (2008). A Neogene giant landslide in Tarapacá, northern Chile: A signal of instability of the westernmost Altiplano and palaeoseismicity effects. *Geomorphology* 102, 532–541. doi:10.1016/j.geomorph.2008.05.044.

Portenga, E. W., and Bierman, P. R. (2011). Understanding Earth's eroding surface with 10Be. *GSA Today* 21, 4–10. doi:10.1130/G111A.1.

Rech, J. A., Currie, B. S., Michalski, G., and Cowan, A. M. (2006). Neogene climate change and uplift in the Atacama Desert, Chile. *Geology* 34, 761–764. doi:10.1130/G22444.1.

Regard, V., Saillard, M., Martinod, J., Audin, L., Carretier, S., Pedoja, K., et al. (2010). Renewed uplift of the Central Andes Forearc revealed by coastal evolution during the Quaternary. *Earth and Planetary Science Letters* 297, 199–210. doi:10.1016/j.epsl.2010.06.020.

Reutter, K.-J., Scheuber, E., and Chong, G. (1996). Geodynamics of The AndesThe Precordilleran fault system of Chuquicamata, Northern Chile: evidence for reversals along arc-parallel strike-slip faults. *Tectonophysics* 259, 213–228. doi:10.1016/0040-1951(95)00109-3.

Reyment, R. A., and Jvreskog, K. G. (1996). *Applied Factor Analysis in the Natural Sciences*. Cambridge University Press.

Rutllant, J. A. (2003). Climate dynamics along the arid northern coast of Chile: The 1997–1998 Dinámica del Clima de la Región de Antofagasta (DICLIMA) experiment. *Journal of Geophysical Research* 108. doi:10.1029/2002JD003357.

Safran, E. B., Bierman, P. R., Aalto, R., Dunne, T., Whipple, K. X., and Caffee, M. (2005). Erosion rates driven by channel network incision in the Bolivian Andes. *Earth Surf. Process. Landforms* 30, 1007–1024. doi:10.1002/esp.1259.

Schaller, M., von Blanckenburg, F., Hovius, N., and Kubik, P. W. (2001). Large-scale erosion rates from in situ-produced cosmogenic nuclides in European river sediments. *Earth and Planetary Science Letters* 188, 441–458. doi:10.1016/S0012-821X(01)00320-X.

Scherler, D., Bookhagen, B., and Strecker, M. R. (2014). Tectonic control on 10Be-derived erosion rates in the Garhwal Himalaya, India. *J. Geophys. Res. Earth Surf.* 119, 2013JF002955. doi:10.1002/2013JF002955.

Scheuber, E., and Andriessen, P. A. M. (1990). The kinematic and geodynamic significance of the Atacama fault zone, northern Chile. *Journal of Structural Geology* 12, 243–257. doi:10.1016/0191-8141(90)90008-M.

Scheuber, E., and Gonzalez, G. (1999). Tectonics of the Jurassic-Early Cretaceous magmatic arc of the north Chilean Coastal Cordillera (22°–26°S): A story of crustal deformation along a convergent plate boundary. *Tectonics* 18, 895–910. doi:10.1029/1999TC900024.

Scheuber, E., and Reutter, K.-J. (1992). Magmatic arc tectonics in the Central Andes between 21° and 25°S. *Tectonophysics* 205, 127–140. doi:10.1016/0040-1951(92)90422-3.

Schulz, N., Boisier, J. P., and Aceituno, P. (2012). Climate change along the arid coast of northern Chile. *International Journal of Climatology* 32, 1803–1814. doi:10.1002/joc.2395.

Schwanghart, W., and Scherler, D. (2014). Short Communication: TopoToolbox 2 – MATLAB-based software for topographic analysis and modeling in Earth surface sciences. *Earth Surface Dynamics* 2, 1–7. doi:10.5194/esurf-2-1-2014.

Strahler, A. N. (1957). Quantitative analysis of watershed geomorphology. *Eos Trans. AGU* 38, 913–920. doi:10.1029/TR038i006p00913.

Strasser, M., and Schlunegger, F. (2005). Erosional processes, topographic length-scales and geomorphic evolution in arid climatic environments: the 'Lluta collapse', northern Chile. *International Journal of Earth Sciences* 94, 433–446. doi:10.1007/s00531-005-0491-2.

Summerfield, M., and Hulton, N. (1994). Natural Controls of Fluvial Denudation Rates in Major World Drainage Basins. *J. Geophys. Res.-Solid Earth* 99, 13871–13883. doi:10.1029/94JB00715.

Trauerstein, M., Norton, K. P., Preusser, F., and Schlunegger, F. (2013). Climatic imprint on landscape morphology in the western escarpment of the Andes. *Geomorphology* 194, 76–83. doi:10.1016/j.geomorph.2013.04.015.

Tucker, L. R., and Lewis, C. A reliability coefficient for maximum likelihood factor analysis. *Psychometrika* 38, 1–10. doi:10.1007/BF02291170.

USGS (2016). World Petroleum Assessment - World Geologic Maps: USGS, Energy Resources Program. Available at: http://energy.usgs.gov/OilGas/AssessmentsData/WorldPetroleumAssessment/WorldGeologicMaps.aspx [Accessed June 30, 2016].

Vermeesch, P. (2007). CosmoCalc: An Excel add-in for cosmogenic nuclide calculations. *Geochem. Geophys. Geosyst.* 8, Q08003. doi:10.1029/2006GC001530.

Victor, P., Oncken, O., and Glodny, J. (2004). Uplift of the western Altiplano plateau: Evidence from the Precordillera between 20° and 21°S (northern Chile): ALTIPLANO WEST FLANK. *Tectonics* 23, n/a-n/a. doi:10.1029/2003TC001519.

Vidiella, P. E., Armesto, J. J., and Gutiérrez, J. R. (1999). Vegetation changes and sequential flowering after rain in the southern Atacama Desert. *Journal of Arid Environments* 43, 449–458. doi:10.1006/jare.1999.0565.

von Blanckenburg, F. (2005). The control mechanisms of erosion and weathering at basin scale from cosmogenic nuclides in river sediment. *Earth Planet. Sci. Lett.* 237, 462–479. doi:10.1016/j.epsl.2005.06.030.

von Blanckenburg, F., Hewawasam, T., and Kubik, P. W. (2004). Cosmogenic nuclide evidence for low weathering and denudation in the wet, tropical highlands of Sri Lanka. *J. Geophys. Res.* 109, F03008. doi:10.1029/2003JF000049.

Whipple, K. X. (2009). The influence of climate on the tectonic evolution of mountain belts. *Nature Geosci* 2, 97–104. doi:10.1038/ngeo413.

Whipple, K. X., Wobus, C., Crosby, B., Kirby, E., and Sheehan, D. (2007). New tools for quantitative geomorphology: extraction and interpretation of stream profiles from digital topographic data. *GSA Short Course* 506. Available at: http://www.geomorphtools.org/Tools/StPro/Tutorials/userguides_final.pdf [Accessed September 19, 2016].

Whittaker, A. C. (2012). How do landscapes record tectonics and climate? *Lithosphere* 4, 160–164. doi:10.1130/RF.L003.1.

Wittmann, H., von Blanckenburg, F., Kruesmann, T., Norton, K. P., and Kubik, P. W. (2007). Relation between rock uplift and denudation from cosmogenic nuclides in river sediment in the Central Alps of Switzerland. *J. Geophys. Res.* 112, F04010. doi:10.1029/2006JF000729.

Wobus, C., Whipple, K. X., Kirby, E., Snyder, N., Johnson, J., Spyropolou, K., et al. (2006). "Tectonics from topography: Procedures, promise, and pitfalls," in *Special Paper 398: Tectonics, Climate, and Landscape Evolution* (Geological Society of America), 55–74. Available at: http://specialpapers.gsapubs.org/cgi/doi/10.1130/2006.2398(04) [Accessed June 24, 2016].

Zeilinger, G., Schlunegger, F., and Simpson, G. (2005). The Oxaya anticline (northern Chile): a buckle enhanced by river incision? *Terra Nova* 17, 368–375. doi:10.1111/j.1365-3121.2005.00622.x.

Zeitler, P. K., Meltzer, A. S., Koons, P. O., Craw, D., Hallet, B., Chamberlain, C. P., et al. (2001). Erosion, Himalayan geodynamics, and the geomorphology of metamorphism. *GSA Today* 11, 4–9.

Paper II

Latitudinal variations of vegetation and erosion rates identified along western South America

Jessica Starke[1], Todd A. Ehlers[1] and Mirjam Schaller[1]

[1]Department of Geosciences, Eberhard Karls University Tübingen, 72074 Tübingen, Germany

Published in *Journal of Geophysical Research: Earth Surface*, 25 October 2017.

Abstract

Vegetation influences erosion by stabilizing hillslopes and accelerating weathering. Previous studies investigating vegetation effects on erosion have proved challenging due to poorly understood interactions between vegetation and other factors such as precipitation and surface processes. Here we address these complexities along 3,500 km of the extreme climate and vegetation gradient of the Andean Western Cordillera (6°S to 36°S latitude). We do this using 94 cosmogenic radionuclide-derived erosion rates of millennial time scale and multivariate statistics. We identify regimes where sparse vegetation allows an increase of erosion with increasing precipitation and regimes where dense vegetation inhibit the maximum variation of erosion.

One sentence summary

We identify three different regimes in which variable of vegetation cover affects erosion in the Andean Western Cordillera, South America.

Main manuscript

The impact of vegetation on the shape and evolution of Earth's surface ranges (for example) from the microscopic scale of Mycorrhiza weathering for plant nutrition to macroscopic scales where plants retard hillslope erosion, stabilize environments for sediment deposition, and affect precipitation through evapotranspiration and leaf phenology (1-10). However, defining the influence of vegetation on

catchment-averaged erosion or denudation, rates (the combination of physical erosion and chemical weathering) has proven difficult because of non-linear interactions between vegetation type and cover with precipitation, temperature, and solar radiation (11-14, 80). Disentangling the effects of vegetation and climate on topography requires quantifying catchment-averaged erosion rates over a large range of climate and biogeographic conditions. The production of cosmogenic radionuclides in the upper ~2 m of Earth's surface provides one means for quantifying catchment-averaged erosion rates (15-17) that can be compared to different topographic, climate, and vegetation metrics. Here we quantify the relationships between catchment-averaged erosion rates with vegetation cover, climate, and topographic slope along the extended climate and ecological gradient of the Andean Western Cordillera, South America (Fig. 1 and Fig. 2). Millennial timescale erosion rates are quantified with 11 new, and 83 previously published nuclide-concentrations from river channel sediments (18-30). These 94 catchments are adjacent to a similar tectonic plate boundary (subduction zone). Catchment lithologies range from Oligo-Miocene, Plio-Pleistocene volcanoclastic deposits and ignimbrites to sedimentary deposits of Jurassic and Cretaceous age as well as Paleozoic and Cretaceous granodiorites to Precambrian gneiss (79) (Tab. 6). We identify 13 lithological types including subtypes in the study area. The total lithological-weighted quartz content for each catchment varies between 15% to 49% (Tab. 4, Tab. 7, Fig. S1, Fig S6).

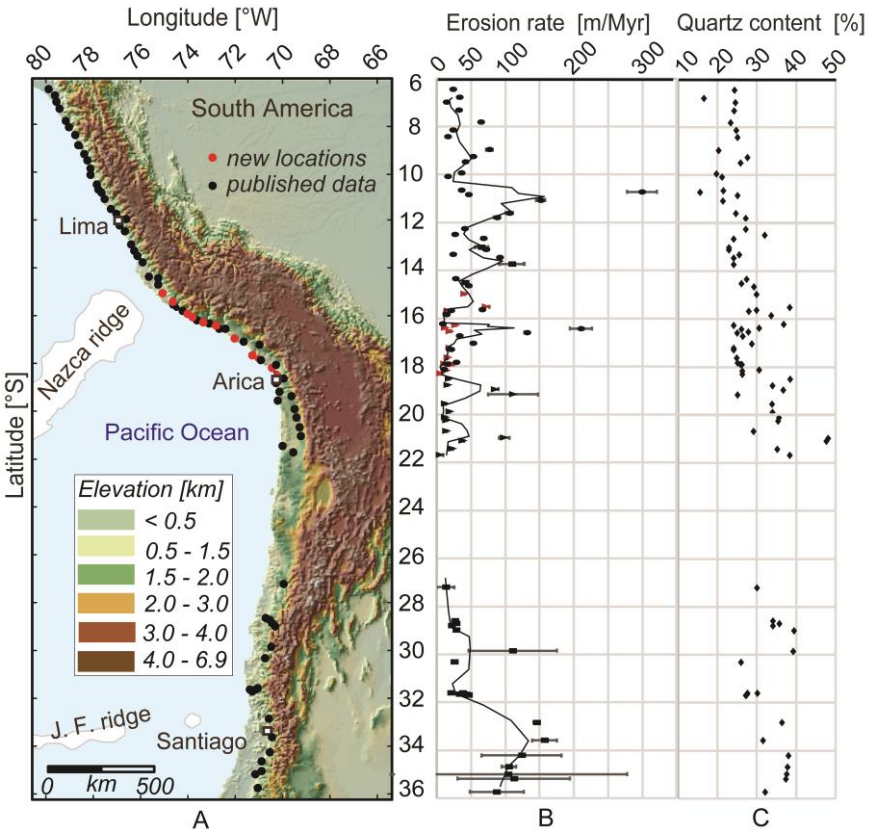

Fig. 1. (A) Topographic map is showing the catchment-averaged erosion rate sample locations of river sediments from the Andean Western Cordillera. Black dots indicate the location of previously published ^{10}Be concentrations (18-30). Red dots are new data presented in this study (Supplement Tables 1, 2). (B) Catchment-averaged erosion rates [m/Myr] are plotted versus latitude [°S]. Uncertainties represent the 1σ error. The black line represents the three-point moving average. All catchment-averaged erosion rates were calculated using the same calculation procedure (see supplemental material). (C) Quartz content [%] for each catchment based on the GLIM lithological map (79). A detailed list of lithological types and quartz content including uncertainties is shown in the supplementary (Table 6).

The Andean Western Cordillera between 6°S to 36°S latitude extends over 3,500 km (Fig.1A) and crosses six climate zones from hyper arid to temperate (31), and four distinct vegetation zones within biogeographic regions (32). Often with conflicting results, cosmogenic nuclide-derived erosion rates and their controlling factors were investigated along the Andean Western Cordillera with an increasing number of studies during the last two decades (18-30, 57, 58). The emphasis of these studies ranges from quantification of erosion rates in the vegetation-limited Atacama Desert (19,30), sediment storage in hyper arid environments (18,22,23), to the rates of canyon incision and hillslope erosion in the Andean Western Cordillera (24,25,27,28). With the exception of work by Carretier et al. (26) few studies have looked at systematic latitudinal variations in erosion rates along this climate and ecological gradient. To the best of our knowledge, no study to date has investigated a latitudinally diverse enough data set to document non-linearities and influence of vegetation-climate effects on catchment erosion in South America.

Here we present the effect of vegetation cover on millennial-scale erosion rates from basins draining the Andean Western Cordillera. Cosmogenic radionuclide concentrations of 10Be (half-life, 1.386 ± 0.016 Myr) (33) were measured from new samples and combined with recently published data from Peru and Chile (Fig. 1A, B) (18-30). All new and existing concentrations were used to recalculate the erosion rates using the same sea level high latitude production rates and production rate scaling (34-38) (Fig. S1A). For each catchment the 2σ range in vegetation cover, mean annual precipitation (MAP) and temperature (MAT), solar radiation, and basin-averaged slope, local relief, quartz content and lithology were determined from MODIS, TRMM, CHELSA, WorldClim, SRTM and GLiM datasets (39-43,79) (Fig. 1C, 2 A, B, C, Fig. S3). We compared TRMM, CHELSA and WorldClim (MAT and MAP values), found no large differences in variability and continued to work with WorldClim. A combined multivariate statistical factor analysis was used to calculate correlation coefficients and covariance between catchment-averaged erosion rates, basin-averaged slopes and local relief from 90m SRTM, MAP, MAT as well as solar radiation from WorldClim (1km resolution), MODIS vegetation cover (1 km resolution), quartz content and lithology (from GliM) (Fig. 2D, E). The details of each method and additional catchment parameters are discussed in the supplementary materials.

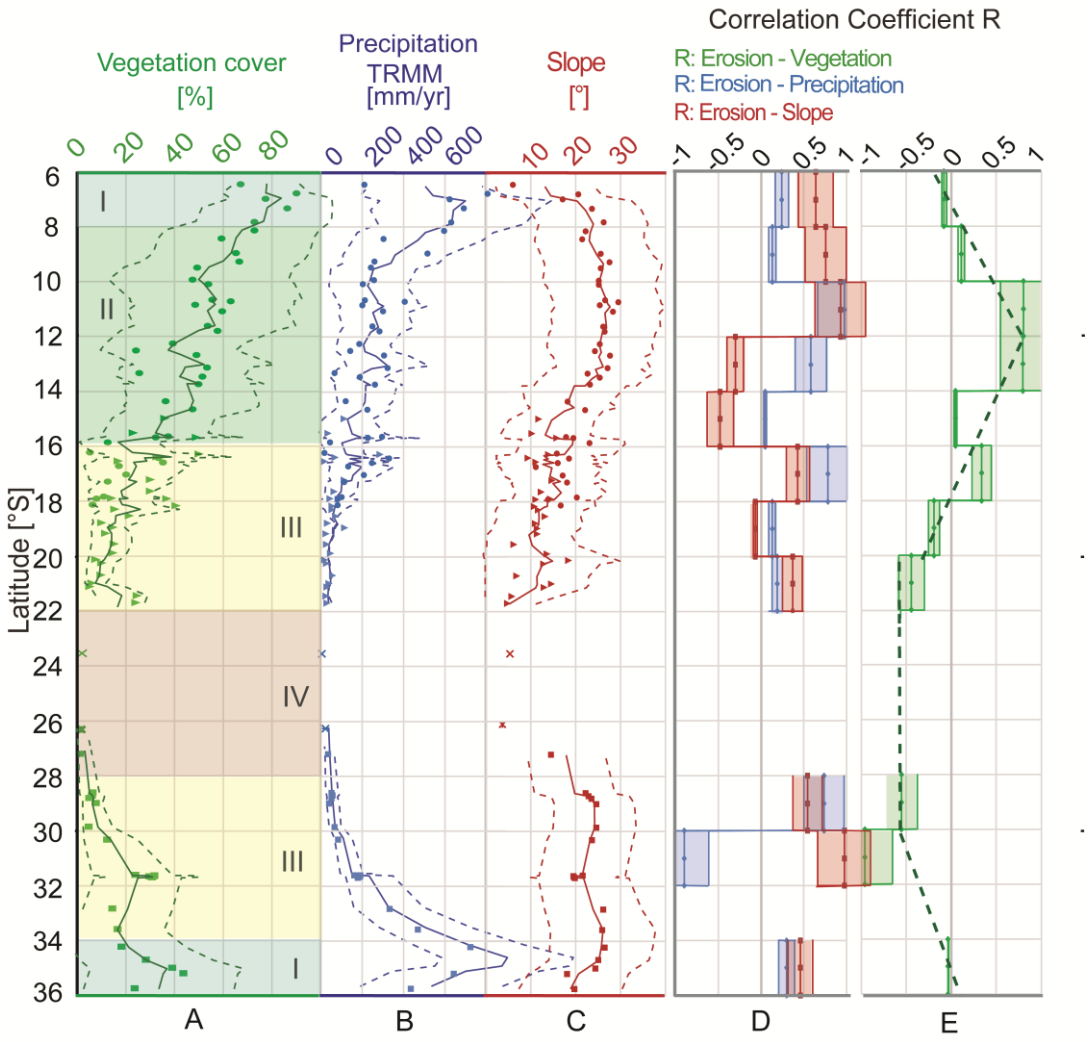

Fig. 2. Latitudinal variations in vegetation cover, precipitation, topographic slope and their correlation with erosion rates from catchments sampled in Fig. 1A. **(A)** Vegetation cover and type plotted versus latitude (see also supplement for vegetation type distribution in each catchment). The solid green line represents the three-point moving average of the mean vegetation cover. The dashed green lines represent the three-point moving averages of the 2σ standard deviation from the mean value. The catchment-wide main vegetation type is highlighted in colored zones. The classification is taken from MODIS 2012 vegetation continuous field data (41). The vegetation type in region I represents mixed forest. Region II is dominated by grassland, and region III is characterized by open shrubland. Region IV shows barren or sparsely vegetated areas. **(B)** Precipitation plotted versus latitude where the blue solid line is the three-point moving average from the mean values. The dashed blue lines represent the three-point moving averages of the 2σ standard deviation from the mean value. Data are derived from TRMM2b (40). **(C)** Slope versus latitude. The solid red line represents the three-point moving average from the mean slope. The dashed red lines represent the three-point moving averages of the 2σ standard deviation from the mean value. Data are derived from 90 m resolution of SRTM data (39). **(D)** Correlation coefficient R plotted versus latitude. The correlation coefficient ranges between -1 to 1. The red lines represent the mean and 1σ error of the correlation coefficient between erosion rate versus slope. The blue lines represent the mean and 1σ error of the correlation coefficient between erosion rate versus precipitation. **(E)** Correlation coefficient R plotted versus latitude. Correlation coefficient and uncertainties calculated with a Monte Carlo analysis. The solid green lines represent the mean and 1σ error of the correlation coefficient between erosion rate versus vegetation cover. The dashed green line represents trends in the correlation coefficient within each zone. Correlation coefficients were calculated from samples within 2° bins, the minimum size possible to provide enough points for a robust analysis. The 1σ errors on the correlation coefficients presented in D and E were calculated using a Monte Carlo analysis of the uncertainties in erosion rates for all samples within each bin (see supplement for details).

Catchment-averaged erosion rates vary between 1.4 and 300 m/Myr (Fig. 1B). Starting in the north (6°S to 12°S) erosion rates display increasing values between 0 to 300 m/Myr. From 12° to 20°S the scatter in erosion rates decreases (0 to 210 m/Myr). The lowest erosion rates are located between 20°S to 30°S (0 to 120 m/Myr). In the south (30°S to 36°S) erosion rates vary between 0 to 150 m/Myr and show increasing values from 30°S to 33.5°S and decreasing values from 33.5°S to 36°S. In general, the quartz content for each catchment ranges from 15% to 50%. From 6°S to 22°S the quartz content is continuously increasing from 15% to 50%. From 26°S to 36°S the quartz content varies from 20% to 40% but shows no clear trend. (Fig. 1C). Starting in the north, catchment vegetation cover and MAP are the highest of the regions studied (70-90% and 600-800 mm/yr, respectively) (Fig 2 A, B). They gradually decrease to a minimum (5% and <50 mm/yr, respectively) at the latitudes of the Atacama Desert (20°S to 30°S). Further south (30°S to 36°S), the vegetation cover and MAP gradually increase to a southern maximum (42% and 700 mm/yr, respectively). Basin-averaged slopes have increasing values up to 30° from 6°S to 12°S. The values gradually decrease towards the south (12°S to 20°S) and vary between 30° to 10°. The lowest slopes (5° to 10°) are situated between 20° to 30°. In the south (30°S to 36°S) topographic slopes increase up to 28° (Fig 2.C)

The calculation of the Pearson correlation coefficients R averaged over 2° latitudinal increments illuminates changes in correlations over large scales. Each correlation coefficient derived of a 2° bin represents the correlation coefficient of n number of catchments between individual parameters (Fig. S10). The 2° increments were chosen as the minimum spatial scale over which sufficient data points are available for a robust analysis. The correlation coefficients were calculated using a Monte Carlo Simulation of the 2 sigma range of values produced by uncertainties in each parameter for all locations (Fig 1 and Fig. 2). The relationship between erosion rate and slope (Fig. 2D) can be classified after (86) into regions with very weak (0.00-0.19), weak (0.20-0.39), moderate (0.40-0.59) and strong (0.60-0.79) and very strong (0.80-1.0) correlations. Starting in the north, a moderate positive correlation between erosion and slope occurs between 6°S to 8°S (~0.7). Strong positive correlations are present from 8°S to 12°S (~0.7-1.0). From 12°S to 14°S a weak negative correlation (~-0.3) can be observed. A further decrease in correlation to moderate negative correlated is shown from 14°S to 16°S (~-0.5). Correlations remain moderate negative correlated between 16°S to 18°S (~0.4) and change to very weak negative correlated from 18°S to 20°S. The last correlation coefficient in the northern part shows a moderate positive correlation (~0.4). Due to low data availability in the latitudinal increments from 22°S to 28°S and 32°S and 34°S correlation coefficients cannot be calculated. However, it is possible to identify a moderate positive correlation from 28°S to 30°S (~0.5), a very strong positive correlation (~0.7-1.0) from 30°S to 32°S and a moderate correlation from 34°S to 36°S (~0.5). Precipitation and erosion rate are weak to moderate but positively correlated (typically >0 to <0.5) between 6°S and 10°S (Fig. 2D). From 10°S to 12°S a very strong positive correlation (~0.7-1.0) occurs but changes to a moderate positive correlation from 12°S to 14°S and to a very weak correlation between 14°S to 16°S. A strong

positive correlation is present from 16°S to 18°S and shifts to a weak and insignificant correlation between 18°S to 22°S. In the south a strong positive correlation occurs from 28°S to 30°S, a strong negative correlation can be found from 30°S to 32°S that is changing to a moderate positive correlation from 34°S to 36°S.

In contrast to the correlations between erosion rate and slope or precipitation, which show many changes in correlation, the correlation between erosion rate and vegetation cover contains only a few changes (Fig. 2E). The correlation coefficient is very weak correlated from 6°S to 10°S. From 10°S to 14°S a very strong positive correlation is present which decreases to a very weak correlation from 14°S to 16°S. Weak positive as well as weak negative correlations can be found between 16°S to 20°S. Moderate negative correlations occur between 20°S to 22°S and 28°S to 30°S. A very strong negative correlation is shown from 30°S to 32°S which is changing to a very weak correlation between 34°S to 36°S. In addition, the statistical analysis shows no correlation or covariance with quartz content or lithology with erosion rate in the study area (Tab. 4, Tab. 7, Fig. S1, Fig. S6).

Results from the multivariate factor analysis of erosion rate, vegetation cover, slope, mean annual temperature, mean annual precipitation, mean annual solar radiation, local relief, quartz content and lithology identify four factors that explain 62% of the data variance (Tab S4, Tab. S5). First, the results highlight the importance of vegetation cover on erosion rate and identifies vegetation and erosion rate as having a high covariance (factor loading of 0.5 to 0.6 in factor 1). In addition, vegetation cover and erosion show an inter-dependency with WorldClim annual precipitation (factor loading >0.9 in factor 1). Second, in factor 2 vegetation cover is also covarying with WorldClim annual temperature (factor loading >0.6) and with the lithological type of acid volcanic rocks ‘va’ (factor loading 0.7). Third, we identify mean slope and mean local relief as having a strong covariance (factor loading > 0.8 in factor 3). The last factor 4 shows that the quartz content and the lithological type of unconsolidated sediments are covarying (> factor loading 0.5). Details of the factor analysis are explained in the supplementary material.

Based on the above results we note that along the 30° latitudinal transect, the correlation coefficient between precipitation and erosion rate does not show a clear variation (except between 6-12° S. latitude), and correlation coefficients oscillate, with few exceptions, between 0 to 0.5 (Fig. 2D). Similarly, there is no clear systematic latitudinal variation in the correlation coefficients between slope and erosion rates. In contrast, vegetation cover-erosion rate correlations show regimes that either clearly coincide or are antithetic in correlation. Starting in the arid (<50 mm/yr) and sparsely vegetated (vegetation cover <15%) regime (20°S to 30°S) the erosion-vegetation correlation indicates a negative relationship which cannot be proven over the whole zone due to low data availability of catchment erosion rates in mostly alluvial fan dominated geomorphological settings (22, 23). The regime between 12°S-20°S and 30°S-36°S shows a transitional signal in which correlation coefficients change with reference to increasing

vegetation cover from negative significant to insignificant and then to positive significant erosion-vegetation correlation. The shift in correlation is between 30°S to 36°S not as clear as between 12°S to 20°S due to low data availability. In contrast, the regime from 6°S to 12°S (Fig. 2E) is characterized by a progressive latitudinal shift in the vegetation cover-erosion rate correlation from insignificant to positive significant (N-S). Due to the northern extent of the study area it is not possible to identify if the correlation coefficients change from insignificant correlation to significant negative correlation like in an opposite behaviour to regime between 12°S to 22°S.

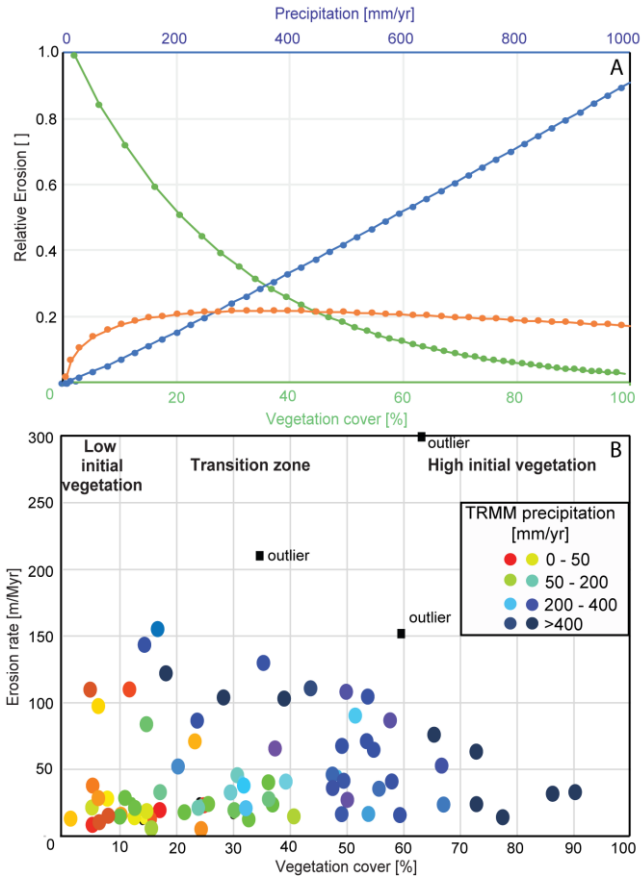

Fig. 3. (A) Modelled relative erosion based on increasing vegetation cover and precipitation. Vegetation cover-derived relative erosion is shown in green and is based on functions reported in Gyssels et. al. and Renard and Freimund (48,86). Vegetation cover (V) is calculated by: $V=Pxa^{\wedge b}$, where P is precipitation, a is 1.55 and b is 0.6 (86). The factors a and b are derived from the calculated exponential relationship of vegetation cover and precipitation of the study area and are shown in the supplementary FigureS4. The equation of relative erosion (R_1) is: $R_1=e^{-a0.062}$ (48) Precipitation-derived relative erosion (R_2) is shown in blue and is based on functions reported in Renard and Freimund (86), $R_2=Pxa^{\wedge b}$, where P is precipitation. We use for the factors a and b the values a=0.82 and b=1.09 reported in Cooper (87). The orange curve represents the relative erosion ($R_{combined}$) derived from the combined effect of increasing vegetation cover and precipitation. It is calculated with the equation $R_{combined}=\sqrt{(R_1*R_2)}$. For further details see also Table 8. **(B)** Observed relationship between erosion rate, vegetation cover and mean annual precipitation (MAP) for each individual catchment. Erosion rates plotted versus vegetation cover in dots. The dots are colour coded according to mean annual precipitation derived from TRMM dataset shown in Fig. 2. Black squares represent outliers most likely resulting from glacier remnants (29). For comparison, supplement Fig. S6A is identical, but colour coded by slope

The previous vegetation related regime can be interpreted as the result of specific surface process and vegetation related factors that superimpose the observed changes in correlation (Fig. 3). From 20°S to 30°S, a regime with non- to sparse vegetation (vegetation cover between 0% to 15%) parameters such as basin slope, and stochastic variations in precipitation (e.g. large rare storms) and sediment storage exert a strong influence on erosion which leads to a high general variance in erosion rates because precipitation is more readily converted into surface runoff, physical erosion, and sediment transport that can increase the range in erosion rates (44-48). Adding vegetation cover in a regime with low initial vegetation leads to large changes in behavior of correlation because the stabilizing, or buffering, effect of vegetation cover is directly present. However, due to the low initial water availability in this regime erosion rates are also relatively low. In the regime from 12°S to 20°S (15% to 50% vegetation cover) a transition takes place where both abiotic (surface) processes and vegetation effects influence erosion rates and cause a shift in correlation. In regions with sufficient water availability but medium to high vegetation erosion rates increase with increasing vegetation. Due to the limits of the study area the effect of high vegetation cover that decreases erosion rates cannot be observed in correlation coefficients. The shift in correlation from positive significant to insignificant indicates that the effect of vegetation (~50% cover) starts to have its maximum (saturated) impact on erosion rate despite a continuing trend of increasing vegetation cover and precipitation (Fig. 2A, B). Although increasing precipitation rates should cause a proportional increase in discharge and therefore a proportional increase in erosion rates (81-83) an increase of vegetation cover seems to act as a biological filter that is limiting the maximum amount of erosion. In this study we observe that a vegetation cover greater than 50% leads to a maintenance of steep mean slopes of 25° to 30° (Fig. S6). In the transitional regime and the regime with initial low vegetation mean slopes vary mainly between 5° to 20° (Fig. S6). Any further change in the vegetation-erosion correlation is muted by factors such as hillslopes at the angle of repose contributing to erosion (49).

In addition, we modelled relative erosion rates based on increasing vegetation cover and precipitation rate (Fig. 3A) (48,86). With increasing vegetation cover relative erosion is decreasing whereas with increasing precipitation relative erosion is also increasing (Fig. 3A). Extracting the root of the multiplied vegetation and precipitation induced relative erosion shows a combining effect of vegetation and precipitation on relative erosion. This effect shows that until 15% vegetation cover relative erosion is increasing, from 15% to 50% relative erosion remains stable and is decreasing from 50% to 100% vegetation cover (Fig. 3A). A similar trend can be observed in the measured erosion rates. We identify a general trend that the maximum variation in erosion is decreasing with increasing vegetation (>15%) despite increasing precipitation rates (Fig.3B), erosion remains stable in the transition zone and starts to decrease and the dense vegetated regime.

The results presented here are consistent with concepts developed in previous soil erosion and sediment yield studies (46,48,84). Previous soil erosion studies document that as the type and density of vegetation cover increases, the resistance of soil to erosion through enhanced slope stabilization increases (6,48,50-52). This concept has also been investigated in modelling studies that implemented surface resistance to hillslope erosion through vegetation induced root cohesion and modification of surface runoff (53-56,85). Recent studies suggest that vegetation shows a non-linear behaviour which is complicated to untangle with methods using linear calculations (80). New simulations show that in a setting with low initial vegetation cover, like we find in this study area, the effect of changing vegetation cover has a larger impact on erosion due to non-linear response of diffusivity and fluvial erodibility compared to the linear behaviour to changes in precipitation (80). Similar findings to ours of a vegetation control on catchment-averaged erosion rates have also been reported for smaller geographic areas in both East Africa (57) and the Himalaya (58). Confirmation of our findings with other study areas means that despite differences in the climate and geomorphic settings, vegetation cover exhibits an influence on erosion rates consistent with the results presented here.

Erosion rates vary with uplift rates in steady-state condition, but the results indicate that the study area is not at steady state because: First, the main phases of mountain building in the Andean Western Cordillera are from 20-10 Ma and terminated around 9 Ma (59-63), and only isolated regions of recent neo-tectonic activity (e.g. surface rupturing faults) have been observed, and with limited displacement (64,65) (Fig. S6). The regimes of vegetation-erosion interactions identified in Figure 2 do not correspond to known patterns of tectonic activity or subducting oceanic ridges (Fig. S6). Second, changes in base level lowering are still propagation through the river profiles. Knickzones in the river profiles are present along the Andean Western Cordillera and are propagating headward at least since the Late Miocene (77) (Fig. S7). Third, the results indicate that hillslopes are in state of transient response. This means that our observed weak correlation between slopes and erosion rates, and occasional strong correlation between vegetation and erosion could be explained by a decoupling between the fluvial channels and hillslopes over protracted timescales. If, and how well, river channels and hillslopes are decoupled from each other need to be investigated further. A second potential caveat is that paleo-precipitation rates could differ in magnitude from the modern (78). However, paleo-precipitation gradients (from Pliocene to modern time) in the investigated region are similar to modern precipitation gradients along the Andean Western Cordillera (66) (Fig. S5). Our identified regimes are therefore unlikely to be relicts of paleo-climate change.

There are several broader implications for the vegetation cover and precipitation effects on erosion that we identify. First, our analysis identifies that the effect of vegetation and precipitation on catchment erosion varies depending on the vegetation cover amount (Fig. 2). Second, the identification of regimes implies that studies focusing on individual catchments with a spatial extent smaller than the larger scale

interactions identified here could poorly resolve vegetation-erosion rate interactions. The results indicate that smaller scale studies are less likely to identify the range of vegetation cover effects on erosion rates documented here and could be located at or across regimes where different behaviors exist. Third, results from previous studies (26,57,58) have shown both correlations and anti-correlations between vegetation cover, precipitation and erosion rates. These conflicting results may have occurred in areas that are located at, or straddle, the regimes identified here. Finally, our results demonstrate that previous concepts of a vegetation control on soil erosion (48) can also be applied to large-scale and long-term erosion rate studies

Acknowledgement

D. Kost and L. Michel are thanked for laboratory and field assistance, respectively. We also thank three anonymous reviewers for their thoughtful comments. Funding: This study was funded by a European Research Council (ERC) consolidator grant (CoG 615703) to T.A. Ehlers. Authors contribution: J. Starke and T.A. Ehlers planned the study. J. Starke is responsible for all sample collection and calculations. J. Starke and M. Schaller are responsible for the laboratory analysis. All authors contributed to manuscript and figure preparation. Competing interest: The authors have no competing financial conflicts of interest with this study. Data and materials availability: Data reported in the paper are presented in the Supplementary Materials.

Supplementary to Paper II

1 Materials

1.1 Cosmogenic nuclides sampling approach

River stream sediments were collected from 11 basins draining the Andean Western Cordillera in Southern Peru from 15°-18.3°S latitude. These detrital sediments were obtained in a regular spacing with ~50km between sampled basins. Catchment sizes vary between 636 km^2 and 14,710 km^2. The lithology was characterized by mostly Jurassic and Cretaceous granodiorites and granites similar to the catchments analysed in northern Chile (30). In the field, the grain size fraction of 500 to 1000µm was sieved. In cases of insufficient quartz mass, the 250 to 500µm grain size fraction was extracted and further cleaned for pure quartz. All newly generated data are summarized in Table 1. Newly collected samples from Southern Peru for measurements of in situ-produced ^{10}Be were dried, separated using magnetic separation followed by etching with 10% HCL and followed by 10% HF. Approximately 300 µg of ^{9}Be was added to ~40 g pure quartz. Be was extracted by using the standard separation method of von Blanckenburg et al. (67). The ratios of $^{10}Be/^{9}Be$ were measured as BeO targets by accelerator mass spectrometry (AMS) at the University of Köln and blank corrected with a blank ratio of 3.06E-15 ± 6.46E-16.

1.2 Literature data

Previous studies have made significant progress in understanding cosmogenic nuclide- derived concentrations, erosion rates and the processes controlling them along the Western margin of South America. In this study, we complement our dataset with the ^{10}Be blank corrected concentrations at sample location (18-30), which are summarized in Table 2. The data from Nishiizumi et al. (18) and Placzek et al. (22) are taken from alluvial sediments in the Central Atacama Desert between 23° to 26.3°S and represent a different geomorphological setting compared to catchments that are exclusively draining the Western Cordillera. The detrital samples from Carretier et al. (26) and Carretier et al. (27) are taken at 13°S and14.5°S in Southern Peru and from 27°S to 35.7°S in Central Chile. Catchments of Central and Southern Peru were sampled by Reber et al. (29) from 6.4°S to 18.1°S.

2 Methods

2.1 Catchment-averaged erosion rates

Catchment-averaged erosion rates over timescales of <~10^6yr were calculated from the blank corrected ^{10}Be concentrations. The cosmogenic isotope concentration (C) of ^{10}Be at the Earth's surface is inversely proportional to the erosion rate (D) assuming that the surface is steadily eroding and described in the following equation:

$$C = P_{Nuc}(0) \times \frac{a_1}{\left(\lambda + \frac{\rho \times D}{b_1}\right)} + P_{\mu stopped}(0) \times \frac{a_2}{\left(\lambda + \frac{\rho \times D}{b_2}\right)} + P_{\mu fast}(0) \times \frac{a_3}{\left(\lambda + \frac{\rho \times D}{b_3}\right)} \quad (1)$$

where C is the isotope concentration (at $g_{(qtz)}^{-1}$), D is the erosion rate (cm yr^{-1}), λ is the decay constant (^{10}Be 4.99E-07 ± 0.43E-08 yr^{-1} (*33*); (68-69)), and ρ is the rock density (2.4 ± 0.2 g cm^{-3}). $P_{nuc}(0)$, $P_{\mu stopped}(0)$, and $P_{\mu fast}(0)$ are the surface production rates of cosmogenic nuclides (at ($g_{(qtz)}$ yr^{-1}) by spallation, stopped and fast muons. The coefficients a_1, a_2 *and* a_3 (dimensionless) and b_1, b_2 *and* b_3 (g cm^{-2}) are used for depth scaling of the production rates and reported by Braucher et al. (38).

Sea level high latitude (SLHL) nucleonic production rates (P_{nuc}) for ^{10}Be are based on the value 3.7 ± 0.57 at ($g_{(qtz)}$ yr)$^{-1}$ (^{10}Be) (37). The stopped and fast muonic production rates use the values 0.012 ± 0.012 at ($g_{(qtz)}$ yr)$^{-1}$ (^{10}Be $P_{\mu stopped}$) and 0.039 ± 0.004 at ($g_{(qtz)}$ yr)$^{-1}$ (^{10}Be $P_{\mu fast}$), provided by Braucher et al. (38). The nucleonic and muonic production rates were scaled using the time-dependent scaling laws of Dunai (34). The catchment-averaged production rate is the average production rate of each DEM pixel (90 m resolution) in the catchment area. Each single production rate was corrected for topographic shielding following the procedure described in Dunne et al. (35) and Norton and Vanacker (36). Corrections for lithology and snow shielding were not applied. We calculate the uncertainties in erosion rates using a Monte Carlo simulation of error propagation. The error propagation includes the production rate error of nucleonic, stopped and fast muonic production, a 5% DEM altitude error for the production rate, the decay constant error, the rock density error and the ^{10}Be concentration error. In order to contain a consistent erosion rate along the Western margin of South America the production rates as well as the erosion rates were recalculated from the blank corrected ^{10}Be concentrations of the literature data (Fig. S1). The new calculated erosion rates are reported in Table 3.

2.2 Factor analysis

Factor analysis is a multivariate statistical method that extracts from a large set of manifest variables a few common latent characteristics. Examples of using a factor analysis in geological research are described in Hartmann and Wünneman (71). The factor analysis performs a multivariate data reduction by detecting linear correlations with a maximum likelihood estimate (72-74). The factor analysis model can be described by:

$$X_{(N\times p)} = F_{(N\times k)}A'_{(k\times p)} + E_{(N\times p)} \quad (2)$$

where X is the data matrix with N elements and p variables, F the factor score matrix with k the number of factors to be used, A' the factor loading matrix, plus the error term E (75). A z-transformation was applied on the X data matrix to provide an interpretation independent of unit dimension. A z-transformation can be calculated from the following formula:

$$z = (V - \mu)/\sigma \quad (3)$$

where z is the z-score, V is the value of the element, μ is the population mean, and σ is the standard deviation. The factor analysis was performed in R-mode, which means that the *X* data matrix is transformed into a correlation matrix R before it starts to compute the factor loadings. The fundamental equation for all forms of a R-mode factor analysis is (75):

$$x = Af + e \quad (4)$$

x is a column vector representing one object of the data matrix X, A is the factor loading matrix, f and *e* are corresponding row vectors of F and E described above. We derive equation 4 by transforming equation 2 in scalar notation. Consequently, for any given value of the data matrix of the nth row and ith column the equation 5 is valid (75):

$$x_{ni} = \sum_{j=1}^{k} f_{nj}a_{ij} + e_{ni} \quad (5)$$

Following equation 5 we obtain for any row (x´) of the data matrix X (75):

$$x' = f'A' + e' \quad (6)$$

The transpose of equation 6 is the fundamental equation 4 for the R-mode factor analysis. The data matrix X, the factor score matrix F, the factor loading matrix A, plus the error term E.

In the first step the factor analysis calculates the Pearson correlation coefficients R and the p-value (Table. 5) over a 2° latitudinal bin and implements a Monte Carlo Simulation to be independent from the mean catchment parameters and to address their uncertainties. The 2° increments were chosen as the

minimum spatial scale over which sufficient data points are available for a robust analysis. The Monte Carlo Simulation repeats the equations 100,000 times, while each repetition iteratively selects random input variables according to the probability distribution function of the data matrix (76). Consequently, the correlation coefficient represents the relationship of two parameters including their uncertainties in a specific region while other parameters are kept constant. In a second step the covariation of parameters from 6°S to 36°S are calculated to identify relationships between parameters that are present over the whole region. A second Monte Carlo Simulation is added after the first step in order to repeat 100,000 times the equations to calculate the covariation. The data matrix *X* contains the catchment parameters including their uncertainties from 6°S to 36°S for each sampled basin. The independent variable of the covariation analysis is the catchment latitude. Only catchments were selected that drain the Western Cordillera and represent catchment-averaged erosion rates of non-alluvial systems. Catchments with an influence of glacial activity are marked as outliers (Fig. 3). The factor analysis was performed in Matlab and the results are documented in Table 4 and Table 5.

2.3 Catchment parameters

Catchment parameters of mean local relief of 10 km radius, mean slope, mean annual precipitation (MAP), mean annual temperature (MAT), mean annual solar radiation, vegetation cover and vegetation type were calculated for comparison to erosion rates. Mean local relief of 10 km radius and mean slope were computed using the Shuttle Radar Topography Mission (SRTM) digital elevation model (DEM) with a resolution of 90m (39). Mean annual precipitation was calculated with the data product TRMM 2B31 5x5km grid (1998-2006) (40) with WorldClim 1 km resolution (42) and CHELSA 1km resolution (43). Mean annual temperature was calculated from WorldClim and CHELSA. Values of mean annual solar radiation were derived from WorldClim. Catchment-wide vegetation cover was analyzed using the 1km Modis- based Green Vegetation Fraction with a time resolution from 2001-2012 (41). The vegetation type was extracted by using MODIS landcover (2001-2012) with a data resolution of 0.5°-0.5°. Quartz content and the lithological types are derived from the Glim dataset (79). The 13 main lithological types that we find in the study area are Basic plutonic rocks (pb), Acid plutonic rocks (pa), Intermediate plutonic rocks (pi), Pyroclastics (py), Carbonate sedimentary rocks (sc), Mixed sedimentary rocks (sm), Siliciclastic sedimentary rocks (ss), Evaporites (ev), Metamorphics (mt), Acid volcanic rocks (va), Basic volcanic rocks (vb), Intermediate volcanic rocks (vi), Unconsolidated sediments (su). Catchment parameters were analyzed using ArcGIS and TopoToolboxv2 (70) and were recalculated to obtain a consistent data set for the literature data (Fig. S2, S3, S4, S5, S6, S8 and Table S3).

3 Tables

All Tables of PAPER II are also archived in the digital appendix. The digital appendix is a CD that sticks to the last page of this thesis.

Table S1: Sample data from this study

Author	Sample name	Sample type	Latitude S °	Longitude W °	Stream Order Strahler count	Grain size mm	^{10}Be conc blank corrected atoms gr^{-1}	Error 1σ atoms gr^{-1}	Normalized ^{10}Be conc. blank corrected	Normalized Error 1σ
this study	16PE002	Western Cordillera	-16.38889	-73.25798	5.0	0,25-0,5	851263	26702	0.7	0.02
this study	16PE003	Western Cordillera	-16.53559	-72.86041	4.0	0,25-0,5	290835	11408	0.2	0.01
this study	16PE013	Western Cordillera	-17.62401	-71.33701	5.0	0,25-0,5	692498	24163	0.6	0.02
this study	16PE016	Western Cordillera	-17.90685	-70.95811	6.0	0,5-1	585362	19088	0.5	0.02
this study	16PE018	Western Cordillera	-18.15887	-70.67024	6.0	0,25-0,5	639356	24039	0.5	0.02
this study	16PE019	Western Cordillera	-18.29308	-70.43336	5.0	0,5-1	1370876	42271	1.2	0.04
this study	16PE031	Western Cordillera	-17.88617	-70.43275	4.0	0,5-1	828646	28656	0.7	0.02
this study	16PE040	Western Cordillera	-17.21526	-70.97372	5.0	0,25-0,5	955937	32854	0.8	0.03
this study	16PE046	Western Cordillera	-16.27236	-72.45062	7.0	0,25-0,5	182413	7572	0.2	0.01
this study	16PE063	Western Cordillera	-15.67173	-74.52261	5.0	0,25-0,5	610920	19367	0.5	0.02
this study	16PE064	Western Cordillera	-15.51300	-74.83815	5.0	0,25-0,5	62609	2754	0.1	0.00
this study	16PE065	Western Cordillera	-14.97702	-74.98862	4.0	0,25-0,5	251486	8738	0.2	0.01

Table S2, part 1: Sample data from literature

Author	Sample name	Sample type	Latitude S °	Longitude W °	10Be conc. blank corrected atoms gr-1	Error 1σ atoms gr-1	Normalized 10Be conc. blank corrected	Normalized Error 1σ
(20)	Pis11	Western Cordillera	-13.73	-75.8855	171000	12000	0.1	0.01
(26)	SAN1	Western Cordillera	-27.2	-69.92	1027511	153842	0.9	0.13
(26)	HUA12	Western Cordillera	-28.6	-70.73	598649	24962	0.5	0.02
(26)	HUA10	Western Cordillera	-28.7	-70.55	588998	16567	0.5	0.01
(26)	HUA7	Western Cordillera	-28.8	-70.46	833051	53481	0.7	0.05
(26)	HUA1	Western Cordillera	-28.99	-70.28	479983	13641	0.4	0.01
(26)	ELK1	Western Cordillera	-29.85	-70.49	177039	23322	0.2	0.02
(26)	HUR1	Western Cordillera	-30.31	-70.73	593076	38635	0.5	0.03
(26)	ILL1	Western Cordillera	-31.6	-71.11	468966	13507	0.4	0.01
(26)	CHO0823S	Western Cordillera	-31.61	-71.4	218067	9450	0.2	0.01
(26)	CHO0820	Western Cordillera	-31.66	-71.22	234948	10795	0.2	0.01
(26)	CHO0822S	Western Cordillera	-31.66	-71.3	198207	5803	0.2	0.00
(26)	CHO1	Western Cordillera	-31.69	-71.27	195648	6708	0.2	0.01
(26)	ACO1	Western Cordillera	-32.83	-70.54	101191	2915	0.1	0.00
(26)	MAI1	Western Cordillera	-33.58	-70.44	87032	5010	0.1	0.00
(26)	CAC1	Western Cordillera	-34.21	-70.53	91404	10713	0.1	0.01
(26)	TIN1	Western Cordillera	-34.68	-70.87	99370	5275	0.1	0.00
(26)	TEN1	Western Cordillera	-34.99	-70.86	73331	48099	0.1	0.04
(26)	LON1	Western Cordillera	-35.18	-71.12	64381	29145	0.1	0.02
(26)	MAU1	Western Cordillera	-35.73	-71.02	129351	14825	0.1	0.01
(26)	GRA1	Western Cordillera	-14.5173	-75.2108	360000	20000	0.3	0.02
(26)	CAN2	Western Cordillera	-13.0275	-76.1932	328000	21000	0.3	0.02
(18)	17	WC/Alluvial Sediment	-26.26	-69.56	12340000	3000000	10.5	2.55
(22)	ADBA-2SD	Alluvial Sediment	-23.5335	-69.0796	8840000	300000	7.5	0.26
(22)	ASOI-SD	Alluvial Sediment	-24.0933	-70.1688	6470000	260000	5.5	0.22
(22)	ADSO-4SD	Channel gravel	-24.0384	-69.8728	6110000	270000	5.2	0.23
(22)	ADSO-8CH	Channel gravel	-24.1529	-68.547	8060000	270000	6.9	0.23
(22)	ADSA-4CH	Channel gravel	-23.2232	-68.5649	4020000	360000	3.4	0.31
(22)	ADSA-1SD	Alluvial Sediment	-23.7857	-68.1071	8040000	580000	6.8	0.49
(22)	ADCRE-8	Channel gravel	-24.7089	-70.369	12580000	270000	10.7	0.23
(22)	ADSA-1SD	Alluvial Sediment	-23.7857	-68.1071	8040000	580000	6.8	0.49
(22)	ADCRW-3	Channel gravel	-24.5682	-70.5411	322000	79000	0.3	0.07
(29)	PRCME-1	Western Cordillera	-18.1191	-70.3274	1019000	22000	0.9	0.02
(29)	PRCME-3	Western Cordillera	-17.824	-70.5046	556000	14000	0.5	0.01
(29)	PRCME-401	Western Cordillera	-17.9073	-70.9562	910000	18000	0.8	0.02
(29)	PRCME-5	Western Cordillera	-17.2865	-70.9895	834000	19000	0.7	0.02
(29)	PRCME-6	Western Cordillera	-17.0288	-71.6908	219000	8000	0.2	0.01
(29)	PRCME-7	Western Cordillera	-16.5849	-72.7285	157000	4000	0.1	0.00
(29)	PRCME-8	Western Cordillera	-16.7192	-72.4187	508000	20000	0.4	0.02
(29)	PRCME-9	Western Cordillera	-16.4217	-73.1153	85000	4000	0.1	0.00
(29)	PRCME-10	Western Cordillera	-16.226	-73.6178	936000	19000	0.8	0.02
(29)	PRCME-11	Western Cordillera	-15.846	-74.2607	659000	16000	0.6	0.01
(29)	PRCME-12	Western Cordillera	-15.672	-74.5232	596000	12000	0.5	0.01
(29)	PRCME-13	Western Cordillera	-15.6286	-74.6368	213000	8000	0.2	0.01

Table S2, part 2: Sample data from literature

	name	type	S °	W °	blank corrected atoms gr-1	1σ atoms gr-1	blank corrected	1σ
(29)	PRCME-1401	Western Cordillera	-14.6476	-75.2424	273000	8000	0.2	0.01
(29)	PRCME-15	Western Cordillera	-14.3448	-75.6858	366000	10000	0.3	0.01
(29)	PRCME-17	Western Cordillera	-13.465	-76.1365	181000	5000	0.2	0.00
(29)	PRCME-18	Western Cordillera	-13.3213	-76.2433	354000	8000	0.3	0.01
(29)	PRCME-19	Western Cordillera	-13.1238	-76.3944	288000	11000	0.2	0.01
(29)	PRCME-20	Western Cordillera	-12.6652	-76.6515	261000	8000	0.2	0.01
(29)	PRCME-21	Western Cordillera	-12.5005	-76.7412	262000	8000	0.2	0.01
(29)	PRCME-22	Western Cordillera	-12.251	-76.8919	306000	6000	0.3	0.01
(29)	PRCME-23	Western Cordillera	-11.6083	-77.2387	141000	5000	0.1	0.00
(29)	PRCME-24	Western Cordillera	-11.0713	-77.586	113000	4000	0.1	0.00
(29)	PRCME-25	Western Cordillera	-10.839	-77.6962	254000	6000	0.2	0.01
(29)	PRCME-26	Western Cordillera	-10.6551	-77.8337	317000	9000	0.3	0.01
(29)	PRCME-27	Western Cordillera	-8.9662	-78.6209	226000	9000	0.2	0.01
(29)	PRCME-28	Western Cordillera	-8.423	-78.7835	620000	26000	0.5	0.02
(29)	PRCME-29	Western Cordillera	-8.14	-79.0076	427000	14000	0.4	0.01
(29)	PRCME-30	Western Cordillera	-7.3234	-79.4807	299000	9000	0.3	0.01
(29)	PRCME-31	Western Cordillera	-6.9804	-79.6335	354000	10000	0.3	0.01
(29)	PRCME-32	Western Cordillera	-6.4519	-79.8572	262000	6000	0.2	0.01
(29)	PRCME-33	Western Cordillera	-6.7882	-79.6043	224000	7000	0.2	0.01
(29)	PRCME-34	Western Cordillera	-7.8193	-79.1728	144000	4000	0.1	0.00
(29)	PRCME-35	Western Cordillera	-9.2627	-78.4313	167000	4000	0.1	0.00
(29)	PRCME-36	Western Cordillera	-9.4815	-78.2945	219000	7000	0.2	0.01
(29)	PRCME-37	Western Cordillera	-9.9359	-78.2186	208000	8000	0.2	0.01
(29)	PRCME-38	Western Cordillera	-10.0847	-78.1504	528000	11000	0.4	0.01
(29)	PRCME-39	Western Cordillera	-11.7923	-76.9914	170000	6000	0.1	0.01
(29)	PAT-ME	Western Cordillera	-10.7203	-77.7695	64000	3000	0.1	0.00
(29)	Pisco	Western Cordillera	-13.7274	-75.8855	171000	12000	0.1	0.01
(30)	15CL002	Western Cordillera	-19.55089	-70.19434	640136	21787	0.5	0.02
(30)	15CL014	Western Cordillera	-19.16528	-70.16817	75031	7309	0.1	0.01
(30)	15CL018	Western Cordillera	-18.51871	-70.18941	759969	25654	0.6	0.02
(30)	15CL019	Western Cordillera	-18.77716	-70.26838	654193	22313	0.6	0.02
(30)	15CL028	Western Cordillera	-21.42659	-70.05085	375624	13095	0.3	0.01
(30)	15CL031	Western Cordillera	-18.95096	-69.49113	254647	9690	0.2	0.01
(30)	15CL041	Western Cordillera	-19.88353	-69.46416	1037114	33845	0.9	0.03
(30)	15CL049	Western Cordillera	-21.6853	-69.52814	1823654	56656	1.6	0.05
(30)	15CL057	Western Cordillera	-20.1191	-69.20985	1424909	46586	1.2	0.04
(30)	15CL058	Western Cordillera	-20.24223	-69.39035	1122409	37972	1.0	0.03
(30)	15CL063	Western Cordillera	-20.69	-69.27	777559	25365	0.7	0.02
(30)	15CL069	Western Cordillera	-20.97284	-69.19701	197467	9247	0.2	0.01
(30)	15CL070	Western Cordillera	-21.09846	-69.29047	502936	17987	0.4	0.02

Table S3, part 1: Catchment data from literature and this study

Sample name	Erosion m/Myr	1σ error m/Myr	App. Age kyr	1σ error kyr	Mean elevation m	10% error m	Area km	10% error km	Mean slope °	2σ error °	Vegetation %	2σ error %	TRMM Precipitation mm/yr	2σ error mm/yr	Solar radiation (kJ m^{-2} day^{-1}) mean	2σ error	Chelsa mean MAP mm/yr	2σ error	Chelsa mean MAT [°C]	2σ error	WoldClim mean MAP mm/yr	2σ error	WoldClim mean MAT [°C]	2σ error
15CL002	12.3	0.5	55.7	6.2	2016.5	201.7	4670.0	467.0	6.3	7.6	15.2	9.2	26.8	2.7	20038	580	33.9	22.8	14.4	4.9	39.9	60.6	13.3	4.1
15CL014	111.3	36.2	6.5	0.7	2062.3	206.2	2283.7	228.4	11.4	9.0	11.5	6.9	25.0	2.5	20203	218	32.0	14.6	14.1	4.6	41.6	47.3	13.4	3.5
15CL018	17.6	0.7	38.7	4.4	2326.3	232.6	1800.7	180.1	13.1	3.6	21.2	12.8	71.3	7.1	19465	601	71.3	38.6	10.3	5.4	120.3	83.8	10.4	4.4
15CL019	15.6	0.6	43.7	5.0	2357.3	235.7	1501.3	150.1	11.0	8.6	10.0	6.1	30.8	3.1	19767	578	42.1	23.0	12.6	5.5	76.4	86.5	12.2	4.7
15CL028	22.9	0.9	30.6	3.5	2099.7	210.0	42616.9	4261.7	5.9	5.9	24.6	14.7	24.7	2.5	20496	526	21.0	18.7	12.4	6.1	23.5	34.8	11.9	4.9
15CL031	84.7	4.7	8.1	0.9	3998.3	399.8	1028.2	102.8	11.4	11.4	14.5	8.7	115.4	11.5	19329	675	73.2	22.7	5.1	1.9	185.4	39.2	5.4	1.9
15CL041	18.4	0.6	36.5	4.2	3706.1	370.6	1565.2	156.5	13.6	13.6	14.6	9.4	47.2	4.7	19663	764	57.5	18.8	6.2	4.1	100.7	42.8	6.5	3.7
15CL049	4.7	4.8	136.1	15.8	2310.2	231.0	23200.6	2320.1	4.8	4.8	24.2	14.8	23.4	2.9	20778	412	18.8	15.4	11.6	5.6	23.8	22.4	11.5	4.5
15CL057	12.4	0.5	53.5	5.9	3667.2	366.7	61.4	6.1	18.4	18.4	7.4	4.6	16.0	1.6	19965	146	36.6	3.3	8.7	2.1	58.1	14.9	8.9	1.8
15CL058	14.1	0.6	47.5	5.1	3304.4	330.4	438.8	43.9	12.8	12.8	10.0	6.1	26.8	2.7	20184	376	33.5	8.0	8.7	4.6	57.1	31.4	8.8	4.0
15CL063	14.2	0.5	47.7	5.4	2769.8	277.0	223.2	22.3	6.9	6.9	9.8	6.3	56.7	5.7	19858	334	41.8	16.9	4.9	3.2	80.2	28.1	11.7	4.3
15CL070	37.9	1.6	18.0	2.0	3647.1	364.7	493.1	49.3	13.0	13.0	5.0	3.2	28.0	3.8	20066	418	29.1	6.5	5.9	4.2	54.2	22.1	6.4	3.7
16PE002	12.2	0.5	55.6	6.2	2583.5	258.4	2028.0	202.8	9.4	10.1	32.6	20.5	67.0	74.9	19562	479	136.6	82.7	11.5	3.7	179.0	161.1	12.8	4.0
16PE003	19.2	1.1	37.8	4.2	2258.0	225.8	1016.1	101.6	11.1	9.7	16.9	10.5	16.3	25.7	19158	813	104.2	64.1	12.3	4.4	89.0	119.0	14.6	4.4
16PE013	15.8	0.7	43.2	4.7	2365.9	236.6	3670.6	367.1	12.3	8.7	30.0	18.1	63.9	74.3	19128	737	102.2	86.1	13.4	6.4	111.6	150.2	13.7	5.7
16PE016	23.5	1.0	29.1	3.1	2746.3	274.6	5689.0	568.9	11.1	8.7	36.8	22.6	82.3	94.5	18797	1120	144.0	129.5	12.2	7.3	163.6	188.8	12.2	6.3
16PE018	14.4	0.7	47.5	5.4	1956.5	195.6	5095.3	509.5	10.8	3.6	40.6	24.7	52.3	68.7	18118	1409	88.5	81.2	15.6	6.9	83.7	118.6	14.6	5.2
16PE019	5.3	1.5	122.5	13.6	810.0	81.0	8396.0	839.6	11.7	9.6	15.4	11.3	53.1	63.8	18231	1277	66.8	48.3	16.1	6.8	61.3	76.5	14.5	4.5
16PE031	11.4	0.5	53.2	6.6	2306.9	230.7	636.0	63.6	14.4	8.6	14.1	8.5	42.9	38.3	19285	701	93.9	38.4	13.4	4.7	74.4	60.7	13.8	3.2
16PE040	19.1	0.7	35.1	4.2	3540.1	354.0	1704.4	170.4	14.7	8.6	30.0	18.1	113.0	81.8	19375	850	170.3	69.4	8.4	5.3	213.3	157.4	9.4	5.3
16PE046	27.0	1.5	27.6	3.2	4015.8	401.6	14710.7	1471.1	13.9	10.5	50.0	29.2	284.3	169.6	17742	1040	469.4	268.9	5.3	5.0	510.3	238.1	6.1	5.5
16PE063	16.1	0.5	42.7	4.9	2805.1	280.5	4417.2	441.7	15.8	10.4	43.0	29.2	231.5	220.4	16814	567	300.3	233.4	12.1	4.7	80.2	28.1	11.7	4.3
16PE064	71.6	4.9	10.9	1.2	1531.4	153.1	1404.3	140.4	10.3	8.5	23.1	13.7	33.7	73.5	18524	675	68.0	83.9	17.0	4.0	112.7	178.0	16.1	3.2
16PE065	40.4	1.6	17.5	2.0	2310.0	231.0	1106.1	110.6	11.8	9.0	36.1	21.2	111.8	153.9	19645	269	161.6	138.8	14.1	5.5	272.5	269.3	13.4	4.9
SAN1	12.66	13.0	53.0	6.7	3037.7	763.1	3749.0	374.9	14.5	8.3	1.1	2.0	34.1	24.5	20779	144	27.4	8.2	7.6	4.2	31.5	15.3	9.2	2.8
HUA12	26.23	1.6	25.9	2.9	3221.4	1073.9	7343.0	734.3	22.2	9.3	6.3	5.2	52.0	34.0	20156	591	71.1	19.3	5.2	5.8	32.4	45.0	4.3	4.6
HUA10	28.34	0.6	24.1	2.8	3382.5	946.4	7189.0	718.9	22.9	9.1	6.0	5.2	54.7	33.0	20128	589	73.3	18.3	4.4	5.1	37.5	42.6	3.7	4.1
HUA7	21.15	3.0	31.9	3.5	3529.9	851.8	2876.0	287.6	23.5	8.9	4.9	4.7	51.8	31.0	20128	535	79.4	16.6	3.3	4.6	108.4	40.9	2.6	3.8
HUA1	27.95	0.7	24.6	2.8	3088.5	643.1	3083.0	308.3	24.6	8.3	7.6	3.3	39.2	13.8	20347	339	87.6	12.0	5.8	3.6	79.5	25.6	5.3	2.8
ELK1	111.11	64.5	6.2	0.8	3713.0	811.2	2868.0	286.8	24.6	9.5	4.6	4.2	64.8	46.7	19625	804	81.4	18.7	2.3	4.3	143.4	45.8	1.3	3.9
HUR1	25.78	3.9	26.5	2.9	3240.6	883.5	1086.0	108.6	23.6	9.8	12.0	11.1	82.5	27.9	19676	633	117.9	28.3	4.4	4.9	157.6	39.8	2.7	4.3
ILL1	20.94	0.6	33.1	3.7	2413.8	997.4	1206.0	120.6	21.5	9.3	23.7	18.3	161.4	56.1	19446	481	238.8	45.3	7.4	5.4	211.9	17.4	5.8	5.1
CHO08235	37.90	2.6	18.9	2.0	1995.8	1126.0	5943.0	594.3	19.5	9.6	31.7	21.0	190.2	86.3	19139	719	238.5	49.1	9.5	6.0	224.9	30.7	7.9	5.8
CHO0820	32.65	2.4	21.9	2.5	1908.1	1064.9	1957.0	195.7	19.6	9.2	29.4	17.0	163.8	64.2	19543	514	231.1	43.1	10.2	5.6	207.0	16.7	8.3	5.2
CHO08225	42.23	1.2	16.9	1.9	2019.8	1113.2	5834.0	583.4	19.6	9.6	31.4	20.8	186.6	82.9	19172	680	239.2	43.3	9.4	5.9	225.3	30.4	7.8	5.7
CHO1	45.80	1.9	15.6	1.7	2144.9	1108.9	3714.0	371.4	19.8	9.7	30.6	21.6	176.9	76.6	18395	686	243.1	51.9	8.6	6.0	236.5	31.8	7.1	5.9
ACO1	145.32	3.9	4.8	0.6	3162.3	841.7	2093.0	209.3	26.1	11.2	14.2	15.9	332.1	209.0	17093	561	263.2	61.9	2.2	4.6	363.7	42.9	1.4	5.3
MAI1	157.31	18.0	4.5	0.5	3164.6	908.7	4685.0	468.5	25.9	11.3	16.5	16.8	468.0	227.8	16385	407	549.5	169.3	1.5	4.8	477.3	62.5	1.7	5.6
CAC1	123.56	57.9	5.8	0.6	2746.7	808.3	2112.0	211.2	26.4	12.3	17.9	23.9	722.1	240.9	16085	177	763.3	143.3	3.0	4.5	588.3	79.9	4.0	5.0
TIN1	105.13	10.1	6.8	0.8	2526.0	864.7	1442.0	144.2	24.9	10.7	28.1	23.2	968.6	348.4	15387	180	798.2	163.8	3.9	4.8	662.7	84.3	4.7	4.8
TEN1	104.28	173.6	7.0	1.0	2065.8	652.7	1203.0	120.3	24.3	10.3	38.8	30.6	1045.5	383.7	15397	114	948.8	198.8	6.1	3.7	722.6	75.5	6.7	3.3
LON1	112.11	81.8	6.6	1.0	1944.0	735.5	1742.0	174.2	18.1	11.5	43.5	36.4	640.1	260.4	15377	171	961.6	191.3	6.6	4.1	755.7	81.2	6.8	3.5
MAU1	87.45	39.1	8.0	0.9	2211.9	555.9	2653.0	265.3	19.7	11.4	23.5	26.6	434.6	440.9	15867	147	817.3	177.6	4.9	3.0	725.3	86.0	5.2	2.6
Pis11	109.46	17.8	6.3	0.7	3465.0	381.2	3642.0	364.2	18.0	10.0	43.8	27.0	262.8	175.5	17305	1015	351.4	211.6	8.5	5.6	490.2	256.0	8.4	5.3
GRA1	41.02	4.3	16.8	1.9	3076.0	461.4	1855.0	185.5	18.8	7.5	57.8	29.0	247.6	118.6	17645	903	358.5	147.8	10.9	5.6	422.3	252.3	10.6	4.9
CAN2	65.21	9.2	10.5	1.2	3777.0	453.2	5794.0	579.4	23.7	9.3	54.7	27.9	342.4	209.4	16876	879	457.7	215.8	7.2	5.2	571.8	235.6	7.5	4.6

Table S3, part 2: Catchment data from literature and this study

Sample name	Erosion m/Myr	1σ error m/Myr	App. Age kyr	1σ error kyr	Mean elevation m	10% error m	Area km	10% error km	Mean slope .	2σ error .	Vegetation %	2σ error %	TRMM Precipitation mm/yr	2σ error mm/yr	Solar radiation (kJ m^{-2} day^{-1}) mean	2σ error	Chelsa mean MAP mm/yr	2σ error	Chelsa mean MAT [°C]	2σ error	WoldClim mean MAP mm/yr	2σ error	WoldClim mean MAT [°C]	2σ error
17					3463.6	573.0			17.2	8.3	0.8	1.2	22.2	10.6	20695	135	23.8	6.2	5.4	3.2	30.9	12.4	8.4	2.9
ADBA-25D					3581.0	737.7			5.3	6.9	1.8	2.8	37.0	41.7										
PROME-1	9.96	0.2	67.2	7.3	2733.0	273.3	1659.0	165.9	16.7	11.9	6.2	5.4	81.3	87.3	18686	898	91.9	55.8	13.8	7.0	87.9	89.8	13.1	5.0
PROME-3	28.46	0.5	24.0	2.7	3105.0	310.5	2154.0	215.4	20.2	11.2	10.7	12.8	100.4	78.2	18673	1054	151.4	89.4	10.2	6.4	169.2	144.8	10.7	5.6
PROME-401	14.89	0.3	45.2	4.9	2668.0	266.8	5821.0	582.1	13.9	10.5	7.8	10.8	81.1	94.9	18800	1120	144.3	123.8	12.2	7.3	163.8	169.1	12.2	6.3
PROME-5	20.83	0.3	32.4	3.7	3398.0	339.8	1785.0	178.5	18.1	10.3	12.4	10.0	112.8	83.2	19010	842	165.2	72.2	8.8	5.5	205.2	158.9	9.8	5.5
PROME-6	52.48	2.8	13.4	1.4	3568.0	356.8	13026.0	1302.6	17.1	11.6	20.1	21.2	206.8	144.6	18175	1172	232.4	203.2	8.0	5.8	362.1	255.0	8.8	5.9
PROME-7	131.47	3.3	5.2	0.6	3635.0	363.5	17557.0	1755.7	16.1	12.4	35.2	28.0	247.0	185.3	17920	1119	409.5	293.6	7.0	6.2	440.3	280.4	7.8	6.7
PROME-8	32.89	1.8	20.8	2.3	3285.0	328.5	13862.0	1386.2	11.2	10.0	16.9	16.3	131.9	142.2	18605	920	168.4	154.2	8.7	6.0	245.7	197.6	9.9	6.4
PROME-9	210.66	16.2	3.3	0.4	3745.0	374.5	16065.0	1606.5	18.5	13.5	33.2	27.1	328.5	208.8	18071	1151	430.1	260.8	7.0	5.2	513.8	273.7	7.4	5.7
PROME-10	7.94	0.1	84.4	9.7	2155.0	215.5	1420.0	142.0	15.7	11.2	5.0	7.1	17.5	34.6	19782	516	64.9	46.4	13.3	3.0	85.6	81.2	14.6	2.8
PROME-11	13.77	0.2	49.7	5.4	2316.0	231.6	1244.0	124.4	23.0	11.3	12.4	14.1	43.4	65.2	19052	785	91.9	54.6	13.4	4.7	158.0	147.8	13.5	4.0
PROME-12	20.58	0.4	33.3	3.5	2797.0	279.7	4361.0	436.1	19.5	12.4	32.1	37.2	227.3	215.9	18816	549	343.3	260.2	12.0	4.8	346.2	251.5	11.7	4.3
PROME-13	66.22	3.1	10.5	1.2	2695.0	269.5	4561.0	456.1	17.9	12.4	37.2	31.2	235.2	258.5	18290	834	343.3	260.2	11.7	5.7	443.8	315.3	11.0	5.3
PROME-140	46.27	1.0	15.1	1.8	2716.0	271.6	5220.0	522.0	22.1	11.0	47.4	23.6	224.2	131.5	18119	753	231.4	160.4	12.6	6.1	356.9	263.0	12.0	5.2
PROME-15	27.58	0.7	25.3	2.9	2204.0	220.4	4715.0	471.5	18.1	12.6	36.1	26.1	119.6	110.5	17835	1011	168.6	133.7	14.3	6.5	238.9	245.9	13.4	5.2
PROME-17	91.30	2.6	7.6	0.8	3197.0	319.7	3113.0	311.3	25.3	12.1	51.4	26.8	188.2	133.7	17416	994	273.9	162.4	9.5	5.7	435.1	233.2	9.4	5.1
PROME-18	23.84	0.3	23.5	3.4	1967.0	196.7	726.0	72.6	22.6	10.9	25.4	25.3	66.4	77.8	17774	1343	122.0	60.7	14.3	5.6	213.4	166.9	13.9	4.3
PROME-19	71.79	3.6	9.5	1.1	3648.0	364.8	6059.0	605.9	27.1	12.5	53.4	28.4	321.7	211.1	16830	943	438.6	224.5	7.8	5.9	552.2	253.5	7.9	5.0
PROME-20	68.16	2.6	10.1	1.1	3294.0	329.4	2337.0	233.7	27.6	11.6	49.0	32.5	304.2	189.0	16854	996	388.0	162.8	9.1	6.3	473.2	264.5	8.8	5.3
PROME-21	26.42	1.0	27.1	2.9	1772.0	177.2	775.0	71.5	24.2	11.6	24.0	23.7	142.3	99.3	17332	1325	193.5	94.0	15.9	4.9	159.8	137.9	14.8	3.7
PROME-22	40.94	0.4	17.0	1.9	2568.0	256.8	1574.0	157.4	25.4	11.9	39.1	23.0	184.3	131.9	16839	1253	232.1	133.6	12.0	6.6	326.2	259.7	11.5	5.6
PROME-23	105.78	5.2	6.6	0.7	2697.0	269.7	3070.0	307.0	26.1	12.1	53.6	34.5	247.5	160.7	16303	960	380.7	211.0	11.8	7.3	423.1	328.2	10.7	6.4
PROME-24	151.80	6.7	4.6	0.5	3134.0	313.4	4322.0	432.2	28.2	12.3	59.5	32.6	298.6	196.9	16164	850	376.5	217.2	10.1	6.8	512.3	297.3	9.3	6.0
PROME-25	46.57	0.7	15.0	1.7	2365.0	236.5	1013.0	101.3	25.4	11.9	48.4	33.7	200.7	153.4	16188	998	181.1	107.8	12.9	7.0	321.9	247.7	12.3	6.0
PROME-26	35.49	1.3	19.7	2.0	2407.0	240.7	2365.0	236.5	26.5	11.3	55.6	36.4	211.9	157.9	16274	895	361.5	165.3	13.3	6.3	299.3	221.1	13.4	5.7
PROME-27	76.71	4.5	9.0	1.0	3262.0	326.2	12385.0	1238.5	25.5	13.1	65.3	33.6	514.4	337.1	15495	888	516.3	208.6	10.0	5.9	531.2	294.2	10.6	6.1
PROME-28	15.40	1.0	44.5	4.8	2246.0	224.6	1695.0	169.5	21.5	11.5	59.3	32.9	302.6	245.5	15739	1007	365.4	152.0	13.6	6.0	250.0	194.1	14.9	4.4
PROME-29	23.72	0.9	23.3	3.2	2307.0	230.7	2120.0	212.0	22.2	11.8	72.8	30.9	593.7	378.2	15479	1126	341.1	171.8	13.5	6.1	310.0	214.3	14.6	4.4
PROME-30	31.67	0.9	22.2	2.5	2292.0	229.2	3901.0	390.1	23.6	11.9	86.3	21.2	689.0	326.5	14894	797	530.2	276.3	14.8	5.0	585.0	260.1	15.3	4.0
PROME-31	13.75	0.4	52.1	5.7	1142.0	114.2	1755.0	175.5	17.1	12.7	77.5	27.7	620.5	515.8	14293	605	373.9	232.8	20.0	5.4	335.4	304.7	19.3	4.0
PROME-32	23.40	0.4	30.8	3.5	1423.0	142.3	1378.0	137.8	6.0	10.0	67.0	12.4	210.3	134.0	13760	836	166.5	39.5	24.6	0.7	113.3	38.6	22.6	0.4
PROME-33	32.89	1.1	21.8	2.4	1844.0	184.4	3552.0	355.2	20.5	11.9	90.3	14.6	804.3	425.5	14431	488	710.0	305.4	17.1	5.2	653.2	356.1	17.0	4.1
PROME-34	63.80	1.4	11.0	1.2	1985.0	198.5	4363.0	436.3	26.2	12.6	72.8	32.9	628.6	383.2	15434	950	374.3	197.3	16.3	5.0	393.6	231.5	16.6	3.7
PROME-35	53.11	1.0	13.2	1.5	2194.0	219.4	1777.0	177.7	27.5	12.7	66.7	31.6	257.9	188.5	15834	559	301.5	113.9	13.4	6.9	239.9	204.6	14.1	6.0
PROME-36	41.57	1.5	17.1	1.9	1938.0	193.8	750.0	75.0	25.5	13.2	49.3	35.3	241.4	176.7	16010	762	313.2	118.3	15.4	7.0	235.5	193.1	15.5	5.8
PROME-37	36.01	1.9	20.0	2.1	1697.0	169.7	685.0	68.5	25.1	12.7	47.4	39.1	255.8	266.2	16258	962	358.0	138.1	16.5	6.2	191.4	182.2	16.2	4.9
PROME-38	16.25	0.2	41.9	4.8	2337.0	233.7	2100.0	210.0	25.1	11.9	53.7	38.3	201.6	148.6	16102	876	419.1	164.8	13.5	7.3	302.3	237.1	13.3	6.4
PROME-39	87.66	4.1	7.9	0.9	2942.0	294.2	1764.0	176.4	26.4	11.5	57.6	34.1	281.8	163.9	16846	858	364.4	191.5	10.3	6.1	447.1	315.0	9.9	5.6
PAT-ME	299.35	21.5	2.3	0.3	3378.0	337.8	4607.0	460.7	23.5	12.6	63.2	32.9	404.9	284.6	16025	782	467.3	218.5	9.2	6.0	535.6	253.8	8.8	5.9
Pisco	109.46	18.2	6.3	0.7	3464.0	346.4	3667.0	366.7	23.1	12.1	43.8	26.8	261.1	176.4	17295	1013	352.0	212.3	8.5	5.6	435.6	256.3	8.3	5.3

Table S4: Factor analysis

Parameter	Factor 1	Factor 2	Factor 2	Factor 4
Erosion rate	0.5	-0.3	0.1	0.2
Vegetation cover	0.6	0.6	0.2	0.3
Slope	0.4	-0.2	0.8	0.2
Area	0.0	-0.1	-0.3	0.0
Worldclim MAP*[1]	0.9	-0.1	0.1	0.2
Worldclim MAT*[2]	-0.1	1.0	-0.1	0.0
WorldClim Solar radiatic	-0.7	-0.5	-0.3	-0.1
Local relief	0.3	-0.3	0.9	-0.1
Quartz content	0.1	0.5	0.1	0.6
Lithology 'pa'	-0.2	0.0	0.2	0.2
Lithology 'ss'	0.0	0.0	0.1	0.4
Lithology 'sumxgl'	0.3	-0.4	-0.2	-0.5
Lithology 'sumxvr'	0.1	0.0	-0.1	0.5
Lithology 'va'	0.2	0.7	0.3	0.1
Lithology 'vivi'	-0.3	-0.1	-0.4	-0.1
Lithology 'vipy'	-0.3	-0.4	0.2	-0.2
KVarEigen [%]	62.0			
eVarEigen [%]	23.1	19.7	11.3	7.8

[1]Acid plutonic rocks (pa), Siliciclastic sedimentary rocks (ss), Acid volcanic rocks (va), Intermediate volcanic rocks (vi) with pyroclastics (vipy), Unconsolidated sediments (su) with mixed grains and glacial remnants (sumxgl) and mixed grains and subordinate volcanics (sumxvr)

Table S5: R-values

Latitude °S	erosion- vegetation		erosion- slope		erosion- precipitation		erosion-temperature		erosion-quartz content		erosion- acid plutonic rocks		erosion- acid volcanic rocks	
	R	p-value	R	p-value	R	p-value	R	p-value	R	p-value	R	p-value	R	p-value
6 to 8	-0.1	0.90	0.6	0.25	0.2	0.70	-0.5	0.39		0.1	0.85	0.1	0.86	-0.10	0.87
8 to 10	0.1	0.83	0.8	0.08	0.1	0.81	-0.8	0.08		0.0	0.93	0.1	0.89	-0.06	0.92
10 to 12	0.8	0.03	0.9	0.00	1.0	0.00	-0.8	0.02		-0.3	0.58	0.4	0.40	-0.64	0.12
12 to 14	0.8	0.01	-0.3	0.43	0.6	0.10	-0.8	0.01		-0.2	0.57	-0.4	0.35	-0.52	0.15
14 to 16	0.0	0.90	-0.5	0.19	0.0	0.91	0.2	0.53		0.5	0.13	-0.5	0.14	0.62	0.15
16 to 18	0.3	0.22	0.4	0.11	0.8	0.00	-0.6	0.02		-0.3	0.34	-0.2	0.48	NaN	NaN
18 to 20	-0.2	0.62	-0.1	0.86	0.1	0.74	-0.3	0.44		-0.3	0.45	-0.4	0.33	NaN	NaN
20 to 22	-0.4	0.32	0.4	0.42	0.2	0.69	-0.7	0.09		-0.5	0.25	-0.4	0.32	NaN	NaN
28 to 30	-0.6	0.33	0.5	0.35	0.7	0.15	-0.7	0.15		-0.9	0.06	-0.7	0.18	NaN	NaN
30 to 32	-1.0	0.12	1.0	0.11	-0.9	0.24	0.6	0.20		0.1	0.90	0.0	0.97	NaN	NaN
34 to 36	0.0	0.96	0.5	0.44	0.3	0.63	-0.2	0.75		-0.3	0.58	0.9	0.06	NaN	NaN

Table S6, part 1: Lithological data

Name	Latitude	Percentage of lithology in each catchment[1]											Quartz content in each lithology [2]												Total quartz content	Uncertainty
		pb	pa	pi	py	sc	sm	ss	ev	mt	va	vb	vi	su	pb	pa	pi	py	sc	sm	ss	ev	mt	va	vb	vi	su[3]		1σ
	[°]	[%]	[%]	[%]	[%]	[%]	[%]	[%]	[%]	[%]	[%]	[%]	[%]	[%]	[%]	[%]	[%]	[%]	[%]	[%]	[%]	[%]	[%]	[%]	[%]	[%]	[%]	[%]	[%]
PRCME-32	-6.4519	0.0003	0	0	0	0	0.0009	0.0008	0	0	0	0	0.0017	0.9964	5	40	22.5	40	1	25	50	1	40	40	5	22.5	24.3	24.4	7.3
PRCME-33	-6.7882	0.0002	0.0048	0	0.0411	0.2306	0.0186	0	0	0	0	0	0.1057	0.5989	5	40	22.5	40	1	25	50	1	40	40	5	22.5	19.5	16.6	5.0
PRCME-31	-6.9804	0.0008	0.0058	0	0.025	0.0097	0.0109	0	0	0	0	0	0.0636	0.8841	5	40	22.5	40	1	25	50	1	40	40	5	22.5	24.5	24.6	7.4
PRCME-30	-7.3234	0.0028	0.0098	0	0.0376	0.0276	0.1089	0	0	0	0	0	0.0994	0.714	5	40	22.5	40	1	25	50	1	40	40	5	22.5	24.3	24.2	7.3
PRCME-34	-7.8193	0.0032	0.0158	0	0	0.025	0.1103	0	0	0	0	0	0.1476	0.6979	5	40	22.5	40	1	25	50	1	40	40	5	22.5	23.7	23.3	7.0
PRCME-29	-8.14	0.0001	0.0259	0	0	0	0.1052	0	0	0	0	0	0.1025	0.7664	5	40	22.5	40	1	25	50	1	40	40	5	22.5	24.6	24.8	7.5
PRCME-28	-8.423	0	0.04	0	0	0	0.0107	0	0	0	0	0	0.112	0.8373	5	40	22.5	40	1	25	50	1	40	40	5	22.5	24.8	25.1	7.5
PRCME-27	-8.9662	0	0.0683	0	0.0035	0.1628	0.1974	0	0	0	0	0	0.1291	0.4388	5	40	22.5	40	1	25	50	1	40	40	5	22.5	21.6	20.3	6.1
PRCME-35	-9.2627	0.0021	0.2422	0	0	0.0043	0.1818	0	0	0	0	0	0.4435	0.1261	5	40	22.5	40	1	25	50	1	40	40	5	22.5	27.3	27.7	8.3
PRCME-36	-9.4815	0.0016	0.17	0	0	0.0017	0.1057	0	0	0	0	0	0.6403	0.0807	5	40	22.5	40	1	25	50	1	40	40	5	22.5	25.8	25.9	7.8
PRCME-37	-9.9359	0.2073	0.0467	0	0	0.007	0.1589	0	0	0	0	0	0.5103	0.0698	5	40	22.5	40	1	25	50	1	40	40	5	22.5	20.1	19.8	5.9
PRCME-38	-10.0847	0.2042	0.1021	0	0	0	0.1757	0	0	0	0	0	0.5068	0.0112	5	40	22.5	40	1	25	50	1	40	40	5	22.5	21.2	21.1	6.3
PRCME-26	-10.6551	0.1405	0.0613	0	0.0013	0	0.2003	0	0	0	0	0	0.3424	0.2541	5	40	22.5	40	1	25	50	1	40	40	5	22.5	22.1	21.5	6.5
PAT-ME	-10.7203	0.0861	0.0282	0	0	0.2415	0.1485	0	0	0	0	0	0.2874	0.2084	5	40	22.5	40	1	25	50	1	40	40	5	22.5	17.1	15.5	4.7
PRCME-25	-10.839	0.0082	0.0675	0	0	0	0.1742	0	0	0	0	0	0.2474	0.5027	5	40	22.5	40	1	25	50	1	40	40	5	22.5	24.9	25.2	7.6
PRCME-24	-11.0713	0.0059	0.1918	0	0	0.2091	0.0825	0	0	0	0	0	0.3713	0.1394	5	40	22.5	40	1	25	50	1	40	40	5	22.5	21.7	21.4	6.4
PRCME-23	-11.6083	0.0165	0.2351	0	0	0.0991	0.0519	0	0	0	0	0	0.409	0.1884	5	40	22.5	40	1	25	50	1	40	40	5	22.5	24.7	24.7	7.4
PRCME-39	-11.7923	0.0027	0.2568	0	0.0015	0.0378	0.0583	0	0	0	0	0	0.4294	0.2135	5	40	22.5	40	1	25	50	1	40	40	5	22.5	26.7	27.2	8.2
PRCME-22	-12.251	0.0671	0.257	0	0.0252	0	0.0079	0	0	0	0	0	0.4289	0.2137	5	40	22.5	40	1	25	50	1	40	40	5	22.5	26.7	27.2	8.2
PRCME-21	-12.5005	0.107	0.4509	0	0.0348	0	0.0318	0	0	0	0	0	0	0.3755	5	40	22.5	40	1	25	50	1	40	40	5	22.5	29.9	32.0	9.6
PRCME-20	-12.6652	0.079	0.289	0	0.0215	0.115	0.0255	0	0	0	0	0	0.4649	0.005	5	40	22.5	40	1	25	50	1	40	40	5	22.5	24.1	24.1	7.2
CAN2	-13.0275	0	0.1097	0	0.0012	0.0833	0.0906	0	0	0	0	0	0.6864	0.0287	5	40	22.5	40	1	25	50	1	40	40	5	22.5	22.9	22.9	6.9
PRCME-19	-13.1238	0	0.0894	0	0.0009	0.0676	0.0752	0.0002	0	0	0	0	0.5569	0.2099	5	40	22.5	40	1	25	50	1	40	40	5	22.5	23.2	23.0	6.9
PRCME-18	-13.3213	0.0014	0.1166	0	0	0	0.0176	0	0	0	0	0	0.4872	0.3773	5	40	22.5	40	1	25	50	1	40	40	5	22.5	25.3	25.6	7.7
PRCME-17	-13.465	0.0036	0.1256	0	0.0064	0.0521	0.0169	0	0	0	0	0	0.5145	0.2809	5	40	22.5	40	1	25	50	1	40	40	5	22.5	24.2	24.1	7.2
Pis11	-13.73	0.0081	0.123	0	0.0062	0.0496	0.0349	0.0002	0	0	0	0	0.4953	0.282	5	40	22.5	40	1	25	50	1	40	40	5	22.5	24.1	24.1	7.2
Pisco	-13.7274	0.0085	0.1229	0	0.0062	0.0496	0.0349	0.0002	0	0	0	0	0.4952	0.2819	5	40	22.5	40	1	25	50	1	40	40	5	22.5	24.1	24.1	7.2
PRCME-15	-14.3448	0.0047	0.0776	0	0.0228	0.0444	0.0576	0.1109	0	0	0	0	0.4377	0.2443	5	40	22.5	40	1	25	50	1	40	40	5	22.5	26.9	27.5	8.2
GRA1	-14.5173	0.0002	0.0947	0	0.0226	0	0.0518	0.0101	0	0	0	0	0.4629	0.3578	5	40	22.5	40	1	25	50	1	40	40	5	22.5	25.6	26.1	7.8
PRCME-1401	-14.6476	0.0002	0.0868	0	0.0881	0	0.0528	0.0781	0	0	0	0	0.4367	0.2573	5	40	22.5	40	1	25	50	1	40	40	5	22.5	28.3	29.3	8.8
16PE065	-14.977	0	0.0197	0	0.2266	0	0	0.0401	0	0	0	0	0.3744	0.3393	5	40	22.5	40	1	25	50	1	40	40	5	22.5	28.5	30.0	9.0
16PE064	-15.513	0.017	0.3873	0	0.2096	0	0.0269	0.0737	0	0.0053	0	0	0	0.2802	5	40	22.5	40	1	25	50	1	40	40	5	22.5	35.3	38.4	11.5
PRCME-13	-15.6286	0.0149	0.2086	0	0.1187	0	0.0582	0.0233	0	0.0014	0	0	0.3909	0.183	5	40	22.5	40	1	25	50	1	40	40	5	22.5	29.1	30.0	9.0
16PE063	-15.6717	0.0209	0.2622	0	0.0272	0.0177	0.0769	0.0063	0	0.0031	0	0	0.3799	0.1947	5	40	22.5	40	1	25	50	1	40	40	5	22.5	27.3	27.9	8.4
PRCME-12	-15.672	0.0198	0.249	0	0.0258	0.0168	0.0731	0.006	0	0.0029	0	0	0.3609	0.185	5	40	22.5	40	1	25	50	1	40	40	5	22.5	33.2	26.5	8.0
PRCME-11	-15.846	0.0265	0.5763	0	0.0009	0.0374	0.2527	0.0303	0	0.0146	0	0	0.0061	0.0553	5	40	22.5	40	1	25	50	1	40	40	5	22.5	33.2	33.6	10.1
PRCME-10	-16.226	0.0188	0.5361	0	0.1456	0	0.1931	0.0441	0	0.049	0	0	0	0.0133	5	40	22.5	40	1	25	50	1	40	40	5	22.5	36.7	36.8	11.1
16PE046	-16.2724	0	0.0134	0.0028	0.0259	0.0113	0.0711	0.0289	0	0.0046	0	0	0.7465	0.0946	5	40	22.5	40	1	25	50	1	40	40	5	22.5	24.2	24.1	7.2
16PE002	-16.3889	0.0118	0.052	0	0.3089	0.0026	0.2459	0	0	0.0686	0	0	0.2768	0.0333	5	40	22.5	40	1	25	50	1	40	40	5	22.5	30.4	30.6	9.2
PRCME-9	-16.4217	0	0.0391	0	0.1367	0.0084	0.0794	0.0031	0	0.015	0	0	0.618	0.0942	5	40	22.5	40	1	25	50	1	40	40	5	22.5	26.0	26.1	7.8
16PE003	-16.5356	0	0.0178	0	0.1506	0	0.1821	0	0	0.0329	0	0	0.3203	0.2963	5	40	22.5	40	1	25	50	1	40	40	5	22.5	27.0	27.8	8.3
PRCME-7	-16.5849	0	0.0141	0.0024	0.027	0.0098	0.1069	0.0249	0	0.0455	0	0	0.6569	0.1116	5	40	22.5	40	1	25	50	1	40	40	5	22.5	24.9	25.0	7.5
PRCME-8	-16.7192	0	0.0511	0.0001	0.047	0.0124	0.0377	0.0075	0	0.0722	0	0	0.4943	0.2753	5	40	22.5	40	1	25	50	1	40	40	5	22.5	26.0	26.4	7.9
PRCME-6	-17.0288	0	0.0564	0	0.037	0.006	0.1243	0.1088	0	0	0	0	0.3824	0.2823	5	40	22.5	40	1	25	50	1	40	40	5	22.5	27.8	28.7	8.6

1 Basic plutonic rocks (pb), Acid plutonic rocks (pa), Intermediate plutonic rocks (pi), Pyroclastics (py), Carbonate sedimentary rocks (sc), Mixed sedimentary rocks (sm), Siliciclastic sedimentary rocks (ss), Evaporites (ev), Metamorphics (mt), Acid volcanic rocks (va), Basic volcanic rocks (vb), Intermediate volcanic rocks (vi), Unconsolidated sediments (su)

2 Quartz content of each lithology is derived from Fischer et al.1984, Streckeisen 1976, Stewart 1963, Leighton and Pendexter 1962, McBride 1963

3 Quartz content of unconsolidated sediments is calculated as a weighted percentage quartz content in bedrock occuring in each catchment

Table S6, part 2: Lithological data

Name	Latitude	Percentage of lithology in each catchment[1]											Quartz content in each lithology [2]												Total quartz content	Uncertainty
	[°]	pb [%]	pa [%]	pi [%]	py [%]	sc [%]	sm [%]	ss [%]	ev [%]	mt [%]	va [%]	vb [%]	vi [%]	su [%]	pb [%]	pa [%]	pi [%]	py [%]	sc [%]	sm [%]	ss [%]	ev [%]	mt [%]	va [%]	vb [%]	vi [%]	su[3] [%]	[%]	1σ [%]
16PE040	-17.2153	0	0.0137	0	0.0055	0	0.0606	0.0018	0	0	0	0	0.2709	0.6475	5	40	22.5	40	1	25	50	1	40	40	5	22.5	24.2	24.2	7.2
PRCME-5	-17.2865	0	0.0137	0	0.0055	0	0.0606	0.0018	0	0	0	0	0.2709	0.6475	5	40	22.5	40	1	25	50	1	40	40	5	22.5	24.2	24.2	7.2
16PE013	-17.624	0	0.0381	0	0.0045	0	0.1026	0.0015	0	0	0	0	0.2336	0.6197	5	40	22.5	40	1	25	50	1	40	40	5	22.5	24.7	24.9	7.5
PRCME-3	-17.824	0	0.0055	0	0.0513	0	0.0598	0	0	0	0	0	0.2417	0.6416	5	40	22.5	40	1	25	50	1	40	40	5	22.5	24.8	25.1	7.5
16PE031	-17.8862	0	0.0018	0	0.0891	0	0.1123	0	0	0	0	0	0.2762	0.5205	5	40	22.5	40	1	25	50	1	40	40	5	22.5	25.3	25.8	7.8
16PE016	-17.9069	0	0.0634	0	0.0358	0	0.131	0	0	0	0	0	0.2272	0.5412	5	40	22.5	40	1	25	50	1	40	40	5	22.5	25.5	26.2	7.9
PRCME-401	-17.9073	0	0.0634	0	0.0358	0	0.131	0	0	0	0	0	0.2272	0.5412	5	40	22.5	40	1	25	50	1	40	40	5	22.5	25.5	26.2	7.9
PRCME-1	-18.1191	0	0.0096	0	0.2285	0	0.0687	0	0	0	0	0	0.0175	0.6758	5	40	22.5	40	1	25	50	1	40	40	5	22.5	28.1	30.6	9.2
16PE018	-18.1589	0	0.0189	0	0.0831	0	0.0861	0	0	0	0	0	0.2225	0.5893	5	40	22.5	40	1	25	50	1	40	40	5	22.5	25.6	26.3	7.9
16PE019	-18.2931	0	0.0189	0	0.0831	0	0.0861	0	0	0	0	0	0.2225	0.5893	5	40	22.5	40	1	25	50	1	40	40	5	22.5	25.6	26.3	7.9
15CL018	-18.5187	0	0	0	0.0333	0.008	0	0.0494	0	0.0047	0.6455	0	0.0511	0.208	5	40	22.5	40	1	25	50	1	40	40	5	22.5	36.0	38.5	11.5
15CL019	-18.7772	0	0	0	0.0534	0	0	0.0096	0.0161	0	0.5128	0.0525	0.0835	0.2723	5	40	22.5	40	1	25	50	1	40	40	5	22.5	31.9	34.0	10.2
15CL031	-18.951	0	0.0007	0	0.3095	0	0	0.0015	0	0	0.4622	0	0.1733	0.0527	5	40	22.5	40	1	25	50	1	40	40	5	22.5	36.2	36.8	11.0
15CL014	-19.1653	0	0	0	0.1014	0.0014	0	0.0039	0	0	0.0176	0.0672	0.1014	0.7071	5	40	22.5	40	1	25	50	1	40	40	5	22.5	24.8	25.1	7.5
15CL002	-19.5509	0	0.0287	0	0.1159	0.0153	0	0.2065	0.02	0	0.0251	0.0228	0.1016	0.4642	5	40	22.5	40	1	25	50	1	40	40	5	22.5	30.8	33.9	10.2
15CL041	-19.8835	0	0.0408	0	0.1744	0.0034	0.0073	0.0188	0	0	0.1999	0.0068	0.0907	0.4579	5	40	22.5	40	1	25	50	1	40	40	5	22.5	30.9	34.0	10.2
15CL057	-20.1191	0	0.0264	0	0.4332	0	0	0	0	0	0.0117	0	0	0.5287	5	40	22.5	40	1	25	50	1	40	40	5	22.5	31.7	35.6	10.7
15CL058	-20.2422	0	0.0331	0	0.4134	0	0.001	0.0079	0	0	0.0195	0.011	0	0.5143	5	40	22.5	40	1	25	50	1	40	40	5	22.5	31.6	35.4	10.6
15CL063	-20.69	0	0.0175	0.0001	0.1767	0.0016	0	0.0382	0.0035	0	0.0425	0.005	0.4112	0.3038	5	40	22.5	40	1	25	50	1	40	40	5	22.5	28.1	29.2	8.8
15CL069	-20.9728	0	0.0039	0	0	0.0003	0	0.7635	0	0	0.0391	0.0072	0	0.186	5	40	22.5	40	1	25	50	1	40	40	5	22.5	44.5	48.2	14.5
15CL070	-21.0985	0	0.0172	0	0	0.0022	0	0.7328	0	0.0024	0.0426	0.009	0	0.1937	5	40	22.5	40	1	25	50	1	40	40	5	22.5	43.9	47.7	14.3
15CL028	-21.4266	0	0.0492	0.0113	0.0847	0.0088	0.0077	0.285	0.0221	0.0149	0.063	0.041	0.1728	0.2391	5	40	22.5	40	1	25	50	1	40	40	5	22.5	33.1	35.2	10.6
15CL049	-21.6853	0	0.0452	0.0217	0.0585	0.0088	0.0081	0.3942	0.0006	0.0155	0.0628	0.0383	0.1388	0.2065	5	40	22.5	40	1	25	50	1	40	40	5	22.5	36.0	38.4	11.5
SAN1	-27.2	0	0.0828	0.0022	0.0657	0.0586	0.064	0.1904	0	0	0.2113	0.2118	0	0.1132	5	40	22.5	40	1	25	50	1	40	40	5	22.5	29.4	30.0	9.0
HUA12	-28.6	0	0.385	0.0632	0.01	0.0325	0.0145	0.0833	0	0.0059	0.2473	0.1013	0.0187	0.0382	5	40	22.5	40	1	25	50	1	40	40	5	22.5	33.8	34.1	10.2
HUA10	-28.7	0	0.4275	0.0083	0.0111	0.015	0.0161	0.0776	0	0.0066	0.2746	0.1	0.0206	0.0425	5	40	22.5	40	1	25	50	1	40	40	5	22.5	35.3	35.7	10.7
HUA7	-28.8	0	0.415	0	0.0177	0.0081	0.0206	0.0591	0	0.0019	0.2884	0.1581	0.0114	0.0196	5	40	22.5	40	1	25	50	1	40	40	5	22.5	33.9	34.1	10.2
HUA1	-28.99	0	0.761	0	0	0.0139	0	0.0119	0	0.0069	0.1568	0	0	0.0495	5	40	22.5	40	1	25	50	1	40	40	5	22.5	38.8	39.5	11.9
ELK1	-29.85	0	0.3822	0	0.0241	0.005	0	0.068	0	0.0086	0.4196	0	0.0682	0.0241	5	40	22.5	40	1	25	50	1	40	40	5	22.5	38.9	39.3	11.8
HUR1	-30.31	0	0.348	0	0	0.0134	0.0268	0.0502	0	0	0.1756	0.2643	0.0204	0.0022	5	40	22.5	40	1	25	50	1	40	40	5	22.5	26.0	26.0	7.8
ILL1	-31.6	0	0.2169	0.0933	0	0	0.1784	0.0105	0	0	0.2904	0.1204	0.0735	0.0166	5	40	22.5	40	1	25	50	1	40	40	5	22.5	30.0	30.1	9.0
CHO0823S	-31.61	0	0.1349	0.1256	0.0228	0.0009	0.253	0.0338	0	0.0023	0.1944	0.1481	0.0293	0.0437	5	40	22.5	40	1	25	50	1	40	40	5	22.5	27.5	27.6	8.3
CHO0820	-31.66	0	0.1357	0.1261	0.0229	0.0009	0.2527	0.0322	0	0	0.1956	0.1491	0.0295	0.0439	5	40	22.5	40	1	25	50	1	40	40	5	22.5	27.4	27.5	8.3
CHO0822S	-31.66	0	0.1641	0.1191	0	0	0.2519	0.009	0	0	0.2239	0.1628	0.0556	0.0138	5	40	22.5	40	1	25	50	1	40	40	5	22.5	27.3	27.4	8.2
CHO1	-31.69	0	0.0853	0.1322	0.0366	0.0014	0.2378	0.0363	0	0	0.2308	0.1646	0.0017	0.0549	5	40	22.5	40	1	25	50	1	40	40	5	22.5	27.0	27.2	8.2
ACO1	-32.83	0	0.0261	0	0.2689	0.0021	0.0228	0.0156	0	0	0.4788	0.0038	0.0914	0.0559	5	40	22.5	40	1	25	50	1	40	40	5	22.5	35.7	36.4	10.9
MAI1	-33.58	0	0.0162	0	0.1923	0.0803	0.1037	0.0039	0	0	0.3126	0.0254	0.0004	0.2568	5	40	22.5	40	1	25	50	1	40	40	5	22.5	30.1	31.6	9.5
CAC1	-34.21	0	0.0231	0	0.1757	0.0098	0.0616	0	0	0	0.6902	0.0012	0.0018	0.0241	5	40	22.5	40	1	25	50	1	40	40	5	22.5	37.7	38.1	11.4
TIN1	-34.68	0	0.0475	0	0.0575	0.0037	0.0633	0.0049	0	0	0.6877	0.002	0	0.119	5	40	22.5	40	1	25	50	1	40	40	5	22.5	36.4	37.9	11.4
TEN1	-34.99	0	0.0144	0	0.0197	0.0155	0.0894	0.0004	0	0	0.761	0.0022	0	0.0963	5	40	22.5	40	1	25	50	1	40	40	5	22.5	36.4	37.6	11.3
LON1	-35.18	0	0.009	0	0.0709	0	0.0175	0	0	0.0035	0.7639	0.0593	0	0.0759	5	40	22.5	40	1	25	50	1	40	40	5	22.5	36.5	37.4	11.2
MAU1	-35.73	0	0.093	0	0.0735	0.0295	0.011	0	0	0.004	0.5855	0.1725	0	0.0214	5	40	22.5	40	1	25	50	1	40	40	5	22.5	31.9	32.1	9.6

1 Basic plutonic rocks (pb), Acid plutonic rocks (pa), Intermediate plutonic rocks (pi), Pyroclastics (py), Carbonate sedimentary rocks (sc), Mixed sedimentary rocks (sm), Siliciclastic sedimentary rocks (ss), Evaporites (ev), Metamorphics (mt), Acid volcanic rocks (va), Basic volcanic rocks (vb), Intermediate volcanic rocks (vi), Unconsolidated sediments (su)

2 Quartz content of each lithology is derived from Fischer et al.1984, Streckeisen 1976, Stewart 1963, Leighton and Pendexter 1962, McBride 1963

3 Quartz content of unconsolidated sediments is calculated as a weighted percentage quartz content in bedrock occuring in each catchment

Table S7: Production rates with varying quartz content

Name	Latitude	Total quartz content in catchment	Uncertainty 1σ	Total Production rate with total quartz content	Production rate with 20% quartz	10% quartz	5% quartz	Erosion total quartz	Uncertainty 1σ	Erosion 20% quartz	Uncertainty 1σ	Erosion 10% quartz	Uncertainty 1σ	Change in erosion 20% quartz	10% quartz	5% quartz
	[°]	[%]	[%]	[at/g]	[at/g]	[at/g]	[at/g]	[m/Myr]	[m/Myr]	[m/Myr]	[m/Myr]	[m/Myr]	[m/Myr]	[%]		
PRCME-32	-6.4519	24.4	7.3	8.51	8.13	7.28	6.86	23.40	0.36	22.44	0.38	20.25	0.23	1	11	15
PRCME-33	-6.7882	16.6	5.0	10.25	10.29	9.58	9.06	32.89	1.15	33.02	0.91	30.88	0.91	0	0	5
PRCME-31	-6.9804	24.6	7.4	6.80	6.49	5.81	5.47	13.75	0.42	13.15	0.42	11.84	0.34	0	9	14
PRCME-21	-12.5005	32.0	9.6	9.65	8.49	7.53	7.05	26.42	0.98	23.46	0.85	20.98	0.59	4	15	20
CAN2	-13.0275	22.9	6.9	31.28	30.38	27.25	25.68	65.21	9.16	63.40	8.30	57.13	8.09	0	0	0
PRCME-9	-16.4217	26.1	7.8	25.81	24.23	21.65	20.36	210.66	16.15	198.54	14.86	178.63	12.79	0	2	7
PRCME-7	-16.5849	25.0	7.5	30.00	28.50	27.00	25.50	131.47	3.33	125.21	2.70	118.94	2.97	0	5	10

Table S8, part 1: Vegetation cover and relative erosion

Precipitation (P) [mm/yr]	Vegetation cover [%]	Relative Erosion (R_1)*2	Relative Erosion (R_2)*3	Relative Erosion $R_{combined}$*4
1	1.5	1.00	0.000	0.022
10	6.2	0.85	0.006	0.071
25	10.7	0.73	0.016	0.109
50	16.2	0.60	0.034	0.144
75	20.6	0.52	0.054	0.166
100	24.5	0.45	0.073	0.182
125	28.0	0.40	0.093	0.193
150	31.2	0.36	0.114	0.201
175	34.3	0.32	0.135	0.208
200	37.1	0.29	0.156	0.213
225	39.8	0.26	0.177	0.216
250	42.4	0.24	0.199	0.219
275	44.9	0.22	0.221	0.221
300	47.3	0.20	0.243	0.222
325	49.7	0.19	0.265	0.223
350	51.9	0.17	0.287	0.223
375	54.1	0.16	0.309	0.223
400	56.3	0.15	0.332	0.222
425	58.3	0.14	0.355	0.222
450	60.4	0.13	0.377	0.221
475	62.4	0.12	0.400	0.220
500	64.3	0.11	0.423	0.218
525	66.2	0.11	0.447	0.217

***1** Calculated vegetation cover based on Renard &Freimund 1994 ($V=Pxa^{\wedge b}$), where P is precipitation, a is 1.55 and b is 0.60 derived from FigureS4.

***2** Relative erosion (R_1) based on Gyssels et al. 2005 ($R_1=e^{-1.55x0.062}$).

***3** Relative erosion (R_2) based on Renard &Freimund 1994 (R2=axP^b), where P is precipitation, a is 0.82, and b is 1.09 derived from Cooper 2011.

***4** Relative erosion ($R_{combined}$) is calculated by $R_{combined} = \sqrt{(R_1 x R_2)}$

Table S8, part 2: Vegetation cover and relative erosion

Precipitation (P) [mm/yr]	Vegetation cover [%]	Relative Erosion (R_1)*2	Relative Erosion (R_2)*3	Relative Erosion $R_{combined}$*4
550	68.1	0.10	0.470	0.215
575	69.9	0.09	0.493	0.214
600	71.7	0.09	0.516	0.212
625	73.5	0.08	0.540	0.210
650	75.3	0.08	0.564	0.208
675	77.0	0.07	0.587	0.206
700	78.7	0.07	0.611	0.204
725	80.4	0.06	0.635	0.202
750	82.0	0.06	0.659	0.200
775	83.7	0.06	0.683	0.198
800	85.3	0.05	0.707	0.196
825	86.9	0.05	0.731	0.194
850	88.4	0.05	0.755	0.192
875	90.0	0.05	0.779	0.189
900	91.5	0.04	0.804	0.187
925	93.0	0.04	0.828	0.185
950	94.5	0.04	0.852	0.183
975	96.0	0.04	0.877	0.181
1000	97.5	0.04	0.901	0.179
1025	98.9	0.03	0.926	0.177
1050	100.4	0.03	0.951	0.175
1075	101.8	0.03	0.975	0.173
1100	103.2	0.03	1.000	0.170

***1** Calculated vegetation cover based on Renard &Freimund 1994 ($V=Pxa^{\wedge b}$), where P is precipitation, a is 1.55 and b is 0.60 derived from FigureS4.

***2** Relative erosion (R_1) based on Gyssels et al. 2005 ($R_1=e^{-1.55x0.062}$).

***3** Relative erosion (R_2) based on Renard &Freimund 1994 (R2=axP^b), where P is precipitation, a is 0.82, and b is 1.09 derived from Cooper 2011.

***4** Relative erosion ($R_{combined}$) is calculated by $R_{combined} = \sqrt{(R_1 x R_2)}$

4 Figures

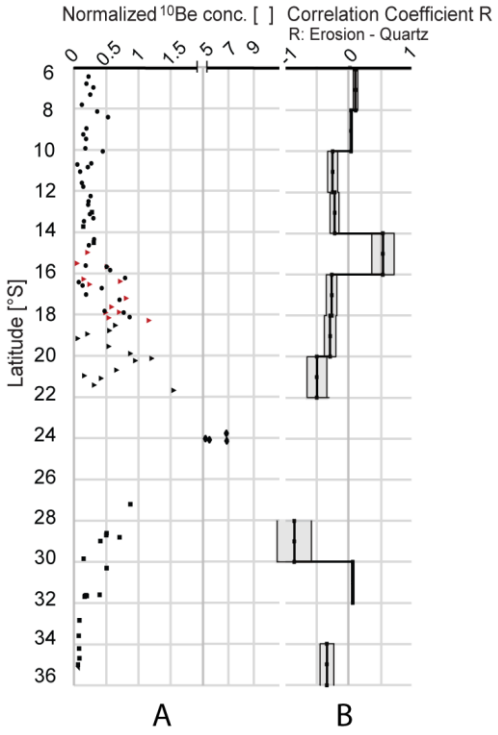

Fig. S1: Normalized ^{10}Be blank corrected concentrations are plotted versus latitude [°S]. The concentrations are normalized with the averaged ^{10}Be concentration of all catchments ($1.18 \cdot 10^6$ at $gr_{(qtz)}^{-1}$). Values of ^{10}Be concentrations vary between $6.3 \cdot 10^4$ and $1.3 \cdot 10^7$ at $gr_{(qtz)}^{-1}$ (Table S1, S2). Normalized ^{10}Be concentrations range between 0 and 10 and progressively increase and then decrease with increasing south latitude (Fig. 1B). For example, starting in the north (6°S to 12°S) values of normalized ^{10}Be concentrations are low and between 0 to 0.5. From 12°S to 20°S the values increase up to 1.5. Values reach a maximum (5 to10) between 20°S to 30°S (Fig. 1B). Further south (30°S to 36°S) concentration values then decrease and range between 0 to 0.5. (B) Correlation coefficients for erosion rate and quartz content averaged over a 2° latitudinal bin. Grey zones display the uncertainty of correlation. From 12°S to 14°S, 16°S to 22°S and 30°S to 36°S correlation coefficients show no clear correlation and vary between 0 to 0.3. Only catchments between 14°S to 16°S and 28°S to 30° S show a clear correlation. From 14°S to 16°S a positive correlation of around 0.5 occurs. Negative correlations of about -0.75 can be found from 28°S to 30°S.

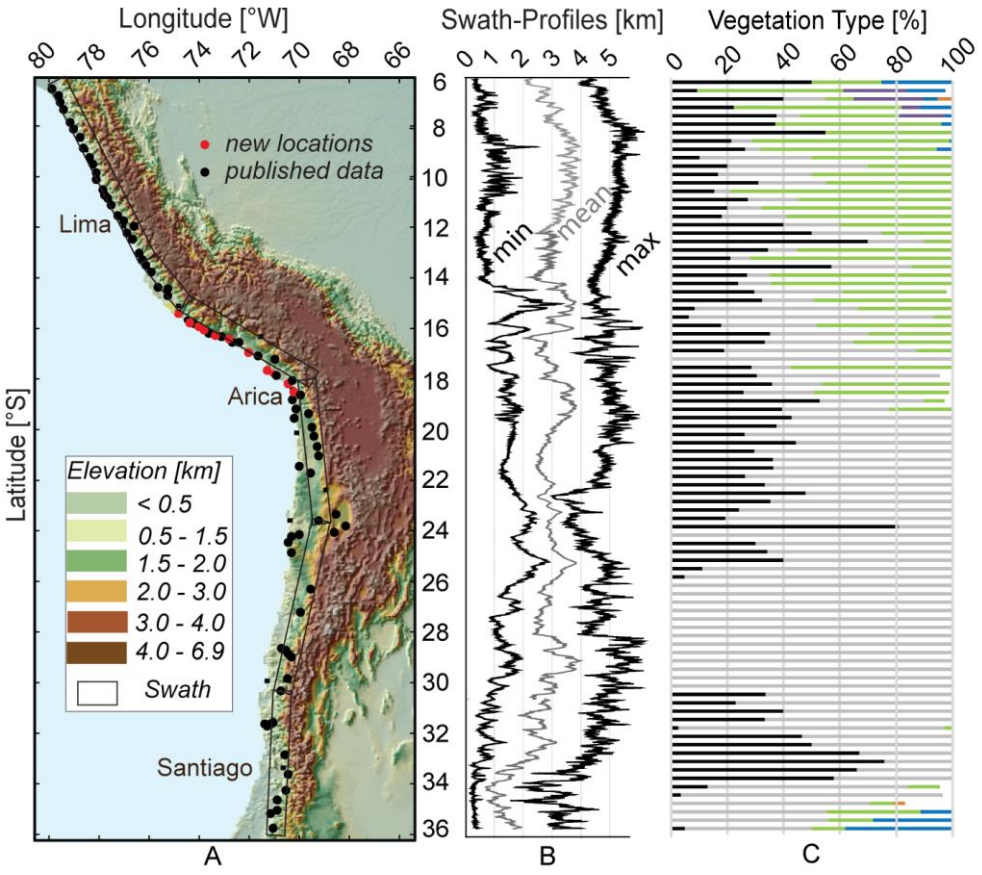

Fig. S2: Latitudinal distribution of relief and vegetation type. (A) Topographic map showing cosmogenic nuclide sample positions. (B) Swath-profiles plotted versus latitude. Swath-profiles have a 100km radius and illustrate from left to right, minimum, mean and maximum elevation. (C) Vegetation type is plotted versus latitude and classified in percent distribution across a 100km latitudinal profile in the Andean Western Cordillera. Grey lines represent barren or sparsely vegetated areas. Black lines show open shrublands. Green lines are grasslands. Purple lines are woody savannas. Blue lines are mixed forests and orange lines are evergreen forest. Values are derived from Modis landcover data (41).

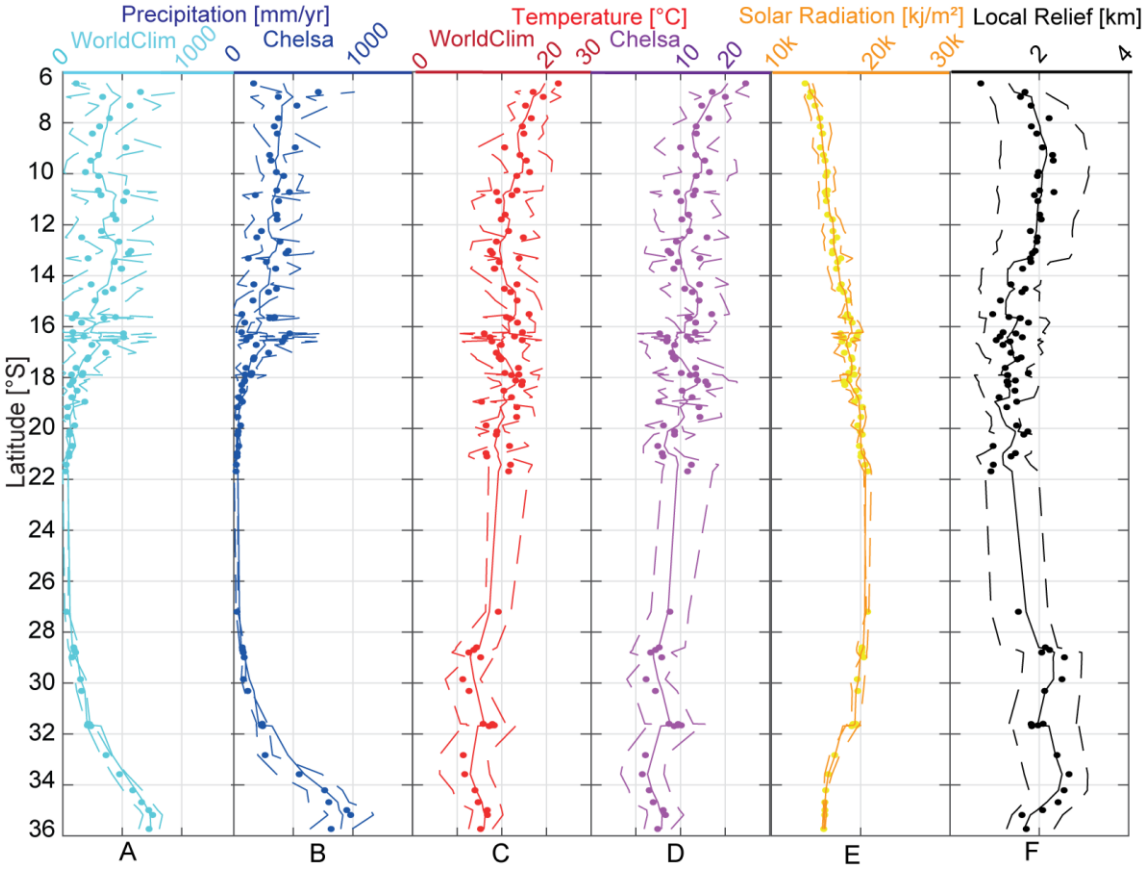

Fig. S3: Comparison of different climatic parameters plotted versus latitude and used in the factor analysis. The solid lines display the three-point moving average of the mean and the dashed lines the 2σ standard deviation from the mean value (A) Mean annual precipitation derived from WorldClim (42). (B) Mean annual precipitation derived from Chelsa (43). (C) Mean annual temperature derived from WorldClim (42). (D) Mean annual temperature derived from Chelsa (43). (E) Mean annual solar radiation derived from WorldClim (42). (F) Mean local relief of 10km radius derived from a 90m DEM.

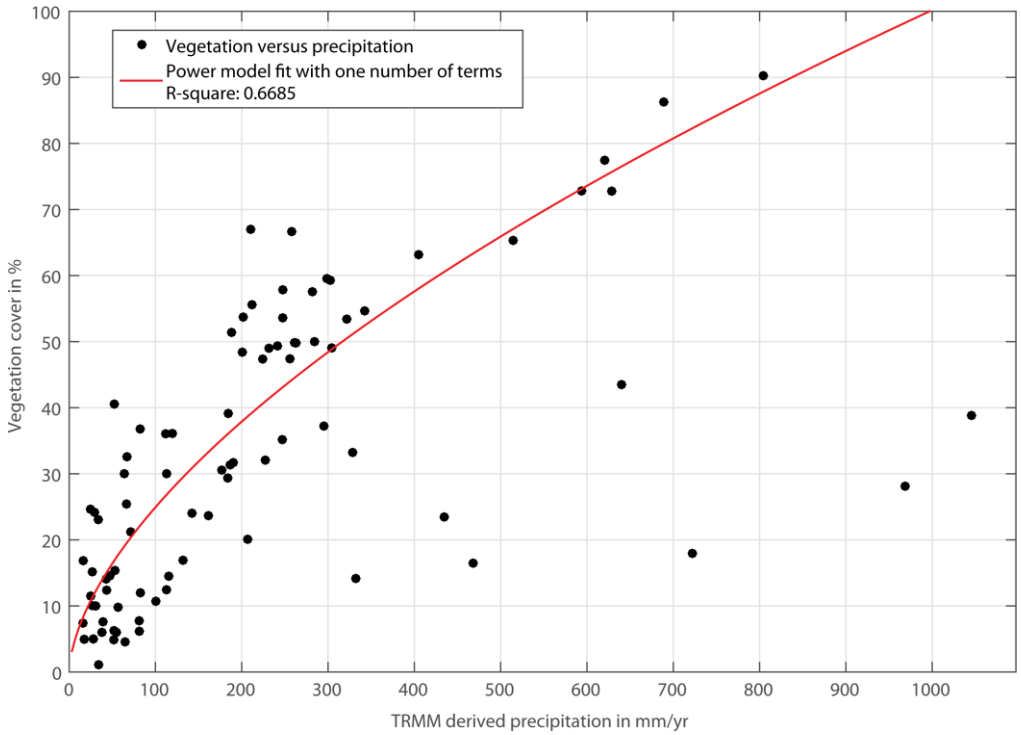

Fig S4: Mean annual precipitation derived from TRMM data plotted versus vegetation cover. A power model fit with one number of terms (f(x) = a*x^ b). Coefficients with 95% confidence bounds: a= 1.545 (0.7671, 2.324) b= 0.6039 (0.5198, 0.688)) have been added as a red line. The goodness of fit is SSE:1.33e+04, R-square: 0.6685, Adjusted R-square: 0.6646 and RMSE: 12.58. The figure shows that with increasing precipitation (>200 mm/yr) the relationship between vegetation cover and precipitation becomes more diverse and the fit of the regression model decreases.

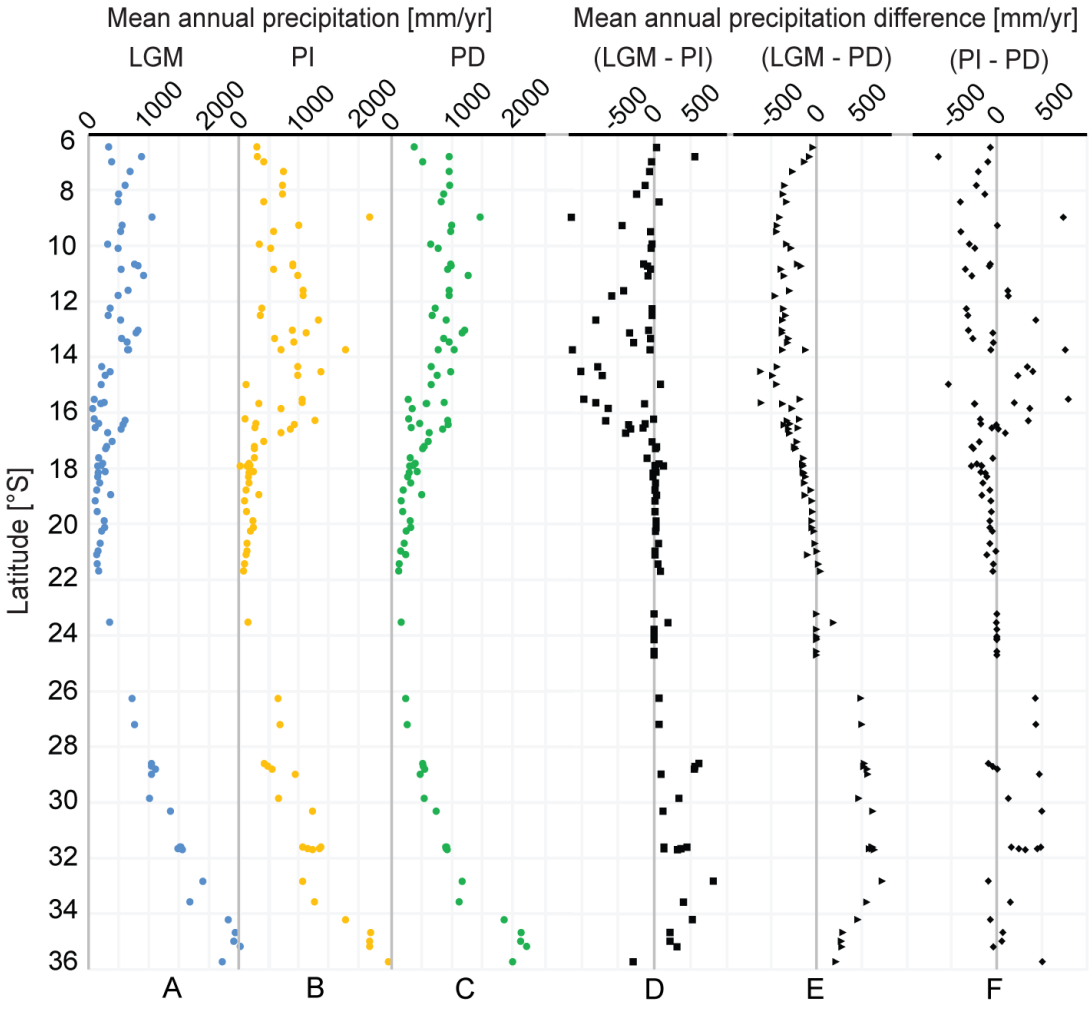

Fig S5: Comparison of predicted precipitation and precipitation differences for different time slices along the western Andean margin. Results were calculated for the Last Glacial Maximum (LGM), Present Day (PD), and Pre-Industrial (PI) conditions with the ECHAM5 global atmospheric general circulation model at a spectral resolution of T159 (~80x80 km)(66). Precipitation rates (A-C) were extracted from the ECHAM simulations (66) for the location of each catchment (Fig. 1 main text). For the precipitation differences (D-F), positive values highlight regions with wetter conditions and negative values indicate regions with dryer conditions relative to the PI simulation. **(A)** Mean annual ECHAM5 predicted precipitation during the LGM. **(B)** Predicted mean annual precipitation during the PI. **(C)** Predicted mean annual precipitation of the PD. **(D)** Mean annual precipitation difference between the LGM and PI from ECHAM5. **(E)** Mean annual precipitation difference between LGM and PD from ECHAM5. **(F)** Mean annual precipitation difference between PI and PD from ECHAM5. LGM mean annual precipitation is included because the apparent ages for the cosmogenic radionuclide data (Table S3) are typically on the order of 10^4 years and cover one or more glacial-interglacial cycles. Based on the similarity in the latitudinal gradient of modern and paleo precipitation gradients with latitude (e.g. compare A, B) the calculated correlation between modern precipitation and erosion rate (Fig. 2D, main text) is not expected to be different when paleoprecipitation is considered. The results indicate that the latitudinal gradient of paleoprecipitation (and hence paleovegetation gradient influenced by precipitation) would not have varied significantly from recent (PD) conditions.

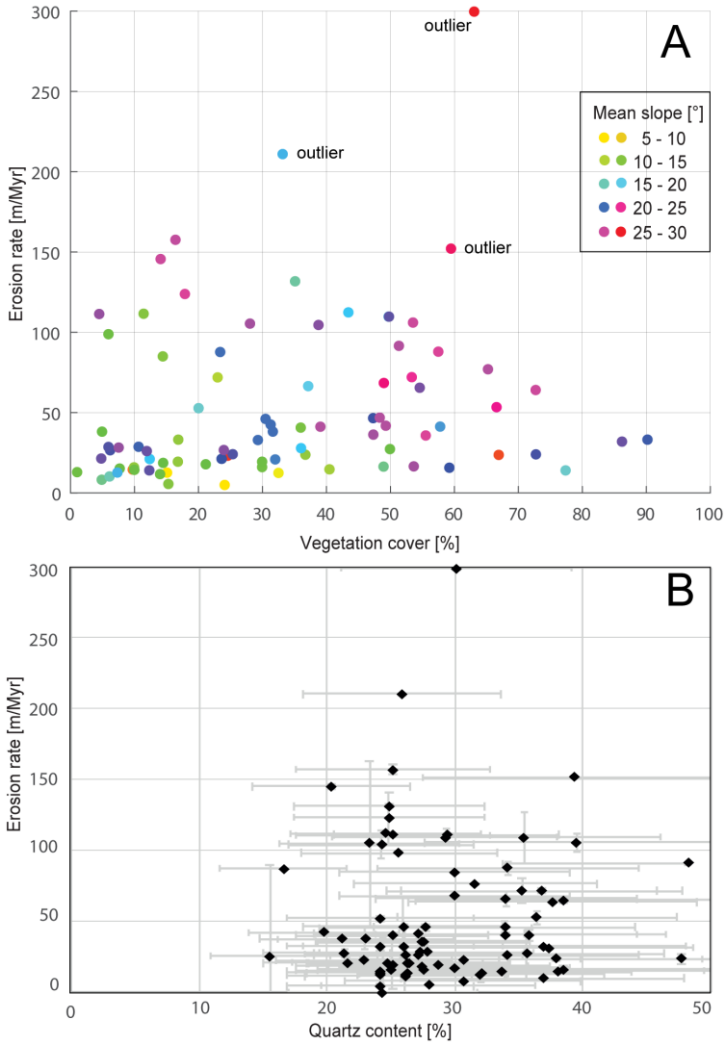

Fig S6: Observed relationship between erosion rate, vegetation cover and mean slope. Erosion rates plotted versus vegetation cover in dots. The dots are color coded according to mean slope that are shown in Fig. 2. Outliers most likely result from glacier remnants (29). The figure highlights that with an increasing vegetation cover (>50%) slopes are stabilized and steeper compared to mean slopes within the transition and abiotic zone. (B) Observed relation between erosion rate and total quartz content for each catchment. Grey bars display the uncertainty.

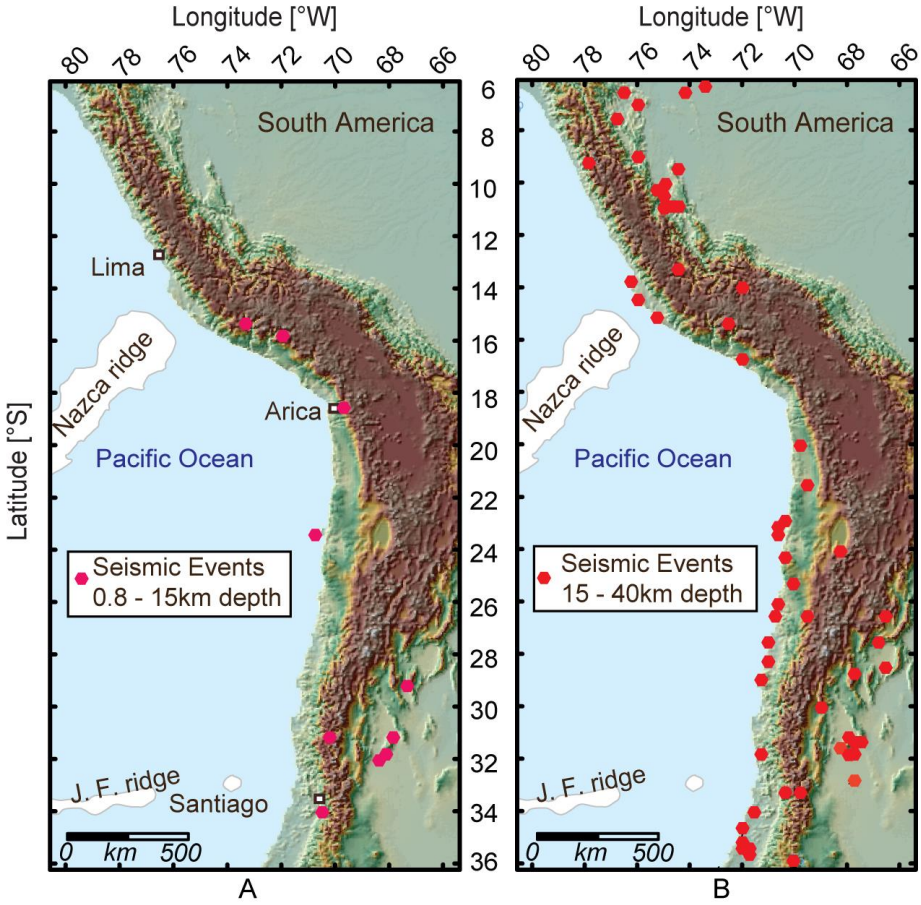

Fig. S7: (A) Distribution of shallow seismic events in South America that occur in 0.8 to 15km depth. Earthquakes of at least magnitude 5 have been considered. The data are derived from the USGS Earthquake Data and display earthquakes from 1973 to 2015. (B) Distribution of shallow seismic events in South America that occur in 15 to 40km depth. Earthquakes of at least magnitude 5 have been considered. The data are derived from the USGS Earthquake Data and display earthquakes from 1973 to 2015.

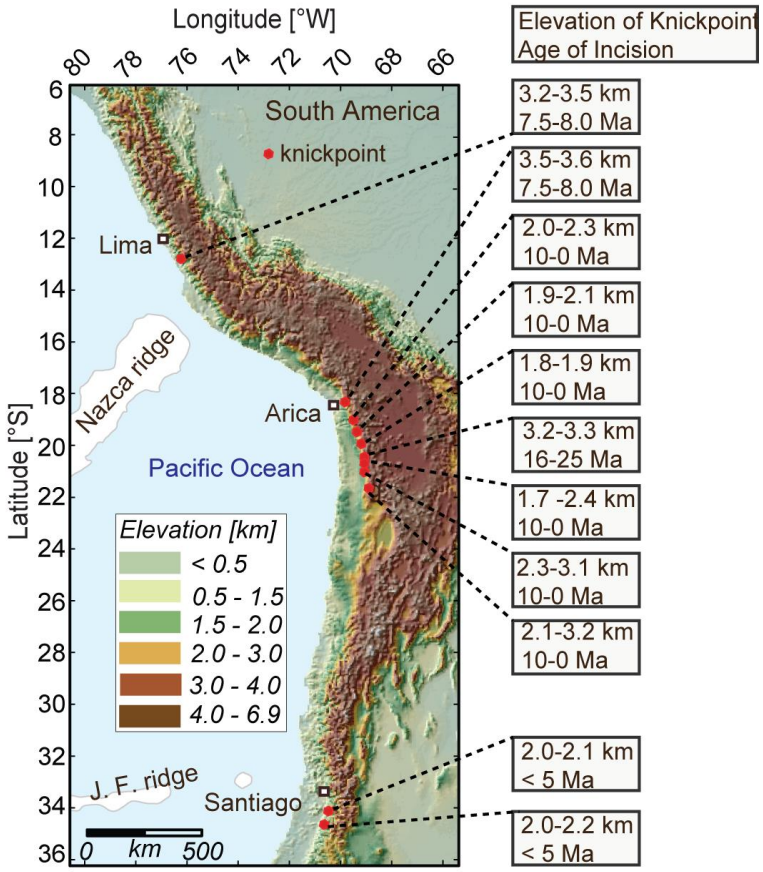

Fig. S8: Elevation of knickpoints and age of river incision from catchments draining the Western Cordillera. Data is derived from Kober et al. (19), Schlunegger et al. (88), Hoke et al. (90), Farías et al. (89), Abbühl et al. (77), Cooper et al. (87).

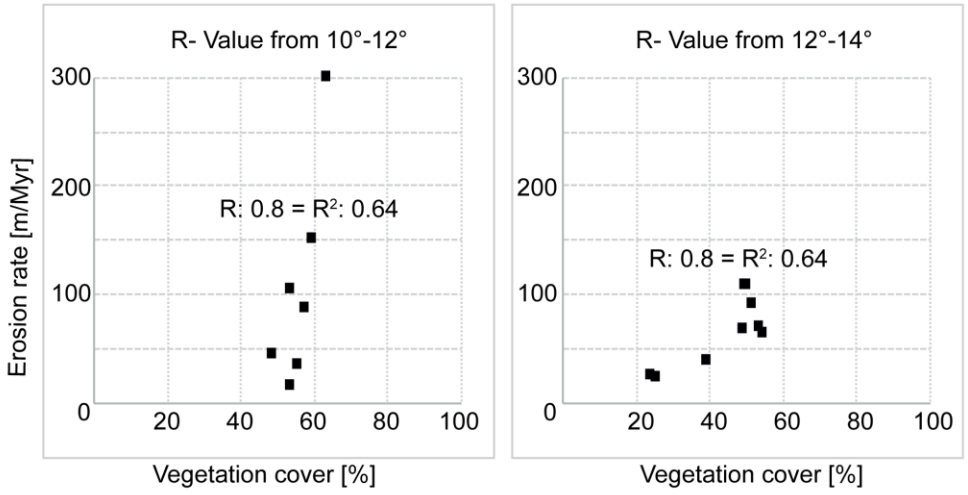

Fig. S9: Comparison of detailed R-values within the latitudinal bins of 10° to 12° and 12°to 14°. Montecarlo-derived uncertainties are not displayed.

Bibliography

1. D. W. Schwartzman, T. Volk, Biotic enhancement of weathering and the habitability of Earth. Nature. 340, 457–460 (1989).
2. R. A. Berner, The Rise of Plants and Their Effect on Weathering and Atmospheric CO2. Science. 276, 544–546 (1997).
3. G. J. Retallack, Early Forest Soils and Their Role in Devonian Global Change. Science. 276, 583–585 (1997).
4. L. A. Derry, Fungi, Weathering, and the Emergence of Animals. Science. 311, 1386–1387 (2006).
5. W. E. Dietrich, J. T. Perron, The search for a topographic signature of life. Nature. 439, 411–418 (2006).
6. A. Stokes et al., in Slope Stability and Erosion Control: Ecotechnological Solutions, J. E. Norris et al., Eds. (Springer Netherlands, 2008; http://link.springer.com/chapter/10.1007/978-1-4020-6676-4_4), pp. 65–118.
7. A. Dosseto, P. P. Hesse, K. Maher, K. Fryirs, S. Turner, Climatic and vegetation control on sediment dynamics during the last glacial cycle. Geology. 38, 395–398 (2010).
8. R. Buitenwerf, L. Rose, S. I. Higgins, Three decades of multi-dimensional change in global leaf phenology. Nat. Clim. Chang. 5, 364–368 (2015).
9. V. Galy, B. Peucker-Ehrenbrink, T. Eglinton, Global carbon export from the terrestrial biosphere controlled by erosion. Nature (2015), doi:10.1038/nature14400.
10. S. Wang et al., Reduced sediment transport in the Yellow River due to anthropogenic changes. Nat. Geosci. 9, 38–+ (2016).
11. A. Ganopolski, C. Kubatzki, M. Claussen, V. Brovkin, V. Petoukhov, The Influence of Vegetation-Atmosphere-Ocean Interaction on Climate During the Mid-Holocene. Science. 280, 1916–1919 (1998).
12. R. D. Alward, J. K. Detling, D. G. Milchunas, Grassland Vegetation Changes and Nocturnal Global Warming. Science. 283, 229–231 (1999).
13. N. Zeng, J. D. Neelin, K.-M. Lau, C. J. Tucker, Enhancement of Interdecadal Climate Variability in the Sahel by Vegetation Interaction. Science. 286, 1537–1540 (1999).
14. N. Zeng, K. Hales, J. D. Neelin, Nonlinear Dynamics in a Coupled Vegetation–Atmosphere System and Implications for Desert–Forest Gradient. J. Climate. 15, 3474–3487 (2002).
15. J. K. Willenbring, F. von Blanckenburg, Long-term stability of global erosion rates and weathering during late-Cenozoic cooling. Nature. 465, 211–214 (2010).
16. D. E. Granger, M. Schaller, Cosmogenic Nuclides and Erosion at the Watershed Scale. Elements. 10, 369–373 (2014).
17. F. von Blanckenburg, J. K. Willenbring, Cosmogenic Nuclides: Dates and Rates of Earth-Surface Change. Elements. 10, 341–346 (2014).
18. K. Nishiizumi, M. W. Caffee, R. C. Finkel, G. Brimhall, T. Mote, Remnants of a fossil alluvial fan landscape of Miocene age in the Atacama Desert of northern Chile using cosmogenic nuclide exposure age dating. Earth and Planetary Science Letters. 237, 499–507 (2005).
19. F. Kober et al., Complex multiple cosmogenic nuclide concentration and histories in the arid Rio Lluta catchment, northern Chile. Earth Surf. Process. Landforms. 34, 398–412 (2009).

20. L. M. Abbühl et al., El Niño forcing on 10Be-based surface denudation rates in the northwestern Peruvian Andes? Geomorphology. 123, 257–268 (2010).

21. L. M. Abbühl et al., Corrigendum to "El Niño forcing on 10Be-based surface denudation rates in the northwestern Peruvian Andes?" [Geomorphology 123 (2010) 257–268]. Geomorphology. 129, 417 (2011).

22. C. J. Placzek, A. Matmon, D. E. Granger, J. Quade, S. Niedermann, Evidence for active landscape evolution in the hyperarid Atacama from multiple terrestrial cosmogenic nuclides. Earth and Planetary Science Letters. 295, 12–20 (2010).

23. M. C. Jungers et al., Active erosion–deposition cycles in the hyperarid Atacama Desert of Northern Chile. Earth and Planetary Science Letters. 371–372, 125–133 (2013).

24. D. McPhillips, P. R. Bierman, T. Crocker, D. H. Rood, J. Geophys. Res. Earth Surf., in press, doi:10.1002/2013JF002837.

25. G. Aguilar et al., Grain size-dependent 10Be concentrations in alluvial stream sediment of the Huasco Valley, a semi-arid Andes region. Quaternary Geochronology. 19, 163–172 (2014).

26. S. Carretier et al., Slope and climate variability control of erosion in the Andes of central Chile. Geology. 41, 195–198 (2013).

27. S. Carretier et al., Erosion in the Chilean Andes between 27 S and 39 S: tectonic, climatic and geomorphic control. Geological Society, London, Special Publications. 399, 401–418 (2015).

28. S. Carretier et al., A note on 10Be-derived mean erosion rates in catchments with heterogeneous lithology: examples from the western Central Andes. Earth Surf. Process. Landforms. 40, 1719– 1729 (2015).

29. R. Reber et al., Environmental controls on 10Be-based catchment-averaged denudation rates along the western margin of the Peruvian Andes. Terra Nova. 29, 282–293 (2017).

30. J. Starke, T. A. Ehlers, M. Schaller, Tectonic and Climatic Controls on the Spatial Distribution of Denudation Rates in Northern Chile (18°S to 23°S) Determined From Cosmogenic Nuclides: 10 Be Denudation Rates in Northern Chile. Journal of Geophysical Research: Earth Surface (2017), doi:10.1002/2016JF004153.

31. M. C. Peel, B. L. Finlayson, T. A. Mcmahon, Updated world map of the Köppen-Geiger climate classification. Hydrology and Earth System Sciences Discussions. 4, 439–473 (2007).

32. S. Rivas Martínez, G. Navarro Sánchez, Á. Penas Merino, M. Costa Talens, Biogeographic Map of South America. An initial advance. International Journal of Geobotanical Research. 1, 21–40 (2011).

33. J. Chmeleff, F. von Blanckenburg, K. Kossert, D. Jakob, Determination of the 10Be half-life by multicollector ICP-MS and liquid scintillation counting. Nuclear Instruments and Methods in Physics Research Section B: Beam Interactions with Materials and Atoms. 268, 192–199 (2010).

34. T. J. Dunai, Scaling factors for production rates of in situ produced cosmogenic nuclides: a critical reevaluation. Earth and Planetary Science Letters. 176, 157–169 (2000).

35. J. Dunne, D. Elmore, P. Muzikar, Scaling factors for the rates of production of cosmogenic nuclides for geometric shielding and attenuation at depth on sloped surfaces. Geomorphology. 27, 3–11 (1999).

36. K. P. Norton, V. Vanacker, Effects of terrain smoothing on topographic shielding correction factors for cosmogenic nuclide-derived estimates of basin-averaged denudation rates. Earth Surf. Process. Landforms. 34, 145–154 (2009).

37. F. M. Phillips et al., CRONUS-Earth calibration samples from the Huancané II moraines, Quelccaya Ice Cap, Peru. Quaternary Geochronology. 31, 220–236 (2016).

38. R. Braucher, S. Merchel, J. Borgomano, D. L. Bourlès, Production of cosmogenic radionuclides at great depth: A multi element approach. Earth and Planetary Science Letters. 309, 1–9 (2011).

39. USGS, Shuttle Radar Topography Mission. 3 Arc Second scene SRTM_u03_n008e004, Unfilled Unfinished 2.0, Global Land Cover Facility, University of Maryland, Collage Park, Maryland. (2000), (available at http://glcf.umd.edu/data/srtm/).

40. B. Bookhagen, High resolution spatiotemporal distribution of rainfall seasonality and extreme events based on a 12-year TRMM~ time series (submitted for publication) (2013), (available at http://www.geog.ucsb.edu/ bodo/TRMM/).

41. P. D. Broxton, X. Zeng, W. Scheftic, P. A. Troch, A MODIS-Based Global 1-km Maximum Green Vegetation Fraction Dataset. J. Appl. Meteor. Climatol. 53, 1996–2004 (2014).

42. S. E. Fick, R. J. Hijmans, WorldClim 2: new 1-km spatial resolution climate surfaces for global land areas: NEW CLIMATE SURFACES FOR GLOBAL LAND AREAS. International Journal of Climatology (2017), doi:10.1002/joc.5086.

43. D. N. Karger et al., Climatologies at high resolution for the earth's land surface areas. Scientific Data. 4, sdata2017122 (2017).

44. M. A. Nearing et al., Modeling response of soil erosion and runoff to changes in precipitation and cover. CATENA. 61, 131–154 (2005).

45. H. Wulf, B. Bookhagen, D. Scherler, Climatic and geologic controls on suspended sediment flux in the Sutlej River Valley, western Himalaya. Hydrology and Earth System Sciences. 16, 2193–2217 (2012).

46. W. B. Langbein, S. A. Schumm, Yield of sediment in relation to mean annual precipitation. Eos Trans. AGU. 39, 1076–1084 (1958).

47. I. P. Prosser, W. E. Dietrich, Field Experiments on Erosion by Overland Flow and Their Implication for a Digital Terrain Model of Channel Initiation. Water Resources Research, 2867–2876 (1995).

48. G. Gyssels, J. Poesen, E. Bochet, Y. Li, Impact of plant roots on the resistance of soils to erosion by water: a review. Progress in Physical Geography. 29, 189–217 (2005).

49. D. R. Montgomery, M. T. Brandon, Topographic controls on erosion rates in tectonically active mountain ranges. Earth and Planetary Science Letters. 201, 481–489 (2002).

50. J. Wainwright, A. J. Parsons, A. D. Abrahams, Plot-scale studies of vegetation, overland flow and erosion interactions: case studies from Arizona and New Mexico. Hydrol. Process. 14, 2921–2943 (2000).

51. R. P. C. Morgan, R. J. Rickson, Slope Stabilization and Erosion Control: A Bioengineering Approach (Taylor & Francis, 2003).

52. E. Nadal-Romero, K. Petrlic, E. Verachtert, E. Bochet, J. Poesen, Effects of slope angle and aspect on plant cover and species richness in a humid Mediterranean badland: TOPOGRAPHY-INDUCED PATTERNS OF VEGETATION IN A HUMID BADLAND AREA. Earth Surface Processes and Landforms. 39, 1705–1716 (2014).

53. D. B. G. Collins, Modeling the effects of vegetation-erosion coupling on landscape evolution. Journal of Geophysical Research. 109 (2004), doi:10.1029/2003JF000028.

54. E. Istanbulluoglu, D. G. Tarboton, R. T. Pack, C. H. Luce, Modeling of the interactions between forest vegetation, disturbances, and sediment yields: MODELING FOREST-EROSION INTERACTIONS. Journal of Geophysical Research: Earth Surface. 109 (2004), doi:10.1029/2003JF000041.

55. E. Istanbulluoglu, R. L. Bras, Vegetation-modulated landscape evolution: Effects of vegetation on landscape processes, drainage density, and topography. J. Geophys. Res. 110, F02012 (2005).

56. E. Istanbulluoglu, O. Yetemen, E. R. Vivoni, H. A. Gutiérrez-Jurado, R. L. Bras, Eco-geomorphic implications of hillslope aspect: Inferences from analysis of landscape morphology in central New Mexico. Geophys. Res. Lett. 35, L14403 (2008).

57. V. T. Acosta et al., Effect of vegetation cover on millennial-scale landscape denudation rates in East Africa. Lithosphere. 7, 408–420 (2015).

58. S. M. Olen, B. Bookhagen, M. R. Strecker, Role of climate and vegetation density in modulating denudation rates in the Himalaya. Earth and Planetary Science Letters. 445, 57–67 (2016).

59. J. B. Barnes, T. A. Ehlers, End member models for Andean Plateau uplift. Earth-Science Reviews. 97, 105–132 (2009).

60. B. L. Isacks, Uplift of the Central Andean Plateau and bending of the Bolivian Orocline. J. Geophys. Res. 93, 3211–3231 (1988).

61. S. Lamb, L. Hoke, Origin of the high plateau in the central Andes, Bolivia, South America. Tectonics. 16, 623–649 (1997).

62. G. Wörner, K. Hammerschmidt, F. Henjes-Kunst, J. Lezaun, H. Wilke, Geochronology (40Ar/39Ar, K-Ar and He-exposure ages) of Cenozoic magmatic rocks from Northern Chile (18-22°S): implications for magmatism and tectonic evolution of the central Andes. Revista geológica de Chile. 27, 205–240 (2000).

63. T. E. Jordan et al., Uplift of the Altiplano-Puna plateau: A view from the west. Tectonics. 29, TC5007 (2010).

64. L. Audin et al., Geomorphological markers of faulting and neotectonic activity along the western Andean margin, northern Chile. J. Quaternary Sci. 18, 681–694 (2003).

65. C. Benavente et al., Tectonics, in press, doi:10.1002/2017TC004523.

66. Mutz, S.G., Ehlers, T.A., Werner, M., Lohmann, G., Stepanek, C., Li, J., (2017), Where is Late Cenozoic climate change most likely to impact denudation? Earth Surface Dynamics. doi: doi.org/10.5194/esurf-2017-47.

67. F. von Blanckenburg, The control mechanisms of erosion and weathering at basin scale from cosmogenic nuclides in river sediment. Earth Planet. Sci. Lett. 237, 462–479 (2005).

68. G. Korschinek et al., A new value for the half-life of 10Be by Heavy-Ion Elastic Recoil Detection and liquid scintillation counting. Nuclear Instruments and Methods in Physics Research Section B: Beam Interactions with Materials and Atoms. 268, 187–191 (2010).

69. G. Balco, G. S. Soreghan, D. E. Sweet, K. R. Marra, P. R. Bierman, Cosmogenic-nuclide burial ages for Pleistocene sedimentary fill in Unaweep Canyon, Colorado, USA. Quaternary Geochronology. 18, 149–157 (2013).

70. W. Schwanghart, D. Scherler, Short Communication: TopoToolbox 2 – MATLAB-based software for topographic analysis and modeling in Earth surface sciences. Earth Surface Dynamics. 2, 1–7 (2014).

71. K. Hartmann, B. Wünnemann, Hydrological changes and Holocene climate variations in NW China, inferred from lake sediments of Juyanze palaeolake by factor analyses. Quaternary International. 194, 28–44 (2009).

72. H. F. Kaiser, The varimax criterion for analytic rotation in factor analysis. Psychometrika. 23, 187–200.

73. L. R. Tucker, C. Lewis, A reliability coefficient for maximum likelihood factor analysis. Psychometrika. 38, 1–10.

74. M. Knott, D. J. Bartholomew, Latent variable models and factor analysis (Edward Arnold, London, UK, 1999; http://www.hoddereducation.co.uk).

75. R. A. Reyment, K. G. Jvreskog, Applied Factor Analysis in the Natural Sciences (Cambridge University Press, 1996).

76. S. Mahadevan, Monte carlo simulation (1997), MECHANICAL ENGINEERING-NEW YORK AND BASEL-MARCEL DEKKER.

77. L. M. Abbühl *et al.*, Erosion rates and mechanisms of knickzone retreat inferred from 10Be measured across strong climate gradients on the northern and central Andes Western Escarpment: ESCARPMENT RETREAT IN THE WESTERN ANDES. *Earth Surface Processes and Landforms*. **36**, 1464–1473 (2011).

78. R. O. Lease, T. A. Ehlers, Incision into the Eastern Andean Plateau During Pliocene Cooling. *Science*. **341**, 774–776 (2013).

79. J. Hartmann, N. Moosdorf, The new global lithological map database GLiM: A representation of rock properties at the Earth surface: TECHNICAL BRIEF. *Geochemistry, Geophysics, Geosystems*. **13** (2012), doi:10/gdm38k.

80. M. Schmid, T. A. Ehlers, C. Werner, T. Hickler, J. P. Fuentes-Espoz, Effect of changing vegetation on denudation: Landscape response to transient climate and vegetation cover. (2018).

81. M. G. Wolman, R. Gerson, Relative scales of time and effectiveness of climate in watershed geomorphology. *Earth Surface Processes*. **3**, 189–208.

82. L. J. Slater, M. B. Singer, Imprint of climate and climate change in alluvial riverbeds: Continental United States, 1950-2011. *Geology*. **41**, 595–598 (2013).

83. G. E. Tucker, R. L. Bras, A stochastic approach to modeling the role of rainfall variability in drainage basin evolution. *Water Resources Research*. **36**, 1953–1964.

84. J. T. Perron, Climate and the Pace of Erosional Landscape Evolution. *Annual Review of Earth and Planetary Sciences*. **45**, 561–591 (2017).

85. D. B. G. Collins, R. L. Bras, Climatic control of sediment yield in dry lands following climate and land cover change. *Water Resources Research*. **44**, doi:10.1029/2007WR006474.

86. K. G. Renard and J. R. Freimund, Using monthly precipitation data to estimate the R-factor in the revised USLE. *Journal of Hydrology* 157, 287–306 (1994). doi:10.1016/0022-1694(94)90110-4.

87. K. Cooper. Evaluation of the Relationship between the Rusle R-Factor and mean annual precipitation (2011).

88. Schlunegger, F., Zeilinger, G., Kounov, A., Kober, F., and Hüsser, B. (2006). Scale of relief growth in the forearc of the Andes of Northern Chile (Arica latitude, 18°S). *Terra Nova* 18, 217–223. doi:10.1111/j.1365-3121.2006.00682.x.

89. Farías, M., Charrier, R., Carretier, S., Martinod, J., Fock, A., Campbell, D., et al. (2008). Late Miocene high and rapid surface uplift and its erosional response in the Andes of central Chile (33°-35°S): UPLIFT AND EROSION IN CENTRAL CHILE ANDES. *Tectonics* 27, n/a-n/a. doi:10/dc9z9f.

90. Hoke, G. D., Isacks, B. L., Jordan, T. E., Blanco, N., Tomlinson, A. J., and Ramezani, J. (2007). Geomorphic evidence for post-10 Ma uplift of the western flank of the central Andes 18°30′-22°S: LATE MIOCENE UPLIFT IN NORTHERN CHILE. *Tectonics* 26, n/a-n/a. doi:10.1029/2006TC002082.

Paper III

Vegetation influence on Holocene catchment-wide erosion rates in northern Patagonia (Chile) determined from cosmogenic radionuclides

Jessica Starke[1], Todd A. Ehlers[1] and Mirjam Schaller[1]

[1]Department of Geosciences, Eberhard Karls University Tübingen, 72074 Tübingen, Germany

In preparation and close to submission.

Key Points

- Analyzing the influence of glacier cover and timing of deglaciation on Holocene catchment-wide erosion rates
- Significant correlation of catchment-wide erosion rates with vegetation cover

Abstract

The presence of the Northern Patagonian Ice Field (NPI) results in a strong glacial impact on Patagonian topography. In the region surrounding the NPI, deep incised U-shaped valleys exist and are infilled with sediment. In situ-produced cosmogenic ^{10}Be is widely used to derive catchment-wide erosion rates. However, in the region of the NPI the influence of post-glacial erosional processes on catchment-wide erosion rates remains unclear. Here, we report 21 new ^{10}Be and 19 new ^{26}Al concentrations from river sediments in six catchments spanning from ~43° to 47°S latitude. Apparent ages of samples are ranging from 0.4 to 3.3 ka and represent catchment erosion after deglaciation. Erosion rates (ranging from 0.3 to 0.9 mm/yr) derived from ^{10}Be concentrations show a decrease in erosion rates with decreasing latitude. Comparison of erosion rates with different topographic metrics (e.g. relief, slope, normalized steepness) and vegetation cover indicate the strongest correlation (R^2=0.7) between erosion rates and vegetation cover, whereby southern catchments with low vegetation cover show higher erosion rates than northern catchments without glacier cover and higher vegetation cover. Potential effects on erosion rates by long wavelength tectonic (slab window) processes or local variations in rock uplift are not

visible. Analysis of erosion rates in different grain sizes from the catchments indicates grain size effects on erosion rates caused by differences in transport distance in the river channel.

1 Introduction

The evolution of mountain landscapes and topography is highly dependent on the spatial variability of erosion. In contrast to purely fluvial settings, the identification of Holocene erosion rates is more complex in glaciated and post-glaciated environments (Koppes et al., 2015; Adams and Ehlers, 2018). Glacial and post-glacial impact on orogen erosion can occur by non-uniform erosion in catchments shaped by glaciers (Stock et al., 2006; Stock et al., 2009) or by the control of sediment distribution on postglacial fluvial dynamics (Norton et al., 2010; Hobbley et al., 2010). Boundary conditions for hillslope erosion can be set by post-glacial trunk streams that erode or aggrade and modify tributary catchments (Burbank et al., 1996; Whipple, 2004).

The Patagonian Andes (38°S to 53°S) in southern Chile are subject to glaciation since approximately 7 Ma (Warren and Sugden, 1993). At present, the Northern Patagonian Ice Field (NPI) is one of the largest ice fields of the temperate zone in the Southern Hemisphere with a surface area of about 4200km^2 and 28 outlet glaciers (Warren and Sugden, 1993). The presence of the NPI results in a strong glacial and post-glacial impact on landscape change and orogen erosion in the Patagonian Andes.

Previous studies have identified the northern and southern Patagonian glacial chronology by means of geochronological methods (e.g. sediment facies, cosmogenic nuclides or luminescence dating) (Glasser and Hambrey, 2002; Ackert et al., 2003; Kaplan et al., 2004; Glasser et al., 2005; Glasser et al., 2006; Kaplan et al., 2007; Ackert et al., 2008; Kaplan et al., 2008; Hein et al., 2009a; Hein et al., 2009b; Hein et al., 2010; Kaplan et al., 2011, Darvill et al,. 2016a; Darvill et al., 2016b; Henríquez et al., 2017). Glacial erosion has been derived from sediment budget of outlet glaciers (45° to 55°S west or south of the NPI) and ranges from 0.1 to 10 mm/yr (Koppes and Montgomery, 2009; Koppes et al., 2009; Koppes et al., 2015). Erosion rates deduced from thermochronological data (e.g. fission track) vary between 0.1 to 1.1 mm/yr and have been documented by for example Thomson et al. (2001), Adriasola et al. (2006), Thomson et al. (2010) and Fernandez et al. (2016). Holocene erosion rates for the Patagonian Andes have been only reported by Breuer et al. (2013) and are identified from lake sediment budgets at 53°S. These Holocene erosion rates vary from 0.08 mm/kyr in the high elevated catchments of granitic rocks to 9.91 mm/kyr in the low vegetated catchments of sedimentary rocks. However, Holocene post-glacial catchment-wide erosion rates derived from cosmogenic ^{10}Be are not reported for the regions adjacent to NPI.

Variations in post-glacial catchment-wide erosion rates in over steepened and heavily glaciated regions are largely unknown for the eastern side and further north from the NPI. Therefore, this study focuses

on the area north of the present-day Northern Patagonian Ice Field (NPI) between 43°S and 47°S that covers the Patagonian Andes (Figure 1, Table 1). This research investigates the latitudinal variation of catchment-wide erosion rates and the influence of differences in glacier cover. We compare partly glaciated and deglaciated catchments and investigate three objectives that are: (1) to identify effects of grain size on calculated erosion rates, (2) to investigate effects of transport distance on erosion rates, and (3) to analyze the potential influence of climate, tectonic parameters, topography and vegetation on erosion rate.

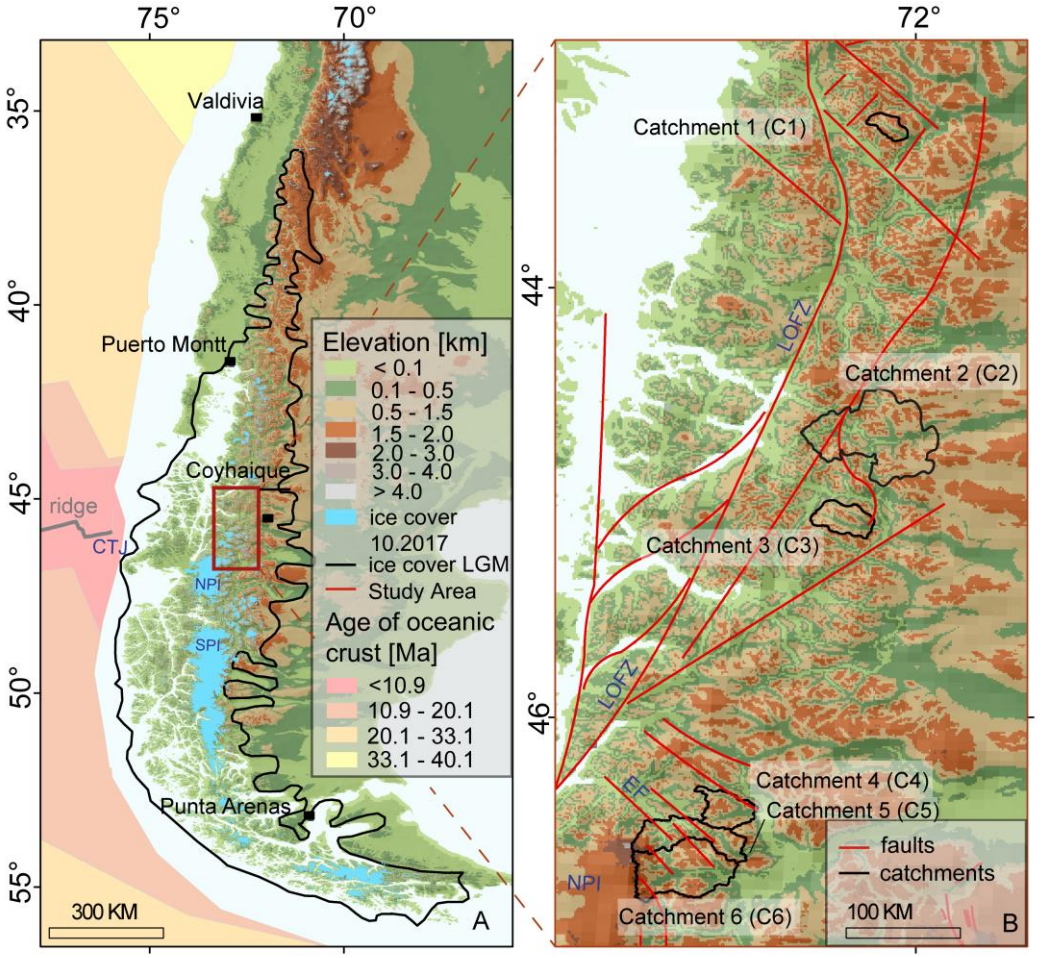

Fig. 1: Overview of the study area. (A) The topographic map shows the elevation distribution. In light blue the recent ice/glacier cover is illustrated which is derived from NSIDC (2018). NPI is the Northern Patagonian Ice field whereas SPI is the Southern Patagonian Ice field. The black line represents the Last Glacial Maximum (LGM) ice cover extend and is derived from Singer et al. (2004) and Thomson et al. (2010). Red to yellow colours represent the age of oceanic crust and location of trench/plate boundaries derived from GPLATES global plate model of Müller et al. (2008) and Seton et al. (2012). CTJ is the Chilean Triple Junction. The red box is the study area and is shown in more detail on the right. (B) Black polygons illustrate the catchments whereas red lines represent the major fault systems of Liquiñe-Ofqui Fault Zone (LOFZ) and Exploradores Faults (EF).

2 Study Area

2.1 Geological and Geomorphological Setting

Subduction of oceanic plates beneath the Chilean continental margin lead to the formation of the southern Andes (Ramos and Ghiglione, 2008). North of 46°30'S, the northeast subduction direction of the Nazca plate initiated at 20 Ma and is ongoing at a rate of ~7cm/yr (Pardo-Casas and Molnar, 1987). South of 46°30'S, the Antarctic plate subducts with a rate of ~2cm/yr since 16 Ma (Breitsprecher and Thorkelson, 2009). The boundary between the two different subducting plates is the Chile Triple Junction (CTJ). All six catchments (Figure 1B) are located north of the CTJ. The three northernmost catchments are situated close to the Liquiñe-Ofqui fault zone (LOFZ), a major geologic feature affecting the southern Andes (Figure 1B). The LOFZ extends >1000km north of the CTJ and is a dextral-transpressional fault system that is seismically active (Cembrano et al., 1996). The three southernmost catchments are located in the Exploradores Faults (EF), an area characterized by reverse faults, north of the NPI (Georgieva et al., 2016).

Distinct variations in topography of the Patagonian Andes can be found north and south of the CTJ location. A maximum and mean elevation of 2000 m and 1000 m, respectively, is representative for the area north of the CTJ. South of the CTJ, mean elevations increase but become more variable and maximum elevations range between 3000 m to 4000 m (Georgieva et al., 2016). The highest peak in the NPI is Mt. San Valentin at 4058 m elevation. Although variations in topography are present, apatite Helium (AHe) ages ranging from 1 Ma to 11 Ma collected at elevations between 0 to 500 m indicate no significant latitudinal trend in cooling ages from 43°S to 47°S (Figure S1; Thomson et al., 2010; Guillaume et al., 2013; and Georgieva et al., 2016).

2.2 Glacier Setting

The NPI is one of the largest ice fields in the Southern Hemisphere (Warren and Sugden, 1993). The glacier accumulation area covers a surface of 2578 km^2 and the ablation area a surface of 1550 km^2. Accumulation and ablation areas are divided by the equilibrium line which is estimated to be located at an elevation between 900 to 1350 m (Aniya, 1988). In recent years the NPI shows an ice retreat of 0.059 ± 0.005 mm/yr (Foresta et al., 2018).

The Patagonian Andes including the NPI are an orographic barrier. The western side of the NPI is characterized by a maritime regime with wet conditions of rain and snow accumulation whereas the eastern side shows a dryer continental climate signal (Thomson et al., 2010; Willis et al., 2012). The glacier accumulation and drainage pattern of the NPI follows the climatic settings of wet and dry climatic regimes. An example is the San Rafael glacier which terminates into the Laguna San Rafael in the east

of the northern NPI (Koppes et al., 2010). The San Rafael glacier is adjacent to this study area but is not draining to the catchments 4 to 6 that are located at the northern eastern side of the NPI.

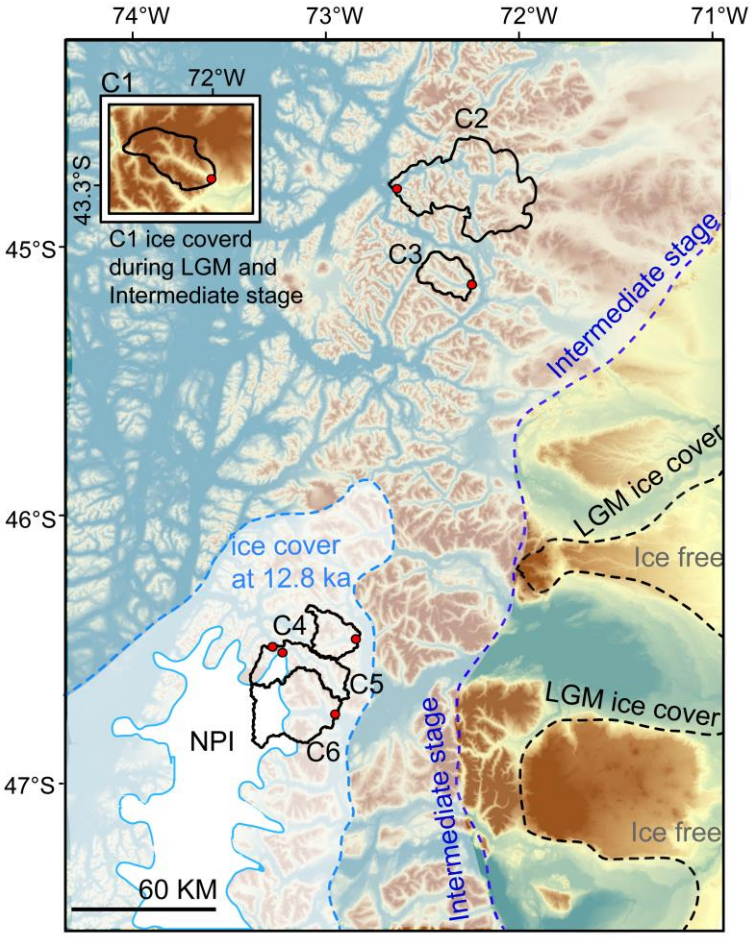

Fig. 2: Summary of deglaciation timing north of the NPI. Four different ice stages are reported. The first stage is shown as a black dashed line that represents the extent of ice cover during LGM. The dark dashed blue line represents an intermediate ice position between LGM and 12.8 ka. The light blue line illustrates the glacier position at 12.8 ka and the solid light blue line shows the current ice extent. All ice stages are modified after Hultan et al. (2002), Turner et al. (2005), Hubbard et al. (2005), Hein et al. (2009) and Bendle et al. (2017).

Figure 2 shows a summary of timing of deglaciation including present-day glacier cover. The last glacial maximum (LGM) covered the six catchments with thick ice from 19 ka to 23 ka ago. Rapid ice retreats produced several intermediate stages and occurred within centuries from 17.5 ka to 17.1 ka and 16 ka to 15 ka in the warmer and therefore more sensitive northern ice sheet domains. A phase of glacier stability occurred between 13.6 ka and 12.8 ka. The final deglaciation and final separation of the NPI and SPI started from 12.8 ka and the present-day margin is believed to be stable since 11 ka with local glacier fluctuations (Hultan et al., 2002; Turner et al., 2005; Hubbard et al., 2005; Hein et al., 2009; Bendle et al., 2017). Reconstructions of the timing of deglaciation indicates that the northern catchments (1 to 3) have been deglaciated earlier than the southern catchments (4 to 6). In addition, catchments 4 to

6 are located very close to the present-day NPI and may have experienced local glacier fluctuations over time (e.g. little ice age).

3 Methods

3.1 Determination of Geomorphic Parameters

Catchment parameters of elevation, slope, local relief (10 km radius), MAP (mean annual precipitation), MAT (mean annual temperature), glacier cover, vegetation cover, normalized channel steepness index (k_{sn}) and lithology are analyzed for comparison to ^{10}Be concentration and erosion rates. The topographic parameters of elevation, slope and local relief are based on an ASTER- DEM (30 m resolution) (USGS 2018). Climate parameters of MAP and MAT are determined from WorldClim (1 km resolution). Vegetation cover is derived from MODIS maximum green vegetation fraction (1 km resolution) (Broxton et al. 2014). Glacier cover and lithology are based on GLIMS Glacier database (NSIDC 2018) and GLiM lithological map (Hartmann and Moosdorf, 2012) (Table 1). Areas covered by ice are masked out in all presented calculations.

The normalized channel steepness index (k_{sn}) (Wobus et al., 2006) is calculated to characterize the geometry of river longitudinal profiles. The stream power law function relates slope and drainage area by:

$$S = k_s \times A^{-\theta}$$

where S is the local channel gradient (m/m), k_s is the steepness index ($m^{0.9}$), A is the upstream drainage area (m^2), and θ is the concavity index (dimensionless) (Hack, 1973; Kirby and Whipple, 2001; Wobus et al., 2006). The advantage of using k_{sn} is the quantification of the local specific channel-steepness to the steepness of an equilibrium river (Ouimet et al., 2009; Whipple, and Granger, 2009; Whittaker, 2012), which enables the comparison between rivers in different regions. We calculated the normalized k_s (k_{sn}) by using a reference concavity of 0.45, a smoothing window of 500 m, and a contour sampling interval of 20 m. The resulting k_{sn} values were clipped to the size of the catchments. All parameters were analyzed using ArcGIS, TopoToolbox 2 (Schwanghart and Scherler, 2014), and the Stream Profiler Matlab scripts of Whipple et al. (2007).

3.2 Cosmogenic Sample processing and Analysis

Detrital sand and pebbles were collected from 6 rivers with catchment sizes between 163 km^2 and about 1416 km^2 for measurements of in situ-produced ^{10}Be and ^{26}Al (Figure 3 and Figure 4, Table 1). In catchment 5, the samples 17PG23 and 17PG24 are directly taken from glacier outwash (Figure 4).

Catchments of similar stream order, similar catchment size, and lithology of similar quartz-content are selected. The catchment lithologies are characterized by mainly (over 60% catchment area) acidic plutonic rocks. From each detrital sample, the 500 to 1000 μm grain size fraction and the 250 to 500 μm grain size fraction was sieved and cleaned to pure quartz. River pebbles of similar size (1.6 to 5.2 cm) were selected, and crushed, and sieved to 500 to 1000 μm and 250 to 500 μm grain size fractions for further treatment. Approximately 300 μg of ^{9}Be was added to approximately ~100 g pure quartz before dissolution of the quartz. Beryllium and Aluminum were separated by using the standard separation method of von Blanckenburg (2005) and Wittmann et al. (2007). The ratios of $^{10}Be/^{9}Be$ and $^{26}Al/^{27}Al$ were measured as BeO and Al_2O_3 targets by accelerator mass spectrometry at the University of Köln. Stable Al concentration measurements were performed by inductively coupled plasma-optical emission spectrometry at the University of Tübingen.

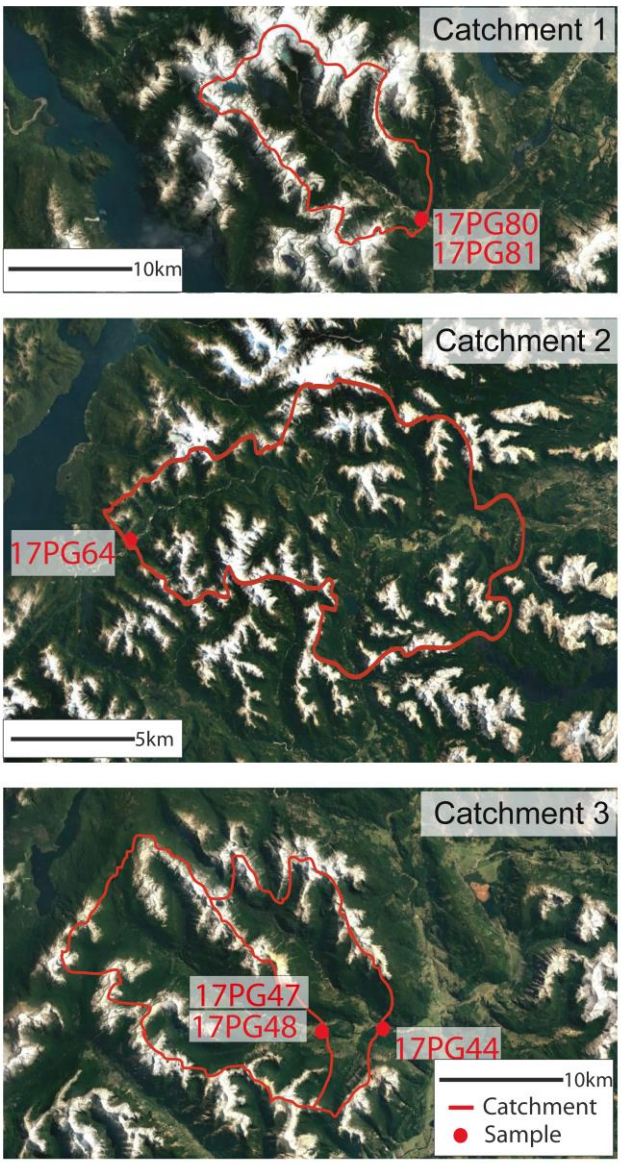

Fig. 3: Aerial photo of catchment sample locations 1 to 3 from 43°S to 45°S latitude and 72°S to 73°W longitude. White areas indicate snow cover.

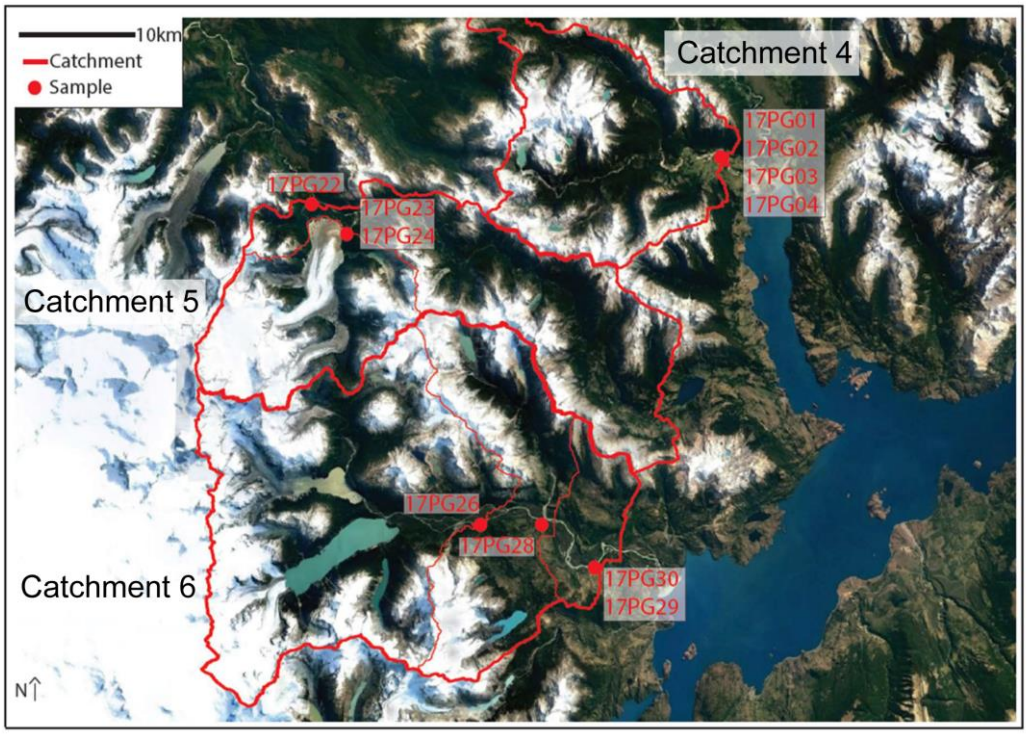

Fig. 4: Aerial photo of catchment sample locations 4 to 6 from 46°S to 47°S latitude and 72°S to 73°W longitude. White areas indicate snow or glacier cover.

3.3 Erosion Rate Calculation

Catchment-wide erosion rates over timescales of <~10^6yr were calculated from the blank corrected ^{10}Be concentrations. Assuming that the Earth's surface is steadily eroding, the cosmogenic isotope concentration (*C*) of ^{10}Be is inversely proportional to the erosion rate (*D)* and described in the following equation:

$$C = P_{Nuc}(0) \times \frac{a_1}{\left(\lambda + \frac{\rho \times D}{b_1}\right)}$$

$$+ P_{\mu stopped}(0) \times \frac{a_2}{\left(\lambda + \frac{\rho \times D}{b_2}\right)}$$

$$+ P_{\mu fast}(0) \times \frac{a_3}{\left(\lambda + \frac{\rho \times D}{b_3}\right)}$$

where C is the isotope concentration (at $g_{(qtz)}^{-1}$), D is the erosion rate (cm yr^{-1}), λ is the decay constant (^{10}Be 4.99E-07 ± 0.43E-08 yr^{-1}; Chmeleff et al., 2010; Korschinek et al., 2010), and ρ is the rock density (2.4 ± 0.2 g cm^{-3}). $P_{nuc}(0)$, $P_{\mu stopped}(0)$, and $P_{\mu fast}(0)$ are the surface production rates of cosmogenic nuclides (at $g_{(qtz)}$ yr^{-1}) by spallation, stopped and fast muons. Depth scaling of the production rates is

based on nucleonic, stopped muonic, and fast muonic adsorption lengths which are 157, 1500, and 4320 g/cm^2, respectively (Braucher et al., 2011).

Sea level high latitude (SLHL) nucleonic production rates (P_{nuc}) for ^{10}Be are based on the value 3.92 atoms/($g_{(qtz)}$ yr) (Borchers et al. 2016). The stopped and fast muonic production rates use the values 0.012 atoms/($g_{(qtz)}$ yr) (^{10}Be $P_{\mu stopped}$) and 0.039 atoms/($g_{(qtz)}$ yr) (^{10}Be $P_{\mu fast}$), provided by Borchers et al. (2016). The nucleonic and muonic production rates were scaled using the procedure of Lifton et al. (2014).

The catchment-wide production rate is the average production rate of each DEM pixel (90 m resolution) in the catchment area. Each single production rate was corrected for topographic shielding following the procedure described in Dunne et al. (1999) and Norton and Vanacker (2009). The ^{10}Be concentrations as well as the ^{26}Al concentrations are blank corrected with a value of 52,804 atoms/g($_{qtz}$) for ^{10}Be and 66,412 atoms/g($_{qtz}$) for ^{26}Al (Table 2). Values of ^{10}Be concentrations are reported to SLHL (Table 2).

Corrections for glacier cover and snow were applied as follows. DEM pixels under present day ice cover are assumed to be 100% shielded and are not included in the average production rate calculation. Snow shielding was calculated from the equations of Gosse and Phillips (2001). Snow depth estimations were performed using the MODIS/Terra Snow Cover Monthly L3 Global 0.05°, Version 6 dataset with a monthly time resolution from 2001 to 2017 (Hall and Riggs, 2015). For each study area the snow cover is given in percent surface cover ranging from 0 to 100%. These values are scaled to snow depth by assuming that 100% snow cover equals the maximum snow depth that was measured by Foster et al. (2001 and 2002). A snow density of 0.25 g/cm^3 for shielding calculations is assumed.

The above reported snow depth estimations introduce uncertainties. Hence, the reported erosion rates should be interpreted as maximum values and the possible effect of snow shielding on the calculation of erosion rates needs to be constrained. Consequently, we calculate the uncertainties in erosion rates using a Monte Carlo simulation of error propagation. The error propagation includes the production rate error of nucleonic, stopped and fast muonic production, a 5% DEM altitude error for the production rate, the decay constant error, the rock density error, and the ^{10}Be concentration error. Erosion rates are reported with a) topographic shielding including glaciated areas, b) with topographic shielding and snow shielding including glaciated areas and c) with topographic and snow shielding excluding areas covered by glaciers in Table 3.

Catchment-wide erosion rates are compared to all available catchment parameters by analysis of linear regression and Person correlation coefficients. Multivariate statistics cannot be performed on this dataset due to a small number of data points which is insufficient to perform a reliable result.

4 Results

4.1 Catchment Parameters

The analyzed geomorphic parameters show following results: Catchment mean elevations are constant within the uncertainty of the measurement and range from 908 ± 379 m to 1057 ± 393 m (Table 1). Similar to the mean elevation, local relief over a 10km radius shows no latitudinal trend between the catchments and vary between 922 ± 76 m to 1174 ± 458m (Figure 1, Table 1). Geomorphic parameters of elevation and local relief equally show no latitudinal trend in the investigated area.

Mean slope and vegetation cover show strong inner catchment variations. Generally, the lowest slopes and highest vegetation cover can be identified in the river valleys, whereas at the valley walls are steep and vegetation cover is low. North of the NPI, former as well as present-day glaciated valleys show generally steep mean slopes but distinct differences in vegetation cover. Catchment mean slopes in the study area range between 19.5 ± 14.5° and 26.2 ± 16.2° but are constant within the uncertainty (Table 1). Figure 5 and Figure 6 illustrate that for all six catchments, slopes lower than 15° can only be found in the valley floors that are infilled with Quaternary sediments. On the contrary, steeper slopes (>15°) are mainly concentrated at the valley walls consisting of acid plutonic rocks. The vegetation is highest at locations of shallow slopes and Quaternary sediments. In contrast to mean slopes, mean vegetation cover shows a latitudinal trend. Catchments closer to the NPI have a lower mean vegetation cover (min 28 ± 37 %) than catchments further north (max 92 ± 10 %) (Table 1).

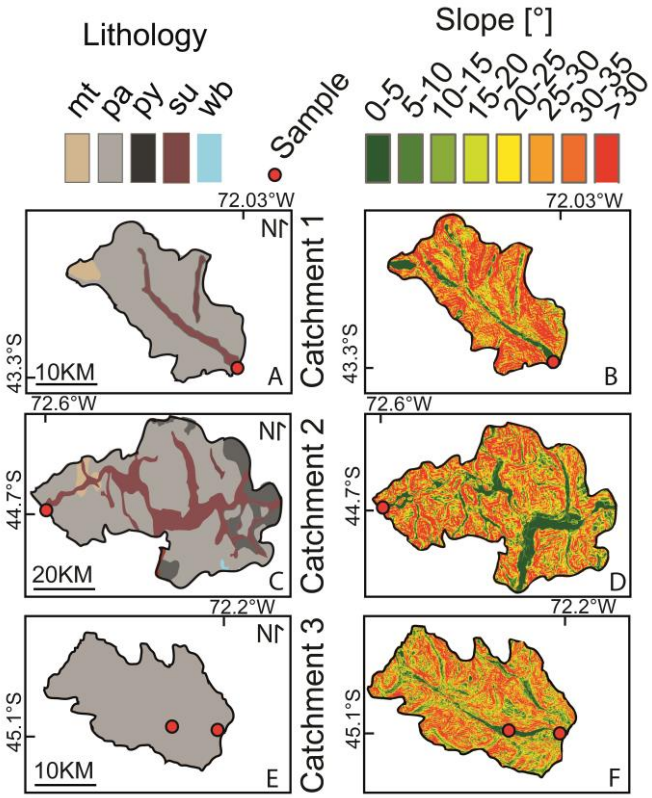

Fig. 5: Lithology and slope of catchments 1 to 3. (A, C, E) Lithological maps showing lithological types of acid plutonic rocks (pa), pyroclastics (py), metamorphics (mt), unconsolidated sediments (su), water body (wb) and glaciers (ice cover) derived from GLiM lithological map (Hartmann and Moosdorf, 2012). The catchments 1 to 3 are not covered by glaciers. (B, D, E) Color coded slope maps showing slope steepness in degrees based on ASTER- DEM (30m resolution) from USGS (2018).

Geological parameters show clear variations. The lithological analysis identifies the types of acid plutonic rocks (pa), pyroclastics (py), metamorphics (mt) and unconsolidated sediments (su) in the catchments (Figure 5 and Figure 6). The dominant lithology is acid plutonic rock that varies from 61% to 100% within the catchment (Table 1.). North of the NPI, the lithological units are characterized by the Jurassic to Miocene Patagonian batholith that mainly consists of acid plutonic rocks. In addition, Jurassic volcanics, Triassic metasediments, Paleozoic metasediments, and Quaternary unconsolidated sediments can be found in this region (Ramos and Ghiglione, 2008). Similar to the general lithological classification, catchment lithologies are mainly composed of acid plutonic rocks (> 60% catchment area) and Quaternary unconsolidated sediments (derived from GLiM by Hartmann and Moosdorf, (2012)). Minor percentages of metamorphic or pyroclastic rocks are mapped (Figure 5 and Figure 6, Table 1).

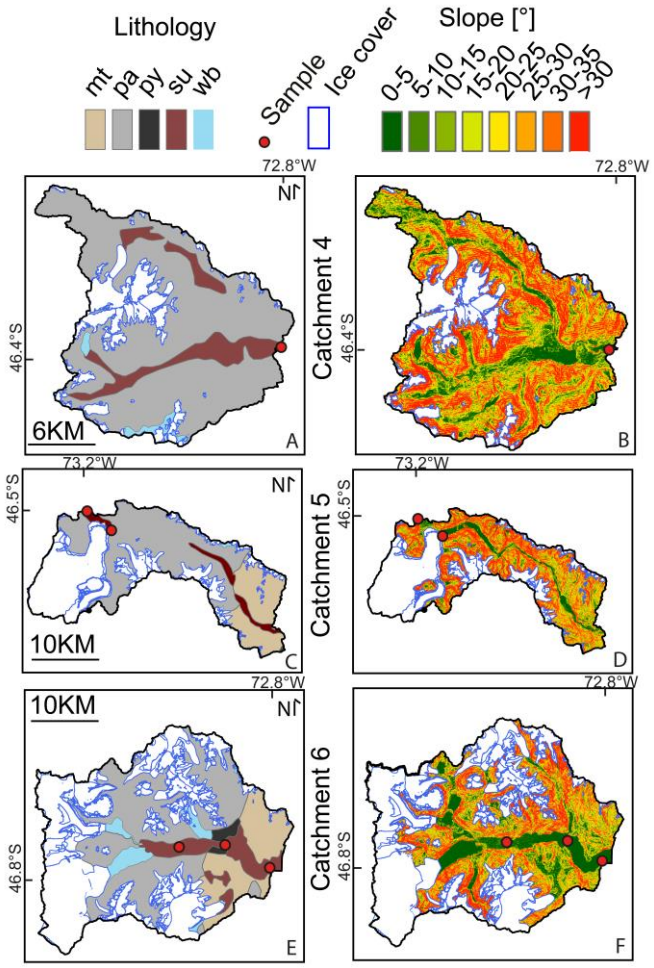

Fig. 6: Lithology and slope of catchments 4 to 6. (A, C, E) Lithological maps showing lithological types of acid plutonic rocks (pa), pyroclastics (py), metamorphics (mt), unconsolidated sediments (su), water body (wb) and glaciers (ice cover) derived from GLiM lithological map (Hartmann and Moosdorf, 2012). (B, D, E) Color coded slope maps showing slope in degree based on an ASTER- DEM (30m resolution) (USGS, 2018).

Faults with incompletely known deformation histories cross the catchment areas. Catchments 1 to 3 are situated in the LOFZ whereas catchments 4 to 6 neighbour the EF zone (Figure 1B). In order to investigate the postglacial deformation history of the faults in more detail the normalized channel steepness index (K_{sn}) is analyzed (Figure 7). Generally, low mean K_{sn} values (< 50) are calculated throughout the catchments in the low elevation, glacial valley portions of the catchments. Maximum K_{sn} values range from 95 to 394. Minimum K_{sn} values vary from 0.01 to 0.02. For all catchments the highest K_{sn} values, indicating knickzones, are found in locations of incoming tributaries of hanging valleys or lithological differences (e.g. compare Figure 4, 5 and 6). Indications for fault-zone produced knickzones and high K_{sn} values cannot be identified.

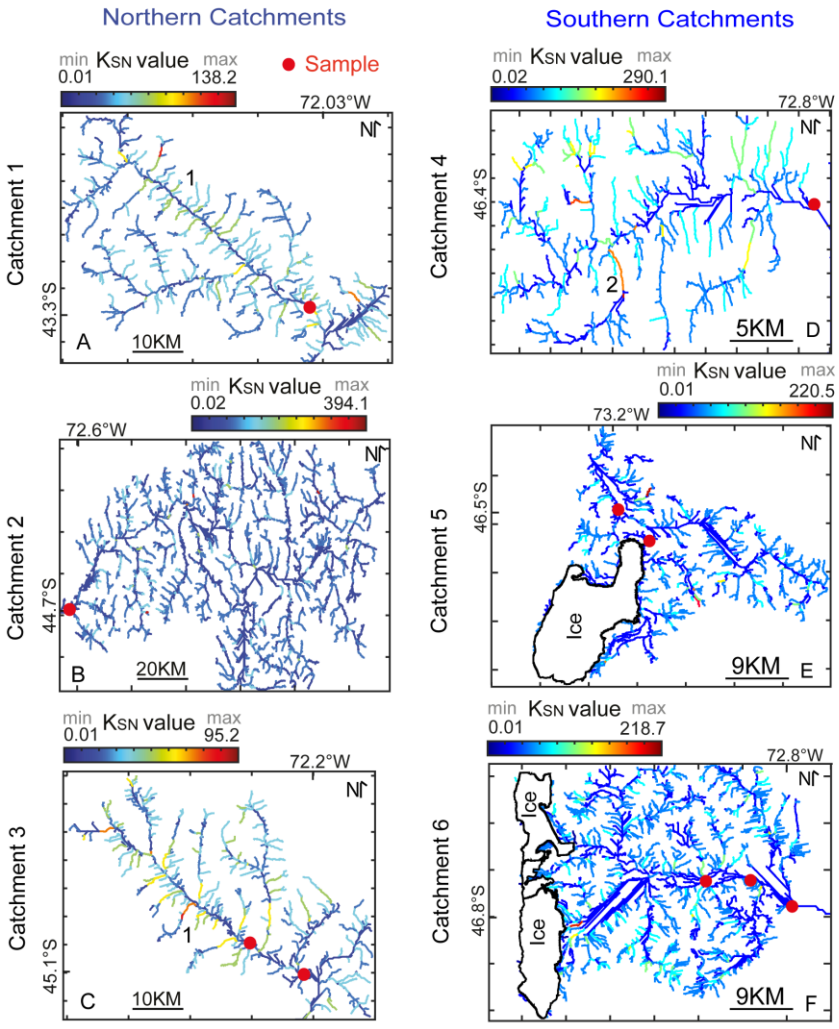

Fig. 7: Normalized channel steepness. Drainage network is color coded by the normalized channel steepness value (K_{sn}). The red dots mark the sample positions. In panel B, D and F the longitudinal river profiles are highlighted. In catchments 1, 3 and 4 the number 1 or 2 is written close to channel. The number 1 means high K_{sn} values are caused by hanging valleys whereas number 2 indicates high K_{sn} values are caused by lithological differences.

Climatic parameters of MAT and MAP show no latitudinal trend for the catchments 1 to 6 and are similar within 2σ standard deviation from the mean (Table 1). Mean annual temperature (MAT) and mean annual precipitation (MAP) derived from WorldClim show no latitudinal trends between the catchments. MAT values range from 3.1 ± 2.9°C to 5.3 ±1.8°C and MAP values vary between 1306 ± 84 mm/yr to 1465 ± 191 mm/yr (Table 1). Catchments 4 to 6 have a glacier cover of 0.4 % to 6.2%, which is caused by smaller glaciers located at the dryer western side of the NPI. The catchments 1 to 3 are located further from the NPI and have a lower glacier cover of 0.02% to 1.9% (Table 1).

4.2 Variation of ^{10}Be Concentration and ^{10}Be-derived Erosion Rates

Values of blank corrected ^{10}Be concentrations normalized to SLHL are reported in Table 2. The concentrations are derived from river sand, river pebbles and glacier outwash. In general, ^{10}Be concentrations of river sand from catchments 1 to 3 in the north are higher than in catchments 4 to 6 in the south. In the north ^{10}Be concentrations of river sand vary from 7,556 ± 435 atoms/g$_{(qtz)}$ to 15,926 ± 723 atoms/g$_{(qtz)}$ whereas concentrations in southern catchments range from 3,811 ± 407 atoms/g$_{(qtz)}$ to 11,182 ±579 atoms/g$_{(qtz)}$. The ^{10}Be concentrations of the coarser grained river pebbles are of same order, but not identical to ^{10}Be concentrations of river sand. In comparison to river sand, the ^{10}Be concentrations of river pebbles are generally lower in the north than sand samples, ranging from 5,032 ± 317 atoms/g$_{(qtz)}$ to 9146 ± 546 atoms/g$_{(qtz)}$ and in the south ^{10}Be concentrations are higher of river pebbles than sand, ranging from 6,418 ± 740 atoms/g$_{(qtz)}$ to 6,975 ± 521 atoms/g$_{(qtz)}$. The lowest ^{10}Be concentrations are observed from the glacier outwash samples (17PG23 and 17PG24) with values of 2,027 ± 319 atoms/g$_{(qtz)}$ and 2,377± 290 atoms/g$_{(qtz)}$. Analytical limitations occur for samples that are processed with a dissolved weighted quartz amount lower than 100g. For these samples it is not possible to calculate a ^{10}Be concentration (Table 2).

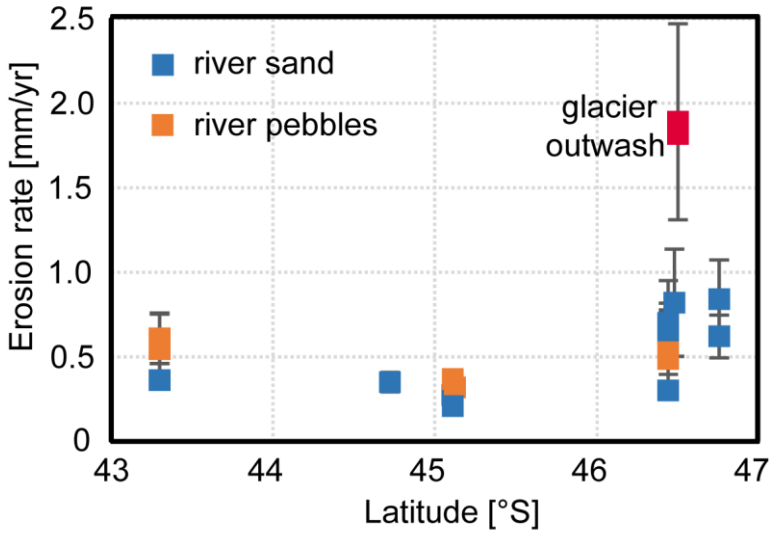

Fig. 8: Erosion rates plotted versus latitude. Erosion rates are reported including topographic and snow shielding. Orange boxes show erosion rates derived from river pebbles and blue boxes show erosion rates from river sand. The single red box reports the only erosion rate derived from glacier outwash.

Erosion rates are calculated in three different ways including: (1) only a topographic shielding correction, (2) topographic shielding correction plus snow shielding correction and (3) topographic plus snow shielding correction with the glaciated areas being removed from the calculation (Figure 8, Table 3). In the following the erosion rates including topographic and snow shielding are reported because it remains unclear if material coming from under the glacier cover contains ^{10}Be or not.

Erosion rates derived from river sand are lower in the northern catchments varying from 0.24 ± 0.03 mm/yr to 0.36 ± 0.05 mm/yr (Figure 8). In comparison, erosion rates from the southern catchments are higher ranging from 0.30 ± 0.03 mm/yr to 0.84 ± 0.23 mm/yr. Erosion rates derived from river pebbles are similar or higher for catchments 1 to 3, and range from 0.37 ± 0.05 mm/yr to 0.61 ± 0.15 mm/yr. In catchments 4 to 6, erosion rates from pebbles are within the uncertainty the same as erosion rates reported for river-sand and range from 0.49 ± 0.09 mm/yr to 0.53 ± 0.24 mm/yr. The highest erosion rate is calculated from sample material of glacier outwash and has a value of 1.89 ± 0.58 mm/yr, however this value is likely not accurate and more likely represents a decreased (or inherited) nuclide concentration of ice-shielded sediment source from under the glacier. Integration time for all types of sampled material range from 423 ± 42 yr to 2727 ± 258 yr (Table 3).

4.3 $^{26}Al/^{10}Be$ ratio in modern river sediments

To investigate the possibility of sediment storage and burial effects, the blank corrected ^{26}Al concentration were analyzed (Table 2). In general, ^{26}Al concentrations of river sand from catchments 1 to 3 in the north are similar or higher compared to catchments 4 to 6 in the south. For example, in the north, ^{26}Al concentrations of river sand vary from 62,420 ± 6496 atoms/g$_{(qtz)}$ to 120,467 ± 8408 atoms/g$_{(qtz)}$ whereas in the south, the ^{26}Al concentrations range from 31,612 ± 7153 atoms/g$_{(qtz)}$ to 89,572 ± 6,323 atoms/g$_{(qtz)}$.

The ^{26}Al concentrations of river pebbles are in the same order, but not identical to ^{26}Al concentrations of river sand. In comparison to river sand, the ^{26}Al concentrations of river pebbles are similar or lower in the north, ranging from 30,652 ± 3,624 atoms/g$_{(qtz)}$ to 74,849 ± 6,519 atoms/g$_{(qtz)}$, and higher in the southern catchments, ranging from 43,984 ± 12,503 atoms/g$_{(qtz)}$ to 67,682 ± 8,833 atoms/g$_{(qtz)}$. Due to analytical limitations it is not possible to determine the ^{26}Al concentration of the glacier outwash sample material (17Pg23 and 17PG24 Table 2). The $^{26}Al/^{10}Be$ ratio is sensitive to the exposure history of a sample due to differences in the radioactive decay rate and can provide an indication of if the samples experience burial (and shielding) prior to measurement. Major burial effects cannot be identified because the ratios vary between 6 to 7 and include a high uncertainty (Figure 9).

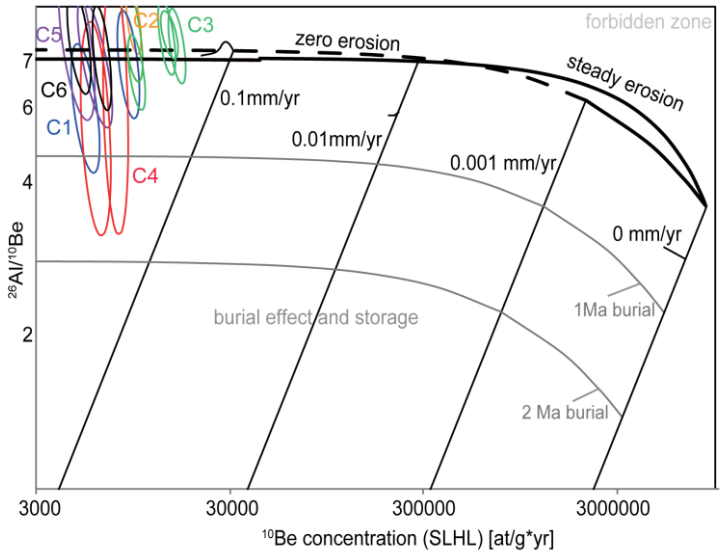

Fig. 9: Erosion island plot ("banana plot") showing the evolution of $^{26}Al/^{10}Be$ with time. The ^{10}Be concentration normalized to SLHL is plotted versus the ratio of $^{26}Al/^{10}Be$. The color coded circles represent the ratios of the six catchments and are labelled accordingly. The solid black line indicates the steady erosion line whereas the black dashed line indicates zero erosion. The area below the steady erosion and zero erosion line is the zone of burial effects. The samples have high uncertainties which is represented by the size of the circle. However, major burial effects cannot be identified.

4.4 Correlation of ^{10}Be concentration and Erosion Rate to Catchment Parameters

The squared Pearson correlation coefficient (R^2) of the ^{10}Be concentration (normalized to SLHL for comparison to each other) is plotted versus topographic, geomorphic, geologic and climatic parameters in Figure S2. Values for river sediments and river pebbles are included to increase the statistical security and calculate a robust correlation coefficient as well as regression. The analysis illustrates that the correlation coefficients of the ^{10}Be concentrations to MAP, MAT, catchment area, local relief, lithology, K_{sn} and slope indicate weak to non-correlations with R^2 smaller than 0.36. The best fit regression combined with the highest correlation is observed for ^{10}Be concentration with vegetation cover (R^2=0.66).

The squared Pearson correlation coefficient (R^2) of the erosion rate is plotted versus topographic, geomorphic, geologic and climatic parameters in Figure 10. The analysis emphasizes that the correlation coefficient of the erosion rates to MAP, MAT, catchment area, local relief, lithology, K_{sn} and slope indicate weak correlations with R^2 smaller than 0.43. Similar to Figure S2, the best fit regression combined with the highest correlation is observed for erosion rate with vegetation cover (R^2=0.7).

5 Discussion

5.1 Reliability of ^{10}Be and ^{26}Al Concentrations and Erosion Rates

The reliability of the calculated erosion rates is dependent on the accuracy of the measured ^{10}Be/^{9}Be ratios. For the samples 17PG24 (pebble with a size of 2.1-4.7 cm in catchment 5), 17 PG30 (pebble with a size of 1.6-5.2 cm in catchment 6), 17PG28 (river sand 500-1000 µm in catchment 6) and 17PG26 (river sand 250-500 µm in catchment 6) a measurement error of larger than 10% exists. This error is caused by insufficient pure quartz material that is dissolved for the measurement. For an accurate measurement a pure quartz >100g of quartz per sample is recommended to measure ^{10}Be in this study area. Erosion rates are only calculated for samples with measurement errors lower than 10%. Similar to the ^{10}Be/^{9}Be ratios, the ^{26}Al/^{27}Al ratios are evaluated based on the measurement accuracy and the samples 17PG23, 17PG24, 17PG26, 17PG28 and 17PG30 are dismissed from further interpretation due to high uncertainties in the measurement. The ^{26}Al/^{10}Be ratio is only calculated for reliable ^{10}Be and ^{26}Al concentrations and ranges from 5.1 ± 1.3 to 9.5 ± 1.7.

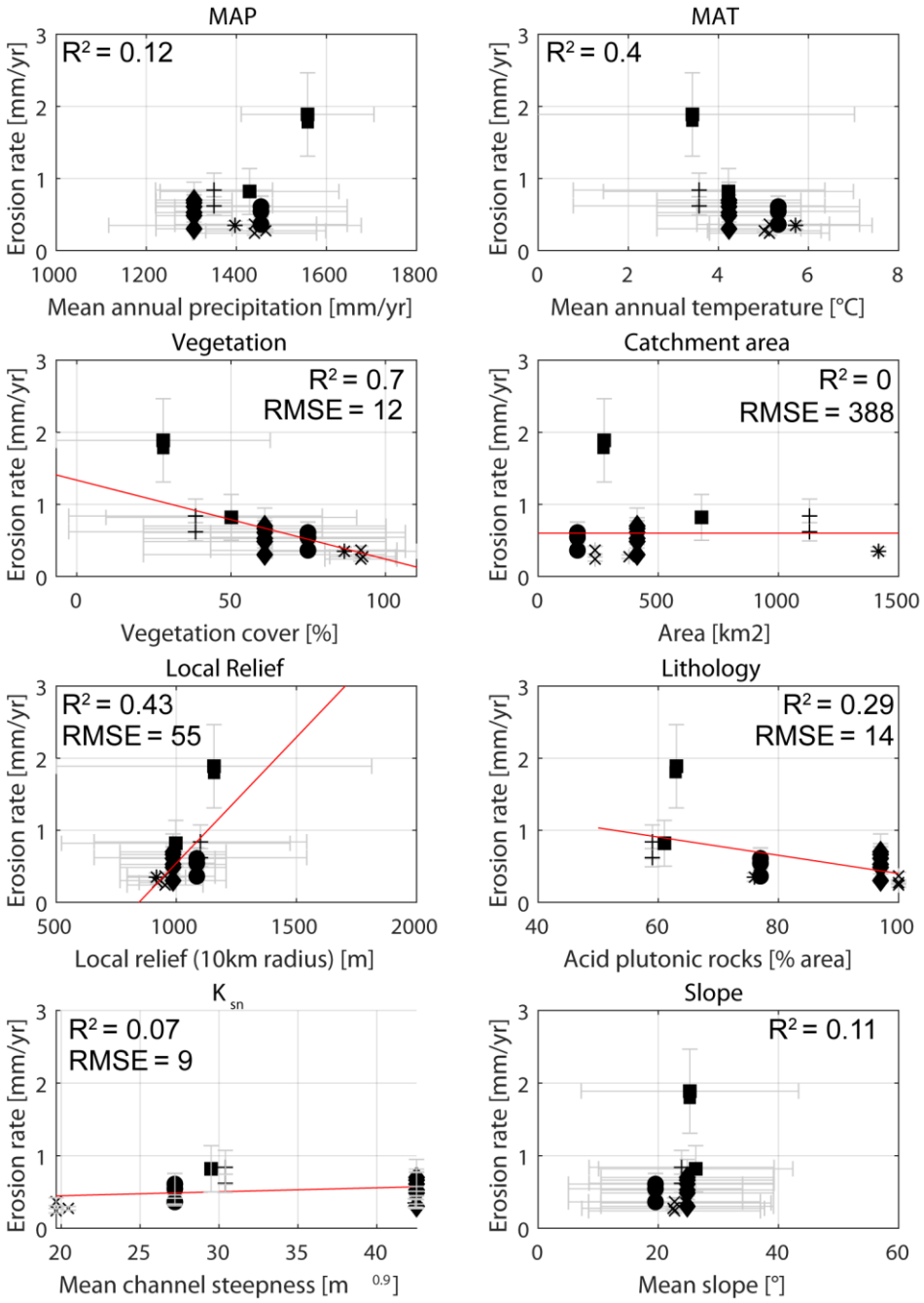

Fig. 10: Erosion rate plotted versus different catchment parameters. In each subplot samples are represented in catchment 1 with a circle sign (●), catchment 2 with an asterisk sign (*), catchment 3 with a cross sign (x), catchment 4 with a diamond sign (♦), catchment 5 with a square sign (■) and catchment 6 with a plus sign (+). Uncertainties are displayed with grey bars, except for catchment area, K_{sn} and lithology where the uncertainty is not available. The red line represents a linear regression. The squared Pearson correlation coefficient (R^2) and the goodness of fit (RMSE) is shown. A RMSE value closer to 1 represents a perfect fit of the regression. Regression line calculations failed for comparisons of erosion rate to mean slope, MAP and MAT.

Erosion rates are calculated with three different shielding options in this study (Table 3): (1) only topographic shielding, (2) topographic shielding and snow shielding including glaciated areas and (3) topographic shielding plus snow shielding without glaciated areas. This study reports and favors the erosion rate calculation based on topographic shielding combined with snow shielding. This is because it remains unclear if the sediment beneath glaciers from glacier outwash contains ^{10}Be or not. The sample 17PG23 (sand 500-1000µm) is taken directly in front of the glacier from glacier outwash in catchment 5. For this sample a ^{10}Be concentration (SLHL) of 2027 ± 319 atoms/g($_{qtz}$) is measured. We cannot disentangle if the sediment contains ^{10}Be because material on top of the glacier or from the sides contributes to the glacier outwash.

5.2 Effect of Sampled Grain Size on Erosion Rate

Potential grain size effects can be investigated in catchments 1, 3 and 4 where erosion rates are derived from river pebbles as well as river sands (Figure 11, Table 2). Minor grain size effects are detected in catchments 1 and 3 whereas in catchment 4 erosion rates for river pebbles and river sediments are similar. Catchments 1 and 3 are characterized by steep main channels and have the smallest catchment area of 163 km^2 and 377 km^2, respectively. For these catchments the investigated erosion rate is higher in the pebble-size fraction compared to the sand samples. On average, large grains are more rapidly exhumed by mass wasting than small grains and indicate deep-seated bedrock landslides (Schuerch et al., 2006; Mücher et al., 2018). Owed to the small catchment area, it seems unlikely that the size of the clasts is significantly reduced during transport in the channel system (Rice and Church, 1998). Consequently, the^{10}Be signal can be diluted by larger grains that did not receive a similar irradiation dose than smaller grains. Similar observations are reported, for example, by Brown et al. (1995) for a densely forest-covered catchment in Puerto Rico or by Belmont et al. (2007) where cobble weathering is diluting the ^{10}Be signal for catchments in Washington State.

In catchment 4 similar ^{10}Be erosion rates are observed for a wide range of grain sizes. This indicates that different-sized grains are (1) homogenously transported downslope by surface wash or debris flows in the channel system and (2) the effect of deep-seated landslides can be excluded. However, this study emphasizes that erosion in catchment 4 is not steady or continuous for samples of similar-sized grains and shows a large variation of derived erosion rates from river sand. For instance, the samples 17PG01 (river sand, 500-1000 µm) and 17PG04 (river sand, 500-1000 µm) are sampled from the same GPS location but different deposits and show a different ^{10}Be concentration and erosion rate (Table 2) within the uncertainty. The sample 17PG04 represents sand material which is not directly taken from the modern channel but instead from a terrace of unknown age, 1 m above the modern channel. The erosion rate of 17PG04 is two times lower than from modern river channel sediment. Consequently, sample 17PG04 demonstrates that river sand is not necessarily well mixed in the river channel.

We find that although the available replicates from similar locations in a channel do not agree within uncertainties, but are close to each other, samples deposited earlier (e.g. terrace samples are different by 0.3 mm/yr). This finding suggests that although river channels for cosmogenic nuclide analysis are often assumed to be well mixed, some variation within a single channel is possible and adds additional uncertainty. Given this, this study recommends that multiple samples of the same location and grain size should be analyzed to derive a reproducible result. In catchment 4, three out of four river sand samples showed the same erosion rate indicating that an erosion rate between 0.61 ± 0.17 mm/yr to 0.66 ± 0.15 mm/yr (17PG03 and 17PG01) is more likely to be the catchment-wide erosion than 0.30 ± 0.03 mm/yr (17PG04).

5.3 Effect of Transport Distance on Erosion Rate

Two effects of transport distance on erosion rate signals can be identified. The first effect has been aforementioned and describes catchment size controlling grain size effects. A second effect occurs with decreasing transport distance to glacier cover (Fig. 10). In catchments 3 and 5 we tested if sampling along the main channel towards the headwaters lead to a change erosion rate. In the present-day non-glaciated catchment 3 two river sand samples (sampling distance between 17PG44 and 17PG48 of ~20km) are analyzed and within the uncertainty show the same erosion rate of 0.28 ± 0.03 mm/yr and 0.25 ± 0.03 mm/yr, respectively. In the upstream glaciated catchment 5 the samples 17PG22 and 17PG24 show large differences in erosion rates, which vary between 0.82 ± 0.32 mm/yr and 1.89 ± 0.58 mm/yr.

The results indicate that with closer proximity to the glacier, the erosion rates increase. This suggests that some low-nuclide concentration sediment is sourced from under the ice and leads to the appearance of higher erosion rates. However, it is notable that the sample 17PG24 contains detectable ^{10}Be although it is sampled directly from glacier outwash. It remains unclear from where exactly the sample material is excavated. Two possibilities can be distinguished: (1) The sample material is sourced further upstream and collecting irradiation doses during transportation or (2) the ^{10}Be containing material is falling down from the top or from the sides of the glacier and incorporated into the glacier outwash. Similar observations and the heterogeneity of glacier erosion upstream in a catchment with ice cover were previously reported by, for example, Hallet et al. (1996), Wittmann et al. (2007), Godard et al. (2012) or Strunk et al. (2017).

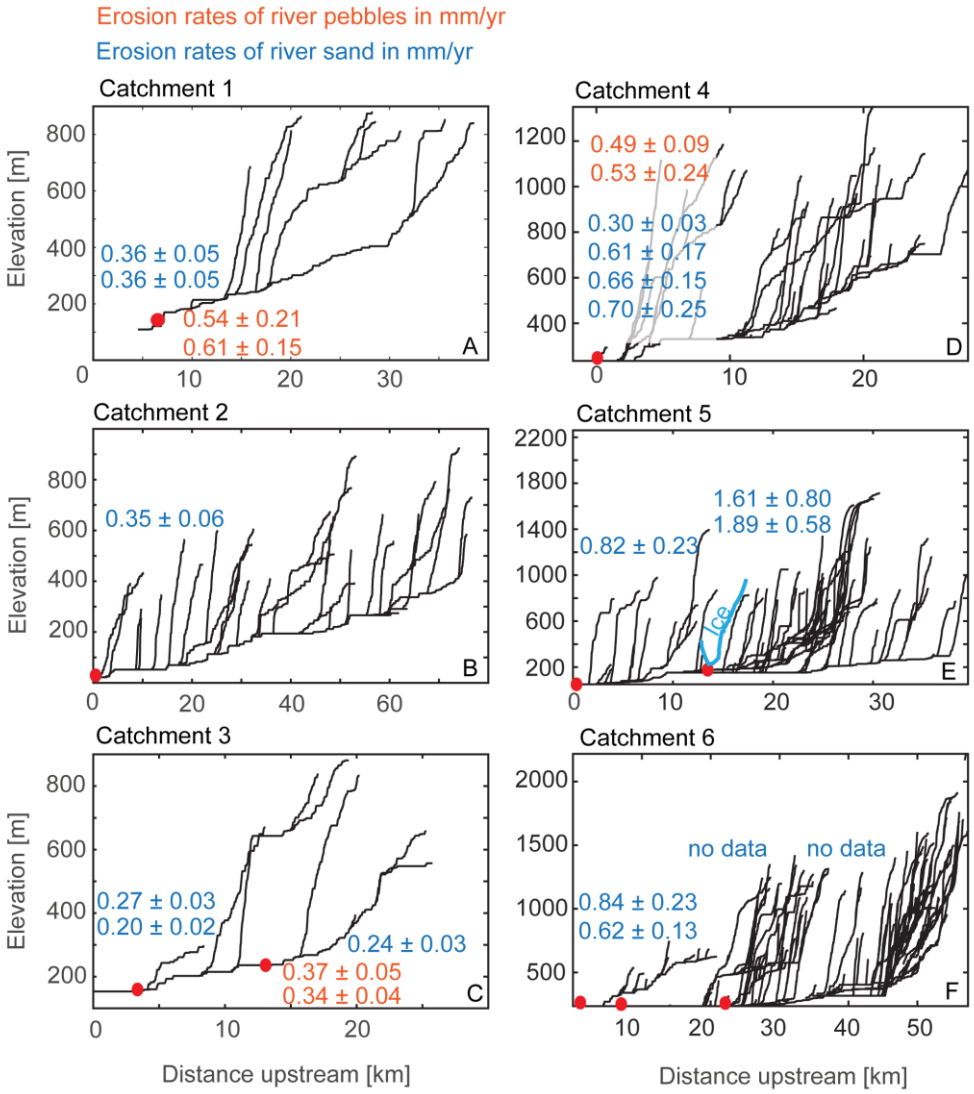

Fig. 11: Summary of longitudinal river profiles and erosion rates for catchments 1 to 6. Erosion rates are reported in mm/yr and shown in blue for river sand and in orange for river pebbles. The red dot marks the sample position. In catchment 5 the glacier ice cover is shown in light blue. In catchment 6 for two sampling positions we were not able to calculate erosion rates due to insufficient quartz. Longitudinal river profiles do not display a steady-state concave geometry. Especially, tributaries contain numerous knickzones. Knickzones in the main river channels are produced by lithological differences, for example at the boundary between unconsolidated sediments to acid plutonic rocks. Further knickzones are caused by calculation uncertainties of flat areas within unconsolidated sediments.

5.4 Other Factors Influencing Erosion Rates: Glacier Cover and Timing of Deglaciation

The results of the correlation coefficient analysis indicate that vegetation cover has the best fit correlation to erosion rate from all available parameters. Previous soil erosion and sediment yield studies document that as the type and density of vegetation cover increases, the resistance of soil to erosion through enhanced slope stabilization increases proportionally (Wainwright et al., 2000; Morgan et al., 2003; Gyssels et al., 2005; Stokes et al., 2008; Nadal-Romero et al., 2014; Riebe et al., 2017). We find a vegetation control on catchment-wide erosion rates (Figure 10). These findings have also been reported for smaller geographic areas in both East Africa (Acosta et al., 2015) and the Himalaya (Olen et al., 2016). However, it remains questionable why the vegetation cover is decreasing from catchment 1 to 6 (from North to South) although MAP and MAT do not show the same latitudinal variations. A possible interpretation can be found in the difference in glacier cover and timing of deglaciation between the catchments. Catchments that have been deglaciated earlier had potentially more time to establish complex and dense vegetation than catchments covered by ice for a longer time. However, it is not possible to disentangle the vegetational from glacial cover influence on erosion rates.

5.5 Synthesis

Erosion rates derived from ^{10}Be concentrations of glaciated and deglaciated catchments of northern Patagonia show significant differences in erosion rates. Erosion rates from glaciated catchments with lower vegetation cover in the south show higher erosion rates than catchments without ice cover and higher vegetation density in the north (Figure 12). Based on the geomorphological setting it is not possible to disentangle the vegetational and glacial (ice cover) influence on erosion rates. This study identifies grain size effects on erosion rates caused by differences in transport distance. Any potential effect on erosion rates by long wavelength tectonic impact or tectonic uplift rates varying locally cannot be identified.

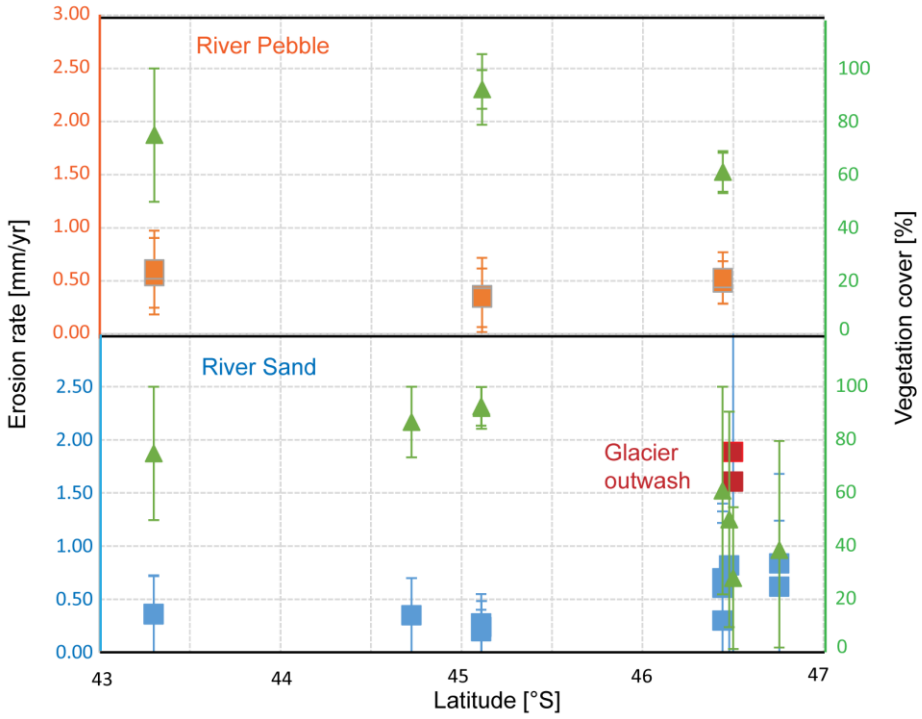

Fig. 12: Summary of main results. In orange erosion rates derived from pebbles are plotted versus latitude whereas erosion rates derived from sand is illustrated in blue. Erosion rates derived from glacier outwash are illustrated in red. Vegetation cover for each catchment-derived erosion rate is shown in green.

The observations from this study are in agreement with previous reported results from Patagonia. At the location of 53°S, Holocene erosion rates show low values in regions of high vegetation cover due to longer ice free periods and fast erosion where glacial impact is still present (Breuer et al., 2013). Global trends in erosion rates as a function of glacial dynamics have been previously documented by Koppes and Montgomery (2009) and Koppes et al. (2015) and show erosion rates for Patagonia that are in the same range as erosion rates from this study. Million-year time-scale erosion rates derived from thermochronological ages are also in agreement with this dataset and report erosion rates varying from 0.1 mm/yr to 1.1mm/yr north of 48°S which is in the same order as the reported values from this study (Fernandez et al., 2016).

6 Conclusion

We analyzed the latitudinal variation of catchment-wide erosion rates and the influence of differences in glacier cover. We identify an influence of sediment transportation distance on the erosion rate that is visible through grain size effects. In catchments with low sediment transport distance, erosion rates derived from river pebbles are up to two times higher compared to erosion rates derived from river sediment. The highest erosion rate of this study area reports a value of 1.89±0.32 mm/yr and is identified

in glacier outwash. Climatic, tectonic and geomorphological parameters show no latitudinal trend for the six catchments. Only the variation in vegetation cover has a strong correlation to the variation of erosion rates (R^2=0.7). The results show lower erosion rates (~0.3 mm/yr) for catchments that have been deglaciated earlier north of the NPI. Faster erosion rates (~0.8 mm/yr) are found in catchments that have been deglaciated later or are still party covered by glaciers due to the close location to the NPI.

Acknowledgement

We would like to thank M. Brenn for the assistance with laboratory work and S. Falkowski for the help in the field. This work was supported by the European Research Council (ERC) consolidator grant to T. Ehlers (ERC-CoG 615703). Further information is included in the supplementary material.

Supplementary to Paper III

Tables

All Tables of PAPER III are also archived in the digital appendix. The digital appendix is a CD that sticks to the last page of this thesis.

Table S1: Catchment data

Basin ID	Sample ID	Lab ID	Lat °	Long °	grain type and size	analytical grain size µ/m	Elevation Area km²	Glacier cover km²	Glacier cover %	MAP mm/yr	std mm/yr	MAT °C	std °C	Veg %	std %	Slope °	std °	Local Relief radius 10km	std radius 10km	Acid plutonic rocks %	Unconsolidated sediments %	Water body %	ksn mean m^0.9	min m^0.9	max m^0.9
C1	17PG80	MB18	-43.3	-72.039	pebble 1.6-4.5cm	500-1000	296	163.34	3.166	1.9	1454.7	191.3	5.3	1.8	74.9	25.1	19.5	1085.3	14.5	75.9	22	0	27.2	0.01	138.2
C1	17PG80	MB28	-43.3	-72.039	pebble 1.6-4.5cm	250-100	296	163.34	3.166	1.9	1454.7	191.3	5.3	1.8	74.9	25.1	19.5	1085.3	14.5	75.9	22	0	27.2	0.01	138.2
C1	17PG81	MB38	-43.3	-72.039	sand 250-500µm	250-100	296	163.34	3.166	1.9	1454.7	191.3	5.3	1.8	74.9	25.1	19.5	1085.3	14.5	75.9	22	0	27.2	0.01	138.2
C1	17PG81	MB29	-43.3	-72.039	sand 500-1000µm	500-1000	296	163.34	3.166	1.9	1454.7	191.3	5.3	1.8	74.9	25.1	19.5	1085.3	14.5	75.9	22	0	27.2	0.01	138.2
C2	17PG64	MB17	-44.724	-72.563	sand 500-1000µm	500-1000	31	1416.5	1.966	0.13	1396.8	280.3	5.7	1.7	86.7	13.3	24.6	917.3	14.2	121.3	1	0	42.43	0.02	394.1
C3	17PG44	MB13	-45.109	-72.199	sand 500-1000µm	500-1000	183	377.89	0.088	0.02	1465.2	133.2	5.0	1.3	92.7	7.3	22.5	922.1	15.2	76.5	0	0	20.45	0.01	95.23
C3	17PG44	MB37	-45.109	-72.199	sand 250-500µm	250-100	183	377.89	0.088	0.02	1465.2	133.2	5.0	1.3	92.7	7.3	22.5	922.1	15.2	76.5	0	0	20.45	0.01	95.23
C3	17PG47	MB14	-45.111	-72.251	pebble 1.9-3.9cm	250-500	320	236.67	0.069	0.03	1440.3	137.5	5.1	1.3	92.1	7.9	22.7	953.2	14.3	158.1	0	0	19.68	0.01	85.33
C3	17PG47	MB36	-45.111	-72.251	pebble 1.9-3.9cm	500-1000	320	236.67	0.069	0.03	1440.3	137.5	5.1	1.3	92.1	7.9	22.7	953.2	14.3	158.1	0	0	19.68	0.01	85.33
C3	17PG48	MB16	-45.111	-72.251	sand 500-1000µm	500-1000	320	236.67	0.069	0.03	1440.3	137.5	5.1	1.3	92.1	7.9	22.7	953.2	14.3	158.1	0	0	19.68	0.01	85.33
C4	17PG01	MB21	-46.442	-72.758	sand 500-1000µm	500-1000	224	411.86	1.827	0.4	1306.0	84.3	4.2	1.6	60.9	39.1	24.8	986.5	14.4	220.8	97	3	0	42.5	0.02	290.1
C4	17PG02	MB2	-46.442	-72.758	pebble 2.0-5.0cm	250-500	224	411.86	1.827	0.4	1306.0	84.3	4.2	1.6	60.9	39.1	24.8	986.5	14.4	220.8	97	3	0	42.5	0.02	290.1
C4	17PG02	MB9	-46.442	-72.758	pebble 2.0-5.0cm	500-1000	224	411.86	1.827	0.4	1306.0	84.3	4.2	1.6	60.9	39.1	24.8	986.5	14.4	220.8	97	3	0	42.5	0.02	290.1
C4	17PG03	MB11	-46.442	-72.758	sand 250-500µm	250-500	224	411.86	1.827	0.4	1306.0	84.3	4.2	1.6	60.9	39.1	24.8	986.5	14.4	220.8	97	3	0	42.5	0.02	290.1
C4	17PG03	MB4	-46.442	-72.758	sand 500-1000µm	500-1000	224	411.86	1.827	0.4	1306.0	84.3	4.2	1.6	60.9	39.1	24.8	986.5	14.4	220.8	97	3	0	42.5	0.02	290.1
C4	17PG04	MB22	-46.442	-72.758	sand 500-1000µm	500-1000	224	411.86	1.827	0.4	1306.0	84.3	4.2	1.6	60.9	39.1	24.8	986.5	14.4	220.8	97	3	0	42.5	0.02	290.1
C5	17PG22	MB1	-46.479	-73.198	sand 500-1000µm	500-1000	65	679.93	41.89	6.2	1429.2	198.3	4.2	2.8	50.1	40.6	26.2	997.9	16.2	475.5	61	0.1	5	29.5	0.01	220.5
C5	17PG24	MB8	-46.501	-73.15	pebble 2.1-4.7cm	500-1000	143	274.55	67.39	24.5	1558.1	147.4	3.4	3.6	28.0	26.7	25.2	1156.9	18.1	656.3	63	2	0	/	/	/
C5	17PG23	MB39	-46.501	-73.15	sand 250-500µm	250-500	143	274.55	67.39	24.5	1558.1	147.4	3.4	3.6	28.0	26.7	25.2	1156.9	18.1	656.3	63	2	0	/	/	/
C5	17PG23	MB23	-46.501	-73.15	sand 500-1000µm	500-1000	143	274.55	67.39	24.5	1558.1	147.4	3.4	3.6	28.0	26.7	25.2	1156.9	18.1	656.3	63	2	0	/	/	/
C6	17PG30	MB3	-46.755	-72.883	pebble 1.6-5.2cm	250-500	214	1129.3	30.18	2.7	1350.5	129.7	3.6	2.8	38.5	41.1	23.9	1100.7	15.4	442.5	59	1	7	30.4	0.01	218.7
C6	17PG30	MB7	-46.755	-72.883	pebble 1.6-5.2cm	500-1000	214	1129.3	30.18	2.7	1350.5	129.7	3.6	2.8	38.5	41.1	23.9	1100.7	15.4	442.5	59	1	7	30.4	0.01	218.7
C6	17PG29	MB24	-46.755	-72.883	sand 250-500µm	250-500	214	1129.3	30.18	2.7	1350.5	129.7	3.6	2.8	38.5	41.1	23.9	1100.7	15.4	442.5	59	1	7	30.4	0.01	218.7
C6	17PG29	MB26	-46.755	-72.883	sand 500-1000µm	500-1000	214	1129.3	30.18	2.7	1350.5	129.7	3.6	2.8	38.5	41.1	23.9	1100.7	15.4	442.5	59	1	7	30.4	0.01	218.7
C6	17PG28	MB6	-46.724	-72.933	sand 500-1000µm	500-1000	224	1075.1	30.18	2.8	1369.4	119.2	3.4	2.3	34.7	40.0	24.5	1136.6	15.5	433.1	58	1	8	/	/	/
C6	17PG26	MB12	-46.722	-73.001	sand 250-500µm	250-500	242	726.89	21.13	2.9	1418.8	103.6	3.1	2.9	28.7	37.6	24.5	1174.2	15.7	457.9	63	1	2	/	/	/

Table S2: Cosmogenic nuclide data

Basin ID	Sample ID	Lab ID	type	Mass Quartz g	10Be/9Be (measu.)	Error %	N (10Be)corr*4	Error SLHL	Snow Shielding factor	26Al/27Al (measu.)	Error %	N(26Al)corr*4 atoms/g(qtz)	Error atoms/g(qtz)	26Al/10Be ratio	Error ratio
C1	17PG80	MB18	pebble	72.3	2.25E-14	6.3	5651		399	0.95	1.50E-14	10.0	42059	4281	7.4	0.9
C1	17PG80	MB28	pebble	113.5	3.05E-14	5.8	5032		317	0.95	1.67E-14	11.6	30652	3624	6.1	0.8
C1	17PG81	MB38	river sand	115.4	5.05E-14	5.3	8436		504	0.95	2.44E-14	7.8	58119	4572	6.9	0.7
C1	17PG81	MB29	river sand	113.3	4.93E-14	5.2	8393		462	0.95	1.64E-14	10.3	62420	6496	7.4	0.9
C2	17PG64	MB17	river sand	96.0	4.70E-14	5.5	7556		435	0.96	1.52E-14	9.7	78717	7695	10.4	1.2
C3	17PG44	MB13	river sand	96.2	7.30E-14	4.4	13682		625	0.98	4.23E-14	6.9	120467	8408	8.8	0.7
C3	17PG44	MB37	river sand	113.3	9.86E-14	4.3	15926		723	0.98	4.12E-14	6.2	113549	7111	7.1	0.6
C3	17PG47	MB14	pebble	96.3	4.41E-14	4.8	9146		467	0.98	3.07E-14	8.6	74849	6519	8.2	0.8
C4	17PG47	MB36	pebble	113.1	5.47E-14	5.4	9761		585	0.98	2.46E-14	7.6	72318	5512	7.4	0.7
C3	17PG48	MB16	river sand	96.1	6.52E-14	4.9	13835		701	0.98	4.86E-14	6.8	132759	9101	9.6	0.8
C4	17PG01	MB21	river sand	111.9	3.11E-14	5.6	5113		418	0.97	1.52E-14	9.1	44308	4095	8.7	1.1
C4	17PG02	MB2	pebble	101.8	3.84E-14	5.7	6975		521	0.97	1.43E-14	28.0	43984	12503	6.3	1.9
C4	17PG02	MB9	pebble	90.1	3.18E-14	9.4	6418		740	0.97	2.47E-14	12.9	67682	8833	10.5	1.8
C4	17PG03	MB11	river sand	95.7	2.50E-14	6.3	4670		462	0.97	1.41E-14	10.1	39426	4072	8.4	1.2
C4	17PG03	MB4	river sand	101.6	3.11E-14	6.7	5556		506	0.97	1.08E-14	22.2	31612	7153	5.7	1.4
C4	17PG04	MB22	river sand	113.2	6.58E-14	4.4	11182		579	0.97	2.80E-14	7.0	89572	6323	8.0	0.7
C5	17PG22	MB1	sand	102.1	2.52E-14	7.3	3811		407	0.98	1.85E-14	14.3	37261	5424	9.8	1.8
C5	17PG24	MB8	pebble	40.9	*4.38E-15*	15.1		/		0.99	*7.49E-16*	70.8	/	/	/	/
C5	17PG23	MB39	river sand	115.6	*1.73E-14*	8.6	2377		290	0.99	*4.06E-15*	15.6	/	/	/	/
C5	17PG23	MB23	river sand	113.5	1.51E-14	7.9	2027		319	0.99	*7.10E-15*	15.1	/	/	/	/
C6	17PG30	MB3	pebble	89.9	*8.95E-15*	10.2	/			0.95	*4.68E-15*	50.2	/	/	/	/
C6	17PG30	MB7	pebble	35.7	*4.75E-15*	14.9	/			0.95	*3.68E-15*	33.6	/	/	/	/
C6	17PG29	MB24	river sand	112.9	2.75E-14	6.1	4387		402	0.95	1.37E-14	11.2	36939	4192	8.4	1.2
C6	17PG29	MB26	river sand	112.9	3.63E-14	5.6	5933		452	0.95	1.48E-14	12.1	42267	5181	7.1	1.0
C6	17PG28	MB6	river sand	16.9	*4.05E-15*	15.4	/	/		0.96	*6.65E-15*	31.9	/	/	/	/
C6	17PG26	MB12	river sand	75.7	*7.25E-15*	10.4	/	/		0.96	*2.87E-15*	20.2	/	/	/	/

*1 10Be including topographic shielding

*2 10Be including topographic shielding and snow shielding

*3 10Be including topographic shielding and snow shielding, area covered with glaciar 100% shielded

*4 Blank corrected

Table S3: Production and erosion rate data

Catchment ID	Sampe ID and comment	LAB. Nr.	Ptot*1 atoms/g*ys	Ptot*2 atoms/g*ys	Ptot*3 atoms/g*ys	Denudation*1 mm/yr	Error mm/yr	App. Age yr	Error yr	Denudation mm/yr	Error mm/yr	App. Age*2 yr	Error yr	Denudation mm/yr	Error mm/yr	App. Age*3 yr	Error yr
C1	17PG80, 500-1000, pebble	MB18	4.155	3.948	3.871	0.57	0.54	0.21	1538	146	0.53	0.21	1568	147			
C1	17PG80, 250-500, pebble	MB28	4.155	3.948	3.871	0.64	0.61	0.15	1374	136	0.60	0.15	1401	141			
C1	17PG81,250-500, river sand	MB38	4.155	3.948	3.871	0.38	0.36	0.05	2325	231	0.35	0.05	2371	238			
C1	17PG081, 500-1000, river sand	MB29	4.155	3.948	3.871	0.38	0.36	0.05	2300	252	0.36	0.05	2346	242			
C2	17PG064, 500-1000, river sand	MB17	4.568	4.385	4.379	0.36	0.35	0.06	2332	224	0.35	0.06	2335	236			
C3	17PG044,500-1000, river sand	MB13	4.757	4.642	4.641	0.28	0.27	0.03	2849	289	0.27	0.03	2849	269			
C3	17PG044,250-500, river sand	MB37	4.757	4.642	4.641	0.24	0.20	0.02	4027	389	0.20	0.02	4028	393			
C3	17PG047,250-500, pebble	MB14	4.277	4.192	4.190	0.37	0.37	0.05	2263	219	0.37	0.05	2264	230			
C3	17PG047,500-1000, pebble	MB36	4.277	4.192	4.190	0.28	0.34	0.04	2431	244	0.34	0.04	2431	237			
C3	17PG048,500-1000, river sand	MB16	4.277	4.192	4.190	0.25	0.24	0.03	3431	320	0.24	0.03	3432	342			
C4	17PG001, 500-1000, river sand	MB21	4.676	4.536	4.515	0.68	0.66	0.15	1247	118	0.66	0.15	1253	129			
C4	17PG002 250-500, pebbles	MB2	4.676	4.536	4.515	0.50	0.49	0.09	1701	182	0.48	0.10	1709	156			
C4	17PG002, 500-1000, pebbles	MB9	4.676	4.536	4.515	0.54	0.53	0.24	1565	149	0.53	0.23	1572	165			
C4	17PG003, 250-1000, river sand	MB11	4.676	4.536	4.515	0.72	0.70	0.25	1204	102	0.70	0.24	1230	103			
C4	17PG003, 500-1000, river sand	MB4	4.676	4.536	4.515	0.63	0.61	0.17	1355	147	0.61	0.17	1361	140			
C4	17PG004, 500-1000, river sand	MB22	4.676	4.536	4.515	0.31	0.30	0.03	2727	258	0.30	0.03	2740	254			
C5	17PG022, 500-1000, river sand	MB1	4.985	4.885	4.584	0.84	0.82	0.32	997	97	0.77	0.29	1062	109			
C5	17PG23, 250-500, river sand	MB39	5.768	5.711	4.309	1.62	1.61	0.80	496	54	1.21	0.60	657	73			
C5	17PG23, 500-1000, river sand	MB23	5.768	5.711	4.309	1.91	1.89	0.58	423	42	1.42	0.22	560	49			
C6	17PG29, 250-500, river sand	MB24	5.316	5.050	4.915	0.88	0.84	0.23	963	100	0.82	0.23	990	95			
C6	17PG29, 500-1000, river sand	MB26	5.316	5.050	4.915	0.65	0.62	0.13	1303	127	0.60	0.12	1339	136			

*1 10Be including topographic shielding

*2 10Be including topographic shielding and snow shielding

*3 10Be including topographic shielding and snow shielding, area covered with glaciar 100% shielded

Figures

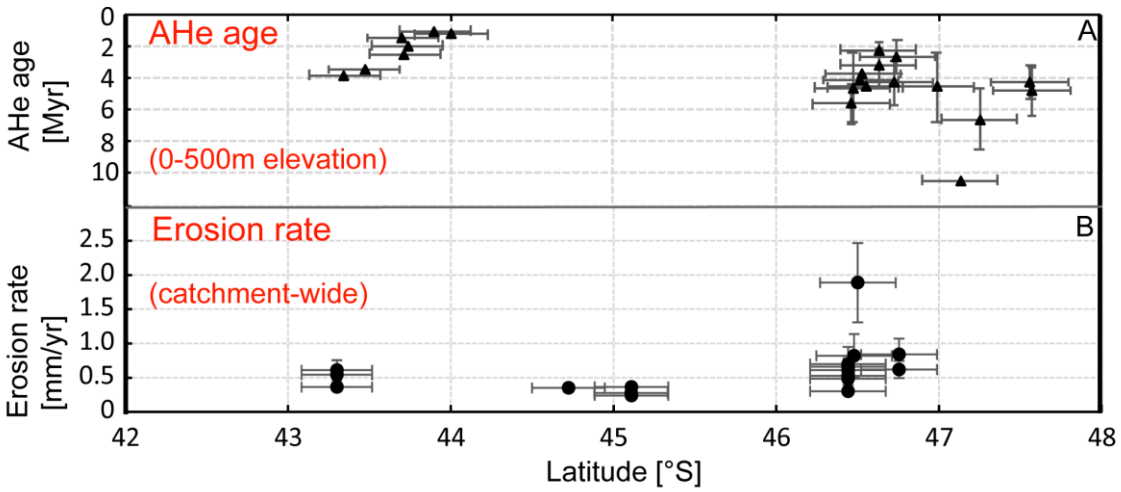

Fig. S1: Latitudinal variation of Apatite Helium (AHe) ages and catchment-wide erosion rates (based on topographic and snow shielding correction). AHe ages are sampled between 0 to 500m elevation and derived from Thomson et al. (2010), Guillaume et al. (2013) and, Georgieva et al. (2016).

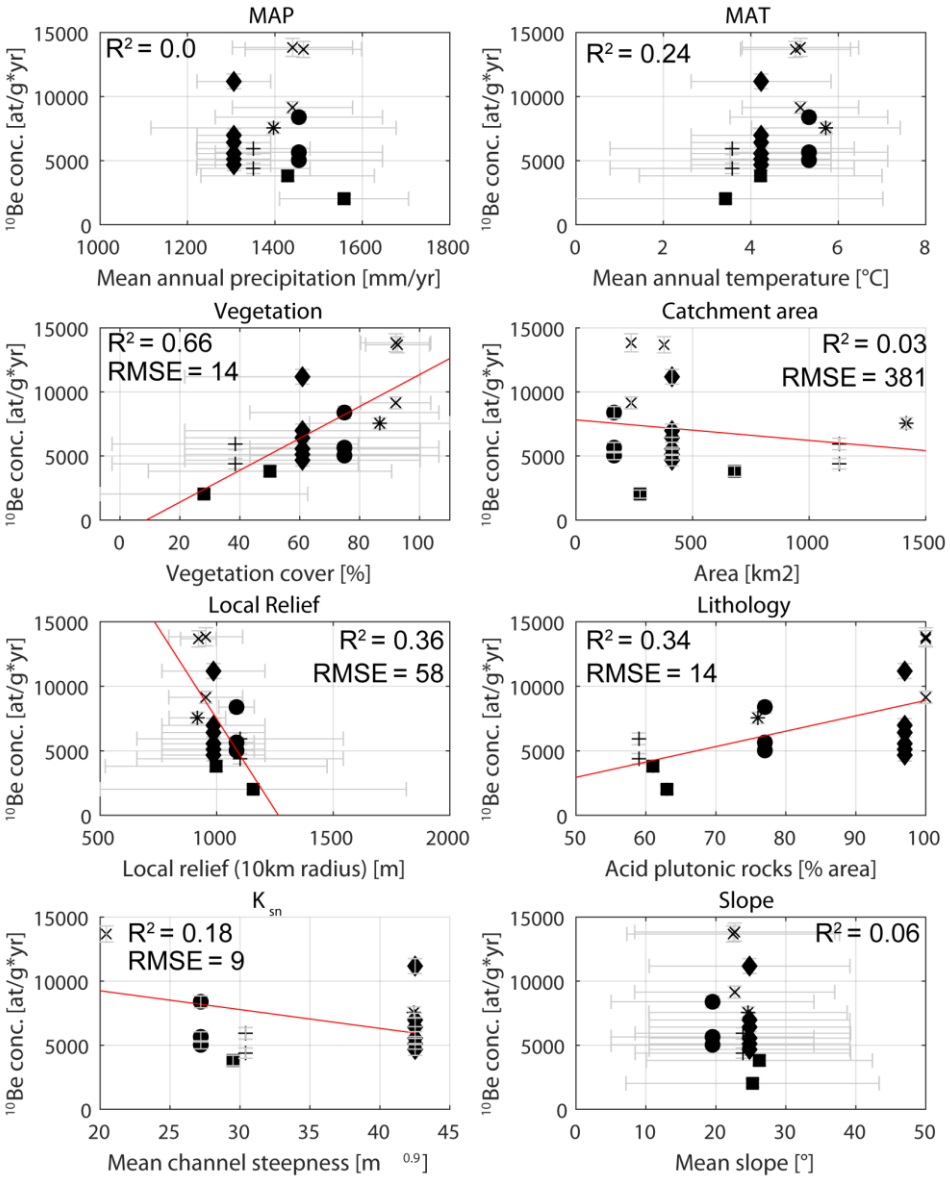

Fig. S2: In situ-produced 10Be concentrations normalized to Sea level high latitude (SLHL) are plotted versus different catchment parameters. In each subplot samples are indicated for catchment 1 with a circle sign (●), catchment 2 with an asterisk sign (*), catchment 3 with a cross sign (x), catchment 4 with a diamond sigh (♦), catchment 5 with a square sign (■) and catchment 6 with a plus sign (+).Uncertainties are displayed with grey bars, except for catchment area, K^{sn}, and lithology where the uncertainty is not representative. The red line represents a linear regression. The squared Pearson correlation coefficient (R^2) and the goodness of fit (RMSE) is shown. A RMSE value of 1 represents a perfect fit of the regression.

Bibliography

Ackert, R. P., Becker, R. A., Singer, B. S., Kurz, M. D., Caffee, M. W., and Mickelson, D. M. (2008). Patagonian Glacier Response During the Late Glacial–Holocene Transition. *Science* 321, 392–395. doi:10.1126/science.1157215.

Ackert, R. P., Singer, B. S., Guillou, H., Kaplan, M. R., and Kurz, M. D. (2003). Long-term cosmogenic 3He production rates from 40Ar/39Ar and K–Ar dated Patagonian lava flows at 47°S. *Earth and Planetary Science Letters* 210, 119–136. doi:10.1016/S0012-821X(03)00134-1.

Adams, B. A., and Ehlers, T. A. (2018). Tectonic controls of Holocene erosion in a glaciated orogen. *Earth Surf. Dynam.* 6, 595–610. doi:10/gdzw94.

Adriasola, A. C., Thomson, S. N., Brix, M. R., Hervé, F., and Stöckhert, B. (2006). Postmagmatic cooling and late Cenozoic denudation of the North Patagonian Batholith in the Los Lagos region of Chile, 41°–42°15′S. *Int J Earth Sci (Geol Rundsch)* 95, 504–528. doi:10.1007/s00531-005-0027-9.

Aguilar, G., Carretier, S., Regard, V., Vassallo, R., Riquelme, R., and Martinod, J. (2014). Grain size-dependent 10Be concentrations in alluvial stream sediment of the Huasco Valley, a semi-arid Andes region. *Quaternary Geochronology* 19, 163–172. doi:10.1016/j.quageo.2013.01.011.

Amundson, R., Dietrich, W., Bellugi, D., Ewing, S., Nishiizumi, K., Chong, G., et al. (2012). Geomorphologic evidence for the late Pliocene onset of hyperaridity in the Atacama Desert. *GSA Bulletin* 124, 1048–1070. doi:10.1130/B30445.1.

Aniya, M. (1988). Glacier Inventory for the Northern Patagonia Icefield, Chile, and Variations 1944/45 to 1985/86. *Arctic and Alpine Research* 20, 179–187. doi:10.1080/00040851.1988.12002663.

Belmont, P., Pazzaglia, F. J., and Gosse, J. C. (2007). Cosmogenic 10Be as a tracer for hillslope and channel sediment dynamics in the Clearwater River, western Washington State. *Earth and Planetary Science Letters* 264, 123–135. doi:10.1016/j.epsl.2007.09.013.

Bendle, J. M., Palmer, A. P., Thorndycraft, V. R., and Matthews, I. P. (2017a). High-resolution chronology for deglaciation of the Patagonian Ice Sheet at Lago Buenos Aires (46.5°S) revealed through varve chronology and Bayesian age modelling. *Quaternary Science Reviews* 177, 314–339. doi:10.1016/j.quascirev.2017.10.013.

Bendle, J. M., Palmer, A. P., Thorndycraft, V. R., and Matthews, I. P. (2017b). High-resolution chronology for deglaciation of the Patagonian Ice Sheet at Lago Buenos Aires (46.5°S) revealed through varve chronology and Bayesian age modelling. *Quaternary Science Reviews* 177, 314–339. doi:10.1016/j.quascirev.2017.10.013.

Binnie, S. A., Phillips, W. M., Summerfield, M. A., and Fifield, L. K. (2007). Tectonic uplift, threshold hillslopes, and denudation rates in a developing mountain range. *Geology* 35, 743–746. doi:10.1130/G23641A.1.

Breitsprecher, K., and Thorkelson, D. J. (2009). Neogene kinematic history of Nazca–Antarctic–Phoenix slab windows beneath Patagonia and the Antarctic Peninsula. *Tectonophysics* 464, 10–20. doi:10.1016/j.tecto.2008.02.013.

Breuer, S., Kilian, R., Baeza, O., Lamy, F., and Arz, H. (2013). Holocene denudation rates from the superhumid southernmost Chilean Patagonian Andes (53°S) deduced from lake sediment budgets. *Geomorphology* 187, 135–152. doi:10.1016/j.geomorph.2013.01.009.

Briner, J. P., and Swanson, T. W. (1998). Using inherited cosmogenic 36Cl to constrain glacial erosion rates of the Cordilleran ice sheet. *Geology* 26, 3. doi:10.1130/0091-7613(1998)026<0003:UICCTC>2.3.CO;2.

Brown et al. 1995.pdf.

Broxton, P. D., Zeng, X., Scheftic, W., and Troch, P. A. (2014). A MODIS-Based Global 1-km Maximum Green Vegetation Fraction Dataset. *J. Appl. Meteor. Climatol.* 53, 1996–2004. doi:10.1175/JAMC-D-13-0356.1.

Burbank, D. W., Leland, J., Fielding, E., Anderson, R. S., Brozovic, N., Reid, M. R., et al. (1996). Bedrock incision, rock uplift and threshold hillslopes in the northwestern Himalayas. *Nature* 379, 505–510. doi:10.1038/379505a0.

Cembrano, J., Hervé, F., and Lavenu, A. (1996). The Liquiñe Ofqui fault zone: a long-lived intra-arc fault system in southern Chile. *Tectonophysics* 259, 55–66. doi:10.1016/0040-1951(95)00066-6.

Chmeleff, J., von Blanckenburg, F., Kossert, K., and Jakob, D. (2010). Determination of the 10Be half-life by multicollector ICP-MS and liquid scintillation counting. *Nuclear Instruments and Methods in Physics Research Section B: Beam Interactions with Materials and Atoms* 268, 192–199. doi:10.1016/j.nimb.2009.09.012.

Codilean, A. T., Fenton, C. R., Fabel, D., Bishop, P., and Xu, S. (2014). Discordance between cosmogenic nuclide concentrations in amalgamated sands and individual fluvial pebbles in an arid zone catchment. *Quaternary Geochronology* 19, 173–180. doi:10.1016/j.quageo.2012.04.007.

Cogez, A., Herman, F., Pelt, É., Reuschlé, T., Morvan, G., Darvill, C. M., et al. (2017). U-Th and 10Be constraints on sediment recycling in proglacial settings, Lago Buenos Aires, Patagonia. *Earth Surface Dynamics Discussions*, 1–38. doi:10.5194/esurf-2017-45.

Curtis, S., Salahuddin, A., Adler, R. F., Huffman, G. J., Gu, G., and Hong, Y. (2007). Precipitation Extremes Estimated by GPCP and TRMM: ENSO Relationships. *J. Hydrometeor* 8, 678–689. doi:10.1175/JHM601.1.

Darvill, C. M., Bentley, M. J., and Stokes, C. R. (2015a). Geomorphology and weathering characteristics of erratic boulder trains on Tierra del Fuego, southernmost South America: Implications for dating of glacial deposits. *Geomorphology* 228, 382–397. doi:10.1016/j.geomorph.2014.09.017.

Darvill, C. M., Bentley, M. J., Stokes, C. R., Hein, A. S., and Rodés, Á. (2015b). Extensive MIS 3 glaciation in southernmost Patagonia revealed by cosmogenic nuclide dating of outwash sediments. *Earth and Planetary Science Letters* 429, 157–169. doi:10.1016/j.epsl.2015.07.030.

Darvill, C. M., Bentley, M. J., Stokes, C. R., and Shulmeister, J. (2016a). The timing and cause of glacial advances in the southern mid-latitudes during the last glacial cycle based on a synthesis of exposure ages from Patagonia and New Zealand. *Quaternary Science Reviews* 149, 200–214. doi:10.1016/j.quascirev.2016.07.024.

Darvill, C. M., Stokes, C. R., Bentley, M. J., Evans, D. J. A., and Lovell, H. (2016b). Dynamics of former ice lobes of the southernmost Patagonian Ice Sheet based on a glacial landsystems approach: DYNAMICS OF THE SOUTHERNMOST PATAGONIAN ICE SHEET. *Journal of Quaternary Science*. doi:10.1002/jqs.2890.

Davies, B. J., and Glasser, N. F. (2012). Accelerating shrinkage of Patagonian glaciers from the Little Ice Age (~AD 1870) to 2011. *Journal of Glaciology* 58, 1063–1084. doi:10.3189/2012JoG12J026.

Dietsch, C., Dortch, J. M., Reynhout, S. A., Owen, L. A., and Caffee, M. W. (2015). Very slow erosion rates and landscape preservation across the southwestern slope of the Ladakh Range, India. *Earth Surface Processes and Landforms* 40, 389–402. doi:10.1002/esp.3640.

Dussaillant, I., Berthier, E., and Brun, F. (2018). Geodetic Mass Balance of the Northern Patagonian Icefield from 2000 to 2012 Using Two Independent Methods. *Front. Earth Sci.* 6. doi:10.3389/feart.2018.00008.

Extended Data Table 1: Glacier characteristics and corresponding erosion rates in Chilean Patagonia and the Antarctic Peninsula. Available at: https://www.nature.com/articles/nature15385/tables/1 [Accessed October 15, 2018].

Fabel, D., Harbor, J., Dahms, D., James, A., Elmore, D., Horn, L., et al. (2004a). Spatial Patterns of Glacial Erosion at a Valley Scale Derived From Terrestrial Cosmogenic ^{10}Be and ^{26}Al Concentrations in Rock. *Annals of the Association of American Geographers* 94, 241–255. doi:10.1111/j.1467-8306.2004.09402001.x.

Fabel, D., Harbor, J., Dahms, D., James, A., Elmore, D., Horn, L., et al. (2004b). Spatial Patterns of Glacial Erosion at a Valley Scale Derived From Terrestrial Cosmogenic 10Be and 26Al Concentrations in Rock. *Annals of the Association of American Geographers* 94, 241–255. doi:10.1111/j.1467-8306.2004.09402001.x.

Fernandez, R. A., Anderson, J. B., Wellner, J. S., and Hallet, B. (2011). Timescale dependence of glacial erosion rates: A case study of Marinelli Glacier, Cordillera Darwin, southern Patagonia. *Journal of Geophysical Research: Earth Surface* 116. doi:10.1029/2010JF001685.

Fernandez, R. A., Anderson, J. B., Wellner, J. S., Minzoni, R. L., Hallet, B., and Smith, R. T. (2016). Latitudinal variation in glacial erosion rates from Patagonia and the Antarctic Peninsula (46°S–65°S). *GSA Bulletin* 128, 1000–1023. doi:10.1130/B31321.1.

Fick, S. E., and Hijmans, R. J. (2017). WorldClim 2: new 1-km spatial resolution climate surfaces for global land areas: NEW CLIMATE SURFACES FOR GLOBAL LAND AREAS. *International Journal of Climatology*. doi:10.1002/joc.5086.

Foresta, L., Gourmelen, N., Weissgerber, F., Nienow, P., Williams, J. J., Shepherd, A., et al. (2018). Heterogeneous and rapid ice loss over the Patagonian Ice Fields revealed by CryoSat-2 swath radar altimetry. *Remote Sensing of Environment* 211, 441–455. doi:10.1016/j.rse.2018.03.041.

Full Text PDF Available at: https://onlinelibrary.wiley.com/doi/pdf/10.1002/esp.1261 [Accessed November 29, 2018].

Georgieva, V., Melnick, D., Schildgen, T. F., Ehlers, T. A., Lagabrielle, Y., Enkelmann, E., et al. (2016). Tectonic control on rock uplift, exhumation, and topography above an oceanic ridge collision: Southern Patagonian Andes (47°S), Chile: Neotectonics and Topography in Patagonia. *Tectonics* 35, 1317–1341. doi:10.1002/2016TC004120.

Glasser, N. F., and Hambrey, M. J. (2002). Sedimentary facies and landform genesis at a temperate outlet glacier: Soler Glacier, North Patagonian Icefield. *Sedimentology* 49, 43–64. doi:10.1046/j.1365-3091.2002.00431.x.

Glasser, N. F., Harrison, S., Ivy-Ochs, S., Duller, G. A. T., and Kubik, P. W. (2006). Evidence from the Rio Bayo valley on the extent of the North Patagonian Icefield during the Late Pleistocene–Holocene Transition. *Quaternary Research* 65, 70–77. doi:10.1016/j.yqres.2005.09.002.

Glasser, N. F., Jansson, K. N., Harrison, S., and Rivera, A. (2005). Geomorphological evidence for variations of the North Patagonian Icefield during the Holocene. *Geomorphology* 71, 263–277. doi:10.1016/j.geomorph.2005.02.003.

Godard, V., Burbank, D. W., Bourlès, D. L., Bookhagen, B., Braucher, R., and Fisher, G. B. (2012). Impact of glacial erosion on ^{10}Be concentrations in fluvial sediments of the Marsyandi catchment, central Nepal: GLACIAL EROSION IN THE HIMALAYAS. *Journal of Geophysical Research: Earth Surface* 117, n/a-n/a. doi:10.1029/2011JF002230.

Grin, E., Schaller, M., and Ehlers, T. A. (2018). Spatial distribution of cosmogenic 10Be derived denudation rates between the Western Tian Shan and Northern Pamir, Tajikistan. *Geomorphology* 321, 1–15. doi:10.1016/j.geomorph.2018.08.007.

Hallet, B., Hunter, L., and Bogen, J. (1996). Rates of erosion and sediment evacuation by glaciers: A review of field data and their implications. *Global and Planetary Change* 12, 213–235. doi:10.1016/0921-8181(95)00021-6.

Hartmann, J., and Moosdorf, N. (2012). The new global lithological map database GLiM: A representation of rock properties at the Earth surface. *Geochemistry, Geophysics, Geosystems* 13. doi:10.1029/2012GC004370.

Hein, A. S., Hulton, N. R. J., Dunai, T. J., Schnabel, C., Kaplan, M. R., Naylor, M., et al. (2009a). Middle Pleistocene glaciation in Patagonia dated by cosmogenic-nuclide measurements on outwash gravels. *Earth and Planetary Science Letters* 286, 184–197. doi:10.1016/j.epsl.2009.06.026.

Hein, A. S., Hulton, N. R. J., Dunai, T. J., Schnabel, C., Kaplan, M. R., Naylor, M., et al. (2009b). Middle Pleistocene glaciation in Patagonia dated by cosmogenic-nuclide measurements on outwash gravels. *Earth and Planetary Science Letters* 286, 184–197. doi:10.1016/j.epsl.2009.06.026.

Hein, A. S., Hulton, N. R. J., Dunai, T. J., Sugden, D. E., Kaplan, M. R., and Xu, S. (2010). The chronology of the Last Glacial Maximum and deglacial events in central Argentine Patagonia. *Quaternary Science Reviews* 29, 1212–1227. doi:10.1016/j.quascirev.2010.01.020.

Henríquez, W. I., Villa-Martínez, R., Vilanova, I., De Pol-Holz, R., and Moreno, P. I. (2017). The last glacial termination on the eastern flank of the central Patagonian Andes (47 ° S). *Climate of the Past* 13, 879–895. doi:10.5194/cp-13-879-2017.

Hobley, D. E. J., Sinclair, H. D., and Cowie, P. A. (2010). Processes, rates, and time scales of fluvial response in an ancient postglacial landscape of the northwest Indian Himalaya. *GSA Bulletin* 122, 1569–1584. doi:10.1130/B30048.1.

Hubbard, A., Hein, A. S., Kaplan, M. R., Hulton, N. R. J., and Glasser, N. (2005). A Modelling Reconstruction of the Last Glacial Maximum Ice Sheet and Its Deglaciation in the Vicinity of the Northern Patagonian Icefield, South America. *Geografiska Annaler: Series A, Physical Geography* 87, 375–391. doi:10.1111/j.0435-3676.2005.00264.x.

Hulton, N. R. J., Purves, R. S., McCulloch, R. D., Sugden, D. E., and Bentley, M. J. (2002). The Last Glacial Maximum and deglaciation in southern South America. *Quaternary Science Reviews* 21, 233–241. doi:10.1016/S0277-3791(01)00103-2.

Kaplan, M. R., Ackert, R. P., Singer, B. S., Douglass, D. C., and Kurz, M. D. (2004). Cosmogenic nuclide chronology of millennial-scale glacial advances during O-isotope stage 2 in Patagonia. *GSA Bulletin* 116, 308–321. doi:10.1130/B25178.1.

Kaplan, M. R., Coronato, A., Hulton, N. R. J., Rabassa, J. O., Kubik, P. W., and Freeman, S. P. H. T. (2007). Cosmogenic nuclide measurements in southernmost South America and implications for landscape change. *Geomorphology* 87, 284–301. doi:10.1016/j.geomorph.2006.10.005.

Kaplan, M. R., Fogwill, C. J., Sugden, D. E., Hulton, N. R. J., Kubik, P. W., and Freeman, S. P. H. T. (2008). Southern Patagonian glacial chronology for the Last Glacial period and implications for Southern Ocean climate. *Quaternary Science Reviews* 27, 284–294. doi:10.1016/j.quascirev.2007.09.013.

Kaplan, M. R., Strelin, J. A., Schaefer, J. M., Denton, G. H., Finkel, R. C., Schwartz, R., et al. (2011). In-situ cosmogenic 10Be production rate at Lago Argentino, Patagonia: Implications for late-glacial climate chronology. *Earth and Planetary Science Letters* 309, 21–32. doi:10.1016/j.epsl.2011.06.018.

Koppes, M., Hallet, B., and Anderson, J. (2009). Synchronous acceleration of ice loss and glacial erosion, Glaciar Marinelli, Chilean Tierra del Fuego. *Journal of Glaciology* 55, 207–220. doi:10.3189/002214309788608796.

Koppes, M., Hallet, B., Rignot, E., Mouginot, J., Wellner, J. S., and Boldt, K. (2015). Observed latitudinal variations in erosion as a function of glacier dynamics. *Nature* 526, 100–103. doi:10.1038/nature15385.

Koppes, M. N., and Montgomery, D. R. (2009). The relative efficacy of fluvial and glacial erosion over modern to orogenic timescales. *Nature Geoscience* 2, 644–647. doi:10.1038/ngeo616.

Koppes, M., Sylwester, R., Rivera, A., and Hallet, B. (2010). Variations in Sediment yield Over the Advance and Retreat of a Calving Glacier, Laguna San Rafael, North Patagonian Icefield. *Quaternary Research* 73, 84–95. doi:10.1016/j.yqres.2009.07.006.

Korschinek, G., Bergmaier, A., Faestermann, T., Gerstmann, U. C., Knie, K., Rugel, G., et al. (2010). A new value for the half-life of 10Be by Heavy-Ion Elastic Recoil Detection and liquid scintillation counting. *Nuclear Instruments and Methods in Physics Research Section B: Beam Interactions with Materials and Atoms* 268, 187–191. doi:10.1016/j.nimb.2009.09.020.

Li, Y., Harbor, J., Stroeven, A. P., Fabel, D., Kleman, J., Fink, D., et al. (2005). Ice sheet erosion patterns in valley systems in northern Sweden investigated using cosmogenic nuclides. *Earth Surface Processes and Landforms* 30, 1039–1049. doi:10.1002/esp.1261.

Lopez, P., Sirguey, P., Arnaud, Y., Pouyaud, B., and Chevallier, P. (2008). Snow cover monitoring in the Northern Patagonia Icefield using MODIS satellite images (2000–2006). *Global and Planetary Change* 61, 103–116. doi:10.1016/j.gloplacha.2007.07.005.

Meier, W. J.-H., Grießinger, J., Hochreuther, P., and Braun, M. H. (2018). An Updated Multi-Temporal Glacier Inventory for the Patagonian Andes With Changes Between the Little Ice Age and 2016. *Front. Earth Sci.* 6. doi:10.3389/feart.2018.00062.

Mouginot, J., and Rignot, E. (2015). Ice motion of the Patagonian Icefields of South America: 1984–2014. *Geophysical Research Letters* 42, 1441–1449. doi:10.1002/2014GL062661.

Mücher, H., van Steijn, H., and Kwaad, F. (2018). "Chapter 2 - Colluvial and Mass Wasting Deposits," in *Interpretation of Micromorphological Features of Soils and Regoliths (Second Edition)*, eds. G. Stoops, V. Marcelino, and F. Mees (Elsevier), 21–36. doi:10.1016/B978-0-444-63522-8.00002-4.

Norton, K. P., Abbühl, L. M., and Schlunegger, F. (2010). Glacial conditioning as an erosional driving force in the Central Alps. *Geology* 38, 655–658. doi:10/b3smhm.

NSIDC, N. S. and I. D. C. (2018). GLIMS, and National Snow and Ice Data Center. 2005, updated 2012. GLIMS Glacier Database. Version 1. [glims_db_20171027]. doi:http://dx.doi.org/10.7265/N5V98602.

Palumbo, L., Hetzel, R., Tao, M., and Li, X. (2010). Topographic and lithologic control on catchment-wide denudation rates derived from cosmogenic 10Be in two mountain ranges at the margin of NE Tibet. *Geomorphology* 117, 130–142. doi:10.1016/j.geomorph.2009.11.019.

Pardo-Casas, F., and Molnar, P. (1987). Relative motion of the Nazca (Farallon) and South American plates since Late Cretaceous time. *Tectonics* 6, 233–248.

Ramos, V. A., and Ghiglione, M. C. (2008). "Tectonic Evolution of the Patagonian Andes," in *Developments in Quaternary Sciences* The Late Cenozoic of Patagonia and Tierra del Fuego., ed. J. Rabassa (Elsevier), 57–71. doi:10.1016/S1571-0866(07)10004-X.

Rice, S., and Church, M. (1998). Grain size along two gravel-bed rivers: statistical variation, spatial pattern and sedimentary links. *Earth Surface Processes and Landforms* 23, 345–363. doi:10.1002/(SICI)1096-9837(199804)23:4<345::AID-ESP850>3.0.CO;2-B.

Riebe, C. S., Sklar, L. S., Lukens, C. E., and Shuster, D. L. (2015). Climate and topography control the size and flux of sediment produced on steep mountain slopes. *Proceedings of the National Academy of Sciences*, 201503567. doi:10.1073/pnas.1503567112.

Rignot, E., Rivera, A., and Casassa, G. (2003). Contribution of the Patagonia Icefields of South America to Sea Level Rise. *Science* 302, 434–437. doi:10.1126/science.1087393.

Riihimaki, C. A., MacGregor, K. R., Anderson, R. S., Anderson, S. P., and Loso, M. G. (2005). Sediment evacuation and glacial erosion rates at a small alpine glacier. *Journal of Geophysical Research: Earth Surface* 110. doi:10.1029/2004JF000189.

Rivera, A., Benham, T., Casassa, G., Bamber, J., and Dowdeswell, J. A. (2007). Ice elevation and areal changes of glaciers from the Northern Patagonia Icefield, Chile. *Global and Planetary Change* 59, 126–137. doi:10.1016/j.gloplacha.2006.11.037.

Schuerch, P., Densmore, A. L., McArdell, B. W., and Molnar, P. (2006). The influence of landsliding on sediment supply and channel change in a steep mountain catchment. *Geomorphology* 78, 222–235. doi:10.1016/j.geomorph.2006.01.025.

Singer, B. S., Ackert, R. P., and Guillou, H. (2004). 40Ar/39Ar and K-Ar chronology of Pleistocene glaciations in Patagonia. *GSA Bulletin* 116, 434–450. doi:10.1130/B25177.1.

Starke, J., Ehlers, T. A., and Schaller, M. (2017). Tectonic and Climatic Controls on the Spatial Distribution of Denudation Rates in Northern Chile (18°S to 23°S) Determined From Cosmogenic Nuclides: ^{10} Be Denudation Rates in Northern Chile. *Journal of Geophysical Research: Earth Surface*. doi:10.1002/2016JF004153.

Stock, G. M., Ehlers, T. A., and Farley, K. A. (2006). Where does sediment come from? Quantifying catchment erosion with detrital apatite (U-Th)/He thermochronometry. *Geology* 34, 725–728.

Stock, G. M., Frankel, K. L., Ehlers, T. A., Schaller, M., Briggs, S. M., and Finkel, R. C. (2009). Spatial and temporal variations in denudation of the Wasatch Mountains, Utah, USA. *Lithosphere* 1, 34–40. doi:10.1130/L15.1.

Strunk, A., Knudsen, M. F., Egholm, D. L., Jansen, J. D., Levy, L. B., Jacobsen, B. H., et al. (2017). One million years of glaciation and denudation history in west Greenland. *Nat Commun* 8. doi:10.1038/ncomms14199.

Thomson, S. N., Brandon, M. T., Tomkin, J. H., Reiners, P. W., Vásquez, C., and Wilson, N. J. (2010). Glaciation as a destructive and constructive control on mountain building. *Nature* 467, 313–317. doi:10.1038/nature09365.

Thomson, S. N., Hervé, F., and Stöckhert, B. (2001). Mesozoic-Cenozoic denudation history of the Patagonian Andes (southern Chile) and its correlation to different subduction processes. *Tectonics* 20, 693–711. doi:10.1029/2001TC900013.

Turner, K. J., Fogwill, C. J., McCULLOCH, R. D., and Sugden, D. E. (2005). Deglaciation of the Eastern Flank of the North Patagonian Icefield and Associated Continental-Scale Lake Diversions. *Geografiska Annaler: Series A, Physical Geography* 87, 363–374. doi:10.1111/j.0435-3676.2005.00263.x.

USGS (2018). ASTER- Global DEM. Available at: https://gdex.cr.usgs.gov/gdex/ [Accessed November 13, 2018].

Warren, C. R., and Sugden, D. E. (1993). The Patagonian Icefields: A Glaciological Review. *Arctic and Alpine Research* 25, 316. doi:10.2307/1551915.

Wenzens, G. (2002). The influence of tectonically derived relief and climate on the extent of the last Glaciation east of the Patagonian ice fields (Argentina, Chile). *Tectonophysics* 345, 329–344. doi:10.1016/S0040-1951(01)00219-0.

Whipple, K. X. (2004). Bedrock Rivers and the Geomorphology of Active Orogens. *Annual Review of Earth and Planetary Sciences* 32, 151–185. doi:10.1146/annurev.earth.32.101802.120356.

Willis, M. J., Melkonian, A. K., Pritchard, M. E., and Ramage, J. M. (2012). Ice loss rates at the Northern Patagonian Icefield derived using a decade of satellite remote sensing. *Remote Sensing of Environment* 117, 184–198. doi:10.1016/j.rse.2011.09.017.

Wittmann, H., Blanckenburg, F. von, Kruesmann, T., Norton, K. P., and Kubik, P. W. (2007). Relation between rock uplift and denudation from cosmogenic nuclides in river sediment in the Central Alps of Switzerland. *Journal of Geophysical Research: Earth Surface* 112. doi:10.1029/2006JF000729.

Appendix

Introduction to the appendix

This appendix is designed to highlight unpublished data and to show new developments in the multivariate statistical analysis. A digital appendix is provided that contains Matlab scripts that have been applied to the research questions of this thesis.

All data of this thesis are archived on the WG Ehlers server under:

General data and working files:	esd01/docs/jstarke/
ArcGIS data:	esd01/share/arc/extreme/Andes/jstarke/ esd01/share/arc/chile/jstarke/

1 Unpublished data

In PAPER II of this thesis new samples were analyzed for southern Peru from 15°S to 19°S latitude. PAPER II investigates ^{10}Be-derived denudation rates that are restricted to catchments draining the Western Cordillera and for catchments that are not similar to already published literature. In Table 1 of this appendix additional ^{10}Be concentrations, ^{10}Be-derived denudation rates and catchment parameters of catchments draining the Western Cordillera and Coastal Cordillera are shown that were not used for publication. In Table 2 unpublished ^{26}Al concentrations and analytical values of PAPER II are reported.

In Table 3 the unpublished ^{10}Be concentrations and ^{26}Al concentrations of the sample GB1 and GB2 are presented. The samples are derived from the marine core GeoB 7136-2. The marine core GeoB 7136-2 is located in northern-central Chile at 29.7167°S and 72.0662°W. The samples GB1 and GB2 are test samples to demonstrate that it is possible to measure in situ- produced ^{10}Be and ^{26}Al in marine core samples in front of the Chilean Coast. The sample GB1 is taken from the core section of 1.3 to 1.9 m depth and GB2 from a core depth of 3.70 to 3.72m. The analyzed grain size spans from 50 to 100µm. Approximately 300 µg of ^{9}Be was added. Future research could focus on the calculation of denudation rates from the calculated ^{10}Be and ^{26}Al concentration.

Table 1: Unpublished ^{10}Be-derived denudation rates and catchment parameters of PAPER II

LAB-ID	Sample name	lat °S	long °W	sample elev. m	mean elev. m	area km^2	mean slope degree	error degree	mean local relief 5km in m	error	mean ksn m$^{0.9}$	error	MAP mm/a	error	Stream Order Strahler	Vegetation cover %	Error %	Grain size mm	blank corr.	^{10}Be conc. at/gr*yr	Den. Rate m/Myr	Error m/Myr	App. Age kyr	Error kyr
Coastal Cordillera																								
JS58	16PE010	-17.000	-72.05	105	709	107	12.4	7.1	757.1	181.6	122.7	67.2	12.8	10.5	2.0	11.1	8.7	0.5-1		639356	21.1	1.0	32	3
JS73	16PE050	-16.249	-73.55	109	1,655	493	5.8	5.8	449.2	220.5	153.5	172.1	9.7	11.7	5.0	2.5	1.7	0.5-1		390932	1.8	0.1	315	33
JS74	16PE052	-16.174	-73.76	57	1,743	458	7.0	6.4	536.4	249.4	171.3	195.8	10.4	24.5	4.0	6.2	5.3	0.5-1		494251	3.2	0.1	195	21
JS76	16PE053	-15.968	-74.04	27	2,021	298	12.9	8.4	708.1	369.2	236.5	160.9	9.9	14.4	3.0	10.0	9.1	0.5-1		2811931	5.8	0.3	112	12
JS79	16PE061	-15.835	-74.29	10	1,427	315	14.5	8.2	813.6	369.8	185.4	97.1	97.1	28.9	3.0	31.6	19.0	0.5-1		1863607	6.9	0.3	98	11
JS86	16PE015	-17.879	-71.04	15	701	95	9.8	4.7	422.0	35.0	141.7	106.0	0.0	0.0	1.0	7.0	4.1	0.25-0.5		1343550	33.3	1.5	21	2
JS88	16PE011	-17.071	-71.93	15	1,171	702	9.9	6.9	778.0	25.0	134.1	89.3	0.0	0.0	1.0	19.3	16.6	0.25-0.5		823651	11.5	0.5	62	6
Western Cordillera																								
JS51	16PE022	-17.927	-70.18	938	3,345	749	18.8	9.0	1241.5	443.6	210.4	132.2	116.4	61.8	5.0	20.3	13.7	0.5-1		590608	18.9	0.9	36	4
JS52	16PE020	-18.186	-70.33	149	1,992	955	12.1	9.1	763.1	400.0	148.0	150.1	42.2	31.9	4.0	5.6	3.6	0.5-1		955937	13.5	0.5	49	5
JS54	16PE035	-17.613	-70.76	549	2,503	435	14.1	8.2	771.5	336.2	176.1	141.0	78.2	78.5	4.0	11.7	8.0	0.5-1		1360862	14.6	0.6	46	5
JS61	16PE004	-16.467	-71.95	1309	3,851	160	7.4	7.4	526.7	315.1	71.5	24.5	6.4	5.5	3.0	9.2	6.3	0.5-1		1832604	42.4	2.3	16	2
JS63	16PE021	-18.122	-70.33	244	2,275	943	11.5	9.6	715.6	408.9	132.0	165.1	77.3	108.5	4.0	12.4	9.6	0.5-1		590608	17.8	0.7	38	4
JS64	16PE023	-17.873	-70.1	1385	3,586	558	20.0	8.1	1181.5	377.9	222.4	86.8	160.0	82.3	3.0	15.5	9.2	0.5-1		537507	9.3	0.5	71	7
JS66	16PE038	-17.646	-70.92	526	1,411	656	7.3	5.7	450.5	184.8	72.7	35.6	23.3	31.5	4.0	10.0	6.3	0.5-1		401492	13.9	0.6	51	6
JS67	16PE047	-16.000	-72.48	624	3,392	435	12.0	9.4	978.9	561.1	310.5	239.6	102.9	60.2	4.0	41.0	25.3	0.5-1		762116	137.0	8.1	5	1
JS69	16PE034	-17.686	-70.84	401	3,009	3,349	12.5	9.2	899.2	416.5	159.2	199.9	113.3	104.0	5.0	36.8	22.6	0.5-1		1015691	26.4	1.3	26	3
JS78	16PE057	-15.556	-73.73	2144	3,346	325	14.3	9.5	846.4	400.3	163.3	142.1	144.8	46.5	4.0	41.3	18.2	0.5-1		366292	49.3	2.3	14	1
JS81	16PE045	-16.343	-72.13	1283	3,738	1,731	13.5	8.7	913.9	372.5	223.0	193.4	133.5	124.6	5.0	40.5	24.5	0.5-1		317308	76.9	3.4	9	1
JS83	16PE005	-16.466	-71.93	1161	3,816	7,992	9.1	7.6	739.6	479.7	315.7	372.4	187.2	147.7	6.0	46.7	27.5	0.5-1		495218	50.5	3.0	13	1
JS89	16PE033	-17.781	-70.49	558	3,125	2,182	16.5	9.3	1131.8	445.3	177.8	146.6	100.6	77.9	5.0	39.8	25.1	0.25-0.5		748115	25.3	0.8	27	3

Table 2: Unpublished ^{26}Al concentrations of PAPER II

Lab ID	Sample name	lat °S	long °W	dissolved quartz g	carrier ^{27}Al ppm	^{27}Al mg	^{26}Al/^{27}Al (meas.)	Error %	^{26}Al/^{27}Al blank corr.	blank corr. ^{26}Al conc. at/gr(qtz)	Error atoms/g(qtz)
JS53	16PE018	-18.1589	-70.6702	24.83	416.6	10.35	3.62E-13	4.44	3.61E-13	3367574	149568
JS54	16PE035	-17.6126	-70.7586	41.09	180.8	7.429	1.11E-12	3.94	1.11E-12	4478884	176492
JS61	16PE004	-16.4671	-71.9536	37.99	45.8	1.74	3.05E-12	3.95	3.05E-12	3114795	123061
JS62	16PE003	-16.5356	-72.8604	38.24	144.9	5.542	4.92E-13	4.3	4.91E-13	1590278	68414
JS72	16PE019	-18.2931	-70.4334	43.71	85.0	3.716	3.96E-12	3.81	3.96E-12	7508315	286087
JS76	16PE053	-15.9676	-74.0382	42.12	64.2	2.704	3.60E-12	3.83	3.60E-12	5152746	197372
JS84	16PE065	-14.977	-74.9886	41.65	163.3	6.8	3.63E-13	5.08	3.62E-13	1322496	67216
JS86	16PE015	-17.8786	-71.0381	41.71	156.4	6.525	6.46E-13	4.22	6.45E-13	2255783	95221

Table 3: Unpublished ^{10}Be and ^{26}Al concentrations of marine core GeoB 7136-2

Lab ID	dissolved quartz g	carrier ^{9}Be g	^{10}Be/^{9}Be (meas.)	Error %	blank corr. ^{10}Be conc. atoms/g(qtz)	Error oms/g(qtz)	carrier ^{27}Al ppm	^{26}Al/^{27}Al (meas.)	Error %	blank corr. ^{26}Al conc. atoms/g(qtz)	Error atoms/g(qtz)
GB1	26.21	0.8838	3.99E-13	3.49	332543	11756	335	2.30E-13	4.03	1719704	69406
GB2	32.96	0.8844	4.63E-13	3.41	307502	10597	271	2.59E-13	3.79	1562971	59313

2 Developed methods and digital appendix

This thesis applies multivariate statistics to answer research questions. In PAPER I and PAPER II a factor analysis was applied and further developed. In PAPER I a simple and classical form of a factor analysis is performed which calculates the results on the basis of mean values. In contrast to PAPER I, results of PAPER II are calculated by a factor analysis which implements a Monte Carlo approach. The advantage of the Monte Carlo approach is to be independent from mean values and to address uncertainties of each value.

The factor analysis is written in Matlab. All versions of the factor analysis are attached in the digital appendix which is archived on a CD that sticks to the last page of this thesis. The CD is structured into the folders Simple_Factor-Analysis and MonteCarlo_Factor-Analysis. In each subfolder the source code, functions and the database are saved. Please note that the computation time of the factor analysis including the Monte Carlo approach can range between several hours and depends on the amount of data analyzed and the general system speed.

The digital appendix contains all Tables from PAPER II and PAPER III in the folders Paper2_Tables and Paper3_Tables.

Acknowledgements

With the last sentences of this thesis, I want to express my gratitude to anyone who helped and supported me during the last years. First of all, I want to thank my colleagues that are not related to research. I am not able to express in words how thankful I am for the help I received by the technicians Dagmar Kost, Dorothea Muehlbayer-Renner, Martina Brenn, Barbara Meier and Simone Schafflick as well as by the secretaries Claudia Jahn und Beate Fritz. I am so thankful because I experienced with them real and honest team work between friends who always care for each other. Without your hard work research at the University would not be possible and I hope that you will receive in future the appreciation you all deserve for your work by the scientists and students. Second, I would like to thank all my research colleagues who supported me to develop new perspectives and to overcome insecurity. I am sorry that I will not mention all names at this point but the acknowledgement section is limited to one page ☺. Thank you all for your encouraging words, lovely goodbye gifts and a lot of proof reading. Third, field work was always my favorite science adventure and I would like to thank Nikita Avdievitch, Lorenz Michel and Sarah Falkowski for help in the field and the funny moments we experienced together. I would also like to thank Silvia Rosas for helping me to ship samples from Peru to Germany without official permission. Fourth, I would like to highlight the support of a special research scientist. A person with a sharp mind who always treated me fair and with respect. She invested always a lot of time into my education and development. Thank you a lot Hella Wittmann. PhD comics illustrates it very well what challenges needs to be solve by a PhD student but nothing prepares you for the emotional roller coaster. It is so important to have family and friends during this time. I thank Katharina Klang and many other friend who listened to my worrier. I thank my mam, Maria Starke, who is my idol and hero in life. She raised me without help and I am thankful that she showed me how beautiful the world is. I thank my husband Florian Steinbach who makes me happy and encourages me to stay positive and enjoy life in any situation and every day. Finally, I would like to thank my supervisors Mirjam Schaller, Todd Ehlers and Tibor Dunai for showing me what it means to be scientist. I acknowledge funding by European Research Council (ERC) Consolidator Grant to T. Ehlers (ERC-CoG 615703).